

UC Berkeley

UC Berkeley Electronic Theses and Dissertations

Title

Seismic Performance Assessment in Dense Urban Environments

Permalink

<https://escholarship.org/uc/item/3z96n4fr>

Author

Mason, Henry Benjamin

Publication Date

2011

Peer reviewed|Thesis/dissertation

Seismic Performance Assessment in Dense Urban Environments

by

Henry Benjamin Mason

A dissertation submitted in partial satisfaction of the
requirements for the degree of
Doctor of Philosophy

in

Engineering - Civil and Environmental Engineering

in the

Graduate Division

of the

University of California, Berkeley

Committee in charge:

Professor Jonathan D. Bray, Chair
Professor Douglas S. Dreger
Professor Bruce L. Kutter
Professor Raymond B. Seed

Fall 2011

Seismic Performance Assessment in Dense Urban Environments

Copyright 2011
by
Henry Benjamin Mason

Abstract

Seismic Performance Assessment in Dense Urban Environments

by

Henry Benjamin Mason

Doctor of Philosophy in Engineering - Civil and Environmental Engineering

University of California, Berkeley

Professor Jonathan D. Bray, Chair

In seismically active, densely populated areas, buildings within a city block interact with one another during an earthquake. This phenomenon, whereby two adjacent buildings interact with each other through the surrounding soil during an earthquake, is often called structure-soil-structure interaction (SSSI). SSSI effects are less understood than soil-foundation-structure interaction (SFSI) effects. There are a lack of high-quality case histories that clearly show SSSI, which is a key reason that SSSI is less understood than SFSI. SSSI effects can potentially be detrimental and lead to more damage within the soil-foundation-structure system. Accordingly, it is important to understand when SSSI effects are important, and include them in engineering analysis and design when necessary.

This dissertation describes three centrifuge tests designed to simulate SSSI and SFSI case histories. All centrifuge test described within this dissertation were performed at the University of California at Davis Center for Geotechnical Modeling (UCD-CGM). The first test, Centrifuge Test-1, examined two inelastic moment-resisting frame structures atop a bed of dry, dense sand. One frame structure represented a prototypical three-story moment-resisting frame structure founded on spread footings. The other frame structure represented a prototypical nine-story moment-resisting frame structure founded on a three-story basement. The two structures were located a significant distance apart, and thus, SSSI effects were masked. Accordingly, the purpose of Test-1 was to examine SFSI effects of inelastic frame structures and to serve as a baseline test (i.e., a control test). The second test, Centrifuge Test-2, examined the same two structures atop a bed of dry, dense sand. In Test-2, however, the two structures were located adjacent to each other. Therefore, the purpose of Test-2 was to examine SSSI effects. By comparing results from Test-1 with results from Test-2, insights into SSSI effects were made.

The third test, Centrifuge Test-3, examined three structures atop a bed of dry, dense sand. Two of the structures were identical, and represented prototypical three-store moment-resisting frame structures founded on spread footings. These structures were nearly identical to the three-story structures used during Test-1 and Test-2. The third structure was a rigid

rocking wall founded on a large mat foundation, which was identified as the transmitter structure. One frame structure, which was identified as the receiver structure, was located adjacent to the transmitter structure. The other frame structure, which was identified as the control structure, was located a significant distance away from the transmitter-receiver pair of structures. The design goal of the transmitter-receiver pair was to maximize interaction between the two structures. By comparing the seismic response of the control structure with the seismic response of the receiver structure, insights into SSSI were made.

The earthquake motions employed during the three centrifuge tests described within this dissertation are critically important. A preliminary centrifuge test (Test-0) was performed after an earthquake motion selection process. The purpose of Test-0 was to calibrate a suite of earthquake motions that could be used at the UCD-CGM. This dissertation describes an earthquake motion selection and calibration process that future researchers can use to create test-specific earthquake motions for their research projects.

Kinematic SFSI and SSSI effects were examined during Test-1 and Test-2. Specifically, the earthquake motions recorded in the free-field at the surface, which is the earthquake motion most often used by practicing engineers for dynamic analyses, was compared to the earthquake motion recorded under the basement, in the soil. Because of kinematic interaction effects, which include base slab averaging and embedment effects, the earthquake motion recorded under the basement has smaller amplitude and smaller high-frequency content than the earthquake motion recorded in the free-field at the surface. This is an established observation, and Test-1 and Test-2 data corroborate with current kinematic interaction estimation procedures. When comparing the results from Test-2 with Test-1, however, it was seen that basement-level earthquake motion differed less from the free-field surface motion during Test-2. This result indicates that kinematic interaction effects may be masked in urban environments.

The seismic responses of the shallowly embedded frame structure footings were also examined during Test-1, Test-2, and Test-3. More specifically, the vertical displacement (settlement and uplift), horizontal displacement (sliding), and rocking were examined. By comparing results from Test-2 with results from Test-1, it was seen that the deeply embedded basement “restrains” the adjacent footings. In other words, the adjacent footings displace and rotate less than the footings that are not adjacent to the basement (i.e., the free footings). This asymmetrical footing response leads to additional demands on the superstructure, which may be unacceptable. In addition, the seismically-induced column moments measured above the restrained footings are larger than those measured above the free footings. Therefore, SSSI effects were seen to be potentially detrimental (i.e., lead to more superstructure damage) during Test-2.

During Test-3, the same footing restraining effect observed in Test-2 was found to be not as large. However, there is evidence that the transmitter structure affected the seismic response of the adjacent receiver structure. More specifically, as the transmitter structure rocked and settled during the higher-intensity earthquake motions, the adjacent footings of the receiver structure did uplift, and this caused asymmetry in the superstructure. A general

observation from Test-3 is that the seismic footing response of frame structures founded on shallowly-embedded footings is erratic. Future work in this area will examine possible explanations for the observed erratic response.

To Bessie Bigger Mason,
and in memory of Lewis Henry Wallace and Annie Wilmouth Wallace

True masters of grandparent-grandchild interaction (GGI).

Contents

List of Figures	iv
List of Tables	ix
1 Introduction	1
2 Literature Review	7
2.1 Soil-foundation-structure interaction	7
2.1.1 Kinematic interaction	9
2.1.2 Inertial interaction	13
2.1.3 Complete SFSI analysis methods	17
2.1.4 Detrimental and beneficial SFSI effects	18
2.2 Structure-soil-structure interaction	21
2.3 Site-city effects	25
2.4 Geotechnical centrifuge testing	26
3 Earthquake Motion Selection	31
3.1 Project location and local seismicity	31
3.2 Near-fault and ordinary earthquake motions	32
3.3 Developing a design response spectrum	36
3.3.1 Deterministic seismic hazard analysis	37
3.3.2 Probabilistic seismic hazard analysis	39
3.3.3 Developing a design response spectrum	40
3.3.4 Developing forward-directivity design response spectra	42
3.4 Selection of earthquake motions	48
3.5 Calibrating selected earthquake motions for centrifuge testing	56
4 Centrifuge Tests 1 & 2	61
4.1 Introduction	61
4.2 Experimental setup	62
4.2.1 Soil properties	62

4.2.2	Structural models	62
4.2.3	Instrumentation	67
4.2.4	Model construction	69
4.2.5	Earthquake motions plan	74
4.3	Experimental results	76
4.3.1	Kinematic interaction	76
4.3.2	Seismic footing response	87
4.4	Summary of findings	96
4.4.1	Kinematic interaction	96
4.4.2	Seismic footing response	97
5	Centrifuge Test-3	100
5.1	Introduction	100
5.2	Experimental setup	102
5.2.1	Structural models	102
5.2.2	Instrumentation	105
5.2.3	Earthquake motions plan	105
5.3	Experimental results	107
5.3.1	Transient vertical displacement response	109
5.3.2	Permanent vertical displacement response	116
5.3.3	Transient horizontal displacement response	120
5.4	Summary of findings	128
6	Conclusions & Recommendations	130
6.1	Summary	130
6.2	Conclusions	131
6.3	Recommendations for future research	133
6.3.1	Soil-foundation-structure interaction	133
6.3.2	Kinematic interaction	134
6.3.3	Structure-soil-structure interaction	135
6.3.4	Urban earthquake engineering	135
	Bibliography	137
A	Known Limitations & Instrumentation Tables	147
A.1	Known Data limitations	147
A.2	Tables of Important Instrumentation	148

List of Figures

1.1	A state-of-the-practice SFSI analysis using the direct approach. The shortcoming of this approach is that an individual SFS system is examined at the surface, which does not account for SSSI.	2
1.2	The urban areas after an earthquake. Reliable data showing SSSI effects are hard to gather in this situation for numerous reasons. Picture from Ansal et al. (1999)	3
1.3	The project concept: the city block within the centrifuge container.	4
1.4	The progression of the centrifuge tests described within this dissertation. Note that the soil layer is removed from this rendering for clarity.	5
2.1	An illustration of the importance of SFSI effects: (left) for the fixed-base (SFSI effects unimportant) case the damage localizes in the shear wall; (right) for the flexible-base (SFSI effects important) case the damage localizes in the frame. This figure highlights SFSI of a nonlinear frame structure. (After ATC-40 1996; Harden et al. 2005).	8
2.2	Transfer functions used to estimate kinematic interaction. After Kim and Stewart (2003).	13
2.3	The relationship between $1/\sigma$ and \bar{h}/r with \tilde{T}/T and β_f . Note that ζ_0 in this figure is analogous to β_f . After Kramer and Stewart (2004)	16
2.4	A pseudo-spectral acceleration response spectrum updated to include the effects of inertial SFSI. After Kramer and Stewart (2004).	17
2.5	A schematic showing the key steps of the substructure approach. After Kramer and Stewart (2004).	19
2.6	Pseudo-acceleration response spectrum recorded near the Hanshin Expressway during the 1995 Kobe earthquake. After Mylonakis et al. (2006)	20
2.7	The oversized foundation versus the undersized foundation. For the oversized case, a plastic hinge can form in the superstructure and lead to catastrophic damage. For the under-designed case, the plastic hinge forms at the soil-foundation interface. Thus, the under-designed SFS system can have better structural performance than the oversized system. This is a manifestation of beneficial SFSI. After Anastasopoulos et al. (2010).	22

3.1	A seismic hazard deaggregation for N34.082 W118.224 for a period of 0.0 sec (PGA). The probability of exceedance is 10% in 50 years and the shear wave velocity is 760 m/sec (rock site). This deaggregation was made using the USGS Interactive Deaggregation tool (2008 edition).	33
3.2	A seismic hazard deaggregation for N34.082 W118.224 for a period of 1.0 sec (PGA). The probability of exceedance is 10% in 50 years and the shear wave velocity is 760 m/sec (rock site). This deaggregation was made using the USGS Interactive Deaggregation tool (2008 edition).	34
3.3	Directivity: The rings represent the radiation pattern of seismic waves propagating from a ruptured fault at an instance in time. A wave front characterized by a short, intense pulse develops in the direction of propagation, which is called forward-directivity. In the direction opposite of rupture, the wave front spreads out, leading to a longer duration motion, which is called backward-directivity.	35
3.4	The motions recorded at the Lucerne and Joshua Tree stations during the 1992 Landers earthquake represent forward-directivity and backward-directivity motions, respectively.	36
3.5	The developed DSHA spectrum: average of four NGA relationship predictions, 5% damping, 84th-percentile, rotated to maximum horizontal response direction	39
3.6	The “lower limit” deterministic response spectrum. Figure 21.2-1 in ASCE 7-10 (2010).	40
3.7	The developed PSHA spectra for various return periods. Damping = 5%. . .	42
3.8	The design response spectrum developed using the ASCE 7-10 (2010) guidance for the rock site. This spectrum does not include forward directivity effects. Damping = 5%.	43
3.9	The design response spectrum developed using the ASCE 7-10 (2010) guidance for the soil site. This spectrum does not include forward directivity effects. Damping = 5%.	44
3.10	The El Centro Array # 5 recording from the 1979 Imperial Valley earthquake. The pulse period of the characteristic velocity pulse dominates the long-period region of the response spectrum. After Shahi and Baker (2011).	45
3.11	Geometry defined for the Somerville et al. (1997) method	46
3.12	Site specific geometrical parameters used with the Somerville et al. (1997) method	48
3.13	Definition of the geometrical terms C and S for the Spudich and Chiou (2008) method	49
3.14	Definition of the geometrical term R_{r_i} for the Spudich and Chiou (2008) method	50
3.15	Site specific geometrical parameters used with the Spudich and Chiou (2008) method	51
3.16	The design response spectra developed using the ASCE 7-10 (2010) guidance for the rock site and soil site considering both ordinary and forward directivity earthquake motions. Damping = 5%.	54

3.17	The ordinary (left) and forward-directivity (right) design response spectra along with important PSHA spectra and the selected earthquake motions. Damping = 5%.	56
3.18	Predictive transfer functions as described by Equation 3.6. After Mason et al. (2010).	59
4.1	Location of (Left) MS1F_SF80 with Phase II Beams and (Right) MS3F_B during Test-2. All measurements are in prototype scale. Only select instrumentation is shown; refer to Mason et al. (2011b) for complete instrumentation plans.	65
4.2	Pictures of the instrumented model buildings: (a) 3-story frame structure on spread footings (modeled as a 1-story structure and denoted as MS1F_SF80), and (b) 9-story frame structure on a 3-level basement (modeled as a 3-story structure and denoted as MS3F_B). The height of the MS1F_SF80 structure is the same as one floor of the MS1F_B structure.	66
4.3	Instrumentation: (a) ICP accelerometer, (b) MEMS accelerometer, (c) linear potentiometer (displacement gauge), (d) strain gauge, (e) analog camera, and (f) high-speed camera.	69
4.4	Schematics of (a) Test-1 and (b) Test-2 with important soil instrumentation locations; circles = horizontal accelerometers; triangles = vertical accelerometers; lines = displacement gauges. All measurements are in prototype scale, meters.	70
4.5	Pluviation at the UCD-CGM: (a) the large pluviater used to pour dense sand, and (b) using the pluviation calibration chamber.	71
4.6	Model construction process: (a) pluviation of a soil lift, (b) grooming the soil surface, (c) measuring the elevation of the soil lift, (d) placing accelerometers in the soil, (e) placing a structure in the soil model, and (f) moving the model onto the centrifuge arm.	72
4.7	Strain gauging: (a) gluing a strain gauge onto a sanded and cleaned beam, and (b) close-up of the gluing process.	73
4.8	Close-up of a bridge completion board used to connect the strain gauges to the DAQ.	73
4.9	Zoomed-in acceleration time-series for the JOS_L_1, SCS_L_1, and LCN earthquake motions. This plot includes the free-field surface ground motions and the foundation-level earthquake motions.	79
4.10	Experimental transmissibility functions (basement / free-field surface) calculated for the JOS_L_1, SCS_L_1, and LCN earthquake motions.	83
4.11	Transmissibility functions (basement / free-field surface) estimated during Test-1 for the JOS_L_1 motion for different window sizes: (a) 4096, (b) 2048, (c) 1024, and (d) 512.	84

4.12	Transmissibility functions (basement / free-field surface) estimated during Test-2 for the JOS_L_1 motion for different window sizes: (a) 4096, (b) 2048, (c) 1024, and (d) 512.	85
4.13	Total transient vertical displacement-time series for the SCS_L_1 and LCN motions for Test-1 (left) and the SCS_L_1 and LCN_1 motions for Test-2 (right). All of the footing accelerometers malfunctioned during the JOS_L_1 motion recorded in Test-1, which is why these measurements are not shown.	88
4.14	Peak transient settlement versus surface free-field <i>PGV</i> for (left) Test-1 and (right) Test-2.	89
4.15	Cumulative settlement summary plot comparing the North Footing and the South Footing for Test-1 and Test-2.	91
4.16	Initial and final footing locations measured during Test-2.	92
4.17	Moment-rotation relationships for (left) the free North Footing and (right) the restrained South Footing recorded during Test-2 for the SCS_H motion. After Trombetta et al. (forthcoming).	93
4.18	Permanent settlement versus surface free-field <i>PGV</i> for Test-1 (left) and Test-2 (right). The displacements of the reference frame (displacement rack) was removed from the data to make the comparisons equitable.	94
4.19	Transient horizontal displacement-time series recorded during Test-1 (left) and Test-2 (right) for the SCS_L_1, LCN and LCN_1 motions for the North and South Footings.	95
4.20	Transient horizontal footing displacement versus surface free-field <i>PGV</i> for Test-1 (left) and Test-2 (right).	96
5.1	Schematic of Test-3 with important soil instrument locations; circles = horizontal accelerometers; triangles = vertical accelerometers; lines = displacement gauges. All measurements are in prototype scale units, meters.	101
5.2	Schematic of the frame structures used in Test-3; i.e., the control and receiver structures	105
5.3	Schematic of the rigid rocking wall used in Test-3; i.e., the transmitter structure	106
5.4	Pictures of the instrumented model buildings: (a) 3-story frame structure on spread footings (modeled as a 1-story structure), and (b) 6-story rocking shear wall on a large mat foundation (modeled as a 2-story rocking wall).	107
5.5	The transient vertical displacement recorded during the JOS_L_4 motion on all the footings on the control and receiver structures. Positive values indicate downward movement, and negative values indicate upward movement.	110
5.6	The transient vertical displacement recorded during the LCN motion on all the footings on the control and receiver structures. Positive values indicate downward movement, and negative values indicate upward movement.	111

5.7	The transient vertical displacement recorded during the SCS_L.1 motion on all the footings on the control and receiver structures. Positive values indicate downward movement, and negative values indicate upward movement. . . .	112
5.8	The transient vertical displacement recorded during the WVC_H motion on all the footings on the control and receiver structures. Positive values indicate downward movement, and negative values indicate upward movement. . . .	114
5.9	Peak transient vertical displacement recorded for each motion on the control structure footings versus peak transient vertical displacement recorded for each motion on the receiver structure footings. The one-to-one line is plotted as a dashed line. For the receiver structure, Footings 1 and 3 are restrained and Footings 2 and 4 are free. For the control structure, all Footings are free. . .	115
5.10	Peak transient vertical displacement of the control structure footings versus surface free-field PGV for each earthquake motion. All Footings are free. . .	117
5.11	Peak transient vertical displacement of the receiver structure footings versus surface free-field PGV for each earthquake motion. Footings 1 and 3 are restrained, and Footings 2 and 4 are free.	118
5.12	The permanent vertical displacement of each footing of the (a) control structure, and the (b) receiver structure for each earthquake motion. In the legend, “free” indicates that the footing was free, and “res.” indicates that the footing was restrained.	119
5.13	The transient sliding recorded during the JOS_L.4 motion on all the footings on the control and receiver structures.	121
5.14	The transient sliding recorded during the LCN motion on all the footings on the control and receiver structures.	122
5.15	The transient sliding recorded during the SCS_L.1 motion on all the footings on the control and receiver structures.	123
5.16	Peak transient sliding recorded for each motion on the control structure footings versus peak transient vertical displacement recorded for each motion on the receiver structure footings. The one-to-one line is plotted as a dashed line. For the receiver structure, Footings 1 and 3 are restrained and Footings 2 and 4 are free. For the control structure, all Footings are free.	124
5.17	Moment-rotation relationships for (a) Footing 4 of the control structure, and (b) Footing 4 of the receiver structure recorded during Test-3 for the SCS_H.1 motion.	124
5.18	Peak transient sliding of the control structure footings versus surface free-field PGV for each earthquake motion. All footings are free.	125
5.19	Peak transient sliding of the control structure footings versus surface free-field PGV for each earthquake motion. Footings 1 and 3 are restrained and Footings 2 and 4 are free.	126

List of Tables

1.1	Summary and purpose of the centrifuge tests described within this dissertation	5
2.1	Important scaling parameters for geotechnical centrifuge testing	28
3.1	Important parameters used to develop the DSHA response spectra	37
3.2	Rotation factors used to convert the DSHA spectra from the GMRotI50 direction to the maximum horizontal response direction. After Huang et al. (2008)	38
3.3	Data used to create the design response spectrum for the rock site not considering forward-directivity effects	41
3.4	Data used to create the design response spectrum for the soil site not considering forward-directivity effects	41
3.5	Fault normal rotated spectral directivity correction factors from Somerville et al. (1997)	47
3.6	GMRotI50 to fault-normal rotation factors. After Huang et al. (2008).	47
3.7	Important site specific geometric and fault parameters used with the Spudich and Chiou (2008) method	52
3.8	Important calculated values for the Spudich and Chiou (2008) method	53
3.9	Forward directivity correction factors (“Amp Factors”) for the four NGA relationships	53
3.10	Final directivity correction factors	54
3.11	Earthquake motions selected before calibration with the centrifuge shaking table	55
3.12	Final earthquake motions used for the NCB tests	60
4.1	Important soil properties for Nevada sand (from January 2008 tests performed by Cooper Labs)	62
4.2	Key structural parameters for representing idealized models	63
4.3	Design goal and achieved geometric, modal, and strength parameters. All values are in prototype scale.	66
4.4	Spectral accelerations and predicted damage quantities for individual earthquake motions used in Test-1 and Test-2. After Chen et al. (2010).	74

4.5	Earthquake motions achieved during Test-1 at the base.	75
4.6	Earthquake motions achieved during Test-2 at the base.	76
4.7	Earthquake motions achieved during Test-1 at the surface in the free-field.	77
4.8	Earthquake motions achieved during Test-2 at the surface in the free-field.	78
4.9	MATLAB code used to calculate H_3 and coherency	80
4.10	MATLAB code used to perform the nonlinear regression to fit Equation 2.4 with the experimentally determined transmissibility functions and determine κ_a	81
4.11	Apparent incoherency factors estimated for Test-1 and Test-2	86
5.1	Target dimensionless parameters governing the design of the transmitter structure (Pitilakis et al. 2008)	104
5.2	Earthquake motions achieved during Test-3 at the base.	108
5.3	Earthquake motions achieved during Test-3 at the surface in the free-field.	109
5.4	Equations for the linear regression lines from the peak transient vertical displacement data along with their corresponding R^2 values. In this table, c is the control structure peak transient vertical displacement, and r is the receiver structure peak transient vertical displacement.	115
5.5	Equations for the regression lines from the peak transient sliding data along with their corresponding R^2 values. In this table, F1 = Footing 1, F2 = Footing 2, F3 = Footing 3 and F4 = Footing 4. Additionally, ρ is the peak transient sliding and PGV is the surface free-field PGV	127

Acknowledgments

Sir Isaac Newton humbly proclaimed, “If I have seen further, it has been standing on the shoulders of giants.” The most striking word of this sentence—especially given its proclaimer—is the first understated *If*. I will use this humble proclamation to frame my acknowledgments, and to thank the many giants who helped me complete and submit this dissertation. It is difficult to make this list exhaustive, as I have interacted with many people who have helped me during my journey. Therefore, I would first like to make a blanket statement: “many thanks to all of those who have had an impact on my life.”

I should first note that this dissertation results from a multi-investigator research project. Without the support of the student team, none of this work would be possible. Nicholas “Newt” Trombetta read significant parts of this dissertation while it was being prepared and provided insightful comments and suggestions. In addition, he took the lead on a majority of the data analysis and reduction. Without Newt’s substantial help, this dissertation would not have been possible. We complement each other’s strengths and weaknesses to make a dynamic duo, and I look forward to working with him for many years to come. You should look forward to reading his dissertation, which will be submitted to the University of California, San Diego Department of Structural Engineering a year or so after this dissertation appears. His dissertation should be viewed as a (better) complement to this one, and the two should ideally be shelved or binded together.

Katherine Jones read the entire manuscript and provided detailed editorial comments. She deserves a special thanks for this substantial effort. All typographical and style errors are of course my own. Other student members of the research team, who were also instrumental to my success, are ZhiQiang Chen, Benjamin Choy, Josh Zupan, Hamilton Puangnak, Chandrakanth Bolisetti, Jack Montgomery, Roshani Patel, Clayton Proto, Stefanie Gille, and Johnny Lund.

The principal investigators of the NEES City Block project are also phenomenal. Many thanks to Jonathan Bray, Bruce Kutter, Tara Hutchinson, Gregg Fiegel, Andrew Whittaker, and Bob Reitherman. It was on the sturdy shoulders of the NEES City Block giants, both student and principal investigator, that I was able to see a little further and complete this dissertation.

This journey was principally made possible by the most important giants in my life: my immediate family members. My grandparents, to whom I have dedicated this dissertation, touted the value of education from day one, and importantly, taught me that hard, focused work can compensate for intelligence (they were intelligent hard workers, which is the best case scenario). My parents, Dale and Linda Mason, who let me make my own decisions, but were always there to support me when the times got tough, were instrumental cheerleaders through the tougher times of this worthwhile ordeal. My brother, Matt Mason, taught me how to lose gracefully when I was bettered and win big when I had an advantage—in a word, he taught me patience, which is truly a virtue when completing a dissertation.

I have lots of giants to thank at Georgia Tech. The first is Associate Dean Larry Jacobs.

Due to serendipitous circumstances, Larry was chosen to be my freshman adviser. Little did I know that this somewhat random pairing would change the course of my life. I worked in his lab for nearly two years investigating micro-cracking in concrete using ultrasonic waves. Larry had a very direct way of talking to me, which worked well with my personality. He spent an enormous amount of time guiding me to various opportunities that would strengthen my knowledge of civil engineering and help me with my graduate career. Importantly, he is also the best teacher I have ever had, and my lecture style is more or less a plagiarism of his (dream on Ben). Larry also introduced me to great laboratory partners, who have all had a positive influence on my journey: Jan, Spoon, Helge, Susanne, Christian, Florian, Koreck, Bo and P-Eck. Finally, I would be remiss if I did not also thank Professors Glenn Rix and Reggie DesRoches, who have continued to be dedicated advisers.

My adviser, Professor Jonathan Bray, is the giant most responsible for guiding me through this dissertation. Jon is a person who enjoys the creativity of our field, and this makes it a pleasure to work with him. Interacting with him has given me a different (and better) perspective for how to conduct research and teach. He stuck with me through some difficult funding times, which I am very grateful for. I have him to thank for all of the advice, for valuing my opinion, for limiting the bureaucracy, and maybe most importantly, for never making me guess what he was thinking. Also, I will forever be grateful for the patience he showed me while I was writing this dissertation.

At Berkeley I have many giants to thank. Professor Ray Seed has been an excellent teacher and dedicated mentor. He participated on both my qualifying examination committee and my dissertation committee, and he has also provided me with abundant career advice and guidance. Professor Juan Pestana recruited me to come to Berkeley and found me financial support, for which I am grateful. He also participated on my qualifying examination committee. Professors Nicholas Sitar and Michael Riemer were dedicated teachers and provided me with excellent advice. Professor Douglas Dreger has made me a better-rounded earthquake engineer, and participated on both my qualifying examination and dissertation committees. I also want to thank Professor Sanjay Govindjee for agreeing to participate on my qualifying examination committee on short notice. Finally, perhaps the largest giants at Berkeley were my peers, from whom I have learned the most. Many thanks to the peers from my MS class, the peers from MS classes since, and my fellow PhD students. I want to especially thank my officemates from 443 Davis Hall: Xavier Vera-Grunauer, Adda Athanasopoulos-Zekkos, Shideh Dashti, Joseph Weber and Katherine Jones. Special thanks go to Shideh for mentoring me during a centrifuge experiment. Finally, I would like to thank my structural engineering friends, who helped get me through my difficult structural engineering minor: Sanaz Rezaeian, Vesna Majstorovic and Hong Kim.

I was lucky to have an unofficial co-adviser for my research project, Professor Bruce Kutter of UC Davis, who has been another giant for my career. Bruce adopted me during my centrifuge experiments at UC Davis and spent tireless hours mentoring me. Bruce has made me a better scientist and scholar, and he was also a patient member of my dissertation committee. Because of this connection with Bruce, I was able to establish a connection

with UC Davis during my time as a PhD student and become a guest member of their graduate student association. I want to thank Professors Ross Boulanger and Jason DeJong as well as all the students for this amazing opportunity. A special thanks goes to Lijun “LJ” Deng for sharing his abundant knowledge (and MathCAD sheets) with our team as well as Brina Mortensen, Jackee Allmond, Doug Wahl, Dong-Soon Park, Joe Tom and Manny Hakhamaneshi for all the good times at the ‘fuge.

My dissertation research was performed at the UC Davis Center for Geotechnical Modeling; accordingly, I need to thank the incredible staff. Dan Wilson, who is the manager and lead scientist of the Center, provided lots of good advice and input over the years. Ray Gerhard and Anitoliy Genchenko deserve special thanks. These gentlemen giants worked hard, long hours to make all the centrifuge tests described within this dissertation possible. Additionally, Lars Pederson, Chad Justice, Peter Rojas, Jenny Chen and the numerous student employees of the Center provided lots of support and many hours of laughs.

Finally, I have the giants from my personal life who have always been there for me during this sometimes arduous journey. I need to thank my friends from other lifetimes—Joe Michael, Dale Manning, Robert Kinner, Joe Wood, and Alfredo Ramos—for the numerous e-mails and jokes over the years. Thanks to my California friends who have not previously been listed—Peter Ryan, Jake Massey and Kristen O’Hanlon—for countless laughs. I send a special thanks to Eileen Hidayetoglu for being a key supporter during my entire doctorate. Finally, I want to thank the best dog in the world, Dylan, for the unconditional love and support. I thought about dedicating this dissertation to Dylan, but decided that it would not be politic. She gets a dedication honorable mention, however.

I am looking forward to starting the next phase of my career as an assistant professor at Oregon State University. The many giants I have interacted with along the way have prepared me for this next step. I move forward with great humility, and I hope that one day at least one person can climb onto my feeble shoulders to perhaps see a little further.

Part of Chapter 4 of this dissertation is incidentally based on material from a manuscript entitled “Nonlinear dynamic foundation response and kinematic interaction observed in geotechnical centrifuge experiments,” which was submitted to *Earthquake Engineering & Structural Dynamics* on 8 April 2011 for possible publication. I was the lead author of this paper, and Nicholas Trombetta, ZhiQiang Chen, Jonathan Bray, Tara Hutchinson and Bruce Kutter were co-authors. In addition, elements from a manuscript entitled “Nonlinear dynamic foundation and frame structure response observed in geotechnical centrifuge experiments,” which was submitted to *Earthquake Engineering & Structural Dynamics* on 11 April 2011 for possible publication, were also helpful for preparing Chapter 4 of this dissertation. This

paper was authored by Nicholas Trombetta, and I served as a co-author along with ZhiQiang Chen, Jonathan Bray, Tara Hutchinson, and Bruce Kutter. The help and dedication of all of the co-authors is gratefully acknowledged.

The material in this dissertation is based upon work supported by the National Science Foundation under Grant No. CMMI-0830331. Any opinions, findings, and conclusions or recommendations expressed in this material are those of the author and do not necessarily reflect the views of the National Science Foundation. Experiments were conducted at the Center for Geotechnical Modeling at the University of California at Davis, which is supported by the NSF George E. Brown, Jr. Network for Earthquake Engineering Simulation (NEES) program under Grant No. CMMI-0402490.

A theory is something nobody believes, except the person who made it. An experiment is something everybody believes, except the person who made it.

— Albert Einstein

Chapter 1

Introduction

During an earthquake, superstructures interact with supporting foundations and foundations interact with the surrounding soil. This is called soil-foundation-structure interaction (SFSI). Figure 1.1 shows the finite-element mesh used in a state-of-the-practice SFSI analysis. This type of analysis—known as the *direct approach*—examines the seismic response of the soil, foundation, and structure simultaneously.

There is a shortcoming with the model shown in Figure 1.1; namely, the seismic response of only one soil-foundation-superstructure (SFS) system is examined. In reality this case is rare, especially in densely populated, seismically active areas, where buildings are arranged in city blocks. Adjacent buildings within city blocks interact through the soil. This phenomenon is called structure-soil-structure interaction (SSSI) and is currently not well understood. One reason for this lack of understanding is a dearth of experimental and field case history data that clearly exhibit SSSI.

Field case history data that exhibit SSSI effects are difficult to gather. The first issue is that the soil, foundations, and SFS systems in urban areas are rarely sufficiently well-instrumented to gather high-quality data during earthquakes. There has been a lack of research funding for fully instrumented SFS systems because it is impossible to know when the next large earthquake will occur. The SFS systems that have been fully instrumented, like the Millikan Library on the campus of the California Institute of Technology (e.g., Luco et al. 1988), are usually isolated from other SFS systems. The second issue is that urban areas are complex. Figure 1.2 shows the urban landscape following the 1999 Kocaeli Earthquake in Turkey. The damage to the built environment is widespread; accordingly, even if the area shown in Figure 1.2 was well-instrumented before an earthquake, it would be nearly impossible to isolate the SSSI effects from the data.

To avoid the two issues raised above, it is possible to take direct measurements of displacements following earthquakes. This is especially possible using Light Detection and Ranging (LIDAR) technology (e.g., Kayen et al. 2006; Rathje and Adams 2008). There are several issues with this, however. First, countries affected by large earthquakes start the rebuilding process immediately to limit the time that the population is displaced. This

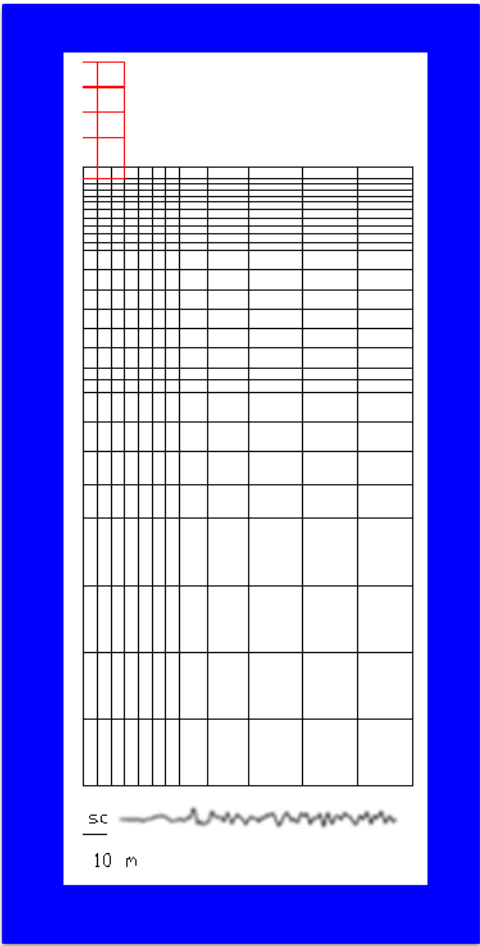


Figure 1.1: A state-of-the-practice SFSI analysis using the direct approach. The shortcoming of this approach is that an individual SFS system is examined at the surface, which does not account for SSSI.

noble pursuit erases valuable data. Second, the direct displacement measurements of post-earthquake damage are useful, but they are most useful if the pre-earthquake measurements are also available. Third, the direct displacement measurements cannot provide reliable estimates of the seismic response of embedded foundations and soil. Finally, the direct displacement measurements do not provide dynamic data (e.g., time series of acceleration, displacement, strain). The dynamic data are crucial for understanding SSSI as well as SFSI.

The fact that field case histories that provide quantitative insights regarding SSSI are not available is a major limitation in advancing the profession’s understanding. A typical paradigm for understanding new phenomena in the earthquake engineering community is as follows: (1) field case history data that help describe the phenomenon are collected and examined, (2) the field case history data are back-analyzed with numerical models, which



Figure 1.2: The urban areas after an earthquake. Reliable data showing SSSI effects are hard to gather in this situation for numerous reasons. Picture from Ansal et al. (1999)

allows for the calibration of numerical models, (3) the calibrated numerical models are used to perform sensitivity analyses, and (4) the results of the sensitivity analyses are used to develop a deeper understanding of the phenomenon and perhaps develop guidance for the earthquake engineering community.

Given the aforementioned difficulties with field case histories that exhibit SSSI effects, the decision was made to develop a series of “model case histories” that exhibit SSSI effects using the geotechnical centrifuge located at the University of California at Davis Center for Geotechnical Modeling (UCD-CGM). The project concept, therefore, is to test a city block within the centrifuge, then use the gathered “case history” data to carry out the typical paradigm described in the previous paragraph. Figure 1.3 illustrates the project concept: the city block within the centrifuge container.

Using the geotechnical centrifuge at the UCD-CGM is advantageous for several reasons.

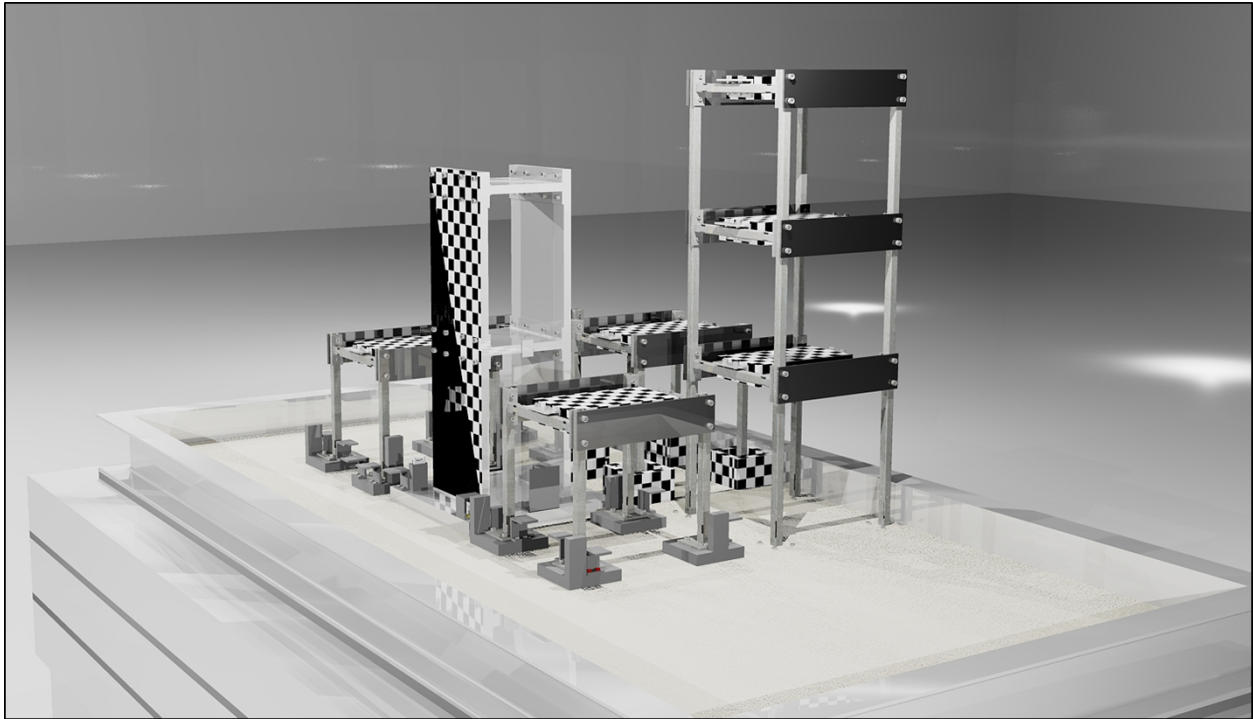


Figure 1.3: The project concept: the city block within the centrifuge container.

First, models can be built in a well-controlled laboratory environment and spun in the centrifuge to represent realistic field case histories. This allows the researcher to control important parameters of the model, and thus design robust case histories. Second, the geotechnical centrifuge at the UCD-CGM is large, which allows complex models to be built and tested. Third, the geotechnical centrifuge at the UCD-CGM also has a robust shaking table, which allows realistic earthquake motions to be simulated. Finally, centrifuge technology is particularly advantageous for performing SFSI-related research, because the soil, foundation, and superstructure can be modeled simultaneously.

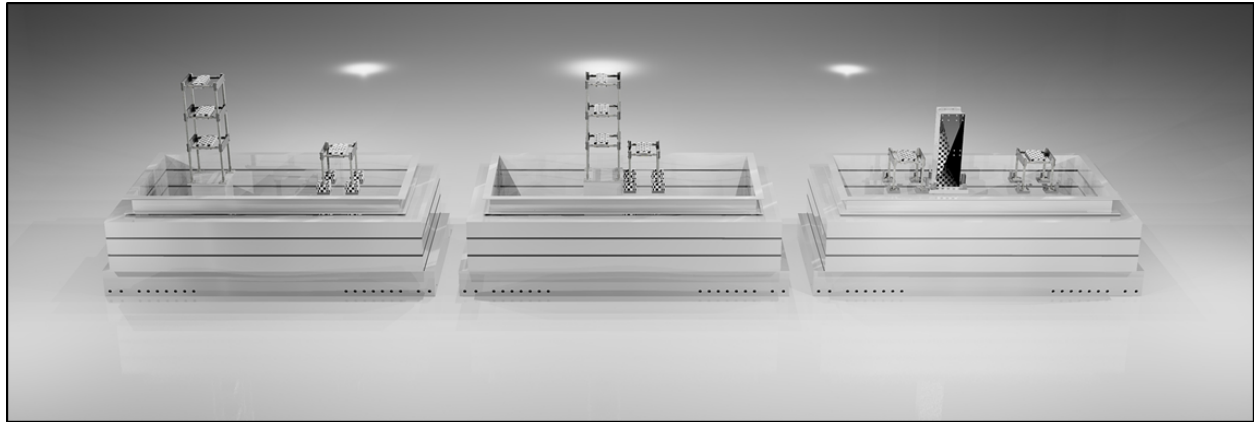
This dissertation research project is part of a \$1.7 Million NSF-funded project, which is nicknamed the NEES City Block (NCB) project. This dissertation describes the earthquake motion selection and calibration process and three centrifuge tests that were performed as part of the NCB project. Table 1.1 contains a summary of the three centrifuge tests, including their purposes. A preliminary centrifuge test, Test-0, was performed to create a suite of earthquake motions suitable for use with the UCD-CGM shaking table.

Examining Table 1.1, it can be seen that there was a “stepping-stone” philosophy for the three centrifuge tests. Test-1 started by examining SFSI of two individual inelastic frame structures. These frame structures were designed to replicate prototypical structures found in Los Angeles. In Test-2, these same two inelastic frame structures were moved adjacent to one another. Test-2, therefore, was the first test that examined SSSI effects. In Test-3, three

Table 1.1: Summary and purpose of the centrifuge tests described within this dissertation

Test	Soil	Structures	Purpose
1	Dry, dense Nevada sand	Two individual inelastic frame structures	Examine SFSI of inelastic structures
2	Dry, dense Nevada sand	Two adjacent inelastic frame structures	Examine SSSI of inelastic structures
3	Dry, dense Nevada sand	Two inelastic frame structures and one elastic rocking wall	Exacerbate SFSI and SSSI effects

structures were examined. Two structures were identical inelastic frame structures (similar to those used in Test-1 and Test-2). The third structure was a rigid rocking wall that was massive compared to the frame structures. Test-3 was designed to exaggerate SFSI effects, and accordingly, exaggerate SSSI effects. Figure 1.4 illustrates the progression of centrifuge tests.

**Figure 1.4:** The progression of the centrifuge tests described within this dissertation. Note that the soil layer is removed from this rendering for clarity.

This dissertation is organized as follows:

- Chapter 2: Literature Review

This chapter contains an important literature review that frames the rest of this dissertation. This literature review includes an introduction to soil-foundation-structure interaction, structure-soil-structure interaction, site-city effects, and geotechnical centrifuge testing.

- Chapter 3: Earthquake Motion Selection

This chapter describes the earthquake motion selection procedures used to develop a suite of earthquake motions for the research project. This includes a discussion of developing the design response spectra, selection of the motion, near-fault versus ordinary earthquake motions, and performing a centrifuge test dedicated to calibrating a suite of earthquake motions for the centrifuge shaking table.

- Chapter 4: Centrifuge Tests-1 & 2

This chapter describes the experimental setup of Centrifuge Test-1 and Test-2. Additionally, important results from Test-1 and Test-2 are described. Specifically, the difference between kinematic SFSI observed during Test-1 and Test-2, and the seismic footing response observed during Test-1 and Test-2 is explored. By comparing the results between Test-1 and Test-2, important findings that highlight SSSI effects are discovered and discussed.

- Chapter 5: Centrifuge Test-3

This chapter describes the experimental setup of Centrifuge Test-3. Additionally, important results for this test are described. Specifically, the seismic footing response is explored. Finally, important findings from Test-3 are discussed.

- Chapter 6: Findings and Conclusions

Overarching conclusions are drawn from the findings discussed in Chapters 4 and 5. Finally, ideas for future research that stem directly from this dissertation research are discussed.

Centrifuge data described in this dissertation for Tests-1, 2 and 3 are available online at the NEES Hub (<http://www.nees.org>). Additionally, three data reports are available at the NEES UC Davis website (<http://nees.ucdavis.edu>). These data reports contain comprehensive information regarding the experiments and contain all of the time series that were recorded as part of the testing (Mason et al. 2011a; b; c).

More information about this research project can be found at the NCB project website: <http://www.nees-cityblock.org/>.

Chapter 2

Literature Review

2.1 Soil-foundation-structure interaction

During an earthquake, seismic waves propagate outward from a source. These waves propagate through rock and soil layers, and they can either reach the ground surface or a built environment. If they reach the ground surface away from the presence of any structures, then the recorded motions are called free-field surface ground motions.

If the seismic waves reach a built environment, then they will interact with soil-foundation-superstructure (SFS) systems. The impedance contrast between the relatively rigid foundation and the relatively compliant surrounding soil changes the amplitude, frequency content, and duration of the motions recorded at the foundation level. Additionally, the superstructure vibrates, and this vibrational energy propagates back into the foundation and the surrounding soil. The vibrational energy further changes the characteristics of the motions recorded at the foundation level, as well as other places within the SFS system. The motions in the soil surrounding a structure are changed with respect to the free-field ground motion due to the complex interactions of the SFS system. The phenomenon described within this paragraph is called soil-foundation-structure interaction (SFSI) or soil-structure interaction (SSI). The more complete term, SFSI, will be used in this dissertation, to highlight the importance of the foundation.

The earthquake engineering literature contains many studies related to SFSI. Seminal references, that primarily examine SFSI of linearly elastic structures, and that were useful for preparing this chapter are: Merritt and Housner (1954), Housner (1957), Luco (1969), Parmelee et al. (1969), Duke et al. (1970), Jennings (1970), Veletsos and Wei (1971), Trifunac (1972), Jennings and Bielak (1973), Veletsos and Verbic (1973), Veletsos and Meek (1974), Veletsos and Nair (1975), Bielak (1975), Luco and Wong (1986), Luco and Mita (1987), Luco et al. (1988), Veletsos and Prasad (1989), Gazetas (1991), Veletsos et al. (1997), Stewart et al. (1999a), Stewart et al. (1999b), Kim and Stewart (2003), Kramer and Stewart (2004), FEMA-440 (2005), and Mylonakis et al. (2006). Kramer and Stewart (2004) serves as a

primary source for this chapter. This list of references is not meant to be exhaustive, but will provide the reader with a solid SFSI background. For more interested readers, Kausel (2010) provides a concise and insightful history of SFSI research that spans back to the work of Lord Kelvin.

Figure 2.1 illustrates an important aspect of SFSI (ATC-40 1996). The left side of the figure shows a structure on a rigid subsurface; the superstructure is fixed to a rigid foundation, which is perfectly bonded to an elastic halfspace. This represents the *fixed-base* assumption often employed during dynamic analyses. It is the case where SFSI is not considered. Contrastingly, the right side of the figure shows a structure on a flexible subsurface. In this case, flexibility is allowed at the soil-foundation interface. This represents the *flexible-base* assumption and is the case where SFSI is considered. Comparing the two structures, it can be seen that their seismic response differs significantly. In the case where SFSI is neglected (left), the damage localizes in the shear wall, but the frame remains largely undamaged. In the case where SFSI is not neglected (right), the shear wall is allowed to rock and tilt, and most of the damage localizes in the frame. Accordingly, if a “fixed-base” assumption is made, but SFSI is important, the earthquake engineer can predict the wrong damage mechanism. Therefore, it is important to consider SFSI in engineering design.

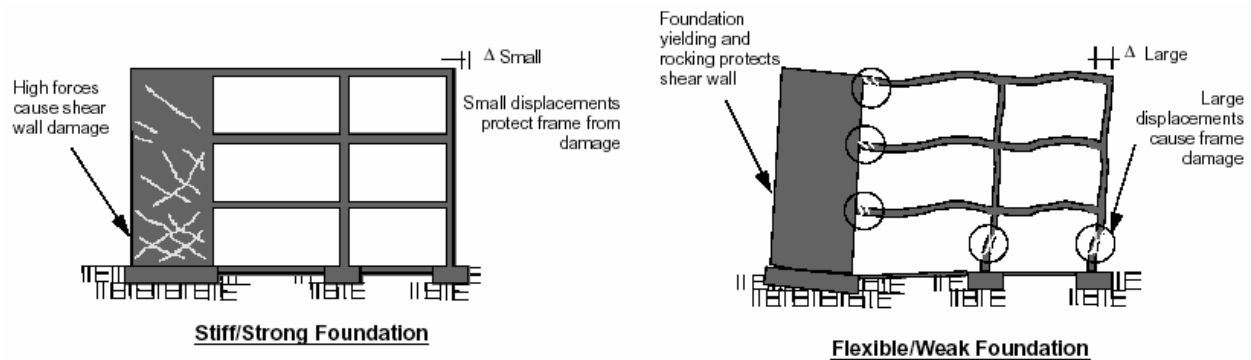


Figure 2.1: An illustration of the importance of SFSI effects: (left) for the fixed-base (SFSI effects unimportant) case the damage localizes in the shear wall; (right) for the flexible-base (SFSI effects important) case the damage localizes in the frame. This figure highlights SFSI of a nonlinear frame structure. (After ATC-40 1996; Harden et al. 2005).

SFSI is usually split into three subcomponents: (1) kinematic SFSI, (2) inertial SFSI, and (3) foundation flexibility (Kramer and Stewart 2004). Foundation flexibility is rarely considered, because the foundation is often rigid compared to the surrounding soil and supported superstructure; accordingly, it will not be considered further in this dissertation.

2.1.1 Kinematic interaction

When seismic waves impinge upon a foundation, they are changed with respect to the seismic waves that reach the ground surface in the free-field (i.e., away from the influence of any structure). The seismic waves are changed mainly due to two mechanisms: (1) base slab averaging, and (2) embedment effects (Stewart et al. 1998). The difference between the foundation-level motion and the surface free-field motion is caused by kinematic SFSI, which is often shortened to kinematic interaction. This is important because most earthquake engineers use the free-field surface as input for dynamic analyses. In reality, however, they should be using the foundation-level motion. Kinematic interaction effects are important for short-period buildings, for buildings with larger mat foundations, or for buildings founded on deeply embedded basements (FEMA-440 2005).

The foundation-level motion is usually called the foundation-input motion. Strictly, kinematic interaction analysis is performed assuming that the foundation and supported superstructure are massless (this is why it is called *kinematic* interaction). When examining experimental kinematic interaction results, however, this assumption is impossible to uphold, but this does not render the experimental results useless. As Stewart (1996) notes, “the effects of structural inertia on foundation motions tend to be concentrated near the first-mode structural frequency, so kinematic effects can be approximately evaluated across the remainder of the frequency spectrum.” In this dissertation, the term foundation-level motion is used to refer to the experimentally recorded motion, which includes the effects of the foundation and superstructure mass (i.e., inertial interaction). The term foundation-input motion is reserved for the theoretical case of a massless foundation and superstructure.

Base slab averaging is an important subcomponent of kinematic interaction. In the absence of a foundation at the surface, the earthquake motions recorded are spatially variable. The seismic waves arrive at different angles of incidence because of complex reflections and refractions that occur in the subsurface. The amplitudes of the seismic waves are also highly variable because they attenuate at different rates depending on their travel path. In the presence of a foundation, however, there is a large impedance contrast at, or near, the surface. The foundation is relatively rigid compared to the relatively compliant soil layer. The presence of this rigid foundation acts to *average* the seismic waves of the area of the foundation (Stewart et al., forthcoming). This averaging causes the foundation-input motion amplitude to be “less than the localized maxima that would have occurred in the free-field (FEMA-440 2005).” This statement is true for translational motion, which is reduced by the presence of the foundation. Torsional and rotational motion, however, are introduced (Mylonakis et al. 2006).

Base slab averaging also decreases the high-frequency content of the foundation-level motion compared to the surface free-field ground motion (Kim and Stewart 2003). The foundation, therefore, acts as a low-pass filter.

Transfer functions may be used to describe the difference between the free-field surface ground motion and the foundation-level motion. Transfer functions are the ratio of the FFT

amplitude of an output signal, $Y(\omega)$ to an input signal, $X(\omega)$.

In some cases, the values of $X(\omega)$ may not exist locally, or they may be extremely small. In these cases, the transfer function will approach infinity. These *spurious spikes* can cause trouble when employing the transfer functions for converting a free-field surface ground motion to a foundation-input motion. It is inconceivable for the foundation-input motion to be dominated by several frequencies where these spurious spikes exist. For this reason, most kinematic interaction researchers use transmissibility functions for examining kinematic interaction (Kim and Stewart 2003).

Transmissibility functions, $H(j\omega)$, are ratios of power spectral density functions (S_{xx} , S_{yy}) and cross spectral density functions (S_{xy}), which always exist locally. More information about spectral density functions can be found in digital signal processing and modal analysis references (e.g., Johansson 1993; Ewins 2000; Oppenheim and Schaffer 2009)

Transmissibility functions can be defined three ways

$$H_1(j\omega) = S_{xy}(\omega)/S_{xx}(\omega) \quad (2.1a)$$

$$H_2(j\omega) = S_{yy}(\omega)/S_{xy}(\omega) \quad (2.1b)$$

$$|H_3(j\omega)| = \sqrt{S_{yy}(\omega)/S_{xx}(\omega)}. \quad (2.1c)$$

Fenves and DesRoches (1994) performed sensitivity analyses with the transmissibility functions given in Equation 2.1 and found that H_1 is sensitive to input noise, H_2 is sensitive to output noise, and H_3 is in the middle of H_1 and H_2 . For these reasons, Kim and Stewart (2003) use H_3 for kinematic interaction analyses, which is a practice continued in this dissertation.

The *quality* of H_3 can be determined by examining the coherence function, γ , which is defined as

$$\gamma^2(j\omega) = \frac{H_1(j\omega)}{H_2(j\omega)} = \frac{|S_{xy}(\omega)|^2}{S_{xx}(\omega)S_{yy}(\omega)}. \quad (2.2)$$

Kim and Stewart (2003) note that “if the coherence is close to one, it may be inferred that the noise level is low and that there is a nearly linear response between input and output.” A lower coherency value can indicate a number of issues (Ewins 2000):

1. There is nonlinearity in the system. The transmissibility functions above are developed using linear systems theory (Johansson 1993). During strong motion, the soil responds nonlinearly (thus the input is nonlinear), and the SFS system responds nonlinearly (thus the output is nonlinear). This is a major reason that γ is less than one for measured transmissibility functions.
2. Noise is affecting one or both of the signals. This can occur if there is a faulty accelerometer measuring either the foundation-level motion, the free-field surface ground motion, or both.
3. Resonance is occurring in the system, which affects the linear systems theory assumptions.

4. One or both of the signals are aliased. This can be avoided if the signal processing is performed carefully.

The coherency can be calculated across the entire frequency range of interest at discrete frequencies to understand the quality of the transmissibility function, and a *high-coherency* threshold can be specified. When the coherency is above this high-coherency threshold, the value of the transmissibility function at that frequency is considered reliable. Likewise, when the coherency is below this high-coherency threshold, the value of the transmissibility function at that frequency is considered unreliable. Kim and Stewart (2003) define the high-coherency threshold as 0.8. The same high-coherency threshold is adopted in this dissertation.

Transfer functions (and transmissibility functions) calculated for experimentally measured input motions and output motions (i.e., free-field surface ground motions and foundation-level motions) typically decrease as a function of frequency. This indicates that base slab averaging decreases the high-frequency content of the foundation-input motion compared to the free-field surface ground motion, which is the case, as previously discussed. Harichandran and Vanmarke (1986) defined an analytical transfer function, G , that accounts for base slab averaging effects as

$$G = \Gamma(|\mathbf{r}_1 - \mathbf{r}_2|, \omega) \exp \left[- \left(\frac{j\omega}{(V_{s,r})_H} \cdot |\mathbf{d}_1 - \mathbf{d}_2| \right) \right], \quad (2.3)$$

where \mathbf{r}_1 and \mathbf{r}_2 are position vectors of two points of interest, \mathbf{d}_1 and \mathbf{d}_2 are the components of \mathbf{r}_1 and \mathbf{r}_2 in the direction of wave propagation, and $(V_{s,r})_H$ is the horizontal, apparent velocity of the wave front. This velocity is reduced to correspond to the shear strain in the soil caused by the earthquake. The Γ term is a non-dimensional *incoherence factor* given as (Luco and Wong 1986)

$$\Gamma(|\mathbf{r}_1 - \mathbf{r}_2|, \omega) = \exp \left[- \left(\left(\frac{\kappa\omega}{V_{s,r}} \right) \cdot |\mathbf{r}_1 - \mathbf{r}_2| \right)^2 \right], \quad (2.4)$$

where κ is a dimensionless incoherence parameter.

The function presented in Equation 2.3 can be fitted to the experimentally determined transmissibility functions. Previous researchers have completed this by considering that the exponential term in Equation 2.3 is equal to one, which is true if \mathbf{d}_1 equals \mathbf{d}_2 . This leaves the Γ term, which is given in Equation 2.4. Nonlinear regression is used to fit the functional form in Equation 2.4 with the experimentally determined transmissibility function by changing the value of κ . The “best-fit” κ is renamed κ_a , because it is an apparent incoherency factor, derived from experimental data (Kim and Stewart 2003). The apparent incoherency parameter can be used as an indicator of base slab averaging effects, with larger κ_a values indicating that more base slab averaging is occurring. In other words, a large κ_a indicates that the free-field surface ground motion deviates more significantly from the

foundation-level motion. Kim and Stewart (2003) developed a semi-empirical method for evaluating κ_a as a function of the shear wave velocity of the soil:

$$\kappa_a = 0.00074 \cdot (V_s - 50)[m/sec]. \quad (2.5)$$

Kim and Stewart (2003) contains a method for calculating the foundation-input motion from the surface free-field ground motion considering base slab averaging effects. First, the value of κ_a is determined with Equation 2.5 by using an appropriate shear wave velocity. Second, the dimensionless frequency parameter \tilde{a}_0 is calculated as

$$\tilde{a}_0 = \begin{cases} a_0 \sqrt{\kappa^2 + \sin^2 \alpha_v} & \text{circular} \\ \frac{\omega b_e}{V_{s,r}} \sqrt{\kappa^2 + \sin^2 \alpha_v \left(\frac{b}{b_e}\right)^2} & \text{rectangular} \end{cases} \quad (2.6)$$

where α_v is the angles of incidence, $a_0 = \omega r / V_{s,r}$, and $b_e = \sqrt{ab}$ (i.e., the equivalent radius). From Equation 2.6, it can be seen that \tilde{a}_0 is frequency-dependent and is a function of κ , the shear wave velocity of the soil, the foundation geometry, and the angle of incidence of the incoming seismic waves. Third, the value of the transfer function is obtained from charts found in Veletsos and Prasad (1989) and Veletsos et al. (1997). Figure 2.2 shows one of these charts for the case where $\alpha_v = 0^\circ$ (i.e., vertically incident seismic waves). In this figure $\sqrt{S_{uu}/S_{gg}}$ is the transfer function for rectangular foundations and $\sqrt{S_{cir}/S_{gg}}$ is the transfer function for circular foundations. Fourth, the magnitude of the FFT of the free-field surface ground motion is multiplied by the appropriate transfer function value. Finally, an inverse FFT of the aforementioned product is taken to yield the foundation-input motion.

More recently, Mylonakis et al. (2006) have developed updated expressions for transfer functions. The same process described in the previous paragraph applies for obtaining a foundation-input motion from a free-field surface ground motion using this method. In addition, FEMA-440 (2005) provides a method for incorporating base slab averaging by using the ratio of response spectra (RRS), which is more straightforward than using frequency-domain transfer functions.

The second subcomponent of kinematic interaction is embedment effects. Embedment effects are likely the most important subcomponent of kinematic interaction for deeply embedded foundations. Embedment effects arise because earthquake motions normally increase in amplitude as they propagate upwards through soil layers. Thus, generally speaking, a seismic motion recorded at the bottom of a deep basement has a smaller amplitude than a ground motion recorded nearby, at the surface, and in the free-field. Additionally, the motion experienced at the bottom of the basement is lower in amplitude than the motion experienced at the top of the basement. This difference can cause the basement to rock in some cases, which is another embedment effect.

Embedment effects are also incorporated into engineering design by using transfer functions; i.e., the free-field surface ground motion is converted a foundation-input motion using a

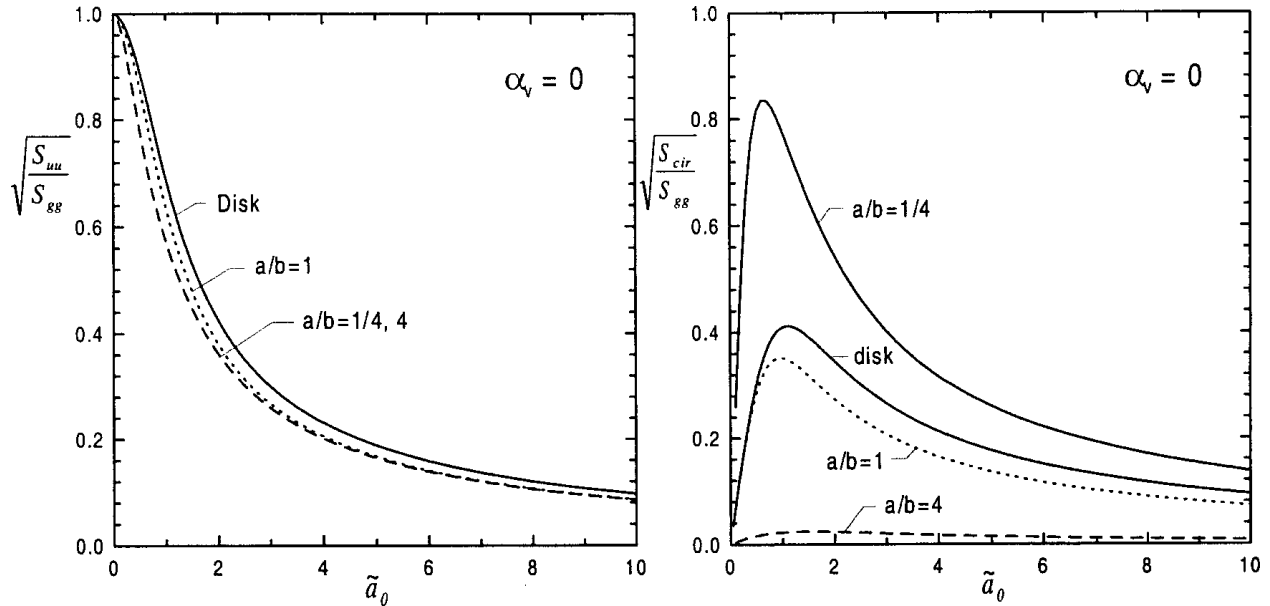


Figure 2.2: Transfer functions used to estimate kinematic interaction. After Kim and Stewart (2003).

frequency-domain transfer function. Kausel et al. (1978) provide transfer functions that are frequency-dependent and are functions of the embedment, the shear wave velocity of the surrounding soil, and the foundation geometry. A summary of this method is given in Kramer and Stewart (2004).

For cases where base slab averaging and embedment effects are both important (e.g., a deeply embedded foundation with a large footprint), then the two separate transfer functions must be multiplied together before the foundation-input motion is determined.

2.1.2 Inertial interaction

During an earthquake, the superstructure vibrates. This vibrational energy then propagates back into the foundation and eventually into the surrounding soil. This is called inertial SFSI, which is often shortened to inertial interaction.

Figure 2.1 focuses on inertial interaction. As the superstructure mass vibrates, the vibrational energy causes movement at the soil-foundation interface. The flexibility of the soil-foundation interface is often modeled by series of springs and dashpots, which can be represented by complex Winkler springs (Allotey and Naggar 2007). This soil-foundation flexibility implies that there are more degrees-of-freedom for the flexible-base SFS system than for the fixed-base system. This, in turn, implies that the period of the flexible-base SFS system is always longer than the period of the fixed-base system. Accordingly, the period lengthening ratio, \tilde{T}/T is a proxy for understanding the importance of inertial interaction.

As this ratio increases, so does the importance of inertial interaction.

Inertial interaction also increases the damping of the flexible-base SFS system with respect to the fixed-base system. Seismic energy is dissipated at the soil-foundation interface when the superstructure rocks, settles, and slides (Gajan et al. 2005). The damping associated with the soil-foundation interface is usually denoted β_f , is called the *foundation damping* and is a subcomponent of the damping of the entire system. The damping of the entire system includes contributions from soil (hysteretic and radiation damping), the soil-foundation interface (β_f) and material damping of the foundation and superstructure.

The period lengthening ratio, assuming a linear system, is calculated as (Veletsos and Meek 1974)

$$\frac{\tilde{T}}{T} = \sqrt{1 + \frac{\bar{k}}{K_y} \left(1 + \frac{K_y \bar{h}^2}{K_\theta}\right)}, \quad (2.7)$$

where K_y is the lateral stiffness of the foundation, K_θ is the rocking stiffness of the foundation, \bar{h} is the effective height of the structure (usually 70% of the total height of the structure), and \bar{k} is the effective stiffness of the superstructure. In Equation 2.7, \bar{k} is the stiffness of the fixed-base structure, which is defined as $\bar{k} = 4\pi^2 [\bar{W}/(gT^2)]$ (ASCE 7-10 2010); where \bar{W} is the effective weight of the superstructure (usually 70% of the total weight of the superstructure), and g is the acceleration due to gravity.

In Equation 2.7, K_y is the lateral stiffness of the foundation-soil interface and K_θ is the rotational stiffness of the foundation-soil interface. These stiffnesses are evaluated by impedance functions. Pais and Kausel (1988), Gazetas (1991), ATC-40 (1996) and Mylonakis et al. (2006) contain databases of impedance functions that apply for different situations. The impedance functions are themselves functions of the effective shear modulus and Poisson's ratio of the soil as well as the geometry and embedment depth of the foundation. The effective shear modulus is of critical importance when calculating the impedance functions, because its value is sensitive to the dynamic properties of the soil. The effective shear modulus should be determined based on the soil strain levels associated with the design earthquake (ASCE 7-10 2010), which requires that a seismic site response analysis be performed.

Finding β_f is more difficult than the period-lengthening ratio. Numerous researchers have proposed closed-form solutions for β_f (e.g., Veletsos and Nair 1975; Wolf 1985). These expressions are functions of the period lengthening ratio, the soil hysteretic damping, the mass of the superstructure, the effective height of the superstructure, the lateral and rotational stiffnesses of the soil-foundation interface, the frequency range of interest, and the lateral and rotational damping ratios. The lateral and rotational damping ratios can be determined by expressions contained in Pais and Kausel (1988). Like the impedance functions for the lateral and rotational stiffnesses, the impedance functions for the lateral and rotational damping ratios are functions of the effective shear modulus and Poisson's ratio of the soil as well as the geometry and embedment depth of the foundation. In addition, the lateral and rotational damping ratios are frequency-dependent.

FEMA-440 (2005) contains a simpler expression for the SFS system damping ratio ($\tilde{\beta}_f$),

which is given as

$$\tilde{\beta}_f = \beta_{fdn} + \frac{\beta_i}{\left(\frac{\bar{T}}{T}\right)^3} \quad (2.8)$$

where β_{fdn} is a foundation damping factor that accounts for radiation damping, and β_i is the estimated damping ratio of the fixed-base structure.

Previous researchers have found a number of dimensionless parameters that correlate well with inertial interaction. Pitilakis et al. (2008) contains a concise summary of these dimensionless parameters. The most important is the structure-to-soil stiffness ratio, $1/\sigma$ (Stewart et al. 1999a). $1/\sigma$ is the inverse of the “wave parameter,” σ , which is discussed in more classical inertial interaction references (e.g., Veletsos and Meek 1974; Veletsos and Nair 1975). As the value of $1/\sigma$ increases, the period lengthening ratio increases, and it follows that the importance of inertial interaction also increases.

The structure-to-soil stiffness ratio is defined as

$$\frac{1}{\sigma} = \frac{\bar{h}}{V_s T} = \frac{1}{4} \cdot \frac{\bar{h}}{H} \cdot \frac{T_s}{T}, \quad (2.9)$$

where \bar{h} is the equivalent height of the structure, V_s is the shear wave velocity of the surrounding soil, T is the fixed-base period of the superstructure, H is the thickness of the soil layer, and T_s is the site period of the soil. The equivalent height is the height of an equivalent single-degree-of-freedom oscillator. This can usually be estimated at 70% of the total height of the structure (FEMA-440 2005). Equation 2.9 shows that inertial interaction is particularly important for the case of a tall, stiff superstructure founded on a soft, shallow soil layer.

Another important dimensionless parameter is the aspect ratio, \bar{h}/r ; where r is the equivalent radius of the foundation. As this ratio increases, the importance of inertial SFSI also increases. Tall, slender structures are more prone to rocking during earthquakes; whereas short, stocky structures are more prone to sliding than rocking. A large \bar{h}/r value implies that the base overturning moment can be large during an earthquake. This is why inertial interaction increases with the aspect ratio (Stewart et al., forthcoming).

Figure 2.3 shows how the structure-to-soil stiffness ratio and aspect ratio affect the period lengthening ratio and damping ratio of a SFS system (Kramer and Stewart 2004). From this figure, it can be seen that the period lengthening ratio increases with increasing values of $1/\sigma$, as previously mentioned. It can also be seen that the foundation damping ratio, β_f , increases with increasing values of $1/\sigma$. Figure 2.3 shows that β_f decreases as \bar{h}/r increases. This indicates that lateral movements of the foundation dissipate energy more efficiently than rocking movements (Kramer and Stewart 2004).

Another dimensionless parameter that correlates with inertial interaction is the structural mass to soil mass ratio, δ (Veletsos and Meek 1974). δ is defined as $m/(4\rho_s Ah)$, where m is the mass of the superstructure, ρ_s is the density of the soil, A is the area of the foundation,

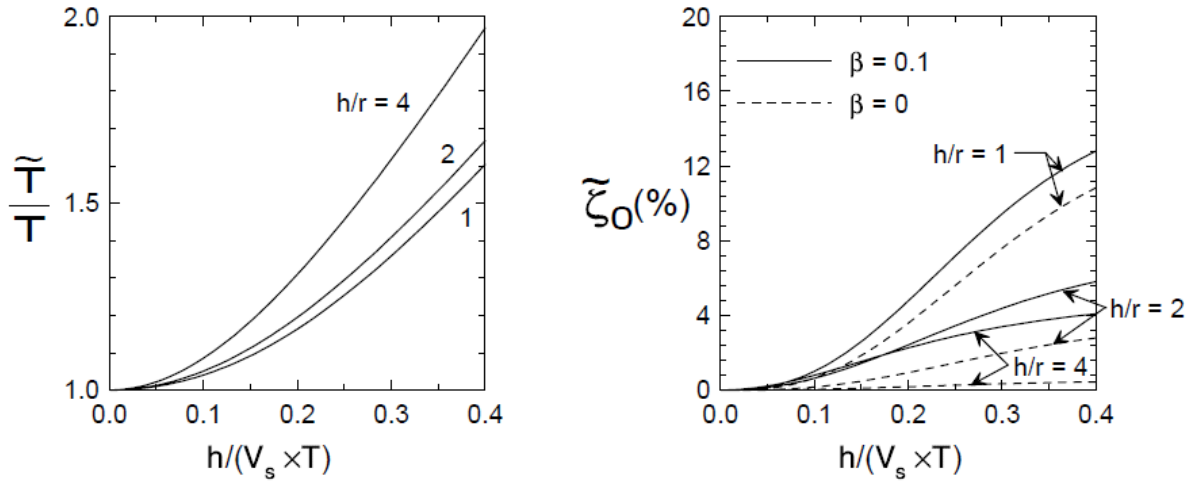


Figure 2.3: The relationship between $1/\sigma$ and \bar{h}/r with \tilde{T}/T and β_f . Note that ζ_0 in this figure is analogous to β_f . After Kramer and Stewart (2004)

and h is the effective height of the structure. Inertial interaction effects generally increase with increasing values of δ (Aviles and Perez-Rocha 1996).

Figure 2.4 shows a pseudo-acceleration response spectrum that has been updated to include inertial interaction effects (Kramer and Stewart 2004). The pseudo-spectral acceleration, S_a , is proportional to the base shear of the superstructure. In many cases, the pseudo-spectral acceleration considering inertial interaction, \tilde{S}_a , is less than that of the fixed-base case. This implies that for many cases, the base shear considering inertial interaction effects is less than the base shear of a fixed-base structure. Therefore, many earthquake engineers neglect inertial interaction when designing structures in seismically active areas, and this omission has historically been considered “conservative.”

Figure 2.4 is a simplistic representation of inertial interaction. There are cases when the structural demands do not decrease when inertial interaction effects are considered; i.e., there are cases when inertial interaction effects are detrimental (Mylonakis and Gazetas 2000). Some of these cases are:

- When \tilde{T} equals the site period resonance can occur
- When the superstructure is more sensitive to spectral displacement than spectral acceleration (spectral displacement at \tilde{T} is usually larger than spectral displacement at T)
- When the site of interest is dominated by soft soils, and the site-specific response spectrum is large in the long period region

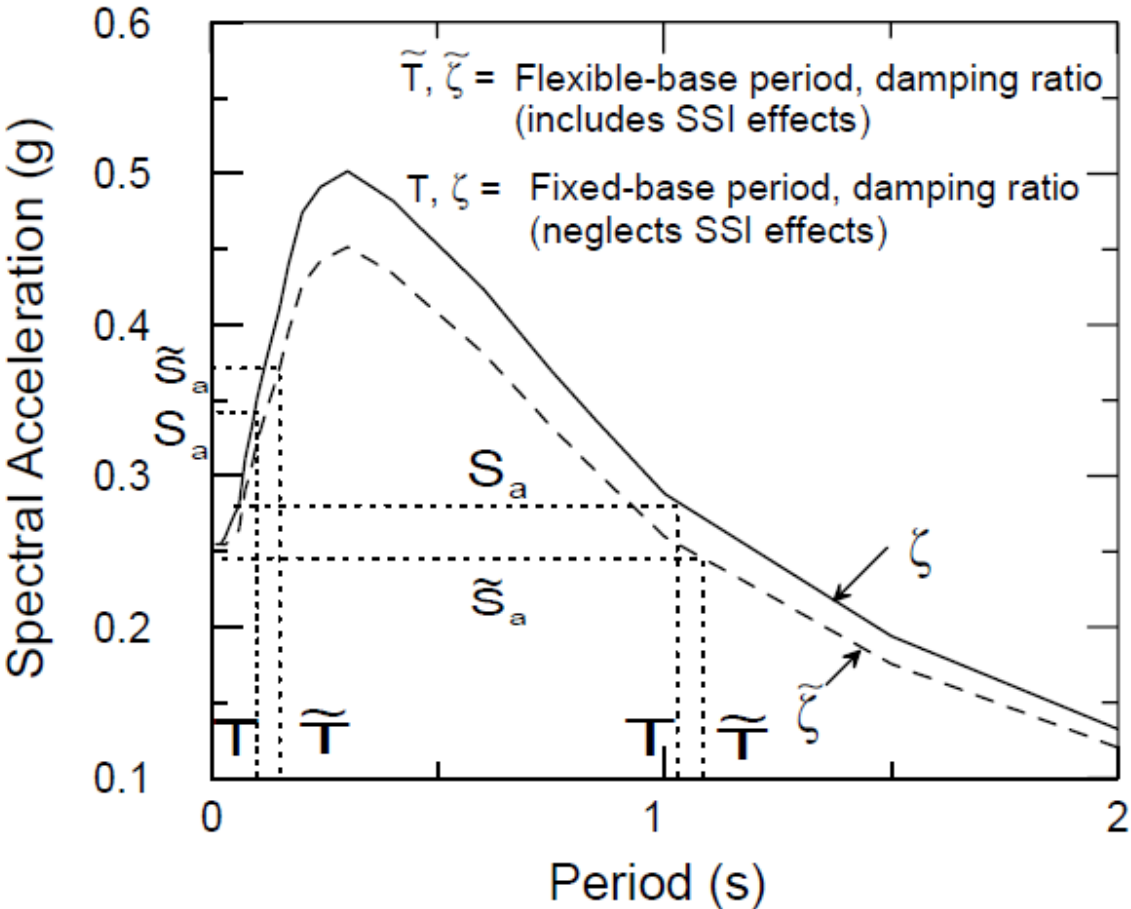


Figure 2.4: A pseudo-spectral acceleration response spectrum updated to include the effects of inertial SFSI. After Kramer and Stewart (2004).

- When rocking, sliding, settlement, or uplift of footings are potentially issues

A case history examining detrimental inertial interaction effects is given later in this chapter.

2.1.3 Complete SFSI analysis methods

The Kinematic Interaction and Inertial Interaction sections of this chapter explain methods for how to incorporate the effects of both kinematic and inertial interaction into engineering design. Importantly, these two types of interaction occur simultaneously during earthquakes. Accordingly, it is important to discuss complete SFSI analysis methods.

The most robust complete SFSI analysis method is the *direct method*. In the direct method, the soil, foundation and structure are modeled within the same finite-element

or finite-difference program. There are currently several limitations that make the direct method unattractive. The first is that it requires a program that all earthquake engineers are comfortable using. Usually, programs are either designed for structural earthquake engineers, or geotechnical earthquake engineers, but not both. Newer, academic software packages, such as OpenSees (<http://opensees.berkeley.edu>), are bridging the gap between the two disciplines. Regardless, there is still much work left to be performed before the direct method becomes an attractive option for earthquake engineers. The second limitation is that performing these analyses requires a highly skilled operator and many hours. Thus, these analyses are very expensive and can only be justified for the most important structures. This type of analysis is usually beyond the design scope of low-to-mid-rise buildings.

Because of these two limitations the *substructure approach* is often used when performing complete SFSI analyses. Stewart et al. (forthcoming) contains a summary of the complete SFSI analysis, utilizing a substructure approach:

... a complete treatment of SFSI effects in the assessment of the seismic response of a structure requires (i) an evaluation of free-field soil motions and corresponding soil material properties, (ii) an evaluation of transfer functions to convert free-field motions to [foundation-input motions], (iii) springs and dashpots (or more complex nonlinear elements) to represent the stiffness and damping at the foundation-soil interface, and (iv) a response analysis of the combined structure-spring/dashpot system to the [foundation-input motion] as input.

Figure 2.5 shows a schematic of the substructure approach.

The substructure approach requires that the principle of superposition is valid. This, in turn, requires that each subcomponent responds linearly to the earthquake shaking. Usually, for strong motions, this assumption is invalid, as both the soil and superstructure can respond inelastically. This is a major limitation of the substructure approach. Considerable engineering judgment is required for the cases where subcomponents of the system undergo significant deformation.

2.1.4 Detrimental and beneficial SFSI effects

Stewart and Tileylioglu (2007) interviewed structural earthquake engineers in Seattle, San Francisco, and Los Angeles about their experience with incorporating SFSI into engineering design. This effort was part of the Pacific Earthquake Engineering Research (PEER) Center's "Tall Buildings Initiative." They found that in most cases, the input earthquake motion is assumed to be the free-field surface ground motion, which implies that kinematic interaction effects are ignored. Additionally, in most cases, the foundation-soil interface is assumed to be fixed, which implies that inertial interaction effects are ignored. In summary, for many earthquake engineering projects on the West Coast of the United States, SFSI is ignored.

The key reason that SFSI is ignored is that it is commonly considered "conservative" to do so (Mylonakis and Gazetas 2000). ASCE 7-10 (2010) states:

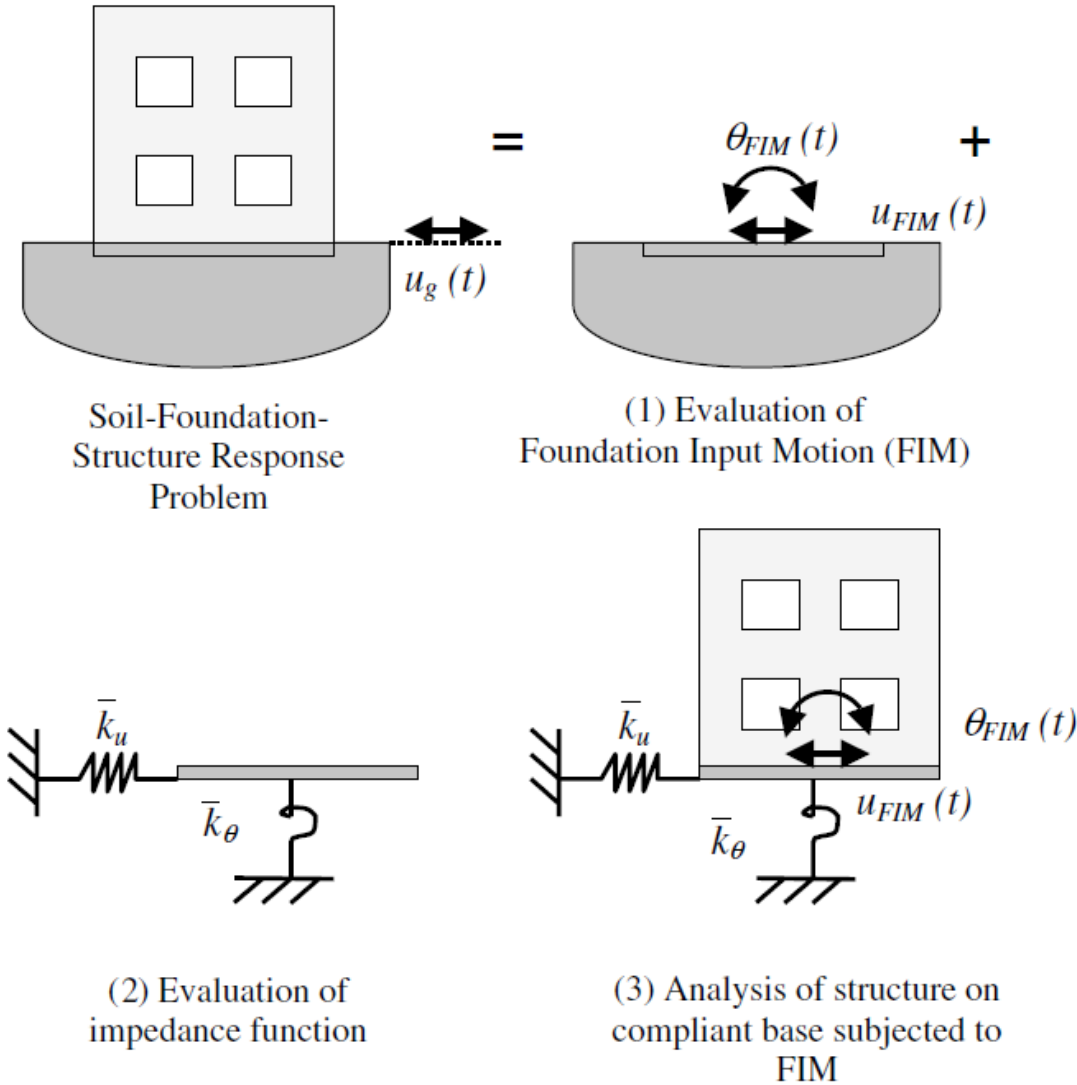


Figure 2.5: A schematic showing the key steps of the substructure approach. After Kramer and Stewart (2004).

The use of these provisions will decrease the design values of the base shear, lateral forces, and overturning moments, but may increase the computed values of the lateral displacements and the secondary forces associated with the P-delta effect.

The word “will” in the above statement implies that including SFSI in engineering design will *always* decrease the base shear, lateral force, and overturning moment. This is not always

the case, as noted in the Inertial Interaction section of this dissertation.

Mylonakis et al. (2006) document a case history from Kobe, Japan following the 1995 earthquake that exhibits the importance of SFSI. These researchers looked at the spectacular failure of the Hanshin Expressway following this earthquake.

Figure 2.6 shows five response spectra calculated from earthquake motions recorded during the 1995 Kobe Earthquake around the expressway site. Mylonakis et al. (2006) calculated the fixed-base period of one pier of the expressway, which is shown on the figure. The fixed-base period, $T = 0.84$ sec, is the period the engineers used to design this expressway. The authors back calculated the flexible-base period to be $\tilde{T} = 1.04$ sec based on modal analysis. Therefore, the period lengthening ratio, \tilde{T}/T is 1.24.

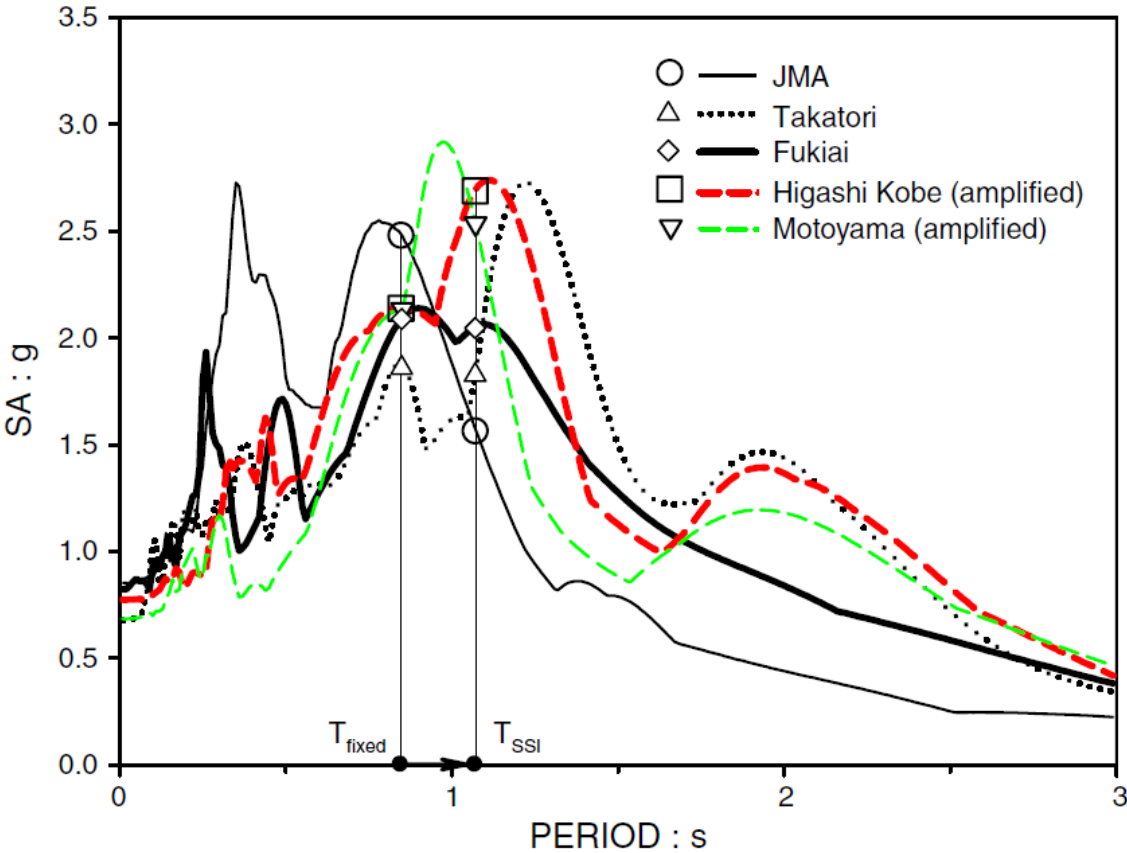


Figure 2.6: Pseudo-acceleration response spectrum recorded near the Hanshin Expressway during the 1995 Kobe earthquake. After Mylonakis et al. (2006)

By examining Figure 2.6, it can be seen that SFSI effects were detrimental for three of the earthquake motions, minor for one, and slightly beneficial for another. Therefore, for three of recorded motions, the spectral demands at \tilde{T} were larger than the spectral demands at T . This observation, among others, led Mylonakis et al. (2006) to conclude that, “[t]he above findings contradict a widespread view of an always-beneficial role of [soil-foundation-structure interaction] in seismic response.”

The prior case history examined the detrimental effects of SFSI. There are also beneficial effects of SFSI. Recent work (e.g., Gajan and Kutter 2008; Anastasopoulos et al. 2010; Kutter et al. 2010) has focused on the beneficial effects of SFSI. These researchers focus on the fact that most foundations are overdesigned to prevent bearing type failures, and the superstructure above is then heavily reinforced to prevent damage. In this typical design scenario, plastic hinges form at the base of the superstructure columns during earthquake loading. The mantra of these researchers is “a hinge is a hinge is a hinge.” They aim to *under-design* the foundation, and allow the plastic hinge to form at the soil-foundation interface—thus taking advantage of SFSI (i.e., the flexible soil-foundation interface).

Figure 2.7 shows schematics and pictures of this beneficial SFSI concept (Anastasopoulos et al. 2010). The left column of this figure shows the conventional design paradigm of overdesigning the foundation. In this case, the plastic hinge that develops during earthquake loading necessarily locates itself in the superstructure. If the demands are larger than the capacity, then this can lead to catastrophic collapse, like the case of the Hanshin Expressway discussed above. The right column of this figure shows the new design paradigm of under-designing the foundation. In this case, the hinge is allowed to locate itself at the soil-foundation interface. This case takes advantage of the flexibility of this interface and accordingly, takes advantage of SFSI. If the demands are larger than the capacity in this case, chances are likely that the superstructure will tilt, but not collapse. This is what is shown in the figure, which is a case history in Turkey following the 1999 Kocaeli Earthquake.

In summary, SFSI effects can be beneficial, neutral, or detrimental for a given SFS system during an earthquake. SFSI effects should not be neglected summarily, and their omission should not automatically be considered “conservative.” Earthquake engineers should investigate when SFSI effects are significant, and they should try to incorporate SFSI into engineering design for these cases. Moreover, when SFSI effects have the potential to be beneficial, earthquake engineers should use this to improve design of SFS systems to prevent catastrophic collapse.

2.2 Structure-soil-structure interaction

Structure-soil-structure interaction has received relatively less attention in the earthquake engineering literature compared to the related phenomenon of SFSI. A reason for this disparity is the dearth of experimental results and case history data that clearly show SSSI. Regardless, some analytical studies have been performed to understand SSSI. In this section, some of

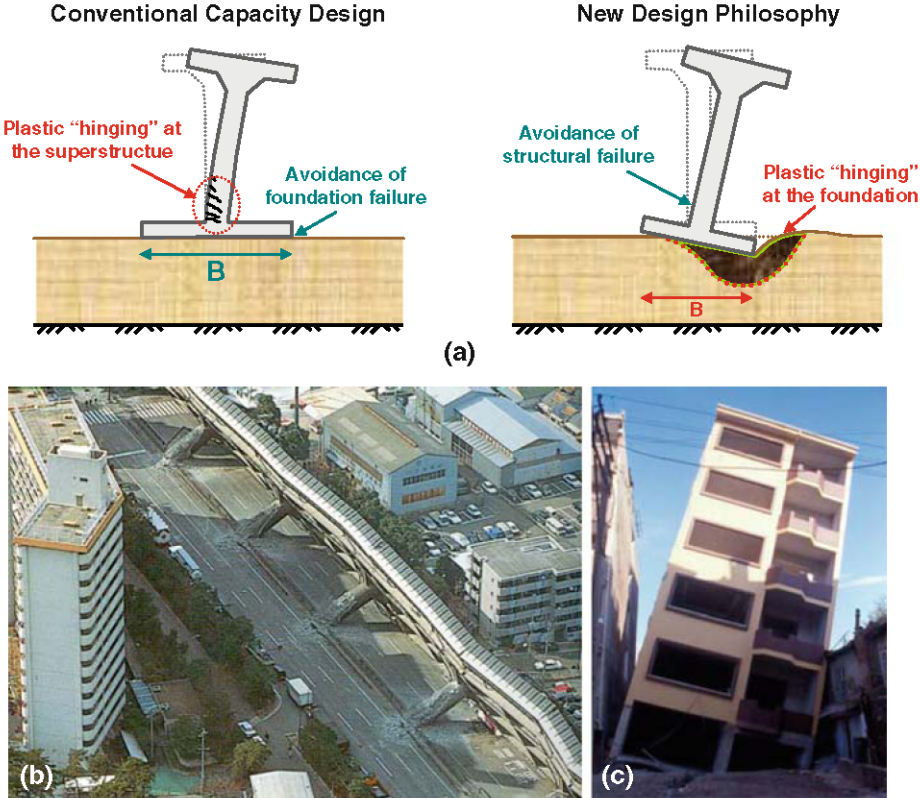


Figure 2.7: The oversized foundation versus the undersized foundation. For the oversized case, a plastic hinge can form in the superstructure and lead to catastrophic damage. For the under-designed case, the plastic hinge forms at the soil-foundation interface. Thus, the under-designed SFS system can have better structural performance than the oversized system. This is a manifestation of beneficial SFSI. After Anastasopoulos et al. (2010).

these methods are examined.

One of the earliest structure-soil-structure interaction studies was performed by Luco and Contesse (1973). In this study, the researchers looked at two adjacent shear walls. A number of simplifying assumptions were needed to make this problem tractable:

1. The shear walls are infinitely long and infinitely parallel
2. The foundations are rigid and perfectly-bonded to the soil
3. The soil is an elastic, homogeneous, and isotropic halfspace
4. The seismic excitation is represented by vertically-propagating, harmonic SH waves

5. The particle motion of the seismic excitation is parallel to the infinite direction of the shear walls

Item 5 above is of particular interest. This indicates that the Luco and Contesse (1973) study was concerned with two infinitely long walls with shaking along the length of the walls; that is, they were concerned with how the buildings interact in the direction perpendicular to wave propagation.

The authors of this study solve a partial differential equation (i.e., the equation of motion) with appropriate boundary conditions determined by the assumptions listed above. They develop expressions for the displacement of the shear walls in the out-of-plane direction as a function of the free-field displacement of the ground surface, the heights and widths of the shear walls, the radii of the foundations, the center-to-center distance between the shear walls, the densities of the soil, foundations, and structures, the shear moduli of the soil and structures, and the frequency of the harmonic excitation. In other words, the displacement of the shear walls is a function of the seismic excitation, the geometry of the problem, and the properties of the soil, foundations and structures. After performing sensitivity analyses with the developed displacement expressions, the authors drew the conclusion that structure-soil-structure interaction effects are particularly important for the case of a smaller shear wall located adjacent to a larger shear wall. As Luco and Contesse (1973) note, “[i]n this case, the base motion and shear forces of the smaller structure will be significantly different from the corresponding results obtained by ignoring the presence of the larger shear wall.” This effect is hard to quantify, because it varies as a function of frequency and structure geometry; however, these researchers found that at certain frequencies, a smaller shear wall that is half the size (in all dimensions) as an adjacent larger shear wall can experience base displacements two to three times larger during an earthquake motion.

Wong and Trifunac (1975) extended the Luco and Contesse (1973) study by considering the effects of non-vertically incident SH waves. They left the other assumptions made by Luco and Contesse intact. They solved an equation of motion to develop expressions for the displacements of the shear walls as a function of the parameters listed above and the angle of incidence. The authors of this study also examined the interaction of many parallel, infinitely long shear walls (i.e., more than two).

Wong and Trifunac (1975) drew the following conclusions from their study: (1) if a small shear wall is located in front of a larger shear wall, then the displacement of the small shear wall will likely differ greatly from the case of an individual shear wall; (2) if a small shear wall is located in the rear of a larger shear wall, then the displacement of the small shear wall will likely mimic the displacement of the larger shear wall; and (3) if a smaller shear wall is located between two (or more) larger shear walls, then the response of the smaller shear wall is complex, and is highly dependent on the geometry of the problem. In the three cases above, when the small shear wall is “in front,” it experiences the seismic waves before the large shear wall. Likewise, when the small shear wall is “in rear,” it experiences seismic waves after the large shear wall.

Wong and Trifunac (1975) also commented on how the arrangements of buildings affected the surrounding earthquake motions. They noted that the scattering and interference of waves near the structures could substantially alter the earthquake motions in the buildings' vicinity, and that these earthquake motions could be substantially different than the free-field surface ground motion. This insight was the start of the field of site-city effects, which is the topic of the next subsection.

Lee and Wesley (1973) performed SSSI analyses around the same time as Luco and Contesse (1973) and Wong and Trifunac (1975). Their analyses, however, were geared towards the nuclear power industry. For this reason, they examined the case of three 3-D structures located adjacent to one another. This is the case of a nuclear reactor with two twin containment vessels, which are all built on separate foundations.

Lee and Wesley (1973) made the following assumptions for their analyses: (1) the superstructures are flexible, and are represented by discretized linear systems, (2) the foundations are rigid disks perfectly bonded to the soil, (3) the soil is an elastic halfspace, and (4) the structures are subjected to harmonic excitation in the in-plane direction. This last assumption is contrary to the work of Luco and Contesse (1973) and Wong and Trifunac (1975), who examined out-of-plane shaking. With these assumptions, they solved a series of equations to determine the seismic response of the three structures subjected to input earthquake motions. They found that the seismic response of the reactor can be significantly altered by the seismic response of the adjacent containment structures; which is to say that they found SSSI to be an important factor to consider during the design of nuclear structures. They also found that the SSSI results were sensitive to the soil's shear modulus, with SSSI effects generally increasing as the soil's shear modulus decreased.

The three studies mentioned above were completed analytically by defining a partial differential equation (PDE) that governs motion, and then solving the PDE using boundary conditions defined by a set of simplifying assumptions. These were fundamental studies into SSSI, and were the impetus for later studies that were more computational intensive. Qian and Beskos (1995) used a frequency-domain boundary element method (BEM) to study SSSI. They focused their attention on the seismic response of adjacent footings with arbitrary shape. They assumed that the footings were massless, rigid, on the surface (i.e., not embedded), and perfectly bonded to the soil. Furthermore, they assumed that the soil was an elastic halfspace. The footings were subjected to harmonic motions.

A key conclusion from the Qian and Beskos (1995) work is that the foundation-soil flexibility is affected by adjacent footings; that is, there is cross-interaction between adjacent footings during earthquakes. In summary, their study found that SSSI is important to consider not only between two adjacent structures, but also within the same structure. Footings that support the same superstructure can affect each other during earthquakes.

Following this work, Mulliken and Karabalis (1998) developed a discrete model of frequency-independent springs and dashpots to examine the seismic response of adjacent footings using nearly the same assumptions as Qian and Beskos (1995). These researchers drew similar conclusions as Qian and Beskos; that is, adjacent footings affect each other during

earthquakes.

More recently, Padrón et al. (2009) developed a boundary element method (BEM)/finite element method (FEM) model for investigating the seismic response of adjacent structures founded on piles. In their model, the soil is modeled with the BEM, and the piles are modeled as Bernoulli beams with the FEM. Padrón et al. (2009) conclude that SSSI effects are important for adjacent structures that have approximately the same dynamic characteristics. In contrast, they conclude that SSSI effects are relatively unimportant for adjacent structures that have considerably different dynamic characteristics

2.3 Site-city effects

Site-city effects occur in urban areas. The arrangement of structures within the urban environment affects the earthquake motions recorded nearby (Taborda 2010). As seismic waves reach the built environment, the vibrational energy from the superstructures, caused by inertial interaction, re-interacts with the surrounding soil. This is a complex re-interaction, and as a result, constructive, destructive, and neutral interference of the waves occur simultaneously. Thus, the ground motions recorded in an urban area at the ground surface are spatially variable. This spatial variability is a function of the arrangement of the structures, as well as the important properties of the SFS systems.

Numerous researchers have examined site-city effects. Some of the earliest work is by Jennings (1970). This study examines seismometer recordings around the Millikan Library in Pasadena, California following forced-vibration tests. It was found that the Library's horizontal and vertical vibrations can be recorded within several kilometers of the building. Other researchers studying the seismic response of the Millikan Library have come to similar conclusions following other forced-vibration tests, earthquakes and ambient vibrations (e.g. Luco et al. 1988). In a similar vein, Kanamori et al. (1991) studied the effects of a space shuttle re-entering the atmosphere near Los Angeles. This study found that the larger buildings in downtown Los Angeles picked up the energy from the sonic boom of the re-entering shuttle, and then transferred that energy into the surrounding soil. Seismometers in the area recorded this phenomenon.

Wirgin and Bard (1996) examined how high-rise buildings in Mexico City changed the seismic recordings in the nearby soil following the 1985 Michoacán earthquake. These researchers, by using numerical techniques, found that a typical high-rise building found in Mexico City could increase the intensity and duration of earthquake motions recorded within 1 km of the building. This study was performed for the soft clay that underlies Mexico City. Other researchers have built and examined more complicated numerical models examining other structural configurations and other soil types (e.g., Guéguen et al. 2000; Clouteau and Aubry 2001; Ghergu and Ionescu 2009). In addition, other researchers have performed field experiments using release tests on constructed buildings (e.g., Mucciarelli et al. 2003; Gallipoli et al. 2006; Ditommaso et al. 2010). In these tests, the buildings were pushed at their tops,

and then released suddenly. Instruments in the surrounding soil captured the movement of the seismic waves caused by the building. These studies led to the conclusion that the inertia of a building does affect the earthquake motion of the surrounding soil, and especially when the period of the building is close to the period of the site. This was the case in Mexico City, and is a large reason why site-city effects were so important for this earthquake (Wirgin and Bard 1996). These studies found that site-city effects are a function of the structural properties of the buildings within the city, their arrangement, the soil properties of the surrounding soil, and the characteristics of the seismic waves that approach the site.

As part of the NCB project, Choy (2011) performed forced-mass vibration tests of centrifuge structural models. A wave attenuation prediction model based on the vertical component of Rayleigh waves was developed to estimate the acceleration at a specific point on the soil surface away from the vibrating centrifuge structural models by considering both geometric and material damping. This acceleration can be used as an input parameter to estimate the response of a structure due to the vibration of its neighboring structure.

Site-city effects are intimately connected to the similar phenomenon of structure-soil-structure interaction. In fact, one could argue that SSSI is a subset of site-city effects. There are two differences between the two phenomenon, which warrants splitting them. The first difference is that site-city effects research aims to determine how an entire urban area interacts during an earthquake. In contrast, SSSI studies usually concentrate on two or at most three adjacent structures. The second difference is that site-city effects researchers are usually engineering seismologists or have strong engineering seismology backgrounds. This is required, because this type of research requires modeling a complex wave propagation problem over a large spatial area. SSSI researchers, in contrast are usually structural earthquake engineers or geotechnical earthquake engineers. The focus in SSSI research is much more localized; i.e., how does this structure affect that structure and the surrounding soil?

The focus of this thesis is on SSSI research, because the centrifuge tests were performed using only two or three structures. This is only a small step, however. In the future, site-city effects researchers and SSSI researchers will have to collaborate to further the field of urban earthquake engineering.

2.4 Geotechnical centrifuge testing

Soil strength and stiffness are nonlinear functions of the state of stress; in other words, soil response is strongly dependent on the existing state of stress. The principle of geotechnical centrifuge testing is to simulate realistic stresses within a relatively small model. This allows researchers to investigate field-scale phenomena at a relatively small scale, which saves time and money. Additionally, it allows researchers to study earthquake engineering phenomena without having to wait for devastating earthquakes to occur.

A centrifuge model is constructed in a well-controlled laboratory environment. This allows the researcher to control important properties, such as the relative density of the soil, the

stiffness of the structural members, *et cetera*. The centrifuge model is then placed on the end of the centrifuge arm and spun to a desired centrifugal acceleration. As the centrifuge “spins-up,” the model tilts-up 90° such that the extra gravitational field produced by the centrifugal acceleration points straight down within the model. The researcher defines the centrifugal acceleration. Additionally, the researcher defines the depth within the centrifuge model where that specified centrifugal acceleration is experienced. This is accomplished by changing the counterbalance of the centrifuge. For smaller centrifuges, the difference in centrifugal acceleration along the depth of the model must be taken into account.

For this research, the large centrifuge located at the University of California at Davis Center for Geotechnical Modeling was employed. This facility is one of the 14 equipment sites that are part of the George E. Brown, Jr. Network for Earthquake Engineering Simulation (NEES) funded by the National Science Foundation (NSF). The centrifuge has an arm radius of 9.1 m and a maximum payload capacity of 4,500 kg. Additionally, the centrifuge has a robust shaking table controlled by a hydraulic servo-actuator, which allows realistic earthquake motions to be recreated. The shaking table has a payload capacity of 2,700 kg and can operate in centrifugal accelerations of up to 75 g. The centrifuge has a data acquisition system (DAQ) that can record around 200 channels of streaming data simultaneously. More details about the technical specifications of the centrifuge, the shaking table, and the DAQ can be found at the Center for Geotechnical Modeling website (<http://nees.ucdavis.edu/>) as well as Kutter et al. (1994) and Kutter (1995).

The stresses in a centrifuge model are the same that would occur in the prototype. This is the power of centrifuge testing, as mentioned earlier; the state of stress in the model is the same as in a field-scale model, which allows researchers to make important soil response observations without having to build or instrument full-scale models and wait for events to occur. Accordingly,

$$\sigma_m = \sigma_p \quad (2.10)$$

where σ_m is the stress at model scale and σ_p is the stress at prototype scale.

Expanding the expression in Equation 2.10 yields:

$$\rho_m g_m z_m = \rho_p g_p z_p \quad (2.11)$$

where ρ_m and ρ_p are the soil densities at model scale and prototype scale, respectively; and g_m and g_p are the acceleration due to gravity at the model scale and prototype scale, respectively. In Equation 2.11, the densities can be considered to be equal (i.e., $\rho_m = \rho_p$). In addition, the acceleration due to gravity at model scale is given as $N g_p$, where N is the desired centrifugal acceleration. Manipulating Equation 2.11 with the aforementioned givens yields:

$$\frac{z_p}{z_m} = N \quad (2.12)$$

Equation 2.12 indicates that the depth at the prototype scale is the product of the desired centrifugal acceleration, N , and the depth at the model scale. Therefore, N is an important

Table 2.1: Important scaling parameters for geotechnical centrifuge testing

Parameter	Model Dimension/ Prototype Dimension
Length	N
Area	N^2
Mass	N^3
Density	1
Force	N^2
Stress	1
Strain	1
Acceleration, gravity	$1/N$
Acceleration, dynamic	$1/N$
Time, dynamic	N
Frequency, dynamic	$1/N$

parameter, and is usually referred to as the scaling factor. In a similar fashion, scaling factors for other important quantities can be determined. Some of these derivations are given in Kutler (1995) as well as Garnier et al. (2007). Table 2.1 contains some of the more important scaling parameters for this project.

The factors for length, time, and frequency in Table 2.1 are of particular interest for earthquake engineering problem, and especially SFSI problems on dry, dense sand. Length (prototype to model) is scaled by N . Thus, when designing structural models, on one hand it is desirable to have a large scale factor, so that the models can fit within the centrifuge container without experiencing significant boundary effects; on the other hand, measurement errors are exacerbated as the scaling factor increases. Time (prototype to model) is scaled by $1/N$. The input earthquake motions, therefore, must be reproduced very quickly on the centrifuge shaking table. Frequency (prototype to model) is scaled by N . If the input earthquake motions have a dominant frequency range of interest of 0.1 to 15 Hz, for instance, then the shaking table must reproduce a frequency range of $0.1N$ to $15N$ Hz. Reproducing earthquake motions with such high frequencies in such a short duration is troublesome for the hydraulically-controlled shaking table. This difficulty is explored further in the next chapter of this dissertation.

Given the difficulties discussed in the previous paragraph, a centrifugal acceleration, and thus scaling factor of 55 was used for this research project. This scaling factor was large enough to build satisfactory model structures within the boundary constraints of the centrifuge model container. Additionally, a suite of earthquake motions could be well-calibrated with the centrifuge shaking table at this scaling factor. Finally, the RPM associated with 55 g does not excite the torsional resonant frequency of the centrifuge drive system (Wilson, pers. comm.), and previous researchers had had success with it (e.g., Dashti 2009).

Geotechnical centrifuge testing is a useful for understanding earthquake engineering problems. This is especially true of SFSI problems, because the SFS system can be modeled together, and the response of this system can be monitored. These tests are relatively inexpensive to perform, and a wide range of conditions can be examined. Kutter (1995) and Liu and Dobry (1994) note some key advantages of centrifuge testing. First, the stress scaling factor is one, which means that well-controlled laboratory-built models represent much larger field scale models, which is the true power of centrifuge testing. Second, the experimental results are repeatable and future models can be built sequentially based on results from previous tests. This was the philosophy of the testing series described in this dissertation. A “building-block” approach was taken, and subsequent models were built based on lessons learned from previous tests; that is, observation aided the design of future models. Third, modes of failure and deformations can be directly observed during testing via cameras and after testing. These observations allow the researcher to discover new mechanisms of failure as well as develop fundamental insights into old ones. Fourth, centrifuge technology is efficient and cost-effective compared to full-scale field testing. This is especially true of earthquake engineering problems. An instrumented building in the field may not experience strong earthquake motions for many years. Fifth, realistic earthquake motions are able to be inputted into the model via a robust hydraulically-controlled shaking table. For tests built using dry, dense sand (like the testing series described in this dissertation), this is a particular benefit, because more than 20 earthquake motions can be performed for each test. This allows the researcher to gather many data points, and tests multiple scientific objectives within one test. Finally, centrifuge data can be used to calibrate numerical models. The calibrated numerical models, in turn, can be used to perform sensitivity analyses and generalize results.

Along with the many advantages of centrifuge testing, there are a number of disadvantages, or limitations (e.g., Hausler 2002; Dashti 2009). The first, as noted earlier, is that the increased centrifugal acceleration experienced by the model varies as a function of depth within the model. The location where the desired centrifugal acceleration is experienced determined by the researcher. For the tests described in this dissertation, this was set as 1/3 of the depth of the model from the ground surface. This is a typical depth to use for SFSI problems. This limitation is minor because the centrifuge arm at the UC Davis CGM is large. The centrifugal accelerations at the very bottom of the model and at the center-of-gravity of the tallest structure used were approximately 57 g and 54 g, respectively. This variation can be modeled numerically, which also reduces the effect of this limitation.

The second potential limitation is that the centrifuge container has finite dimensions, and boundary effects can be an issue. Boundary effects are manifested in different ways. First, the walls of the container can increase the lateral resistance and limit lateral deformations. Second, the soil and the soil-container boundary can arch. Third, the container walls can provide “support” to structural models if they are located too close to the boundaries. This additional “support” would affect the structural response of the structural models, and possibility lead to incorrect conclusions. Fourth, the bottom boundary is rigid compared

to the overlying soil, which creates an unrealistic impedance contrast. This can change the earthquake motions as they propagate through the soil later compared to earthquake motions that would be recorded in the field. Fifth, SSSI is caused by radiation of waves from one structure to the surroundings and these waves will reflect from the model container in complex patterns. Choy (2011) suggested that reflections off the wall have a similar effect at image structures. More work is needed in this area to understand how these complex wave reflections affect SSSI. Finally, the total stresses are changed due to the friction at the soil-container interface, which is called the “silo effect.” The silo effect works to reduce the vertical deformation of the soil. To minimize all of these boundary effects, the flexible shear beam container with installed “shear rods” was employed (Kutter 1995). Additionally, the structures were placed away from the boundaries and were offset from the centerline. Ilankatharan and Kutter (2010) created a numerical model that incorporates the centrifuge shaking table, centrifuge container and the soil model. The key finding from their study is that the shaking table-container-model interaction should be taken into account when interpreting results from centrifuge tests.

A third potential limitation is measurement error. As mentioned earlier, this can be significant for models spin at higher centrifugal accelerations. The testing described in this dissertation was performed at 55 g. Therefore, a one mm measurement error in model scale corresponds to a 55 mm measurement error in prototype scale. Best practices are observed to try to minimize this limitation, but it must always be kept in mind when interpreting centrifuge test results.

Chapter 3

Earthquake Motion Selection

Centrifuge researchers have noted the importance of using realistic earthquake motions for centrifuge testing (e.g., Fiegel and Kutter 1994; Kutter 1995). Using simplified sine waves as input motions, while theoretically attractive, can overemphasize some results and underemphasize others. Accordingly, this project utilizes a suite of modified earthquake motions. This chapter describes the earthquake motion selection procedure and describes how the motions are calibrated for use with the centrifuge at the University of California at Davis Center for Geotechnical Modeling (UCD-CGM). The term “earthquake motion” is preferred over “ground motion” in this dissertation, because motions recorded at locations other than the ground surface are also important.

3.1 Project location and local seismicity

A site in downtown Los Angeles, California was chosen for this research project. The site coordinates, used for subsequent seismic hazard analysis, were chosen to be N34.082 W118.224.

This project location was chosen based on the following criteria:

1. It is located in a dense, urban area
2. Typical structures in the generally vicinity of the chosen location are low-to-mid-rise buildings (i.e., three to nine-stories)
3. It is located in tectonic region that experiences shallow, crustal earthquakes
4. It is located in an area that is affected by near-fault earthquake motions, as well as earthquake motions located at distances larger than 30 km (i.e., “ordinary” earthquake motions)

The first requirement was specified to meet the fundamental goal of this research. The second requirement was specified because low-to-mid-rise structures dominate the building stock of urban areas; yet, these types of structures are least likely to be designed using state-of-the-art seismic design procedures. It is these types of structures that require simplified design procedures. The third requirement was specified because Los Angeles is located in a shallow, crustal tectonic region. The fourth requirement was specified by necessity. The seismic hazard in urban areas is affected by both near-fault earthquake motions as well as earthquake motions located at intermediate distances.

Figure 3.1 and Figure 3.2 show the seismic hazard deaggregations for the project location for periods of 0.0 sec (PGA) and 1.0 sec, respectively. These deaggregations were made using the 2008 Interactive Deaggregation tool developed by the United States Geologic Survey (USGS), which is available online at: <http://eqint.cr.usgs.gov/deaggint/2008/index.php> (Peterson et al. 2008). A probability of exceedance of 10% in 50 years (i.e. a return period of 475 years) and a shear wave velocity of 760 m/sec were assumed to create these deaggregations. This shear wave velocity corresponds to a “rock site.”

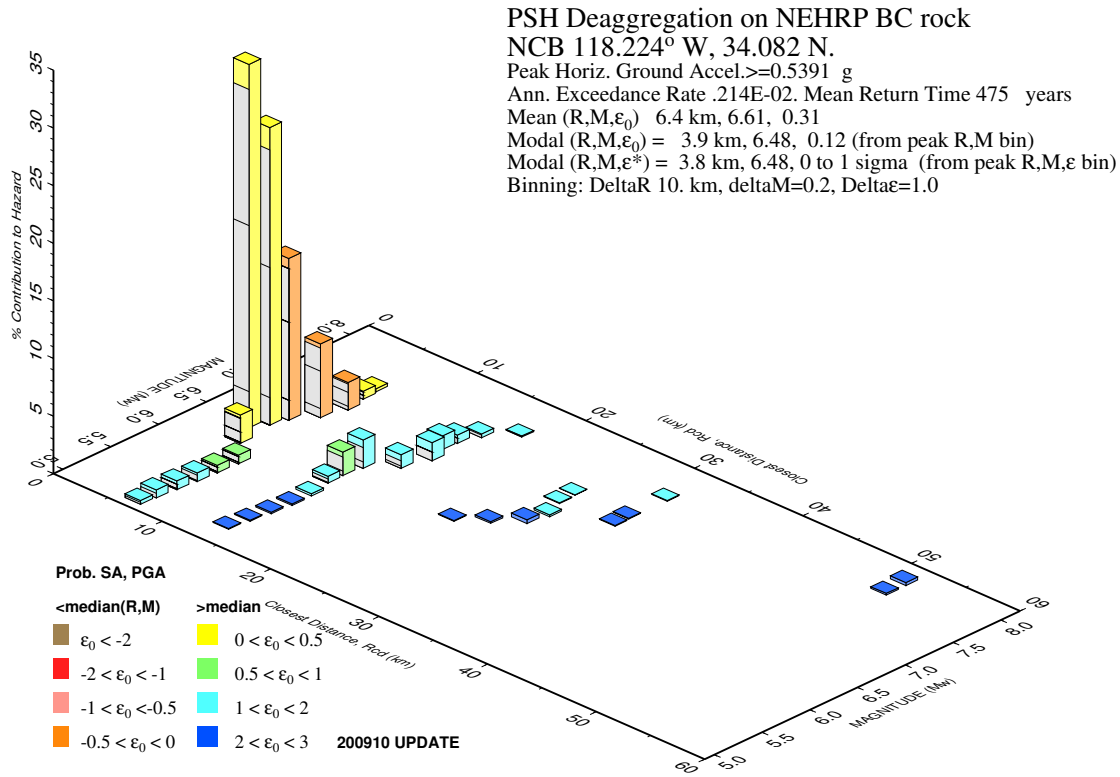
Examining these figures, it can be seen that the seismic hazard at the project location is dominated by events located around 4 to 8 km away that have moment magnitudes of roughly 6.5. Accordingly, the seismic hazard at the project location is dominated by the nearby Upper Elysian Park fault. Detailed information about this fault, its seismic hazard and its geology can be found in Oskin et al. (2000). The nearby Raymond fault also contributes to the seismic hazard of the selected project location.

The regional geology of the Los Angeles basin is described in Chang et al. (1994). The basin contains Pleistocene and Holocene deposits with depths ranging up to 1 km in some locations. The Holocene deposits are characterized by “fine to very coarse grained stream, channel, alluvial fan, flood plain, and dune deposits.” The Pleistocene deposits are characterized by “fine to very coarse grained alluvium and marine terrace deposits.” The shear wave velocity of these surficial Holocene and Pleistocene deposits ranges from 120 to 300 m/sec. The basin is contains a complex series of faults with a variety of faulting mechanisms, many of which are blind.

3.2 Near-fault and ordinary earthquake motions

Urban areas in shallow, crustal tectonic regions are often underlain by active faults (e.g., Los Angeles, San Francisco Bay Area, Tokyo); therefore, near-fault earthquake motions are important to consider. Near-fault earthquake motions are typically located within 20 km of an active fault (Bray and Rodriguez-Marek 2004).

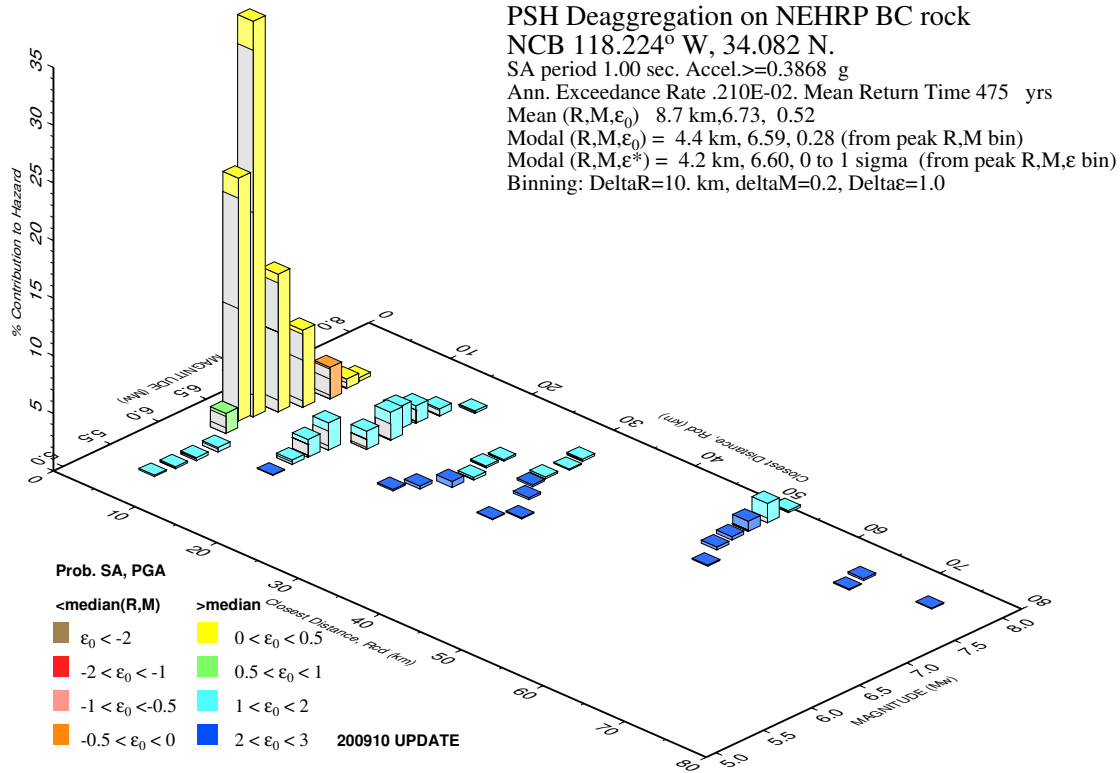
Near-fault earthquake motions have the potential to be more damaging than earthquake motions produced at further distances. One reason is that the seismic waves have less distance to travel between the source and the site in the near-fault case. Accordingly, radiation damping is less effective at attenuating the intensity of the waves.



GMT 2011 Apr 6 16:46:01 Distance (R), magnitude (M), epsilon (E0,E) deaggregation for a site on rock with average vs= 760. m/s top 30 m. USGS CGHT PSHA2008 UPDATE Bins with lt 0.05% contrib. omitted

Figure 3.1: A seismic hazard deaggregation for N34.082 W118.224 for a period of 0.0 sec (PGA). The probability of exceedance is 10% in 50 years and the shear wave velocity is 760 m/sec (rock site). This deaggregation was made using the USGS Interactive Deaggregation tool (2008 edition).

Another reason why near-fault earthquake motions can be more damaging is related to the concept of directivity (Somerville et al. 1997). Directivity arises because faults typically rupture along a plane. The rupture starts at a point, and propagates in a rupture direction. The velocity of the rupture is on the order of 80% of the shear wave velocity of the surrounding geologic media (Somerville et al. 1997). This causes a shear wave front to develop in the direction of propagation, which is shown in Figure 3.3. Sites located towards the direction of rupture experience intense, short-duration, pulselike motions. This phenomenon is called forward-directivity. Forward-directivity has caused extensive damage to built environments during past earthquakes (e.g., Bertero et al. 1978; Alavi and Krawinkler 2001; Luco and Cornell 2007).



GMT 2011 Apr 6 16:47:33 Distance (R), magnitude (M), epsilon (E0,E) deaggregation for a site on rock with average vs= 760. m/s top 30 m. USGS CGHT PSHA2008 UPDATE Bins with lt 0.05% contrib. omitted

Figure 3.2: A seismic hazard deaggregation for N34.082 W118.224 for a period of 1.0 sec (PGA). The probability of exceedance is 10% in 50 years and the shear wave velocity is 760 m/sec (rock site). This deaggregation was made using the USGS Interactive Deaggregation tool (2008 edition).

Figure 3.4 shows the velocity-time series recorded at the Lucerne station during the 1992 Landers earthquake, which is a forward-directivity earthquake motion. An intense velocity pulse can be seen in this record around 8 sec. This velocity pulse can be characterized by the pulse period, the number of pulses, and the pulse amplitude, which is related to PGV (Bray and Rodriguez-Marek 2004). This figure shows the fault-normal component of the recorded earthquake motion, which is generally larger than the fault-parallel component (Somerville et al. 1997). Recent research, however, shows that the largest pulse amplitude can be in a different orientation than fault normal due to complex fault geometries (Shahi and Baker 2011).

In the direction opposite of rupture, back-directivity can occur. Backward-directivity is

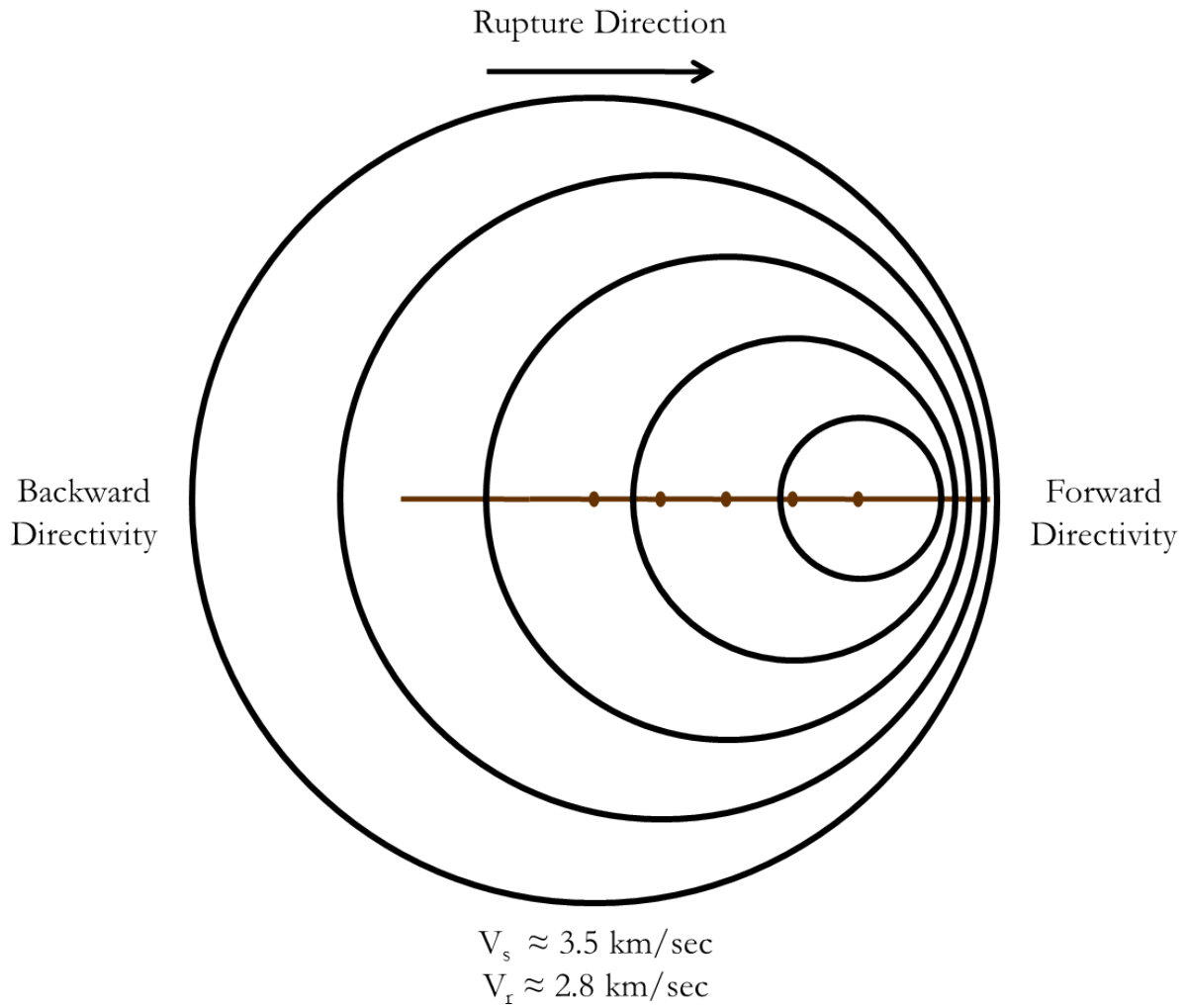


Figure 3.3: Directivity: The rings represent the radiation pattern of seismic waves propagating from a ruptured fault at an instance in time. A wave front characterized by a short, intense pulse develops in the direction of propagation, which is called forward-directivity. In the direction opposite of rupture, the wave front spreads out, leading to a longer duration motion, which is called backward-directivity.

characterized by long-duration, but lower-intensity earthquake motions. Usually, backward-directivity earthquake motions are less damaging to the built environment than forward-directivity earthquake motions, but this depends on whether the structure of interest is sensitive to longer-duration earthquake motions (e.g., liquefiable soils). Figure 3.4 shows the velocity-time series recorded at the Joshua Tree station during the 1992 Landers earthquake, which is a backward-directivity earthquake motion.

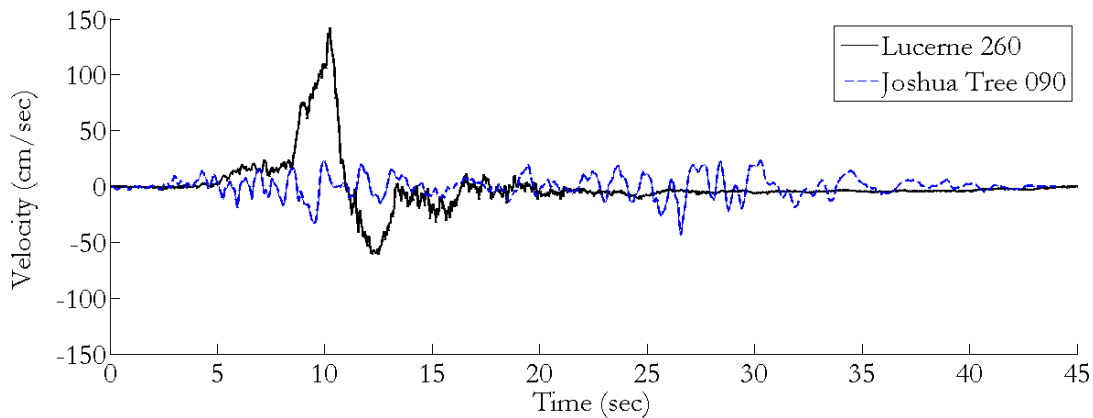


Figure 3.4: The motions recorded at the Lucerne and Joshua Tree stations during the 1992 Landers earthquake represent forward-directivity and backward-directivity motions, respectively.

Another near-fault phenomenon is *fling-step*, which is permanent ground displacement. This can also be very damaging, especially to structures located very close to faults. Fling-step is impossible to simulate on the UCD-CGM centrifuge, however, so it will not be considered further in this dissertation. It is mentioned here for completeness.

Near-fault earthquake motions are important in urban areas, but so are *ordinary* earthquake motions. Ordinary earthquake motions are generally produced at larger distances from the site of interest. They typically have lower amplitudes, but longer durations than near-fault forward-directivity earthquake motions. In general, ordinary motions are not dominated by a velocity pulse. Depending on the regional geology, however, ordinary earthquake motions can potentially be very damaging. This was exhibited during the 1989 Loma Prieta earthquake. Intense earthquake motions were experienced in Oakland, California, which is located over 70 km from the earthquake source (Hanks and Brady 1991).

For the selected project location, both ordinary and forward-directivity motions are important; therefore, both of these types of motions were selected.

3.3 Developing a design response spectrum

Earthquake motions for this project were selected using guidance from ASCE 7-10 (2010). This method required that both a deterministic seismic hazard analysis (DSHA) and a probabilistic seismic hazard analysis (PSHA) be performed. A detailed discussion of PSHA and DSHA is beyond the scope of this dissertation. Interested readers can find a more complete literature review on these subjects in Kramer (1996).

For purpose of developing design response spectrum, a “rock” site ($V_s = 760$ m/sec) was specified, which represents a ASCE 7-10 (2010) site class BC (very dense soil and soft rock

to rock). A rock site was chosen to comply with the specifications of the ASCE 7-10 (2010) code.

3.3.1 Deterministic seismic hazard analysis

The DSHA was performed using the 2008 Next Generation Attenuation (NGA) relationships (Power et al. 2008). For this research, the models of Abrahamson and Silva (2008), Boore and Atkinson (2008), Campbell and Bozorgnia (2008), and Chiou and Youngs (2008) were used.

The controlling scenario for the DSHA is an earthquake produced on the Upper Elysian Park fault (see Figures 3.1 and 3.2). With this information, parameters were developed to perform the DSHA, which are shown in Table 3.1.

Table 3.1: Important parameters used to develop the DSHA response spectra

Parameter	Value
Moment Magnitude	6.6
Top of Rupture (km)	3
Fault Type	Reverse
Dip (degrees)	50
Rupture Width (km)	15.7
Rupture Distance (km)	3.4
Joyner-Boore Distance (km)	0
Horizontal Distance (km)	0
Hanging Wall	Yes
Z1.0 (km)	0.320
Z2.5 (km)	2.574

The values of moment magnitude, rupture width, depth to top of rupture and dip are from the 2008 USGS seismic hazard maps (Peterson et al. 2008). There are two values given for moment magnitude, M_W , which are obtained by two competing models: the Ellsworth (2003) model and the Hanks and Bakun (2002) model. The models estimate M_W as 6.7 and 6.5, respectively; therefore, $M_W = 6.6$ was chosen as a representative value.

Using the fault information from Peterson et al. (2008), the rupture distance, Joyner-Boore distance and horizontal distance were calculated. The values of Z1.0 and Z2.5 were obtained from the NGA Flatfile, which is available online at: <http://peer.berkeley.edu/nga/flatfile.html>. Earthquake motions that occurred within the latitude and longitude box of 33.782 to 34.382 and -117.924 to -118.524 were examined, and median values of Z1.0 and Z2.5 were calculated from this subset of earthquake motions. The fault type and hanging wall information was obtained from Oskin et al. (2000) as well as knowledge of the local area.

The ASCE 7-10 (2010) code specifies that the median plus one standard deviation (84th-percentile) response spectra must be calculated. In addition, the code requires that the DSHA

Table 3.2: Rotation factors used to convert the DSHA spectra from the GMRotI50 direction to the maximum horizontal response direction. After Huang et al. (2008)

Period (sec)	Rotation Factor
0.0	1.8
0.1	1.7
0.2	1.7
0.3	1.9
0.5	2.1
1.0	2.3
2.0	2.5
3.0	2.6

spectra be calculated “in the direction of maximum horizontal response. . .” DSHA spectra developed using the NGA relationships are in the GMRotI50 direction (Power et al. 2008). The method by Huang et al. (2008) is used to rotate the DSHA spectra to the maximum horizontal response direction. Table 3.2 shows the rotation factors that were used.

Figure 3.5 shows DSHA spectra (5% damping, 84th-percentile, rotated to maximum horizontal response direction) calculated using the NGA relationships. The ASCE 7-10 (2010) code specifies that the DSHA spectra shown in Figure 3.5 shall not be lower than a “lower limit” response spectrum determined in accordance with Figure 3.6. In this figure, F_a and F_v are determined to be 1.0 and 1.15, respectively, based on guidance within the code. Additionally, the values of S_S and S_1 are taken as 1.5 and 0.6, respectively.

In summary, the final DSHA spectrum was determined by the following method:

1. The 84th-percentile DSHA spectra were developed using the NGA relationships.
2. The average of the Abrahamson and Silva (2008), Boore and Atkinson (2008), Campbell and Bozorgnia (2008), and Chiou and Youngs (2008) 84th-percentile DSHA spectra was taken to yield a single DSHA spectrum.
3. The rotation factors presented in Table 3.2 were applied to the DSHA spectrum developed in step 3.
4. The ordinates of the spectrum developed in Step 4 were checked against those shown in Figure 3.6 and the highest ordinate was used at each period.

These steps led to the final DSHA spectrum. For this case, the 84th-percentile DSHA spectrum was larger than the spectrum developed using Figure 3.6 at all periods. Therefore, the final DSHA spectrum is the spectrum presented in Figure 3.5.

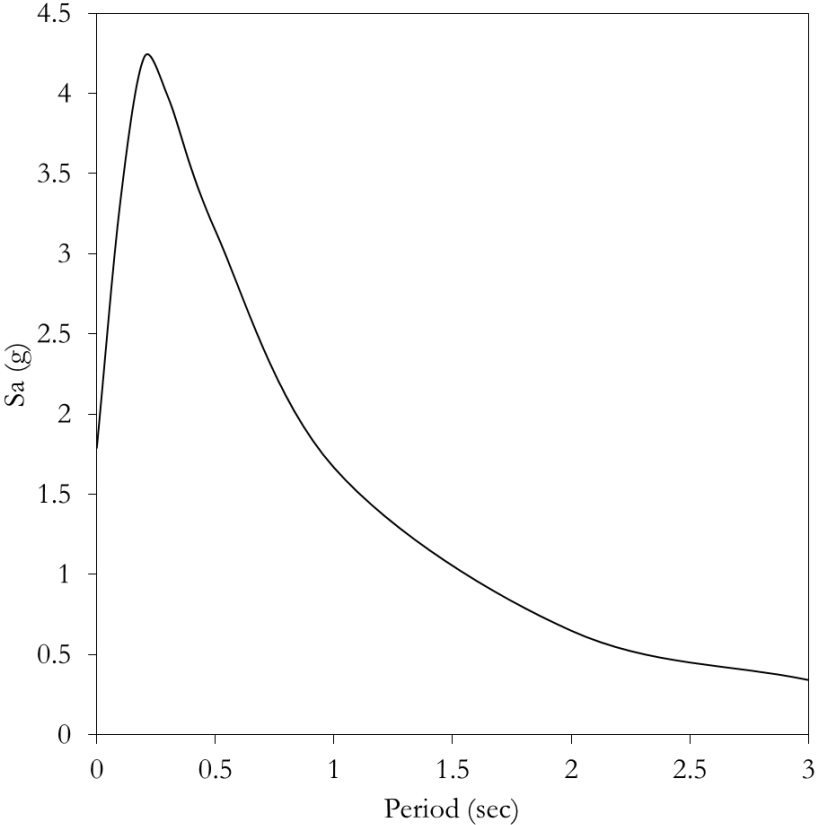


Figure 3.5: The developed DSHA spectrum: average of four NGA relationship predictions, 5% damping, 84th-percentile, rotated to maximum horizontal response direction

3.3.2 Probabilistic seismic hazard analysis

The PSHA was performed using the Interactive Deaggregation tool developed by the USGS (Peterson et al. 2008). This tool requires the input of a shear wave velocity, V_s , a probability of exceedance, and a location. Figure 3.7 shows PSHA spectra for a various return periods (72, 224, 475, 975, and 2475 years) calculated for this project location and the rock site.

The PSHA spectra used for determining the design response spectra were calculated based on “Method 1,” which is outlined in Section 21.2.1.1 of the ASCE 7-10 (2010) code. Method 1 requires the calculation of a risk coefficient, C_R . This risk coefficient is then multiplied by the PSHA spectrum with a 2% probability of exceedance in 50 years (2475 year return period). For the project location, the value of C_R is equal to 1.0 across the entire period range. Therefore, the PSHA spectra calculated using Method 1 is equivalent to the PSHA spectrum with a 2% probability of exceedance in 50 years.

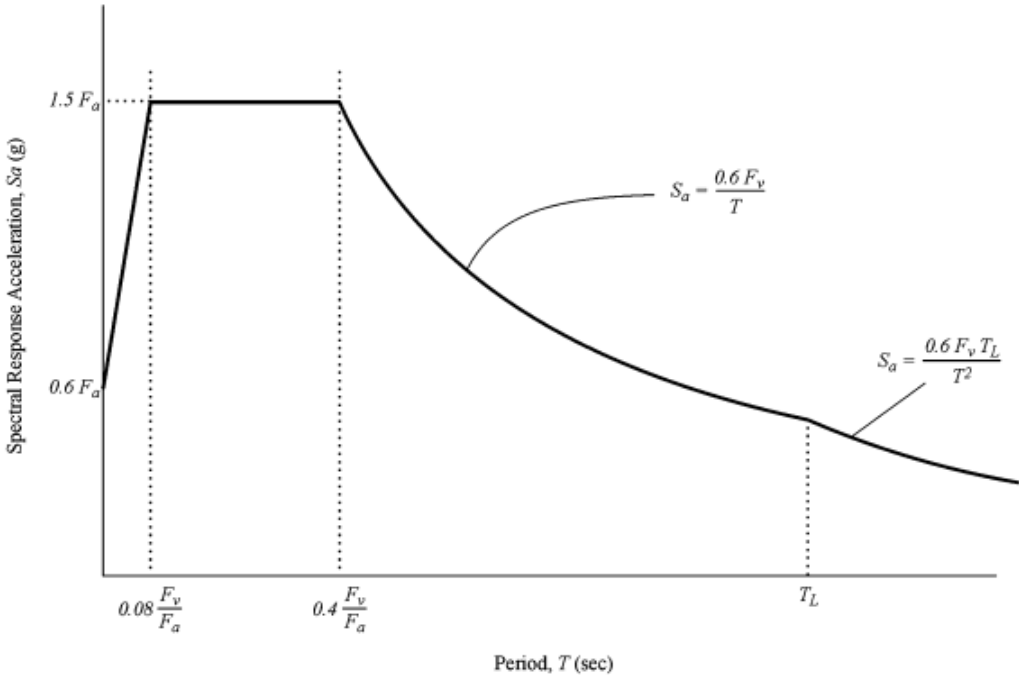


Figure 3.6: The “lower limit” deterministic response spectrum. Figure 21.2-1 in ASCE 7-10 (2010).

3.3.3 Developing a design response spectrum

First, the *risk-targeted maximum considered earthquake spectrum* (MCE_R) was developed. The ASCE 7-10 (2010) code specifies that this spectrum is the lower ordinate of the site-specific, 84th-percentile, maximum-rotated DSHA spectrum (Figure 3.5) and the PSHA spectrum calculated using Method 1 (Figure 3.7). The final design response spectrum, which is used to select site-specific earthquake motions, is calculated by multiplying the spectral ordinates of the MCE_R spectrum by 2/3. Figure 3.8 shows the site-specific MCE_R and design response spectrum calculated for the project locations considering a rock site. The data used to plot this spectrum is given in Table 3.3. These data do not account for forward-directivity effects.

At this stage, it was decided to also create a design response spectrum for a “soil site.” The main reason for this decision was that the Los Angeles basin is characterized by a deep basin of coarse to fine-grained alluvium, as discussed above. The soil site was considered to have a V_s of 275 m/sec, which corresponds to a site class D (ASCE 7-10 2010). The design response spectrum was developed using the same steps described above for the rock site. Figure 3.9 shows the MCE_R and design response spectra developed for the soil site. Table 3.4 contains the data used to plot this figure. The data in this figure and table do not contain forward directivity effects.

Table 3.3: Data used to create the design response spectrum for the rock site not considering forward-directivity effects

T (sec)	PSHA	DSHA	Fig. 21.2-1	MCE_R	Design
0.0	1.05	1.79	0.60	1.05	0.70
0.1	2.23	3.34	1.50	2.23	1.49
0.2	2.69	4.23	1.50	2.69	1.79
0.3	2.24	3.98	1.50	2.24	1.50
0.5	1.60	3.14	1.38	1.60	1.07
1.0	0.79	1.67	0.69	0.79	0.52
2.0	0.31	0.65	0.35	0.31	0.20
3.0	0.17	0.34	0.23	0.17	0.11

Table 3.4: Data used to create the design response spectrum for the soil site not considering forward-directivity effects

T (sec)	PSHA	DSHA	Fig. 21.2-1	MCE_R	Design
0.00	0.96	1.55	0.60	0.96	0.64
0.10	1.58	2.21	1.35	1.58	1.06
0.20	1.99	2.82	1.50	1.99	1.32
0.30	2.08	3.39	1.50	2.08	1.39
0.50	1.99	3.65	1.50	1.99	1.33
1.00	1.35	2.66	0.90	1.35	0.90
2.00	0.65	1.29	0.45	0.65	0.44
3.00	0.38	0.71	0.30	0.38	0.26

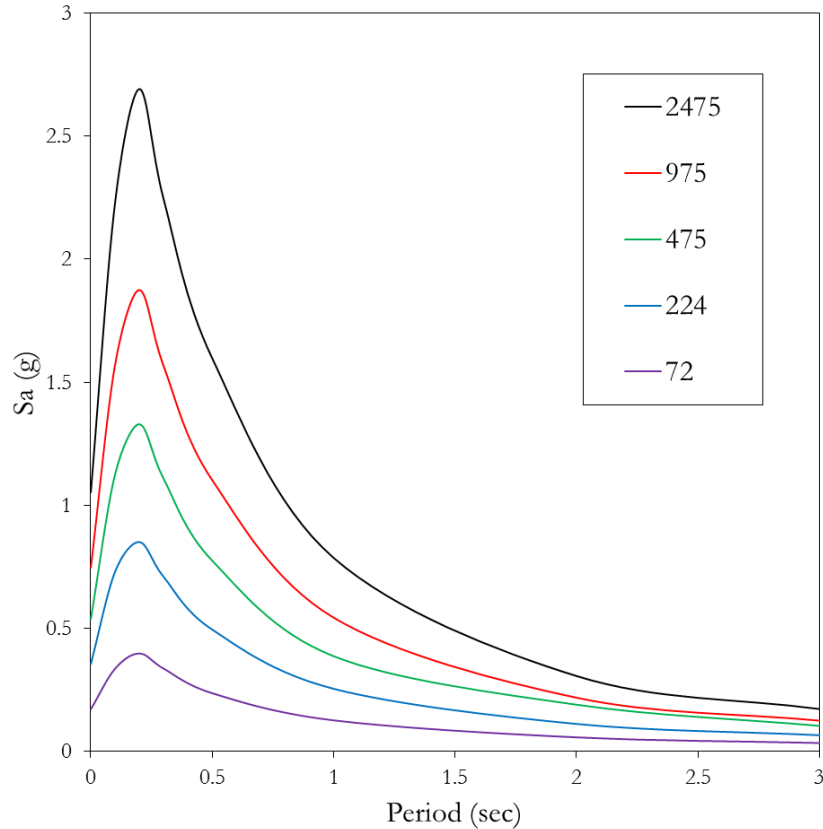


Figure 3.7: The developed PSHA spectra for various return periods. Damping = 5%.

3.3.4 Developing forward-directivity design response spectra

Forward-directivity earthquake motions are characterized by an intense, short duration velocity pulse (or pulses), as previously discussed. The pulse (or pulses) can be decomposed from the motion (Baker 2007) and can be characterized by the pulse period and pulse amplitude, which is related to the PGV of the overall motion (Bray and Rodriguez-Marek 2004). The pulse period, T_p , dominates the pseudo-acceleration response spectra of forward-directivity motions, which is shown in Figure 3.10. This figure shows the pseudo-acceleration response spectrum of the El Centro #5 array recording during the 1979 El Centro earthquake (Shahi and Baker 2011). In this figure, it can be seen that the long-period portion of the spectrum has higher amplitude, which is typical for forward-directivity earthquake motions. Therefore, when updating a design response spectrum to include forward-directivity effects, it is important to increase the amplitude of the long-period portion of the spectrum. For this dissertation research, two methods were used to update the design response spectra for forward-directivity effects: (1) Somerville et al. (1997), and (2) Spudich and Chiou (2008)

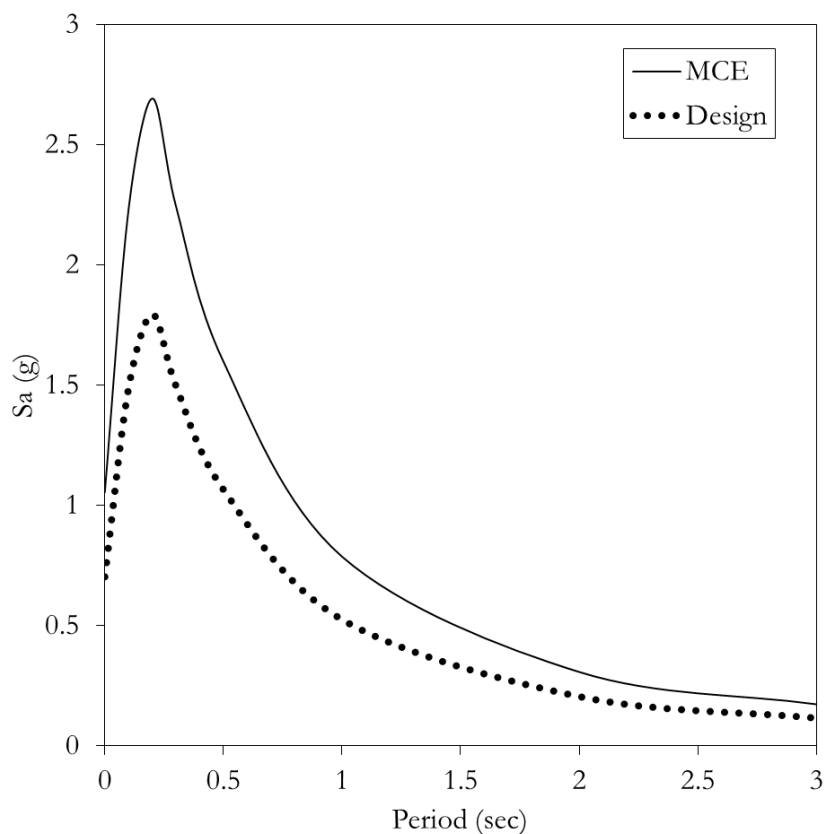


Figure 3.8: The design response spectrum developed using the ASCE 7-10 (2010) guidance for the rock site. This spectrum does not include forward directivity effects. Damping = 5%.

Somerville et al. 1997

The Somerville et al. (1997) method is often used in conjunction with the Abrahamson (2000) method for strike-slip faults. The Abrahamson (2000) method provides a critical update, which more accurately accounts for typical fault geometries. The method by Abrahamson (2000) is not calibrated for reverse faults, however, which is why it is not employed in this research.

To employ the Somerville et al. (1997) method, the following parameters need to be determined: d , W , and ϕ . The definitions of these three parameters are shown in Figure 3.11. Since the hypocenter can theoretically be located anywhere on the fault plane (though in practice, it is usually located within the central portion of the fault plane, and not within 10 to 20% of the boundaries), the researchers must pick the most representative location. In this case, $Y = d/W = 0.85$ was chosen as being a realistic “most damaging scenario.” With this assumption, Figure 3.12 shows a sketch of the parameters determined for the Upper Elysian Park fault and used with the Somerville et al. (1997) directivity model. Table 3.5 contains

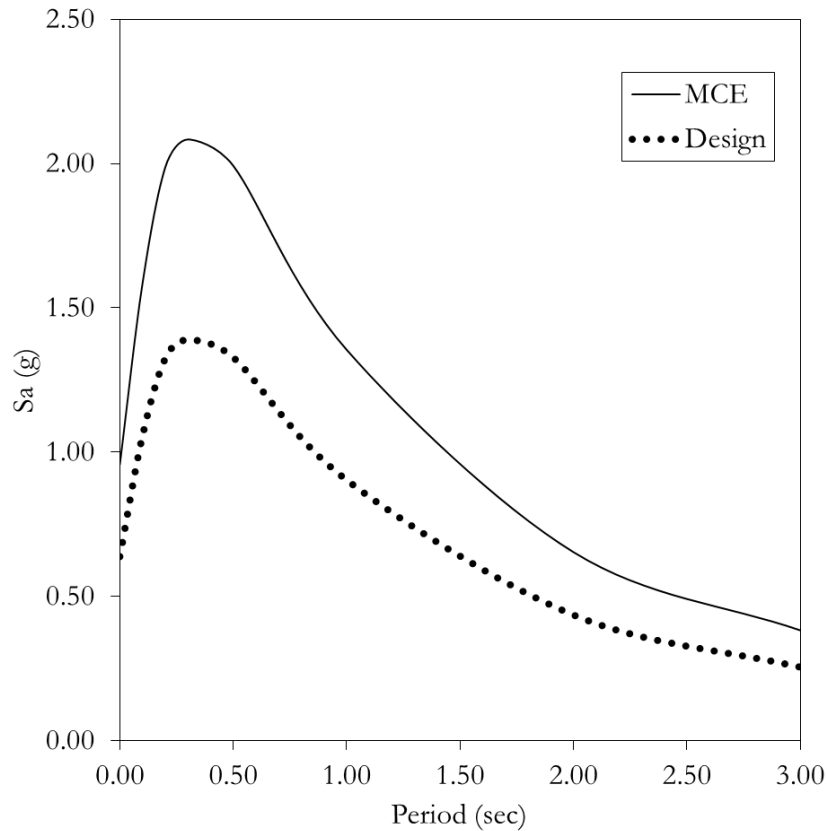


Figure 3.9: The design response spectrum developed using the ASCE 7-10 (2010) guidance for the soil site. This spectrum does not include forward directivity effects. Damping = 5%.

a table of the directivity correction factors used to modify the design response spectra for forward directivity effects using the Somerville et al. (1997) method. In this table, forward directivity effects are rotated to the fault normal direction, which approximately represents the most severe direction for most earthquake motions.

Spudich and Chiou 2008

The Spudich and Chiou (2008) method for incorporating forward-directivity effects relies on isochrones theory, which “simplifies the computation of synthetic seismograms to an analytical expression, from which one can identify directivity effects (Spudich and Chiou 2008).”

The isochrones predictor variable, IDP , is defined as the product of three terms

$$IDP = CSR_{ri}, \quad (3.1)$$

where C is similar to X or Y in the Somerville et al. (1997) method, S is similar to $\cos \theta$

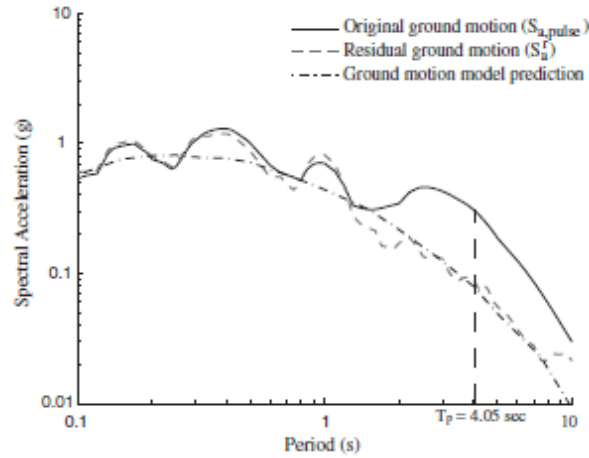


Figure 3.10: The El Centro Array # 5 recording from the 1979 Imperial Valley earthquake. The pulse period of the characteristic velocity pulse dominates the long-period region of the response spectrum. After Shahi and Baker (2011).

or $\cos \phi$ in the Somerville et al. (1997) method, and R_{ri} is the radiation pattern amplitude. Details for calculating the terms in Equation 3.1 are given in Spudich and Chiou (2008) as well as the Electronic Appendix A of the paper (Spudich and Chiou 2008). Ultimately, the functional form of the directivity correction factor is

$$F_D = f_r(R_{RUP})f_M(M)(a + b \cdot IDP), \quad (3.2)$$

where f_r is a distance taper, f_M is a magnitude taper, and the variables a and b are from regression analyses of empirical data. f_D is then used in conjunction with the four NGA relationships to correct them for directivity effects.

Developing geometrical parameters is important for employing the Spudich and Chiou (2008) method. Figure 3.13 shows the required geometrical terms used to calculate C and S , and Figure 3.14 shows the required geometrical terms used to calculate R_{ri} .

The Spudich and Chiou (2008) method is specific for each NGA relationship. The NGA relationships predict the GMRotI50 component of the earthquake motion, and this must be rotated to the maximum component for this method, and Huang et al. (2008) provides a simplified method for performing this rotation, as previously discussed.

Notably, however, the Somerville et al. (1997) method provides results in terms of the fault normal component. Therefore, to be able to compare the Somerville et al. (1997) and Spudich and Chiou (2008) results, the results are rotated to the fault normal direction. Huang et al. (2008) note that “it appears that [fault normal] spectral demand can be a surrogate for maximum spectral demand in the near-fault region only, for period [sic] greater than or equal to 2 seconds and closest distance smaller than 3 to 5 km.” Accordingly, the difference between the fault-normal and maximum components is likely minimal for the fault geometry

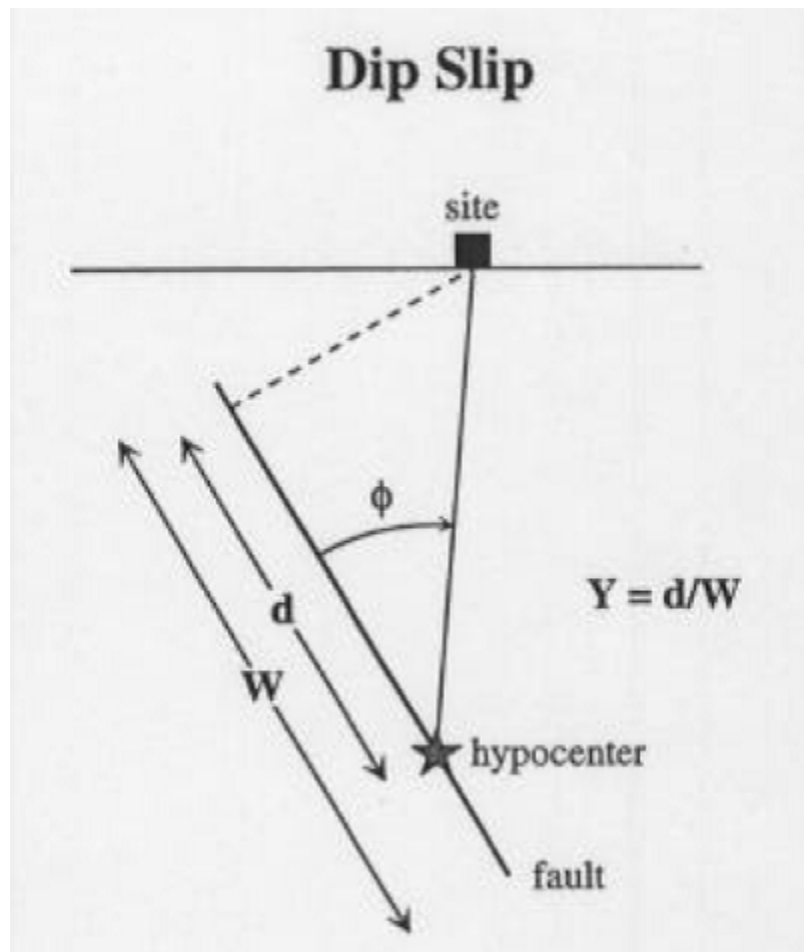


Figure 3.11: Geometry defined for the Somerville et al. (1997) method

in question and this assumption is realistic. Table 3.6 shows the rotation factors used to rotate the NGA relationships to the fault normal direction.

The fault geometry is shown in Figure 3.15 for the Upper Elysian Park fault at the site of interest. For simplicity, the fault was assumed to be planar. Using the geometry shown in Figure 3.15, the important geometrical terms were determined, and these are shown in Table 3.7 along with important fault parameters.

The calculations for the Spudich and Chiou (2008) method were performed and the important parameters are contained in Table 3.8. The values of C , S , R_{ri} , and IDP were determined as 0.948, 2.59, 0.988, and 2.42, respectively. The value of IDP as well as the distance and magnitude taper were used with the values of a and b contained to determine the directivity correction factors for the four NGA relationships. The final directivity correction factors as a function of period calculated using the Spudich and Chiou (2008) method are shown in Table 3.9 for the four NGA relationships used. These directivity correction factors

Table 3.5: Fault normal rotated spectral directivity correction factors from Somerville et al. (1997)

Period (sec)	Directivity Correction Factor
0.5	1.00
0.75	1.06
1.0	1.09
1.5	1.13
2.0	1.16
3.0	1.23
4.0	1.28
5.0	1.31

Table 3.6: GMRotI50 to fault-normal rotation factors. After Huang et al. (2008).

Period (sec)	FN/ GMRotI50
0.00	1.2
0.05	1.2
0.10	1.1
0.20	1.1
0.30	1.2
0.50	1.3
1.00	1.4
2.00	1.5
3.00	1.6
4.00	1.6

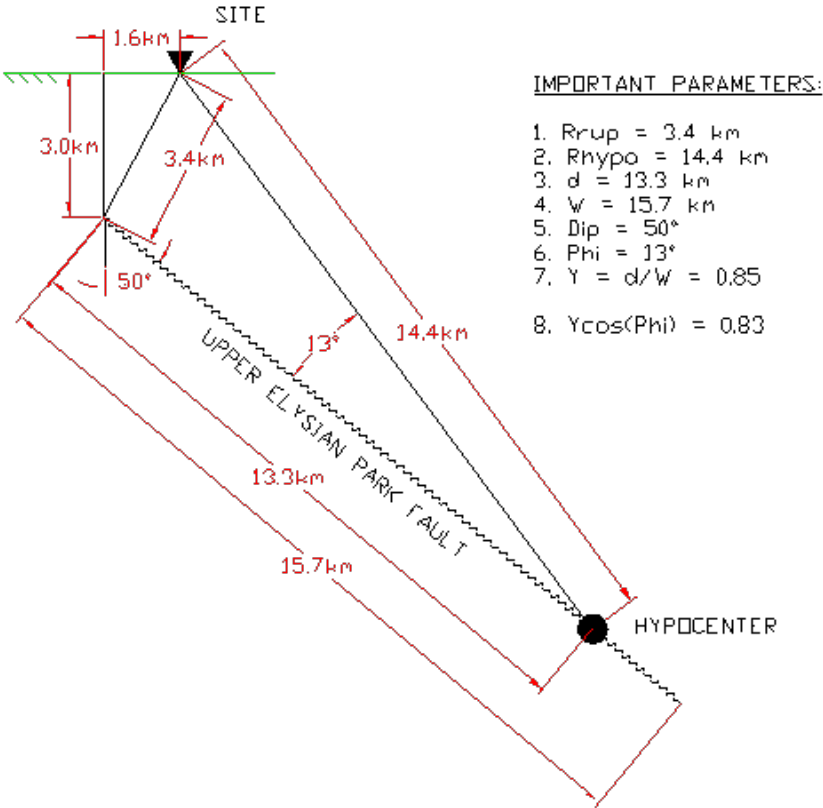


Figure 3.12: Site specific geometrical parameters used with the Somerville et al. (1997) method

were multiplied by the design response spectrum calculated for ordinary earthquake motions to develop the forward-directivity design response spectrum.

Developing the final forward-directivity design response spectrum

The final forward-directivity design response spectra were developed by multiplying the spectral ordinates of the ordinary spectra by the average of the directivity correction factors calculated using the Somerville et al. (1997) method and Spudich and Chiou (2008) method. Table 3.10 contains the final directivity correction factors as a function of period. The final design response spectra considering forward-directivity effects are shown in Figure 3.16.

3.4 Selection of earthquake motions

Earthquake motions were selected using guidance from Bommer and Acevedo (2004) and the semi-automated selection tool SigmaSpectra (Kottke and Rathje 2008), which is

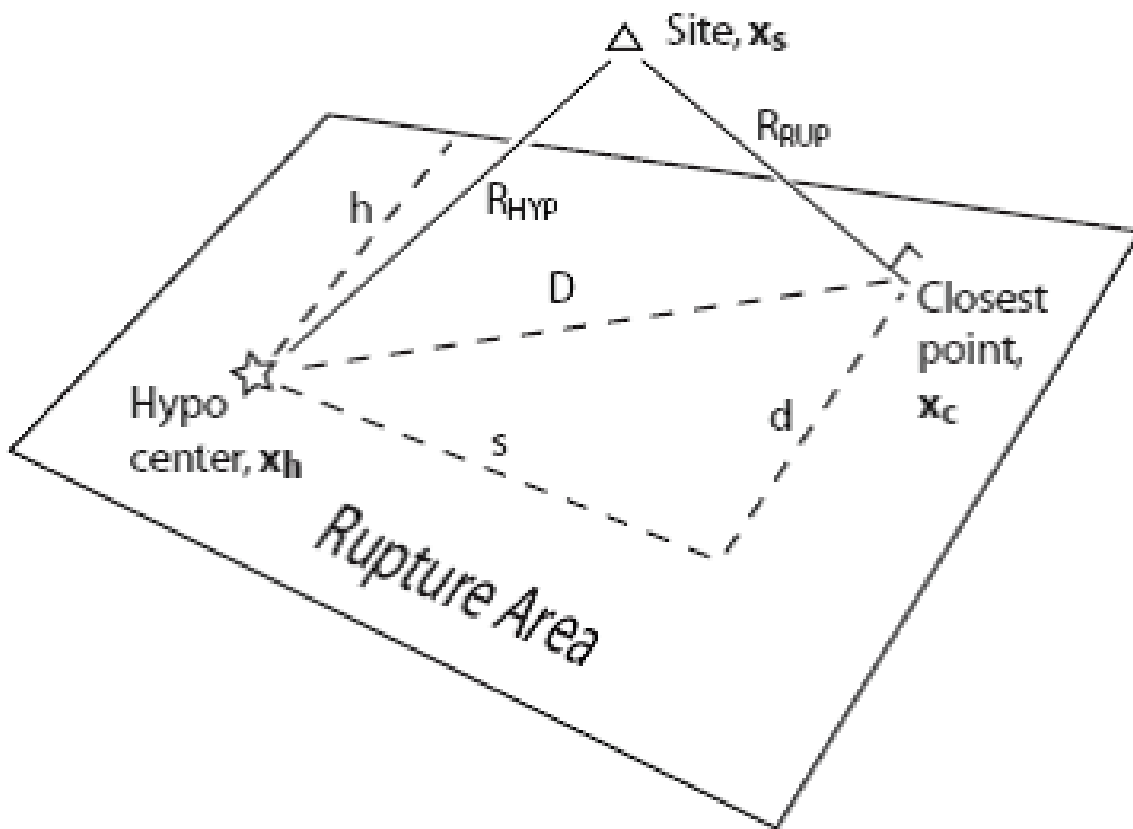


Figure 3.13: Definition of the geometrical terms C and S for the Spudich and Chiou (2008) method

available online: <http://nees.org/resources/sigma spectra>. In addition, specific project needs were considered when selecting the final motions.

The Bommer and Acevedo (2004) study gives general advice that is helpful for selecting an initial database of earthquake motions. The authors state that earthquake magnitude is the most important selection criterion, and recommend that motions be selected within ± 0.2 magnitude units of the target magnitude. The reason for this strict criterion is that earthquake magnitude is known to be highly correlated with the duration, frequency-content (i.e., spectral shape), and amplitude of the earthquake motion (Kramer 1996). The authors also state that matching distance is much less important, and that site classification should ideally be matched, but this criterion can be relaxed if necessary. Finally, they recommend that style of faulting not be considered a criterion, as it may limit the number of available motions (however, this criterion can be used if it is not too restrictive). This study states that distance, site classification and style of faulting do not correlate as strongly with an earthquake motion's duration, frequency content, and amplitude.

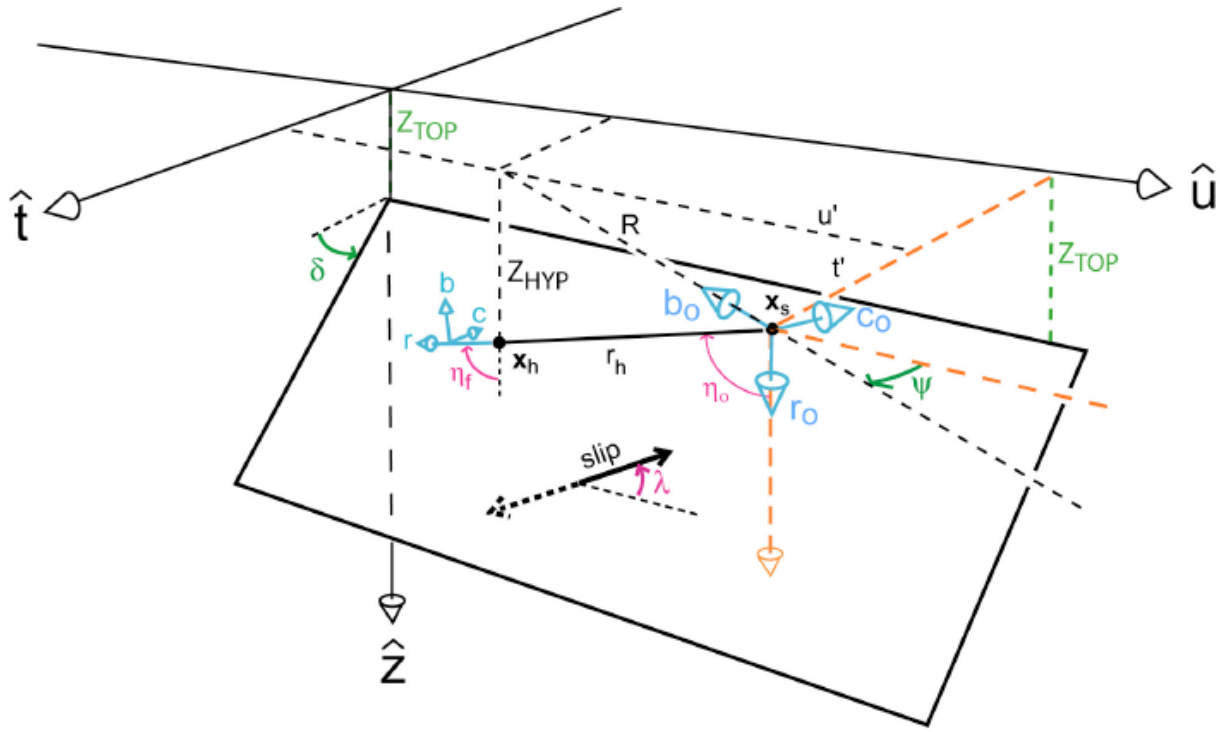


Figure 3.14: Definition of the geometrical term R_{r_i} for the Spudich and Chiou (2008) method

Findings from the Bommer and Acevedo (2004) are not entirely accepted by the earthquake engineering community. An alternate view (Bray, pers. comm.) is that distance is the most important parameter to match, followed by magnitude and style of faulting (with style of faulting being sometimes more important than magnitude). Accordingly, for this research, an initial bin of earthquake motions was selected by considering that magnitude and distance were both critically important.

The Kottke and Rathje (2008) method, which is embodied in the software SigmaSpectra, is a semi-automated procedure used to select earthquake motions. The user inputs a database of motions, and the target spectrum. An automated algorithm then selects and scales the number of earthquake motions the user desires from the given database. Scaling is only applied linearly in the time-domain (i.e., the records are not frequency-scaled to match the target spectrum). The algorithm uses a “goodness-of-fit” parameter, which is quantified by the root mean square error between the target spectrum and the scaled spectrum of interests over a certain period range. A smaller goodness-of-fit parameter indicates a better fit. The earthquake motion database created using the Bommer and Acevedo (2004) and (Bray, pers. comm.) guidance was used in conjunction with SigmaSpectra to select a final suite of linearly-scaled earthquake motions that fit the target response spectra.

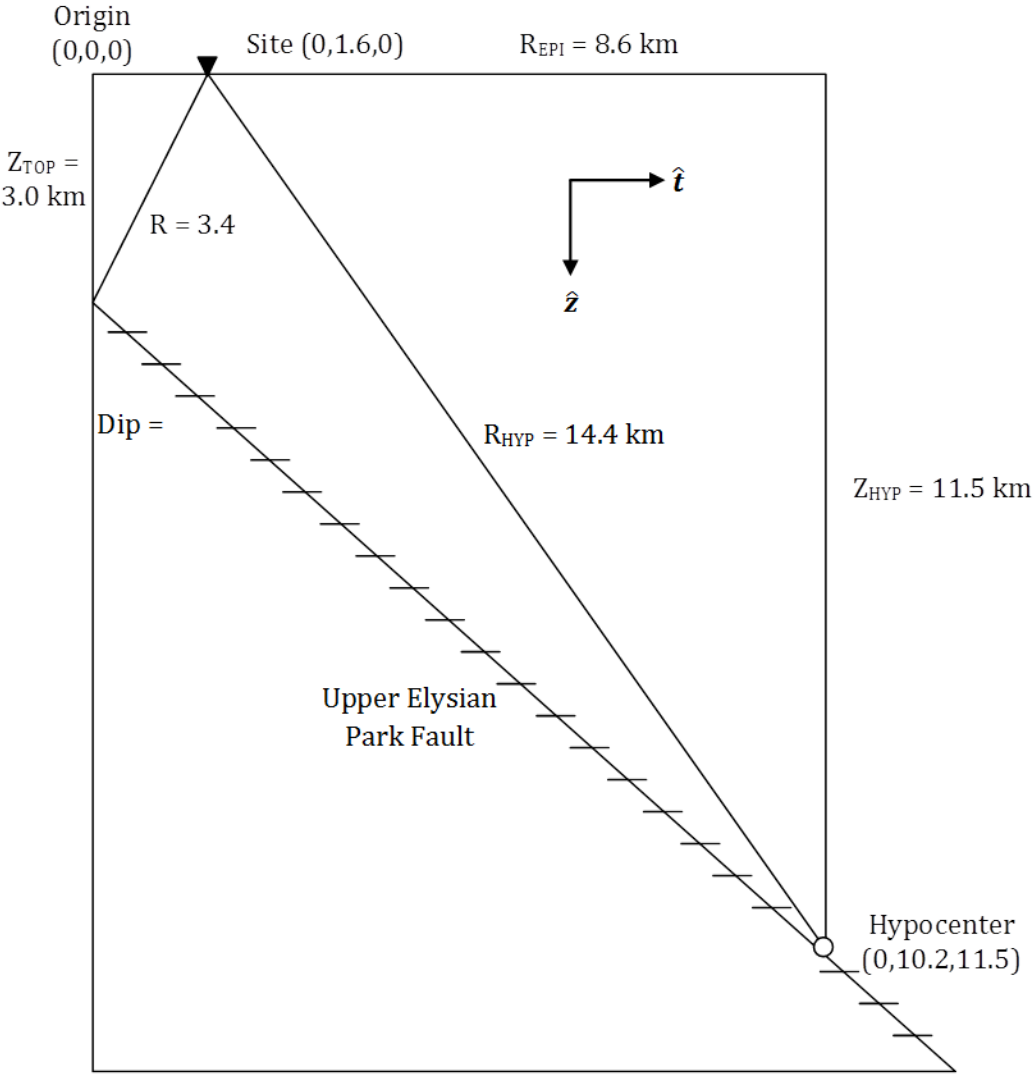


Figure 3.15: Site specific geometrical parameters used with the Spudich and Chiou (2008) method

All motions selected for this project are from the PEER strong motion database, which is available online: http://peer.berkeley.edu/peer_ground_motion_database. Two different types of motions were used for the selection procedure: (1) forward-directivity motions, and (2) ordinary motions. The forward-directivity motions were selected from databases found in Baker (2007) and Bray and Rodriguez-Marek (2004). The ordinary motions were selected from the remaining set of motions (i.e., all motions from the PEER database minus those listed as forward-directivity motions in either Baker (2007) or Bray and Rodriguez-Marek

Table 3.7: Important site specific geometric and fault parameters used with the Spudich and Chiou (2008) method

Parameter	Values
M_W	6.6
R_{RUP} (km)	3.4
R_{HYP} (km)	14.4
D (km)	13.3
s (km)	13.3
h (km)	13.3
V_r/β	0.8
r_h (km)	14.4
R (km)	8.6
u' (km)	0
t' (km)	-8.6
Z_{HYP} (km)	11.5
Dip ($^\circ$)	50
Rake ($^\circ$)	90

(2004)).

In addition to the guidance from Kottke and Rathje (2008), Bommer and Acevedo (2004), and (Bray, pers. comm.), the following project specific motion selection guidelines were devised:

- Use an ordinary sequence motion (i.e., a motion performed three times per test at low, medium and high intensities)
- Use a forward-directivity sequence motion (i.e., a motion performed three times per test at low, medium and high intensities)
- Choose forward-directivity motions of varying intensities with at least three being high intensity
- Choose ordinary motions of varying intensities with at least two being high intensity
- Choose several motion from the 1994 Northridge earthquake since it occurred near the project location and had a reverse faulting mechanism

Table 3.8: Important calculated values for the Spudich and Chiou (2008) method

Parameter	Values
f_r	1.00
f_M	1.00
ζ'	2.36
C	0.948
S	2.59
$\sin / \cos \eta_f$	0.597/0.799
$\sin / \cos \Psi$	-1.000/0.000
$\sin / \cos dip$	0.766/0.643
$\sin / \cos rake$	1.000/0.000
$(\hat{\mathbf{n}} \cdot \hat{\mathbf{r}})$	0.0558
$(\hat{\mathbf{n}} \cdot \hat{\mathbf{b}})$	-0.996
$(\hat{\mathbf{n}} \cdot \hat{\mathbf{c}})$	0.000
$(\hat{\mathbf{s}} \cdot \hat{\mathbf{r}})$	-0.996
$(\hat{\mathbf{s}} \cdot \hat{\mathbf{b}})$	-0.0558
$(\hat{\mathbf{s}} \cdot \hat{\mathbf{c}})$	0.000
$(\hat{\mathbf{u}} \cdot \hat{\mathbf{b}}_0)$	0.000
$(\hat{\mathbf{u}} \cdot \hat{\mathbf{c}}_0)$	-1.000
$(\hat{\mathbf{t}} \cdot \hat{\mathbf{b}}_0)$	1.000
$(\hat{\mathbf{t}} \cdot \hat{\mathbf{c}}_0)$	0.000
R_u	0.000
R_t	0.988
R_{ri}	0.988
IDP	2.425

Table 3.9: Forward directivity correction factors (“Amp Factors”) for the four NGA relationships

T (sec)	Amp Factor			
	AS	BA	CB	CY
0.5	1.000	1.000	—	—
0.75	1.028	1.033	1.000	1.000
1.0	1.048	1.058	1.021	1.023
1.5	1.078	1.093	1.050	1.056
2.0	1.098	1.119	1.072	1.080
3.0	1.130	1.156	1.103	1.115
4.0	1.152	1.183	1.126	1.140
5.0	1.170	1.205	1.144	1.160

Table 3.10: Final directivity correction factors

Period (sec)	Directivity Correction Factor
0.5	1.00
0.75	1.04
1.0	1.07
1.5	1.10
2	1.13
3	1.18

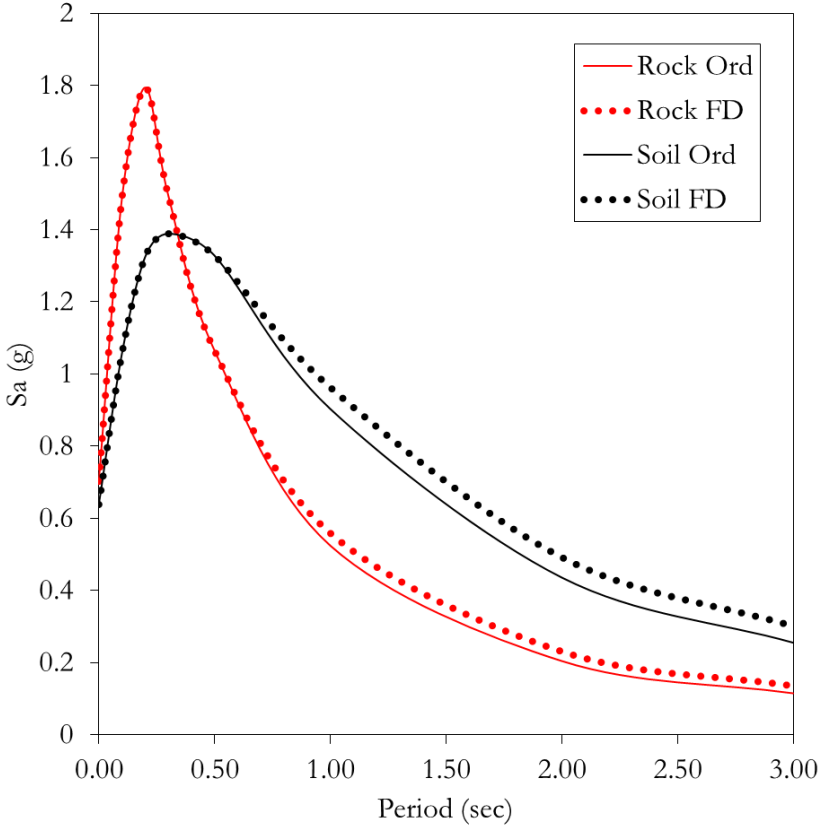


Figure 3.16: The design response spectra developed using the ASCE 7-10 (2010) guidance for the rock site and soil site considering both ordinary and forward directivity earthquake motions. Damping = 5%.

Table 3.11: Earthquake motions selected before calibration with the centrifuge shaking table

ID	Scale	Earthquake	Station	Type
JOS_L	0.53	1992 Landers	Joshua Tree 090	Ord
BRA	1.00	1979 Imperial Valley	Brawley Airport 225	FD
SCS_L	0.54	1994 Northridge	Sylmar Converter Station 225	FD
WVC	1.00	1989 Loma Prieta	Saratoga-W. Valley College 270	FD
WPI	0.73	1994 Northridge	Newhall-W. Pico Canyon 046	FD
TCU	0.45	1999 Chi Chi	TCU078-E	Ord
PEL	1.00	1971 San Fernando	LA Hollywood Storage Lot 180	Ord
PTS	0.66	1987 Superstition Hills	Parachute Test Site 315	Ord
JOS_M	1.17	1992 Landers	Joshua Tree 090	Ord
SCS_M	0.92	1994 Northridge	Sylmar Converter Station 052	FD
LGPC	1.00	1989 Loma Prieta	LGPC 090	FD
RRS	0.73	1994 Northridge	Rinaldi Receiving Station 228	FD
LCN	1.00	1992 Landers	Lucerne 260	FD
SCS_H	1.23	1994 Northridge	Sylmar Converter Station 052	FD
SUP	0.73	1987 Superstition Hills	Superstition Mtn Camera 045	Ord
JOS_H	1.77	1992 Landers	Joshua Tree 090	Ord

¹ Ord = Ordinary earthquake motions

² FD = Forward-directivity earthquake motions

The project specific requirements listed above required that a slightly different earthquake motion selection strategy be adopted. Instead of matching to a single target response spectrum, like the design response spectrum developed with the ASCE 7-10 (2010) code, several target response spectra were defined. Earthquake motions were selected to match the 72 and 475 year return period PSHA spectra as well as the design response spectrum. When selecting the earthquake motions, the target spectra developed considering a soil site were given more weight than the rock site.

The earthquake motions selected using the criteria discussed above are given in Table 3.11. In this table, earthquake motions IDs are used, which will be used to describe the motions throughout this dissertation. The prefix *L* indicates *low-intensity*, *M* indicates *medium-intensity*, and *H* indicates *high-intensity*. These intensities are defined relatively for each earthquake motion.

Figure 3.17 shows the selected ordinary motions plotted with the design response spectrum, and the selected forward-directivity motions plotted with the appropriate design response spectrum.

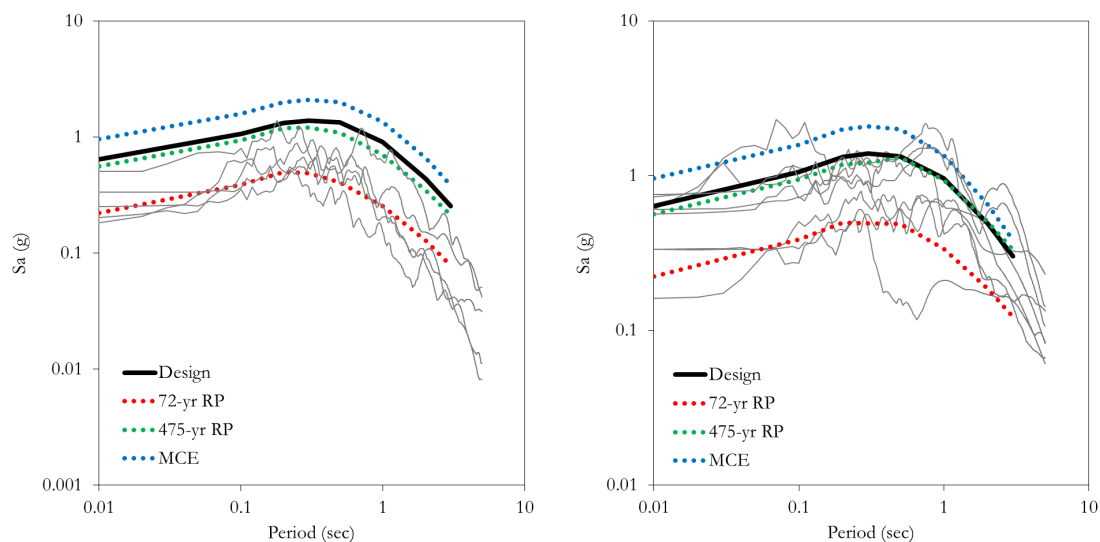


Figure 3.17: The ordinary (left) and forward-directivity (right) design response spectra along with important PSHA spectra and the selected earthquake motions. Damping = 5%.

3.5 Calibrating selected earthquake motions for centrifuge testing

The centrifuge at the UCD-CGM contains robust shakers that are capable of reproducing realistic earthquake motions. The shakers are controlled by servo-hydraulic actuation. The shakers are located on each side of the centrifuge bucket, and attach to the longitudinal sides of the centrifuge model container. This design reduces rocking motions, which can affect results. The shakers move in the longitudinal direction of the centrifuge model container, and are bi-directional. Kutter (1995) and Kutter et al. (1994) contain more information about the design and performance of the UCD-CGM shakers.

The centrifuge shaker-model system is complex, and its dynamic characteristics affects inputted earthquake motions. As a result, four different types of earthquake motions must be considered when performing centrifuge tests: (1) the desired motion, (2) the target motion, (3) the command motion, and (4) the achieved motion.

The desired motion is the researcher’s ideal, usually selected using an acceptable earthquake motion selection procedure. The earthquake motions contained in Table 3.11 represent this project’s desired motions.

The target motion is a filtered version of the desired motion, and is the motion that the researcher hopes to achieve. First, demands that would exceed the shaker’s capabilities—such as large displacements (the shaking table has limited range) and permanent displacements (the shaking table must re-center after the motions)—must be removed. Second, the centrifuge system has a fundamental frequency and higher modes that must be filtered out of the motions

to avoid damage. For the UCD-CGM centrifuge, these are 5 Hz (first mode) and 19 Hz (second mode). For more intense earthquake motions, the frequency band of 100 to 110 Hz should also be avoided. All of these frequencies are reported in model scale.

Appropriate filtering was performed by using fifth-order acausal Butterworth filters, as recommended by Boore and Bommer (2005). A high-pass filter with a corner frequency of 10 Hz (model scale) was used to limit maximum displacements to allowable levels and to remove energy at the first mode of the centrifuge system (i.e., 5 Hz). Notch filters with corner frequencies of 14 to 24 Hz and 95 to 115 Hz were used to filter out potentially damaging higher-mode energy. A low-pass filter with a corner frequency of 400 Hz was used to remove extraneous high-frequency content of the earthquake motions that were beyond the bandwidth of the shaker.

The command motion is what is sent to the servo controller, which controls the servo-valves and actuators. Thus, the command motion “tells” the shakers how to recreate the target motion. At the UCD-CGM the command motion is the relative displacement between the shake table (i.e., container base) and the reaction mass (i.e., centrifuge bucket floor).

The achieved motion is the measured acceleration-time series in the centrifuge model at some specified location on the model/specimen during shaking. The earthquake motions selected for this project are *base motions*; therefore, the achieved motions of interest are recorded at the base of the centrifuge model.

As a first approximation, the command motion is the double-integrated target motion. This command motion, however, will very rarely produce an achieved motion that matches the target motion because the dynamic characteristics of the servo-actuator-shaker-geotechnical model system are not taken into account. A transfer function that converts the double-integrated target motion to an acceptable command motion must be employed. It is difficult to know the dynamic characteristics of the system *a priori*; therefore, it is difficult to prescribe a transfer function. Additionally, the dynamic characteristics of the servo-actuator-shake table-geotechnical model system are nonlinear functions of the geotechnical model stiffness, the centrifugal acceleration, amplitude and frequency of shaking, and other factors. As a result, one transfer function does not fit all tests. This dissertation describes an iterative approach for developing test specific transfer functions that works well at the UCD-CGM.

The first step of this process is obtaining a seed command motion, which is the double-integrated target motion, as described above. This seed command motion ($a_{com}^0(t)$) was used to shake the model and the response was recorded at the base-level of the centrifuge model container, which yielded an initial achieved motion ($a_{ach}^0(t)$). The model container was full of 80% relative density sand. This accurately simulated the dynamic characteristics of the shaker-model system used for Tests-1 through 3.

In the second step, the fast Fourier transform (FFT) of both $a_{ach}^0(t)$ and the target motion ($a_{tar}(t)$) were taken to yield $A_{ach}^0(f)$ and $A_{tar}(f)(= A_{com}^0(f))$, respectively. The observed

initial transfer function of the system, $H^0(f)$, can then be calculated as

$$H^0(f) = \frac{A_{ach}^0(f)}{A_{tar}(f)}. \quad (3.3)$$

The goal of this process is to create a new command motion, $A_{com}^1(f)$ such that $A_{ach}^1(f) = H^1(f)A_{com}^1(f) = A_{tar}(f)$. At this stage, a predictive transfer function, $G(f)$, can be generically written as

$$G(f) = \frac{A_{com}(f)}{A_{tar}(f)}. \quad (3.4)$$

Assuming that $H^1(f) \approx H^0(f)$ and combining Equations 3.3 and 3.4 yields

$$G^0(f) = \frac{1}{H^0(f)} = \frac{A_{tar}(f)}{A_{ach}^0(f)}. \quad (3.5)$$

The third step is to smooth the transfer functions calculated using Equation 3.5. If either $A_{ach}(f)$ or $A_{tar}(f)$ have magnitudes near zero at discrete frequencies, noise or other small errors could result in very large or very small values of $G(f)$ at those frequencies. One guard against this error is to plot $A_{ach}(f)$, $A_{tar}(f)$, and $G(f)$ together, inspect this plot for discrepancies and disregard unreasonable values of $G(f)$. Another guard is to use median smoothing, which helps remove some of the spurious spikes. For this research, $A_{ach}(f)$ and $A_{tar}(f)$ were median smoothed over a 1 Hz window, producing $A_{ach,s}(f)$ and $A_{tar,s}(f)$. The transfer function presented in Equation 3.5 is then updated to a smoothed transfer function

$$G_s(f) = \frac{A_{tar,s}(f)}{A_{ach,s}(f)}. \quad (3.6)$$

In the fourth step, the transfer function $G_s^0(f)$ is used to create a new command motion, $A_{com}^1(f)$, which is used for the next iteration (i.e., $A_{com}^1(f) = G_s^0(f)A_{tar}(f)$). The updated command motion, $A_{com}^1(f)$ may have undesired frequencies, so it may need to be re-filtered using the procedures described above.

In the fifth step, an inverse fast Fourier transform (iFFT) is used to convert the updated command motion to the time-domain, which yields $a_{com}^1(t)$. This updated command motion is then used to shake the model, and the updated achieved motion, $a_{ach}^1(t)$ is recorded. A new predictive smoothed transfer is calculated via Equation 3.6 as $G_s^1(f) = A_{tar,s}(f)/A_{ach,s}^1(f)$.

The final step is to continue this iteration process until an acceptable command motion is produced. For this research, two iterations were needed until the achieved motions were deemed acceptably close to the target motions. This can be described mathematically as

$$A_{com,s}^i(f) = G_s^i(f) \cdot G_s^{i-1}(f) \cdots G_s^1(f) \cdot G_s^0(f) \cdot A_{tar,s}(f), \quad (3.7)$$

where i is the number of iterations.

Figure 3.18 shows a comparison of the predictive transfer functions after the first and second iterations. The transfer functions shown in this figure have been further smoothed over a 10 Hz window to aid visualization. A general purpose predictive transfer function (labeled “DTF”)—which has been used on previous projects at the UCD-CGM to boost the high-frequency content of command motions *a priori*—is shown for comparison purposes. The second iteration transfer function is on average below the first iteration transfer function, which indicates that the achieved motions are approaching the target motions.

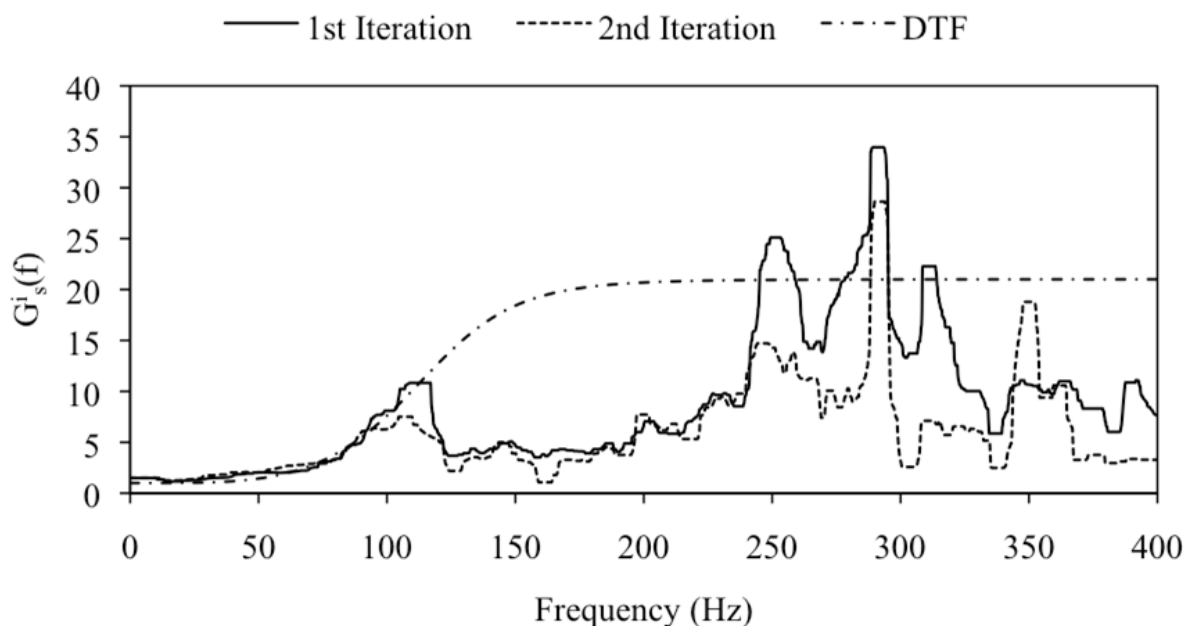


Figure 3.18: Predictive transfer functions as described by Equation 3.6. After Mason et al. (2010).

After the last iteration, the researcher should check the achieved motions to ensure they are still reasonable. In the case of the forward-directivity motions, it is important to make sure that the characteristic velocity pulses are not filtered out or unrealistically changed during this filtering and calibration process. Pulse period, number of pulses, and peak ground velocity (proxy for pulse amplitude) of the last iteration achieved motion can be compared with those of the target motion to ensure reasonableness. The ordinary motions should also be checked to make sure their amplitude, duration and frequency-content are still reasonable.

For this dissertation research project, a number of the originally selected motions were deemed unusable after this iteration process (i.e., they had become unrealistic). The final earthquake motions used for this project are presented in Table 3.12. Notably, the Port Island Motion (PRI) recorded at a depth of 79 m during the 1995 Kobe earthquake is listed on this table, even though it was not an originally selected motion. The PRI motion is a “UCD-CGM legacy motion,” which has been used by many previous researchers. Therefore, this

Table 3.12: Final earthquake motions used for the NCB tests

ID	Earthquake	Station	Type
JOS	1992 Landers	Joshua Tree 090	Ord ¹
LCN	1992 Landers	Lucerne 260	FD ²
PRI	1995 Kobe	Port Island (79 m)	FD
PTS	1984 Superstition Hills	Parachute Test Site 315	Ord
RRS	1994 Northridge	Rinaldi Receiving Station 228	FD
SCS	1994 Northridge	Sylmar Converter Station 052	FD
TCU	1999 Chi Chi	TCU078-E	Ord
WPI	1994 Northridge	Newhall-W. Pico Canyon 046	FD
WVC	1989 Loma Prieta	Saratoga-W. Valley College 270	FD

¹ Ord = Ordinary earthquake motions

² FD = Forward-directivity earthquake motions

motion was selected at this stage to compare this research with previous work. Additionally, comparisons between shaker performance during previous tests and the tests described in this dissertation can be made.

Chapter 4

Centrifuge Tests 1 & 2

4.1 Introduction

Test-1 and Test-2 are discussed in this chapter. The same structural models were used in Test-1 and Test-2. In Test-1, which was the baseline test, the two structural models were located a significant distance apart; accordingly, they did not interact with one another through the soil as the earthquake motions were applied. The purpose of Test-1 was to develop an understanding of the seismic response of two individual structural models. Insights into soil-foundation-structure interaction of inelastic structural models, one of which was founded on spread footings and the other on a basement box, were made.

In Test-2, the same two structural models were moved adjacent to one another (i.e., a separation distance of 5 mm, model scale; or 27.5 cm, prototype scale). Insights into structure-soil-structure interaction were gained by comparing the seismic response of the two structural models, the foundations, and the surrounding soil in Test-1 and Test-2.

Test-1 and Test-2 examined the seismic response of inelastic structural models. The members of the structural models (i.e., beams and columns) were designed to deform during strong shaking. In addition, a modular design approach was employed. The damaged structural members could be changed during the testing. This allowed for many earthquake motions to be performed for each test (i.e., 17 for Test-1 and 21 for Test-2). In addition, the floor masses could be switched during the testing. This allowed the structures to be tuned to have different fundamental periods and higher response modes.

A deep basement box was used during Test-1 and Test-2 (three story prototypical basement). By comparing the surface free-field ground motion and the motion recorded at the bottom of the basement, insights into kinematic interaction could be made. By comparing the Test-1 and Test-2 results, insights into kinematic structure-soil-structure interaction can be made.

Finally, the seismic response of the spread footings is a key contribution of this research. Different seismic responses are recorded for the *free* footing versus the *restrained* footing (i.e.,

the non-adjacent footing versus the adjacent footing) during Test-2. Additional insights can be gained by comparing the footing response results from Test-1 with those from Test-2.

The purpose of this chapter is to synthesize some of the results obtained during Test-1 and Test-2. The focus of these results is on kinematic interaction and seismic footing response. The data recorded during these two tests are available online at the NEES Hub and are described in Mason et al. (2011a) and Mason et al. (2011b) for Test-1 and Test-2, respectively.

4.2 Experimental setup

4.2.1 Soil properties

Test-1 and Test-2 were performed using dry, dense Nevada sand. Nevada sand is a mined, non-processed sand. Accordingly, its soil properties change with each batch delivered to the UCD-CGM. Therefore, it is important to perform soil testing for each batch delivered. Table 4.1 contains important soil properties for the batch of Nevada sand used to construct Test-1 and Test-2, which was tested by Cooper Labs in January 2008.

Table 4.1: Important soil properties for Nevada sand (from January 2008 tests performed by Cooper Labs)

Quantity	Value
Supplier	Gordon Sand Co., Compton, CA
Classification	Uniform, fine sand; SP
Gradation	Poor
Specific Gravity	2.65
Mean Grain Size	0.14 to 0.17 mm
Coefficient of Uniformity	1.67
Maximum Void Ratio	0.748
Minimum Void Ratio	0.510
Friction Angle (for $D_R \approx 80\%$)	40°

4.2.2 Structural models

A key design goal for Test-1 and Test-2 was to design two centrifuge model structures, that when spun-up in the centrifuge, would represent two realistic prototypical structures. Building reduced-scale centrifuge models that represent prototypical structures when subjected to higher centrifugal accelerations is challenging. It is not possible to build exact replicas of buildings at a $1/N$ scale; therefore, the following process was devised: first, the *target prototypes* were converted to *idealized prototypes*. Next, the *centrifuge models* were designed

to match key parameters of the idealized prototypes as closely as possible (in the higher g environment).

A professional practice committee of earthquake engineers comprised of Marshall Lew, Mark Moore, Farzad Naeim, Farhang Ostadan, Paul Somerville, and Michael Willford was consulted during this phase of the research. With their consultation, two types of buildings commonly located in Los Angeles, California were identified:

1. Concrete encased semi-rigid steel moment frames between three and thirteen stories tall, typically built before 1950
2. Steel moment resisting frame buildings between five and fifty-four stories tall with basements between one and five levels deep, built after 1980

Using guidance from the professional practice committee, as well as the work of Ganzua (2006), two fixed-base prototypes were specified: (1) a three-story, special moment resisting frame structure founded on spread footings, and (2) a nine-story, special moment resisting frame structure founded on a three-story basement. These represent the target prototypes. The foundation types of these two target prototypes were specified: (1) to match typically specified foundations in Los Angeles given the regional soil conditions (i.e., a deep basin of dense sandy soils), (2) to study kinematic interaction effects with the deep basement, and (3) to study the cross interaction of spread footings founding a superstructure.

The next step was to convert the target prototypes into idealized prototypes. The three-story idealized prototype was represented by a frame structure with a single lumped mass, which is herein referred to as MS1F_SF80. Likewise, the nine-story idealized prototype was represented by a frame structure with three lumped masses, which is herein referred to as MS3F_B. Three key parameters were chosen to represent the idealized lumped-mass, flexible-base prototypes: (1) the flexible-base fundamental period (\tilde{T}), (2) the yield strength ratio (V_y/W , where V_y is the yield strength in terms of base shear and W is the total superstructure weight), and (3) the yield drift ratio ($\delta_y = \Delta_y/h$, where Δ_y is the system yield displacement and h is the total building height measured from the ground surface). The professional practice committee and the work of Ganzua (2006) were consulted to select appropriate values of the aforementioned key parameters for the two prototype structures. The selected values are provided in Table 4.2.

Table 4.2: Key structural parameters for representing idealized models

Prototype	\tilde{T} (sec)	V_y/W	δ_y
Three-story	1.1	0.3	1.2%
Nine-story	2.3	0.2	1.4%

The next step in this process was to convert the idealized prototypes into centrifuge models. This was completed using the finite-element program OpenSees (<http://opensees>).

berkeley.edu). This design process was iterative. Candidate frames with specified geometric and mass properties were numerically evaluated until the key parameters in Table 4.2 were roughly achieved. A model developed by Scott and Fenves (2006) was used to evaluate the lumped-mass beam and column members. The foundation-soil interface was represented by a discrete nonlinear Winkler-based springs (Raychowdhury 2009). Impedance functions from ATC-40 (1996) were used to develop the elastic spring stiffness values for this process.

During this step, it was realized that achieving all the key parameters listed in Table 4.2 simultaneously for each centrifuge model was unrealistic. Accordingly, the flexible-base period was given the highest priority, and the yield strength and yield drift ratios were allowed to deviate from targeted values.

The numerical modeling performed to design the model structures also predicted that the beams of the MS1F_SF80 model structure would deform significantly during the higher intensity earthquake motions. Because dry, dense Nevada sand was used to construct the centrifuge models, 17 earthquake motions were performed during Test-1 and 21 earthquake motions were performed during Test-2. It was therefore decided that the MS1F_SF80 model structure would be designed so that its beams could be replaced after they were significantly damaged; i.e., the structural models were retrofitted during testing. The beam-column connections were designed as simple bolted connections, and spare beams were available during testing.

The modular design concept was carried a step further. The structural properties of the beams as well as the mass of the MS1F_SF80 structural model could be changed during a retrofit. The structural properties of the beams were changed by changing the size of the beam *fuses*. These fuses are reduced cross-sectional areas that are strategically located within the beams and columns to control the inelastic deformation within the frame. The geometry of the fuses controls the inelastic response, and the differing geometries were designed using the calibrated OpenSees model. Table 4.3 lists the different beam/mass configurations used for the MS1F_SF80 model structure, and it also shows the achieved modal and strength parameters for the MS3F_B model structure. Figure 4.1 is an elevation view of the MS1F_SF80 structural model (left) and MS3F_B structural model (right) with important dimensions marked (the structures are in Test-2 alignment). This figure also notes the locations of different fuses and has a diagram of the different fuses used during testing. Figure 4.2 shows pictures of the two structural models used during the tests.

The modular design concept and the fuses discussed above are unique aspects of the structural design. These are key contributions of this research project, and will hopefully be helpful for future SFSI researchers using centrifuge testing. More details about the structural models used for Test-1 and Test-2 can be found in Chen et al. (2010).

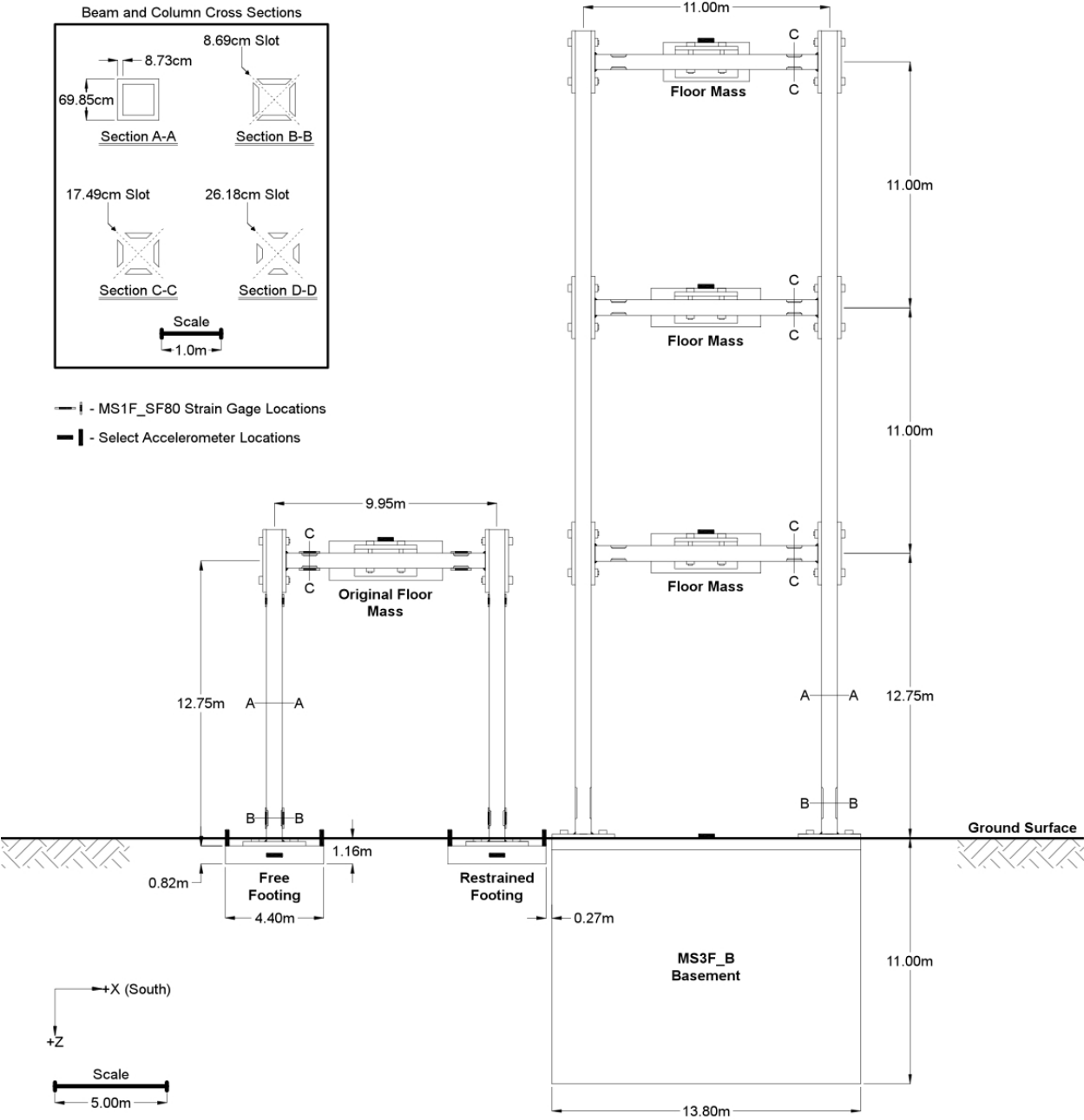
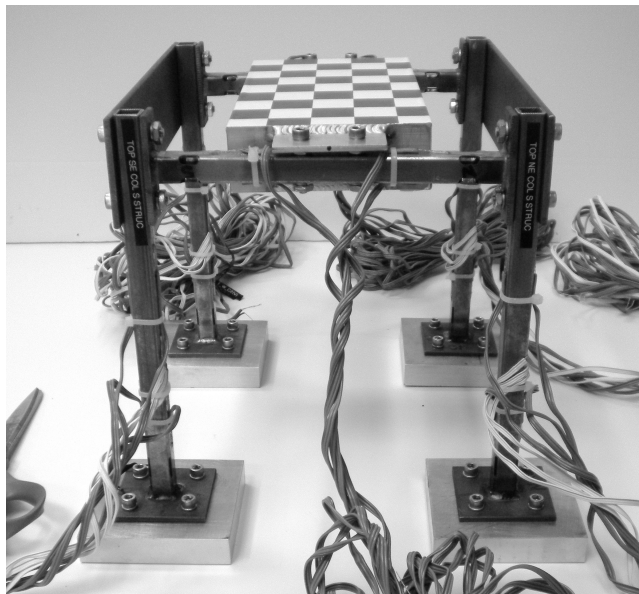


Figure 4.1: Location of (Left) MS1F_SF80 with Phase II Beams and (Right) MS3F_B during Test-2. All measurements are in prototype scale. Only select instrumentation is shown; refer to Mason et al. (2011b) for complete instrumentation plans.

Table 4.3: Design goal and achieved geometric, modal, and strength parameters. All values are in prototype scale.

Structure	Notes	Test-1 Motions	Test-2 Motions	\tilde{T} (<i>sec</i>)	V_y/W	δ_y (%)
3-Story Idealized Prototype		-	-	1.10	0.40	1.40
MS1F_SF80 (I)	Original Mass*, Phase I Beams	1 - 6	1 - 6	1.06	0.41	1.13
MS1F_SF80 (II)	Reduced Mass**, Phase I Beams	7 - 12	-	0.96	0.52	1.40
MS1F_SF80 (III)	Reduced Mass, Phase II Beams	13 - 17	-	0.89	0.74	2.28
MS1F_SF80 (IV)	Original Mass, Phase II Beams	-	7 - 21	0.98	0.59	1.94
9-Story Idealized Prototype		-	-	2.30	0.20	1.40
MS3F_B	-	1 - 17	-	2.26	0.22	1.93

*Original Mass = 4.1 kg *Model Scale*; **Reduced Mass = 3.2 kg *Model Scale*



(a)



(b)

Figure 4.2: Pictures of the instrumented model buildings: (a) 3-story frame structure on spread footings (modeled as a 1-story structure and denoted as MS1F_SF80), and (b) 9-story frame structure on a 3-level basement (modeled as a 3-story structure and denoted as MS3F_B). The height of the MS1F_SF80 structure is the same as one floor of the MS1F_B structure.

4.2.3 Instrumentation

Accelerometers, displacement gauges, strain gauges, and cameras were employed during Test-1 and Test-2 to measure the seismic response of the SFS systems. More information about all the specific instruments used at the UCD-CGM can be found at the website: <http://nees.ucdavis.edu/>.

Two types of accelerometers were employed: Integrated Circuit-Piezometer (ICP) accelerometers (shown in Figure 4.3(a)) and micro electro-mechanical systems (MEMS) accelerometers (shown in Figure 4.3(b)). The ICP accelerometers only measure the dynamic acceleration (i.e., the acceleration caused by actual movement of the accelerometer, and not the centrifugal acceleration). In contrast, the MEMS accelerometers measure dynamic and centrifugal acceleration. If a MEMS accelerometer is oriented such that its chip is exactly perpendicular to the vector of centrifugal acceleration, then its reading will give the exact scalar value of centrifugal acceleration. If the MEMS accelerometer is tilted from this orientation, then the scalar reading will differ. This property of the MEMS accelerometer can be used to calculate tilt.

The ICP accelerometers available at the UCD-CGM have measurement ranges of ± 50 , 100 and 500 g, and the MEMS accelerometers have measurement ranges of ± 50 and 100 g. The resolution of the accelerometers is proportional to the measurement range; i.e., the 50 g accelerometers have the finest resolution and the 500 g accelerometers have the coarsest resolution.

ICP accelerometers have two notable advantages: (1) they are rugged and can handle the harsh centrifuge environment well; and (2) they have dedicated boards on the centrifuge DAQ, which makes troubleshooting issues easiest. The disadvantages of the ICP accelerometers are their size. This is especially an issue for structural model instrumentation. The accelerometers must be placed carefully, or they can change the seismic response of the structural models. Smaller ICP accelerometers are manufactured, which can alleviate this issue; however, the smaller ICP accelerometers have worse resolution than their larger counterparts and they are more vulnerable to damage.

The major advantage of the MEMS accelerometer, other than the ability to measure tilt as noted above, is their shape and size. The MEMS accelerometers are less likely to affect the seismic response of the object to which they are attached.

The displacement gauges are linear potentiometers with strokes of 25, 50, 75 and 100 mm. Figure 4.3(c) shows a picture of a linear potentiometer. The potentiometers are used to measure permanent displacements caused by the earthquake motions. As the potentiometer's rod moves during a shake, a voltage difference is registered, and this change in voltage can be equated to a permanent displacement value by applying a linear sensitivity factor. The sensitivity factors of the linear potentiometers change as a function of time; therefore, their specific sensitivity factors must be determined before each test. There are several challenges associated with using linear potentiometers for centrifuge testing. First, they are relatively large; their length is on the same order as the model structures. Second, they must be

attached to a displacement frame in order to be used. The displacement frame is bulky, because it must be “rigid” to reduce measurement error. The large size of the displacement frame, in addition to the large size of the linear potentiometers, leads to some geometrical challenges during model construction. Third, the linear potentiometers are fragile; their rods can be bent during strong shaking, which affects the quality of their measurements. Finally, special “displacement flags” usually need to be constructed to use the linear potentiometers. These displacement flags are especially required for embedded foundations. The displacement flags rise above the soil surface, and the tip of the linear potentiometer sits on top of them. These displacement flags affect the seismic response of the SFS systems.

Two types of strain gauges were used during Test-1 and Test-2: (1) a standard strain gauge with a range of $\pm 30,000 \mu\epsilon$, and (2) a high-elongation, post-yield strain gauge with a range of $\pm 150,000 \mu\epsilon$. Figure 4.3(d) shows a picture of a strain gauge. The high-elongation strain gauges were used on beams, where significantly yielding occurred during some of the higher intensity earthquake motions. Likewise, the standard strain gauges were used on the columns, which did not show as much seismic damage.

The strain gauges were wired as quarter bridge sensors, which makes them more sensitive to temperature effects. This could explain the significant drift observed during the experiments. The drift makes calculation of static loads impossible. The dynamic strain data measured during each earthquake motion is still valid, however, because the measured drift is insignificant during a shaking event.

Both high-speed and analog cameras were used during Test-1 and Test-2. The analog cameras are capable of capturing 20 frames/sec. The analog cameras were placed in important locations, such as the beam fuses. The analog cameras allowed the team to monitor damage after each earthquake motion, and assess when the model needed to be spun-down to make replacements and repairs. The high-speed cameras capture footage at 200 frames/sec. The high-speed cameras were used to see the seismic response of the structures during the earthquake motions. Figure 4.3(e) shows a picture of an analog camera and Figure 4.3(f) shows a picture of a high-speed camera.

A schematic showing important soil instrumentation is given in Figure 4.4(a) for Test-1 and Figure 4.4(b) for Test-2. More complete instrumentation tables are available in Mason et al. (2011a) and Mason et al. (2011b). In addition, these instrumentation tables are provided in Appendix A of this thesis for reference. In general, the following instrumentation philosophy was used for both tests:

1. Vertical arrays of horizontal accelerometers are used to capture the seismic site response.
2. Base and free-field surface horizontal accelerometers are important for engineering analyses; therefore, redundant sensors must be located at these locations.
3. Horizontal accelerometers located near the footings or basement are used to understand inertial interaction effects (for the footings) and kinematic interaction (for the basement).

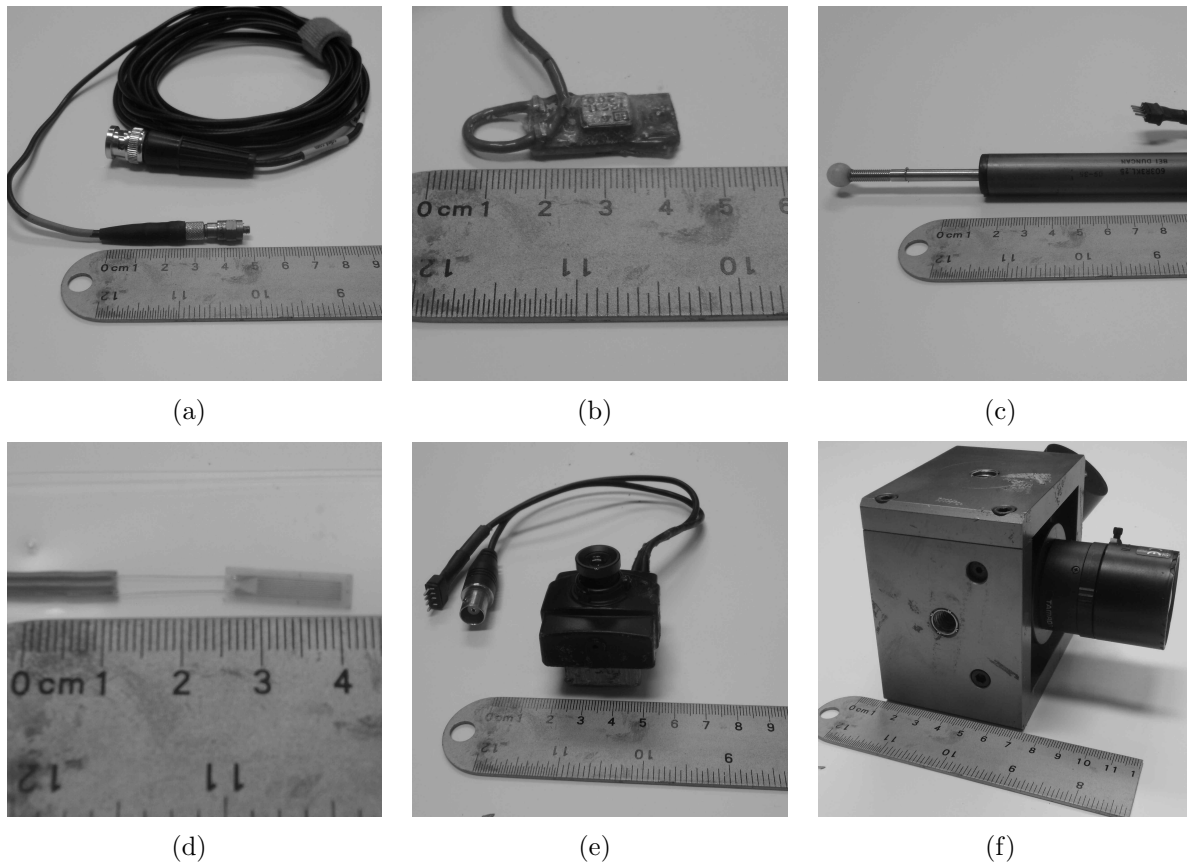


Figure 4.3: Instrumentation: (a) ICP accelerometer, (b) MEMS accelerometer, (c) linear potentiometer (displacement gauge), (d) strain gauge, (e) analog camera, and (f) high-speed camera.

4. Vertical accelerometers are used to understand wave propagation, attenuation, and container boundary effects.
5. A vertical array of displacement gauges is used in the soil to measure the settlement as a function of depth and the vertical strain.
6. Displacement gauges at the soil surface measure the surface settlement of the soil.

4.2.4 Model construction

The flexible shear beam container 2.2 (FSB2.2) was used for Test-1 and Test-2. This container has internal model scale dimensions of 1652 mm (length) by 785 mm (width) by 590 mm (height). More information about this model container can be found at the UCD-CGM website (<http://nees.ucdavis.edu/>).

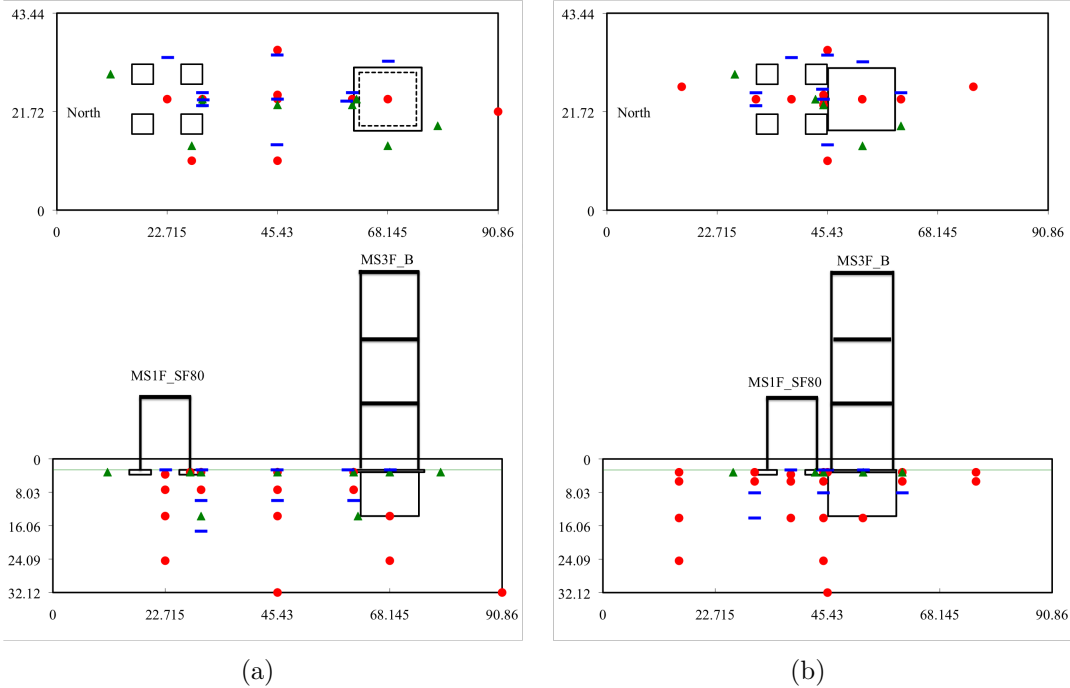


Figure 4.4: Schematics of (a) Test-1 and (b) Test-2 with important soil instrumentation locations; circles = horizontal accelerometers; triangles = vertical accelerometers; lines = displacement gauges. All measurements are in prototype scale, meters.

Nevada sand was dry-pluviated into the container using the large pluviater (see Figure 4.5(a)) to a relative density of approximately 80%. The pluviation calibration chamber (see Figure 4.5(b)) was initially used to calibrate the large pluviater to pour sand at a relative density of approximately 80% given the important Nevada sand properties in Table 4.1. A drop height of 813 mm and a motor speed of 35 rpm was found to satisfactorily produce an 80% relative density sand model for the particular batch of Nevada sand used for these experiments. The Nevada sand was placed in the model in predetermined lifts of designated thicknesses. The pluviater calibration was checked after every lift to ensure that the soil remained uniform throughout the model during construction.

The following list outlines the model construction process. Figure 4.6 illustrates the major steps involved in model construction.

1. The empty container weight was taken.
2. The base accelerometers were placed. This required that they be embedded in modeling clay to hold them in place. The accelerometer wires were held in place with duct tape. Because a flexible shear beam container was used, the wires were given slack at each rubber connection to ensure that the wires would not be stressed or break during strong motion.

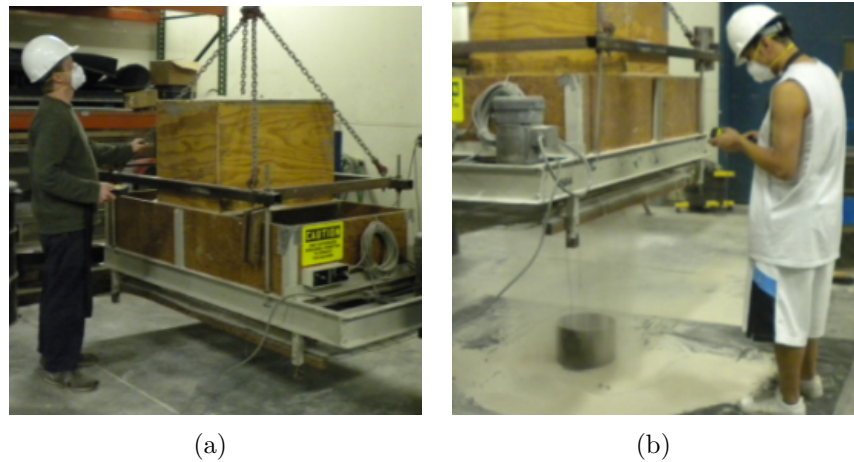


Figure 4.5: Pluviation at the UCD-CGM: (a) the large pluviator used to pour dense sand, and (b) using the pluviation calibration chamber.

3. The Nevada sand was pluviated in lifts, and after each lift, the model weight was taken. Initially, lifts of 100 mm were used to check the relative density. Near the surface, lift thicknesses were planned around the soil instrumentation. The final soil height was 536 mm (model scale), which represents 29.5 m in prototype scale (with $N = 55$).
4. After each lift was pluviated, the surface of the soil was groomed to the desired elevation using a vacuum cleaner. Several times during each grooming session, the vacuum cleaner's filter was cleaned with an air compressor. This was necessary to ensure a constant suction length during grooming so that a correct final elevation could be achieved.
5. Instruments were placed at the desired locations within each instrumentation lift.
6. The model structures were placed in the container at the desired elevations. For Test-2, the model structures were placed 5 mm (model scale) apart. To accomplish this, washers with a total thickness of 5 mm were taped together, and this assembly acted as a spacer. The structures were fully instrumented with strain gauges and accelerometers prior to being placed in the container. Figure 4.7 shows the strain gauging process.
7. The displacement rack was constructed on the model container once the structures were in place. The displacement rack was constructed to be as stiff as possible to minimize deflections due to increases in self-weight after spin-up and during strong shaking. The displacement racks were necessarily different for Test-1 and Test-2, given the different locations of the model structures within the container. The displacement gauges were placed in appropriate places on the displacement rack, then the entire assembly was dismantled before the model was transported to the arm.

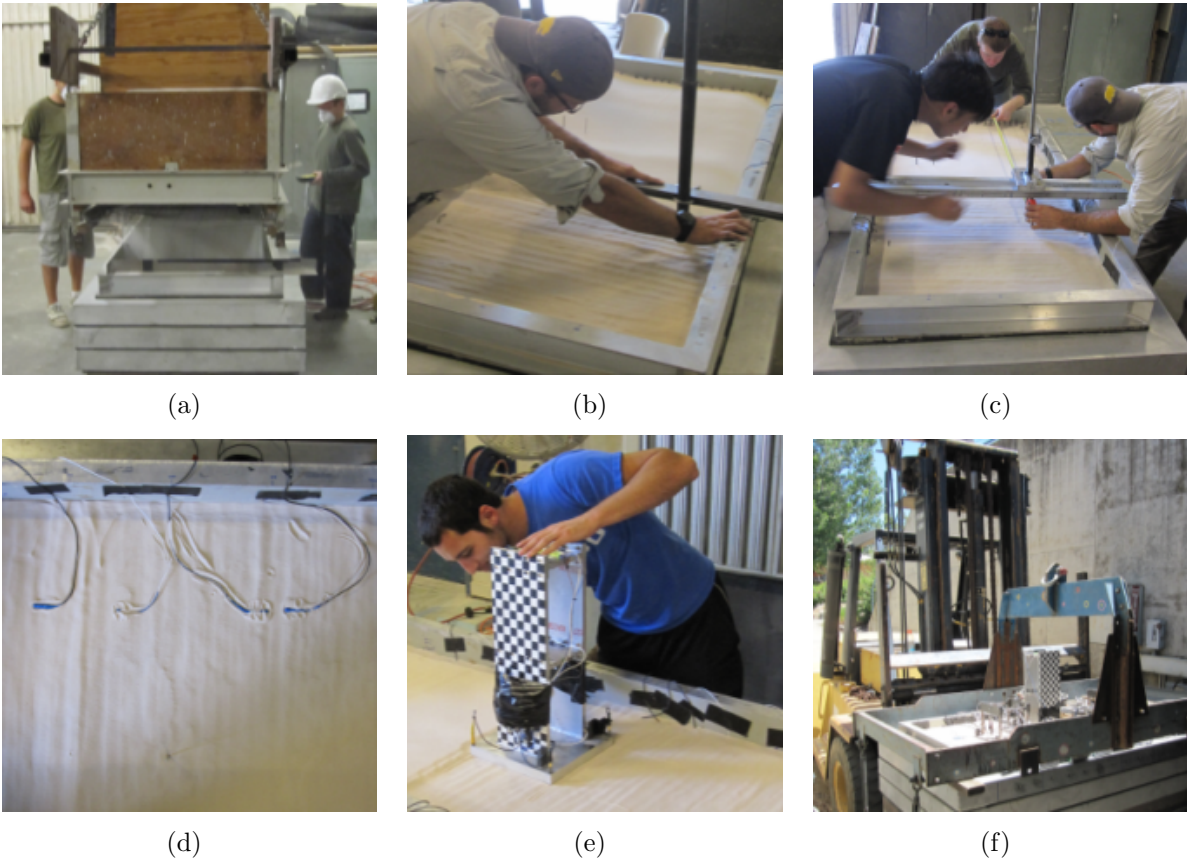


Figure 4.6: Model construction process: (a) pluviation of a soil lift, (b) grooming the soil surface, (c) measuring the elevation of the soil lift, (d) placing accelerometers in the soil, (e) placing a structure in the soil model, and (f) moving the model onto the centrifuge arm.

8. The strain gauges were hooked into the bridge completion boards in their proper places. All the instrumentation wiring was then securely fastened in place to prepare the model for transport. Figure 4.8 shows a bridge completion box.
9. A final weight of the fully constructed centrifuge model was taken. This weight is important for the centrifuge counterbalancing process that must take place before spin-up.
10. The displacement rack was reassembled on the model.
11. Colored sand was placed around each footing. The colored sand allowed rocking and sliding of the foundations to be seen in the camera footage.
12. Instrument cables were placed, routed and connected in their proper places.

13. Cameras and lights were placed and connected.
14. After final inspection, the model was ready for spin-up.

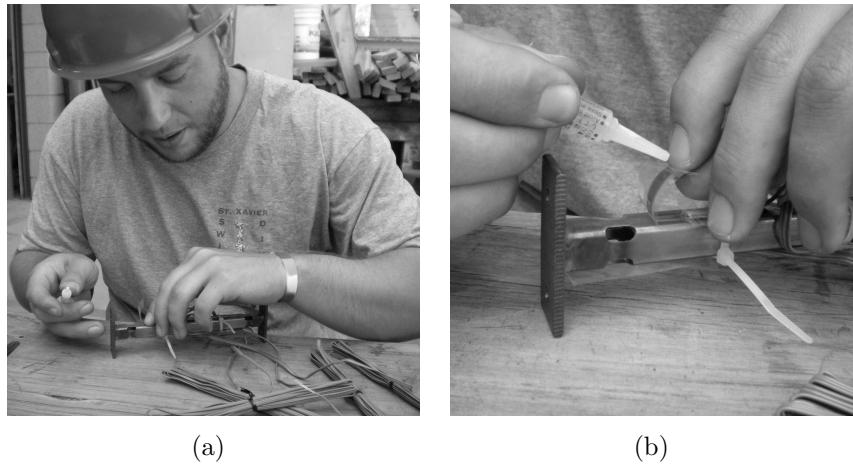


Figure 4.7: Strain gauging: (a) gluing a strain gauge onto a sanded and cleaned beam, and (b) close-up of the gluing process.

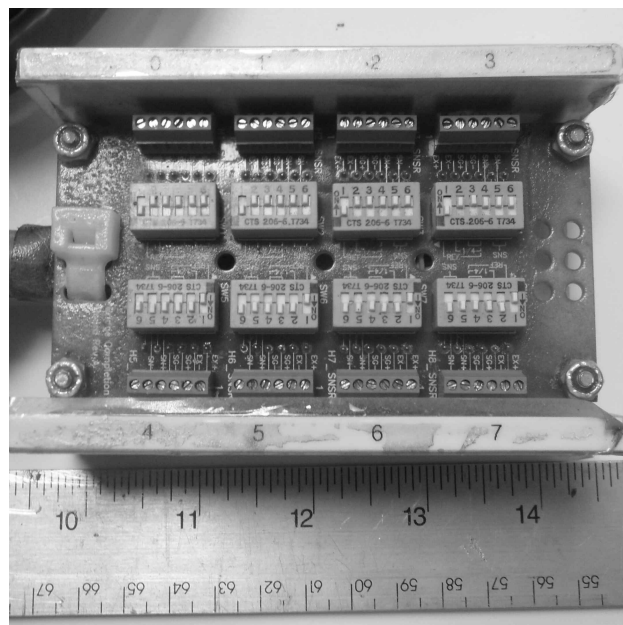


Figure 4.8: Close-up of a bridge completion board used to connect the strain gauges to the DAQ.

4.2.5 Earthquake motions plan

The order of the earthquake motions used in Test-1 and Test-2 was determined by considering each earthquake motion’s potential “destructiveness.” Destructiveness, in this case, refers to the potential for superstructural damage. For the structural models, and especially MS1F_SF80, this refers to deformation of the beam fuses.

The numerical models developed during the structural model design process were used to roughly rank the earthquake motions in order of their potential destructiveness. In particular, the maximum predicted curvature ductility demand (μ_ϕ), the number of inelastic cycles in the fuses, and the spectral acceleration at \tilde{T} were examined in order to estimate potential destructiveness. Table 4.4 shows the values of the aforementioned parameters for each earthquake motion. The earthquake motions in this table are in order of their potential destructiveness using μ_ϕ as the main indicator.

Table 4.4: Spectral accelerations and predicted damage quantities for individual earthquake motions used in Test-1 and Test-2. After Chen et al. (2010).

Motion ID	$Sa(\tilde{T})$		Max μ_ϕ	No. of Inelastic Cycles
	MS1F_SF80	MS3F_B		
JOS_L	0.22	0.05	0.76	0
TCU	0.15	0.02	0.62	0
SCS_L	0.33	0.06	1.29	4
RRS	0.35	0.10	1.31	2
LCN	0.39	0.17	2.47	4
PTS	0.32	0.16	2.84	9
WVC	0.37	0.22	3.42	7
SCS_H	0.71	0.14	3.83	6
JOS_H	0.54	0.11	2.67	5
WPI	0.65	0.16	3.34	5
PRI	0.57	0.20	3.33	12

The earthquake motion ranking shown in Table 4.4 was considered preliminary, and served as a guide for selecting the earthquake motion order for the two tests. The numerical models built during the structural model design process were once again used at this stage. The earthquake motions found in Table 4.4 were inputted into the model in this order. The model properties were not reset after each earthquake motion, and as such, the progressive damage caused by each successive earthquake motion was tracked. The numerical modeling at this stage predicted significant damage to occur in the beam fuses. This finding was a main motivator behind the modular design concept discussed previously.

Tables 4.5 and 4.6 contain the motion order as well as important intensity measures of the achieved motions recorded at the container base for Test-1 and Test-2, respectively. Tables 4.7 and 4.8 contain the same important information as Tables 4.7 and 4.8 for earthquake

motions recorded at the surface of the model in the free-field. The names of the earthquake motions in these tables correspond to those given in Table 3.12, with the exception of either a suffix “L” refers to low intensity or the suffix “H” referring to high intensity. Additionally, the suffix numbers help separate motions that were performed multiple times. The important intensity measures contained in these tables are the peak ground acceleration (PGA), peak ground velocity (PGV), the significant duration (D_{5-95}), the Arias intensity (I_a) and the spectral acceleration at the site period ($T_s = 0.6$) for a damping ratio (β) of 5% ($Sa[T_s]$). The site period, T_s , was determined based on ratio of response spectrum ordinates calculated during Test-0. This site period was reconfirmed during Test-1 and Test-2 during the testing by examining data from the JOS_L_1 earthquake motion. The site period does lengthen for the more intense earthquake motions, as the soil responds inelastically. However, given the large relative density of the Nevada sand, it was found that this period lengthening was insignificant (i.e., within 10%).

Table 4.5: Earthquake motions achieved during Test-1 at the base.

Motion	PGA (g)	PGV (cm/sec)	D_{5-95} (sec)	I_a (m/sec)	$Sa[T_s]^1$ (g)
JOS_L_1	0.06	8.61	20.6	0.07	0.17
TCU_L	0.10	9.03	19.6	0.22	0.19
RRS	0.38	34.5	4.6	0.47	0.61
PTS	0.10	14.5	10.0	0.13	0.29
SCS_L_1	0.18	18.1	8.2	0.34	0.45
LCN	0.27	43.8	6.6	0.35	0.42
JOS_L_2	0.06	8.60	20.9	0.07	0.17
SCS_L_2	0.19	18.0	8.2	0.35	0.45
WVC_L	0.25	34.1	7.6	0.62	0.47
SCS_H	0.58	52.2	15.3	4.31	1.65
JOS_H	0.31	31.7	21.0	2.07	1.02
WPL_L	0.37	44.1	4.8	0.49	0.43
JOS_L_3	0.06	8.48	20.8	0.06	0.15
WPL_H	0.47	50.4	6.8	0.67	0.49
PRI	0.61	41.1	6.8	2.83	0.96
TCU_H	0.26	17.6	19.9	1.18	0.36
WVC_H	0.33	47.4	11.0	1.43	0.55

¹ β = damping ratio = 5%; $T_s = 0.6$ sec

It can be seen that the earthquake motion orders actually performed during Test-1 and Test-2 differs slightly from the order given in Table 4.4. The earthquake motion order performed was changed in the control room during the spin days to reflect incoming information from the analog and high-speed cameras as well as the strain gauges, displacement gauges and accelerometers.

Table 4.6: Earthquake motions achieved during Test-2 at the base.

Motion	PGA (g)	PGV (cm/sec)	D_{5-95} (sec)	I_a (m/sec)	$Sa[T_s]^1$ (g)
JOS_L_1	0.05	6.96	20.1	0.04	0.13
TCU_L_1	0.08	7.84	17.7	0.08	0.17
RRS_1	0.36	32.1	3.4	0.41	0.58
PTS_1	0.12	14.3	9.0	0.11	0.28
SCS_L_1	0.17	16.2	6.6	0.22	0.40
LCN_1	0.26	42.5	5.7	0.29	0.39
JOS_L_2	0.05	7.18	20.1	0.04	0.15
TCU_L_2	0.09	8.49	18.0	0.10	0.18
RRS_2	0.36	33.2	3.5	0.43	0.59
PTS_2	0.12	14.2	9.0	0.11	0.28
SCS_L_2	0.18	17.3	6.3	0.25	0.43
LCN_2	0.27	43.6	5.8	0.31	0.41
JOS_L_3	0.05	7.23	20.1	0.04	0.15
WVC_L	0.28	34.7	7.4	0.60	0.49
SCS_H	0.58	50.8	14.7	4.48	1.64
JOS_H	0.34	34.3	19.4	2.32	1.15
WPI_H	0.41	45.6	4.3	0.53	0.50
PRI	0.64	42.1	6.8	3.01	0.98
TCU_H	0.27	17.9	17.6	1.14	0.43
WVC_H	0.35	49.0	10.2	1.51	0.59
JOS_L_4	0.06	8.05	20.4	0.07	0.21

¹ β = damping ratio = 5%; T_s = 0.6 sec

4.3 Experimental results

The goal of the experimental results section of this chapter is to present some of the more interesting results that have been deduced from the raw data. For each test, nearly 200 channels of instruments were employed and almost 20 earthquake motions were performed. The raw data is available online at the NEES Hub and as an electronic appendix to this dissertation. Tables of instrumentation for each centrifuge test as well as known data limitations are contained in Appendix A of this dissertation.

4.3.1 Kinematic interaction

During Test-1 and Test-2, a deeply-embedded basement structure was employed. Basements are typical in densely populated urban areas, where they serve as parking garages.

The earthquake motion recorded at the foundation-level of the basement differs from the motion recorded nearby in the free-field because of kinematic interaction. Specifically, the

Table 4.7: Earthquake motions achieved during Test-1 at the surface in the free-field.

Motion	PGA (g)	PGV (cm/sec)	D_{5-95} (sec)	I_a (m/sec)	$Sa[T_s]^1$ (g)
JOS_L_1	0.14	16.2	20.9	0.5	0.58
TCU_L	0.23	20.8	22.1	1.8	0.57
RRS	0.38	51.7	5.4	1.4	0.71
PTS	0.19	24.6	11.2	0.9	0.83
SCS_L_1	0.31	32.1	8.3	1.6	0.95
LCN	0.34	52.8	7.7	1.0	0.74
JOS_L_2	0.17	16.5	20.7	0.6	0.64
SCS_L_2	0.31	32.1	8.3	1.6	1.00
WVC_L	0.40	50.6	7.4	2.4	1.18
SCS_H	0.61	76.8	18.3	13.6	2.84
JOS_H	0.47	48.8	21.7	10.9	2.15
WPL_L	0.39	56.2	5.3	1.3	0.71
JOS_L_3	0.16	15.6	20.6	0.5	0.59
WPL_H	0.46	66.8	7.4	1.6	0.59
PRI	0.71	75.3	7.1	8.8	2.01
TCU_H	0.46	35.2	22.4	7.6	0.95
WVC_H	0.44	68.6	11.6	4.9	1.30

¹ β = damping ratio = 5%; T_s = 0.6 sec

frequency-content of the foundation-level motion is different than that of the free-field surface ground motion because of base slab averaging, and the amplitude of the foundation-level motion is lower than that of the free-field surface ground motion because of embedment effects. For the analysis performed in this dissertation, the foundation-level accelerometer was located in the soil, 10 mm (model scale) below the basement. During each test, accelerometers were placed directly on the basement slab, but unfortunately, these sensors malfunctioned during each test, so the data was not usable.

Figure 4.9 shows zoomed-in acceleration time-series recorded during both Test-1 and Test-2 for selected earthquake motions. Kinematic interaction effects are apparent in these time-series; in particular, the high-frequency content of the foundation-level motion is reduced compared to the free-field surface ground motion. In addition, the amplitude of the foundation-level motion is lower than the amplitude of the free-field surface ground motion, because of embedment effects. As noted in Chapter 2, base slab averaging effects arise from seismic waves impinging upon a foundation from different angles of incidence. The centrifuge shaking table is uni-directional, and the soil within the centrifuge models is relatively homogeneous dense sand. Given these facts, the seismic waves produced in the centrifuge model may be more homogeneous than those recorded in the field, and for this reason, base slab averaging effects may be masked in centrifuge test results.

Table 4.8: Earthquake motions achieved during Test-2 at the surface in the free-field.

Motion	PGA (g)	PGV (cm/sec)	D_{5-95} (sec)	I_a (m/sec)	$Sa[T_s]^1$ (g)
JOS_L_1	0.11	12.8	20.6	0.34	0.56
TCU_L_1	0.19	19.5	17.8	0.76	0.53
RRS_1	0.37	52.7	5.1	1.2	0.78
PTS_1	0.26	27.3	8.8	0.88	1.05
SCS_L_1	0.32	32.9	6.8	1.4	1.06
LCN_1	0.32	48.5	6.6	0.86	0.82
JOS_L_2	0.12	13.6	20.5	0.43	0.62
TCU_L_2	0.21	21.8	18.5	0.99	0.62
RRS_2	0.41	55.3	4.9	1.5	0.88
PTS_2	0.26	27.0	8.7	0.86	1.07
SCS_L_2	0.34	34.8	6.5	1.6	1.15
LCN_2	0.35	50.4	6.8	1.0	0.91
JOS_L_3	0.12	13.6	20.6	0.42	0.63
WVC_L	0.42	53.4	6.5	2.3	1.20
SCS_H	0.60	79.8	16.1	13.9	2.56
JOS_H	0.54	57.6	21.4	13.0	2.45
WPI_H	0.44	56.4	4.3	1.4	0.76
PRI	0.68	74.3	7.3	9.6	2.15
TCU_H	0.48	46.0	21.4	8.9	1.22
WVC_H	0.53	72.1	10.1	5.8	1.60
JOS_L_4	0.15	15.1	20.4	0.64	0.76

¹ β = damping ratio = 5%; T_s = 0.6 sec

During Test-1, the basement structure was isolated in the centrifuge container. In contrast, during Test-2, the MS1F_SF80 model structure was adjacent to the basement structure. Accordingly, by comparing the kinematic interaction effects observed during Test-1 and Test-2, observations can be made about the effect of SSSI on kinematic interaction, which is the goal of this section.

Figure 4.9 is instructive for visualizing kinematic interaction. Examining results in the time-domain is important, because it is more intuitive. However, to glean more meaningful information about kinematic interaction, the results should also be viewed in the frequency-domain. As described in Chapter 2, this is typically accomplished by employing transmissibility functions, which are ratios of power and cross spectral densities. For this dissertation, the transmissibility function H_3 was employed, which was defined in Equation 2.1c

For defining the experimental transfer function, S_{yy} is the power spectral density function of the output, which is the recorded foundation-level acceleration time-series. Likewise, S_{xx}

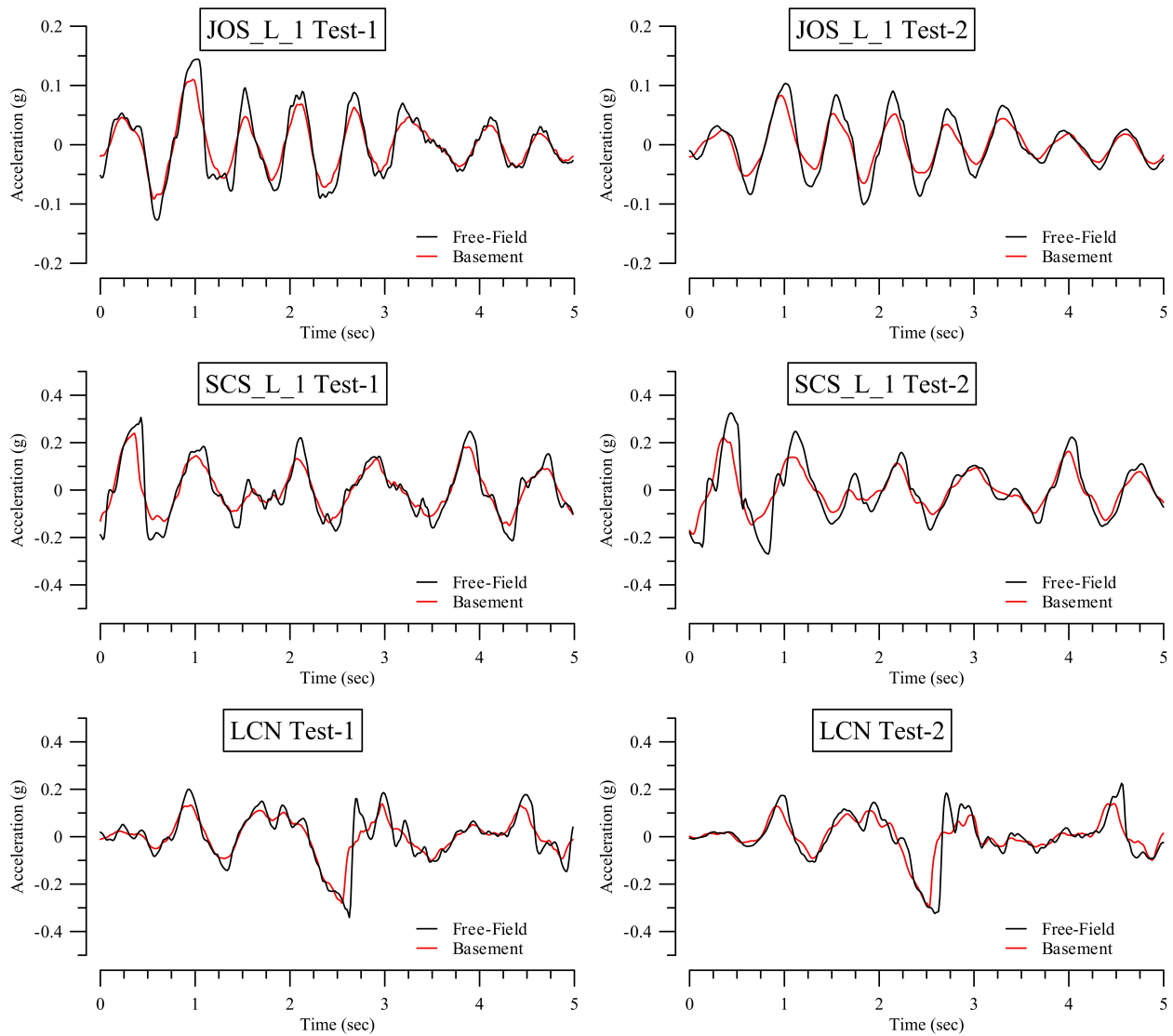


Figure 4.9: Zoomed-in acceleration time-series for the JOS_L_1, SCS_L_1, and LCN earthquake motions. This plot includes the free-field surface ground motions and the foundation-level earthquake motions.

is the power spectral density function of the input, which is the recorded surface free-field acceleration time-series.

The MATLAB code for calculating H_3 and the coherency, γ , is given in Table 4.9. This code was defined based on input from Professor Jonathan Stewart (Stewart, pers. comm.).

The code shown in Table 4.9 is described line-by-line:

1. N helps define the length of the window used to filter the signals (see line 7). This is a user defined parameter, and affects the shape of the transmissibility function. The

Table 4.9: MATLAB code used to calculate H_3 and coherency

```

1 N = 256;
2 param = 15.7;
3 Fs = 1/dt;
4 nfft = length(time);
5 x = FFM time series
6 y = FLM time series;
7 window = kaiser(nfft/N,param);
8 [Syy,f] = psd(y,nfft,Fs>window);
9 [Sxx,f] = psd(x,nfft,Fs>window);
10 Sxy = csd(x,y,nfft,Fs>window);
11 H1 = real(Sxy./Sxx);
12 H2 = real(Syy./Sxy);
13 H3 = sqrt(Syy./Sxx);
14 coh2 = H1./H2;

```

effect of N on the results is discussed later in this section.

2. $param$ is the *windowing parameter* defined for the Kaiser window (see line 7). This is a user defined parameter and has a minor effect on the shape of the transmissibility function. A fixed value of 15.7 was considered for this dissertation research to be consistent with the work of Fenves and DesRoches (1994) and Kim and Stewart (2003).
3. F_s is the sampling frequency, which is defined at the inverse of the sampling time.
4. $nfft$ is the number of points in the acceleration time-series. The number of points must be a power of 2 (i.e., 2^i where i is a positive integer) for the FFT algorithm.
5. x is the free-field surface ground motion acceleration time-series, i.e., the input vector.
6. y is the foundation-level earthquake motion acceleration time-series, i.e., the output vector.
7. $window$ is a signal processing window used to filter the results. This filtering is in addition to a fifth-order, acausal Butterworth bandpass filter with corner frequencies of 0.1 Hz and 25 Hz (prototype scale), which all earthquake motions are filtered with before processing. For this research, a Kaiser window was employed to be consistent with previous kinematic interaction research (e.g Fenves and DesRoches 1994; Kim and Stewart 2003). The Kaiser window requires a window length, which is defined as

$nfft/N$, and a windowing parameter. These values were given in Lines 1 and 2. The effect that the window has on the results is discussed later in this section.

8. S_{yy} is the power spectral density function for the output vector, which is calculated using MATLAB's *psd* function. f is the frequency vector.
9. S_{xx} is the power spectral density function for the input vector, which is calculated using MATLAB's *psd* function. f is the frequency vector.
10. S_{xy} is the cross spectral density function for the input and output vectors, which is calculated using MATLAB's *csd* function.
11. H_1 is a transmissibility function, which was defined in Chapter 2.
12. H_2 is a transmissibility function, which was defined in Chapter 2.
13. H_3 is the preferred transmissibility function, which is defined in Equation 2.1c.
14. *coh2* is the coherency function, γ^2 . The coherency function is described in greater detail within Chapter 2.

As described within Chapter 2, the non-dimensional incoherence factor, Γ , which is defined in Equation 2.4, can be fitted to the experimentally determined transmissibility functions. This is performed by using nonlinear regression and changing the value of the incoherency factor, κ . The κ determined during this analysis is renamed κ_a because it is an apparent incoherency factor, determined from experimental data. κ_a is a proxy for understanding the importance of kinematic interaction effects. As the value of κ_a increases, the importance of kinematic interaction effects also increases; in other words, as κ_a increases, the free-field surface ground motion deviates more from the foundation-level earthquake motion.

Table 4.10 shows the MATLAB code used to perform the nonlinear regression and determine κ_a for each earthquake motion.

Table 4.10: MATLAB code used to perform the nonlinear regression to fit Equation 2.4 with the experimentally determined transmissibility functions and determine κ_a

```

1 w = 2*pi*f(f_l:f_h);
2 Gamma = inline('exp(-(Ka*w*D/Vs).^2)', 'Ka', 'w');
3 kappa_a = nlinfit(w,H3(f_l:f_h), Gamma,0)
4 Gamma_experimental = exp(-(kappa_a*w*D/Vs).^2);

```

The code shown in Table 4.10 is explained line-by-line:

1. w in this case is ω , which is the circular frequency. The frequency vector used to calculate the circular frequency is cut at the high-pass and low-pass corner frequencies (0.1 and 25 Hz).
2. Γ is the incoherency factor, which is defined by Equation 2.4. In this line of code D is equivalent to $|\mathbf{r}_1 - \mathbf{r}_2|$ and V_s is equivalent to $(V_{s,r})_H$ in Equation 2.4. The values of D and V_s must be defined explicitly in this line of code. The values of D are 25.0 m and 39.3 m for Test-1 and Test-2 (prototype scale), respectively. The value of V_s is assumed to be 200 m/sec for both tests. V_s is estimated based on the experimentally observed site period.
3. This line of code estimates κ_a , using a nonlinear regression with the functional form of the incoherency factor, Γ , given in Equation 2.4. Importantly, H_3 in this line of code is modified; only the values of H_3 with high-coherency are used for the regression.
4. $\Gamma_{\text{experimental}}$ is calculated with the value of κ_a determined in the preceding line of code. $\Gamma_{\text{experimental}}$ can be plotted with the experimentally determined transmissibility functions for comparison purposes.

Figure 4.10 shows experimental transmissibility functions calculated for selected earthquake motions recorded during Test-1 (left column) and Test-2 (right column). This plot also shows the points of high-coherency and the nonlinear regression of Equation 2.4. The nonlinear regression is labeled “Incoherency Model” for each subplot in Figure 4.10.

The values of κ_a calculated for each earthquake motion from the experimental data are sensitive to several input parameters; namely: (1) the frequency range over which the nonlinear regression is performed, and (2) the windowing parameters (i.e., the filtering).

In this study, it was decided to examine transmissibility functions over a frequency range of 0.1 to 5 Hz, which corresponds to a period range of 0.2 to 10 sec. This frequency range was thought to encapsulate the fundamental frequencies and important higher modes of the structural models as well as the soil model. Transmissibility functions were examined past 5 Hz, and it was found that the points of high-coherency decreased significantly past 5 Hz for most of the earthquake motions recorded during both tests. As a larger frequency range is considered, the values of κ_a tend to increase, which indicates that the kinematic interaction effects are more important. κ_a increases because the points of high-coherency past 5 Hz tend to have low values, which skews the nonlinear regression.

The values of κ_a are also sensitive to the windowing parameters. A Kaiser window was employed for all the windowing, which follows the work of previous researchers (e.g., Fenves and DesRoches 1994; Kim and Stewart 2003). A detailed description of Kaiser windows is outside the scope of this dissertation, but can be found in digital signal processing literature

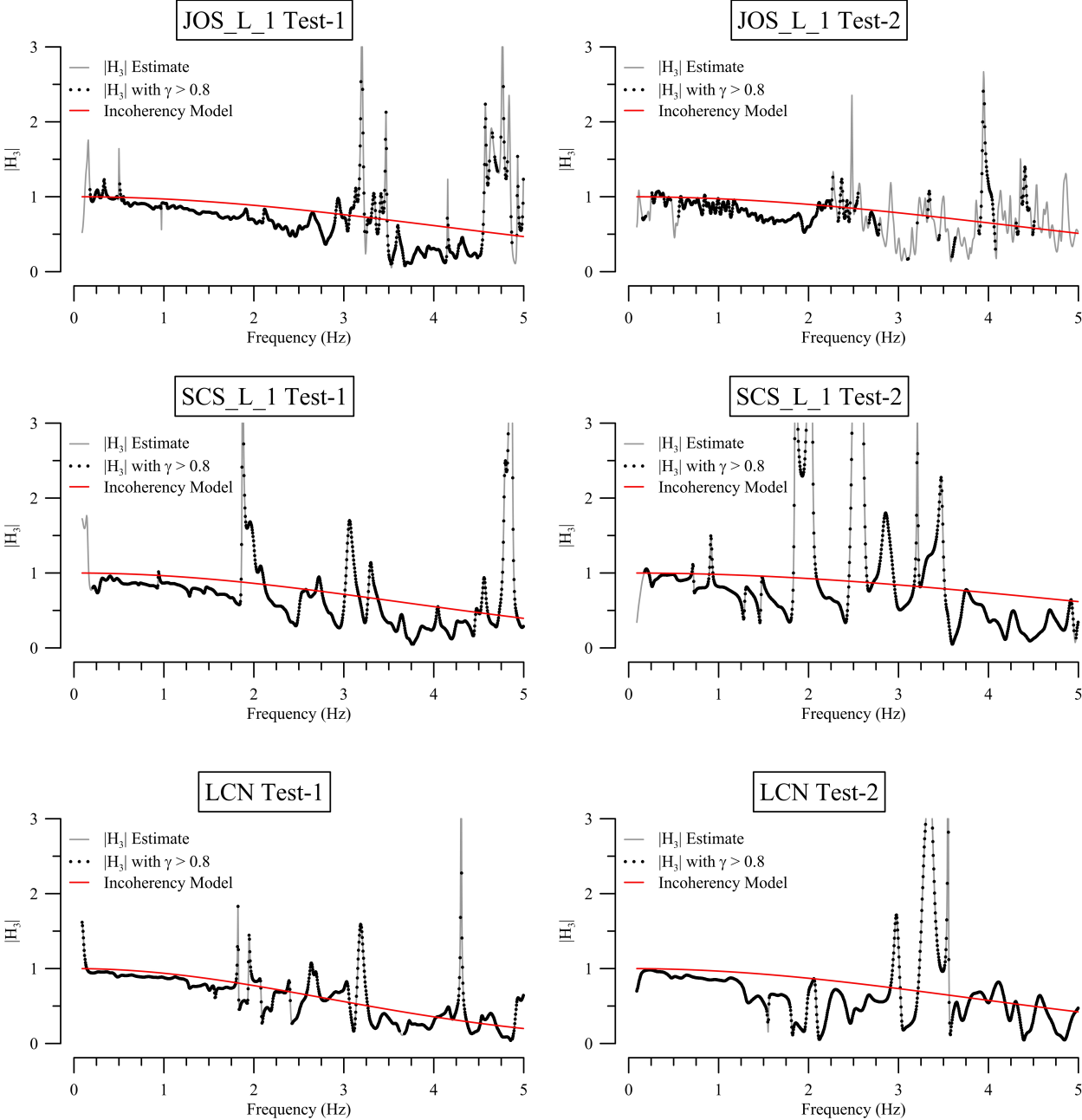


Figure 4.10: Experimental transmissibility functions (basement / free-field surface) calculated for the JOS_L_1, SCS_L_1, and LCN earthquake motions.

(e.g., Oppenheim and Schafer 2009). Two parameters are needed to define a Kaiser window: (1) the window length, and (2) the windowing parameter. The sensitivity of κ_a to the windowing parameter was investigated and found to be minor. For this reason, a value of 15.7 was used for the windowing parameter for this dissertation research to follow the work of Fenves and DesRoches (1994) and Kim and Stewart (2003).

The sensitivity of κ_a to the window length is more significant. As the window size decreases, the transmissibility functions become smoother. The effect of the window size on transmissibility functions is shown in Figure 4.11 for Test-1 and Figure 4.12 for Test-2. From this figure, it can be seen that the value of κ_a can vary significantly as a function of the window length employed. In addition, the nonlinear regression used to estimate κ_a can be unstable for some window lengths, and stable for others for the same earthquake motion.

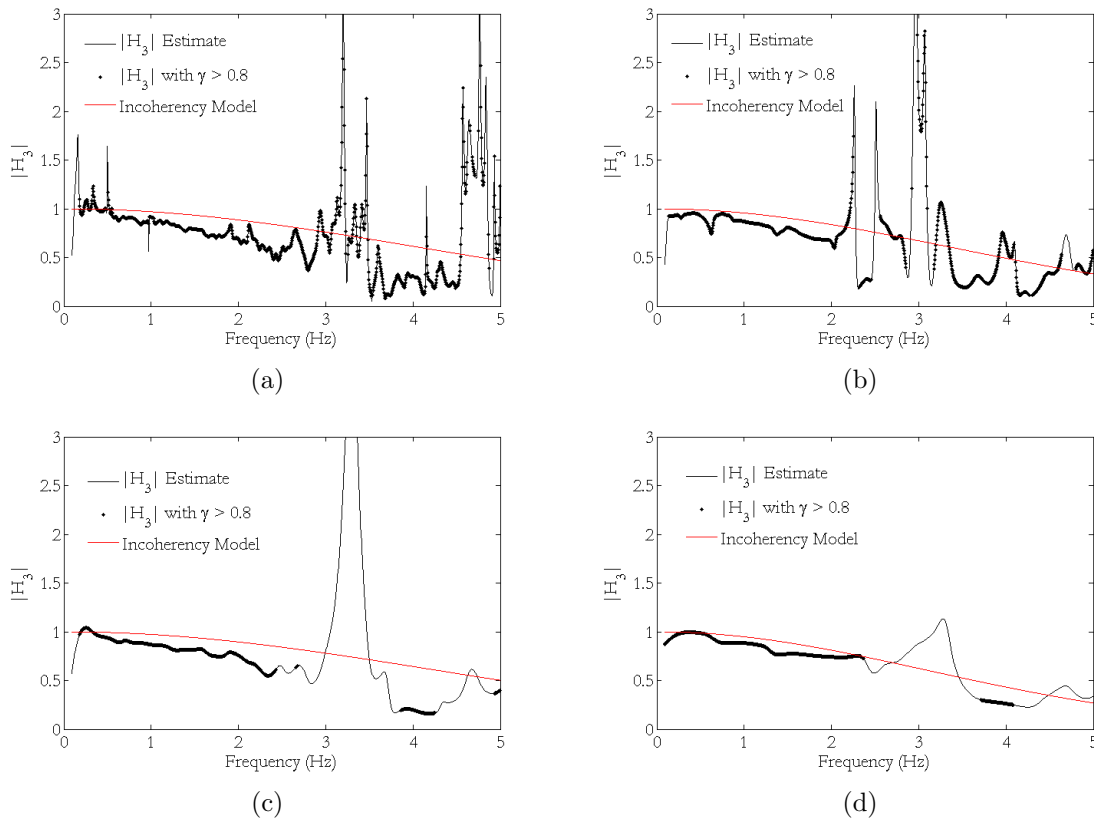


Figure 4.11: Transmissibility functions (basement / free-field surface) estimated during Test-1 for the JOS_L_1 motion for different window sizes: (a) 4096, (b) 2048, (c) 1024, and (d) 512.

For the purposes of comparing κ_a values between Test-1 and Test-2, a window length of 4096 points was considered. This window length was chosen based on careful examination of the transmissibility functions. It was decided that this window length filtered the transmissibility

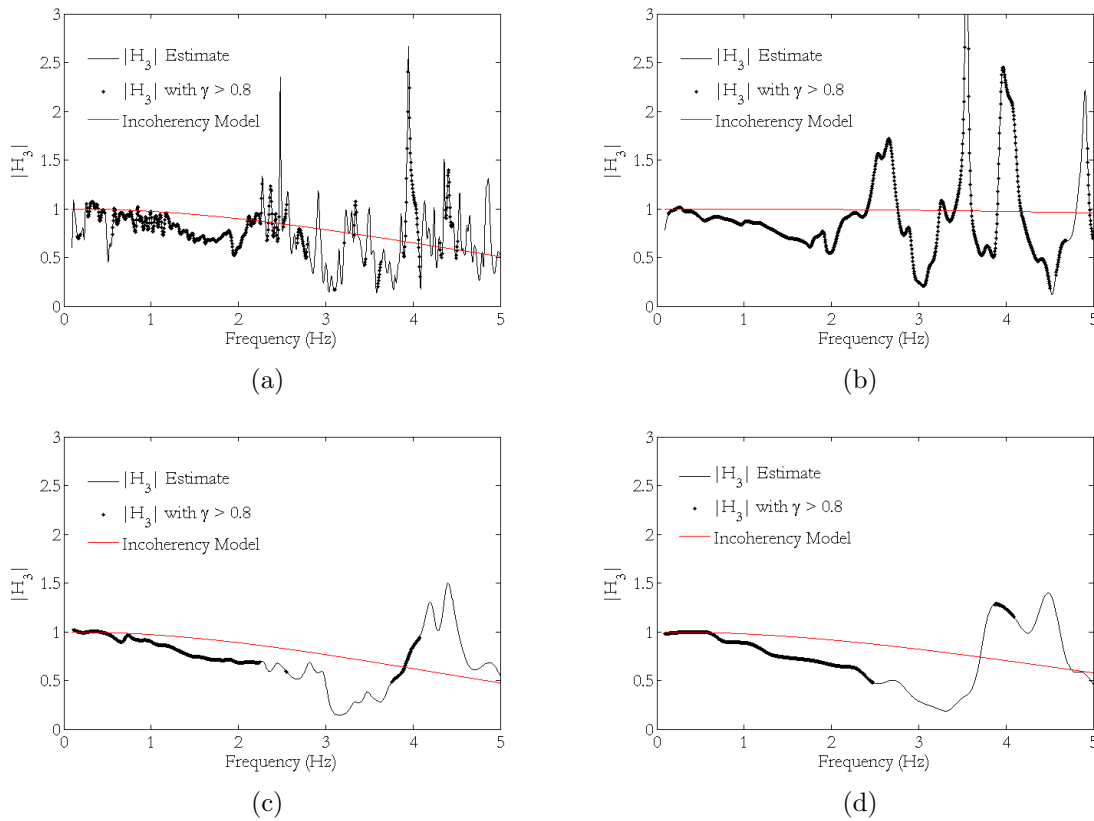


Figure 4.12: Transmissibility functions (basement / free-field surface) estimated during Test-2 for the JOS_L1 motion for different window sizes: (a) 4096, (b) 2048, (c) 1024, and (d) 512.

function well enough for the results to be meaningful, but not so much that important peaks and troughs were removed, shifted, or unrealistically altered. In addition, this window length is on the same order as those used by previous researchers (e.g. Fenves and DesRoches 1994; Kim and Stewart 2003). The κ_a values calculated using this window length are provided in Table 4.11 for earthquake motions recorded during Test-1 and Test-2.

By examining Table 4.11, it can be seen that the κ_a values calculated for the Test-1 earthquake motions are generally about twice as large as those calculated for the Test-2 earthquake motions. This implies that kinematic interaction effects are more important during Test-1 than Test-2. In other words, compared with Test-2, the earthquake motions recorded at the foundation-level of the basement during Test-1 differed more than the surface free-field ground motions recorded during Test-1. This further implies that SSSI may decrease the effects of base slab averaging, and more focused numerical and physical modeling are needed to fully understand it. A possible explanation is that the adjacent MS1F_SF80 structure during Test-2 is adding vibrational energy to the soil (i.e., inertial interaction is occurring),

Table 4.11: Apparent incoherency factors estimated for Test-1 and Test-2

Test-1 Motions	Apparent Incoherency, κ_a	Test-2 Motions	Apparent Incoherency, κ_a
JOS_L_1	0.22	JOS_L_1	0.13
TCU_L	0.29	TCU_L_1	0.10
RRS	0.35	RRS_1	—
PTS	0.25	PTS_1	0.12
SCS_L_1	0.25	SCS_L_1	0.11
LCN	0.32	LCN_1	0.15
JOS_L_2	0.22	JOS_L_2	0.06
SCS_L_2	0.27	TCU_L_2	0.04
WVC_L	0.28	RRS_2	—
SCS_H	0.29	PTS_2	0.08
JOS_H	0.26	SCS_L_2	0.12
WPLL	0.22	LCN_2	0.08
JOS_L_3	0.20	JOS_L_3	0.07
WPLH	0.27	WVC_L	0.16
PRI	0.26	SCS_H	0.10
TCU_H	0.34	JOS_H	0.16
WVC_H	0.22	WPLH	0.15
		PRI	0.13
		TCU_H	0.18
		WVC_H	0.16
		JOS_L_4	—

and some of this vibrational energy is being “picked up” by the adjacent basement wall. The vibrational energy radiating from the MS1F_SF80 structure propagates through the basement walls and eventually boosts the high frequency content of the earthquake motions recorded at the foundation-level on the basement slab. This explanation may be more likely given that the basement used for Test-1 and Test-2 was constructed from aluminum. Seismic waves attenuate less in a solid metal compared to more typical construction materials, like reinforced concrete. For this reason, the difference between the κ_a values recorded during Test-1 and Test-2 may be exaggerated.

Another possible difference that has been investigated is the difference between $|\mathbf{r}_1 - \mathbf{r}_2|$ used to calculate the transmissibility functions during Test-1 and Test-2. Specifically, $|\mathbf{r}_1 - \mathbf{r}_2|$ is 25.0 m for Test-1 and 39.3 m for Test-2. Examining Equation 2.4, it can be seen that as $|\mathbf{r}_1 - \mathbf{r}_2|$ increases, the values of Γ decrease across the frequency range. Accordingly, as $|\mathbf{r}_1 - \mathbf{r}_2|$ increases, kinematic interaction effects become more important. Ideally, this distance would have been the same for both tests, but realistically, the location of the free-field changes

with each test because of the building arrangement. More numerical modeling is needed to understand the importance of this distance on the results.

4.3.2 Seismic footing response

Previous researchers have used the centrifuge as a tool for understanding SFSI (e.g. Gajan et al. 2005; Chang et al. 2006). The centrifuge is an advantageous tool to use for this type of research, because it allows the researcher to model the soil, foundations, and structures simultaneously.

During Test-1 and Test-2, the footings of the MS1F_SF80 structure were instrumented with vertical and horizontal accelerometers as well as vertical displacement gauges. Data from the accelerometers allow for the measurement of the dynamic rocking, sliding, settlement and uplift of the footings during the earthquake motions. Data from the vertical displacement gauges allow for the measurement of permanent footing displacement.

Using measurements from these instruments, insights can be made into SFSI of a three-dimensional moment-resisting frame structure that responds inelastically to strong earthquake motions. In addition, important insights into SSSI can be made. In this section, settlement, uplift, and sliding are reported as the difference between the total footing displacement and the ground surface free-field displacements. Any displacements calculated solely from integrated acceleration measurements are referred to as transient measurements.

The MS1F_SF80 structure has four individual spread footings, which is a unique aspect of this research. To the author's knowledge, there has not been any previous work performed to characterize the SFSI response of individual spread footing founding three-dimensional frame structures (i.e., superstructures with two parallel frames). Within this section, two footings with one frame bay are described: the northwest footing, referred to herein as the North Footing, and the southwest footing, referred to herein as the South Footing. During Test-2, the North Footing is considered *free* and the South Footing is considered *restrained*. This nomenclature refers to the footings' boundary conditions relative to the basement, with the footings located directly adjacent to the basement being considered restrained. Accordingly, in Test-1, both the North and South Footings are free. Examination of the cumulative settlement data, which is presented in this section, justifies the use of the free and restrained descriptors.

Figure 4.13 shows the transient vertical displacement time-series for the SCS_L_1 and LCN motions recorded during Test-1 and the corresponding SCS_L_1 and LCN_1 motions recorded during Test-2 for the North Footing and South Footing. For these results, as well as for the peak value plots presented later in this section, positive displacement refers to settlement and negative displacement refers to uplift. Settlement time-series from all the motions were examined, and the motions shown in Figure 4.13 were chosen as representative of the entire suite of motions. The chosen motions were performed during Test-1 and Test-2 when the MS1F_SF80 structure had the same configuration (see Table 4.3). It was desirable to also include the JOS_L_1 motion for consistency, but unfortunately, all the footing accelerometers

malfunctioned during this motion during Test-1, which prevents its inclusion.

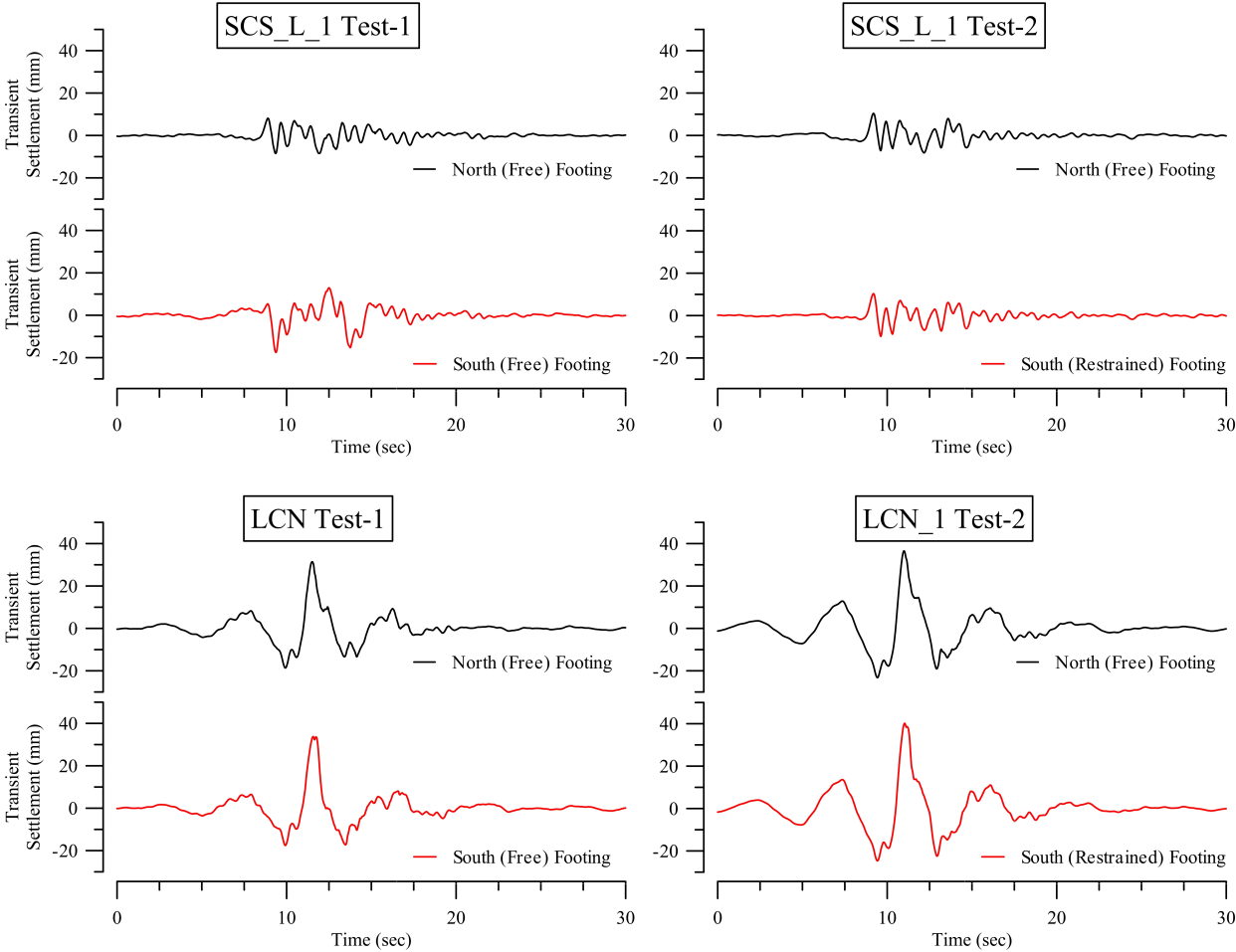


Figure 4.13: Total transient vertical displacement-time series for the SCS_L1 and LCN motions for Test-1 (left) and the SCS_L1 and LCN1 motions for Test-2 (right). All of the footing accelerometers malfunctioned during the JOS_L1 motion recorded in Test-1, which is why these measurements are not shown.

Examining Figure 4.13 yields several insights. First, examining the North Footing settlement time-series recorded during Test-1 and Test-2 for both motions reveals that they are similar in shape; however, there is a noticeable difference in frequency content between the recordings. This could be a manifestation of SSSI. The adjacent MS3F_B structure “puts” energy into the soil, and some of this energy is “picked up” by the MS1F_SF80 structure. This response is also seen when examining the South Footing settlement time-series. Thus, inertial interaction is occurring within the MS3F_B SFS system, and the resulting energy that is transferred to the soil is subsequently picked up by the adjacent MS1F_SF80 structure. This observation of *inertial SSSI* is important, because it indicates that the properties of

adjacent SFS systems should be considered in some cases. If inertial interaction is important for one or both structures, then inertial SSSI can also be important. This observation drove the experimental design for Test-3, which is described in the next chapter.

Another insight gathered from examining Figure 4.13 is that there is a difference between the settlement and uplift recorded for each motion. To examine this difference, Figure 4.14 is plotted to show the free-field surface *PGV* versus peak transient vertical displacement for the North and South Footings for both tests.

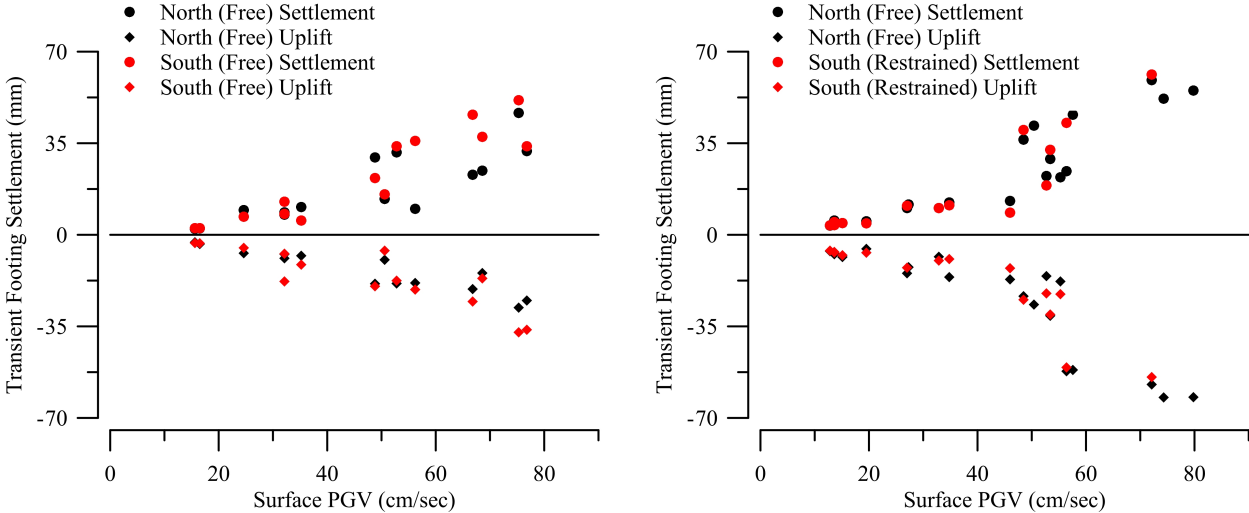


Figure 4.14: Peak transient settlement versus surface free-field *PGV* for (left) Test-1 and (right) Test-2.

Figure 4.14 shows the correlation between a ground motion intensity measure (*PGV*) and an engineering demand parameter (transient footing settlement and uplift). This step—linking a ground motion intensity measure (IM) with an engineering demand parameter (EDP)—is part of the Pacific Earthquake Engineering Research (PEER) Center’s framework for performance-based earthquake engineering (PBEE)(Deierlein et al. 2003). The goal of the PBEE framework is to estimate loss caused by earthquakes. The first step of this framework is to estimate a ground motion IM. Next, a response model is used to understand the system response, which is quantified in terms of an EDP. After this, the EDP is inputted into a damage model, and the physical damage to the system is estimated. Finally, the physical damage is related to the loss via a loss model. Kramer (2011) gives a thorough summary of the PEER PBEE framework and outlines some important examples.

In this study, a preliminary set of IMs (i.e., peak ground acceleration, peak ground velocity, Arias intensity, spectral acceleration at the fundamental period) were investigated. Specifically, the correlation between these IMs and the seismic footing response (i.e., settlement and sliding) was studied. From this preliminary study, it was found that the *PGV* was correlated most robustly with the footing responses being examined. This preliminary correlation

research needs to be expanded to include more IMs and needs to be performed using more robust statistical procedures. This is left for future research.

Several trends can be observed from examining the Test-1 data in Figure 4.14 (i.e., the left plot). This figure shows that in general, beyond a “break-point” PGV value, both settlement and uplift increase linearly as a function of PGV ; that is, as the PGV increases, the settlement and uplift also increase. This figure also shows that in general, settlement and uplift are on the same order of magnitude, with settlement being slightly larger than uplift as a function of PGV . Finally, this figure shows that for the lower-intensity motions (i.e., $PGV < 50$ cm/sec), the settlement and uplift of the North Footing and South Footing are roughly equal. For the higher-intensity motions (i.e., $PGV > 50$ cm/sec), however, the South Footing settlement is generally larger than the North Footing settlement. The uplift is roughly equal for both Footings, other than for the most intense motion near a PGV of 80 cm/sec. A possible explanation for this observation is motion directionality. Horizontal accelerations at the roof level manifest themselves as oscillating vertical loads on the footing, which leads to vertical displacement of the footings. During the more intense motions, which occur later in the testing sequence, there could be residual tilt to the structures that results in lower axial load capacity of the footings on one side. In other words, the structural response becomes more asymmetric as the structure tilts. This asymmetric response exhibits the complexity of the seismic response of three-dimensional inelastic frame structures founded on spread footings.

The right side of Figure 4.14 shows the Test-2 data. Trends similar to those observed from the Test-1 data also occur in the Test-2 data. One noticeable difference is the response of the footings to the higher-intensity earthquake motions (i.e., $PGV > 50$ cm/sec) during Test-2. The relationship between transient footing displacement and PGV appears to be linear, however, it has a much steeper slope after a PGV value of about 50 cm/sec. A PGV of 50 cm/sec, in this case, acts as a “break-point PGV .” Below this break-point value, transient settlement and uplift increase only slightly for increasing values of PGV . Beyond this break-point, however, transient settlement and uplift increase significantly with increasing PGV . This break-point PGV concept needs to be explored more thoroughly via numerical modeling. A possible explanation for its existence is that the MS3F_B structure has a “response threshold.” Below this response threshold, inertial interaction is relatively unimportant, and so energy from the MS3F_B structure is not being “pumped into” the adjacent MS1F_SF80 structure. Above this response threshold, however, inertial interaction becomes important. Accordingly, above this response threshold, SSSI becomes important. The concept of a break-point PGV and correspondingly, a hypothetical response threshold, will likely be important concepts for understanding SSSI.

Finally, from both Test-1 and Test-2 data in Figure 4.14, it can be observed that the uplifts are generally the same for both footings for both tests, as noted above. This observation indicates that uplift is insensitive to the presence of an adjacent building. All observations made from the data shown in Figure 4.14 should be validated for other footing-soil configurations.

Figure 4.15 shows the cumulative settlement of the North Footing versus the South

Footings at the end of each earthquake motion. The cumulative settlement is calculated by adding the total permanent vertical displacement for each motion cumulatively. Two linear potentiometers were mounted on each footing such that the residual rotation of each footing could be determined. The permanent vertical displacement was obtained by averaging the two measurements on each footing and subtracting the settlement of the ground surface so that the results from Test-1 and Test-2 could be prepared. For Test-1, a linear trend through the points is close to the one-to-one line, which indicates that the North Footing and the South Footing settle permanently by similar amounts during each earthquake motion. This type of response is expected for a symmetrical structure.

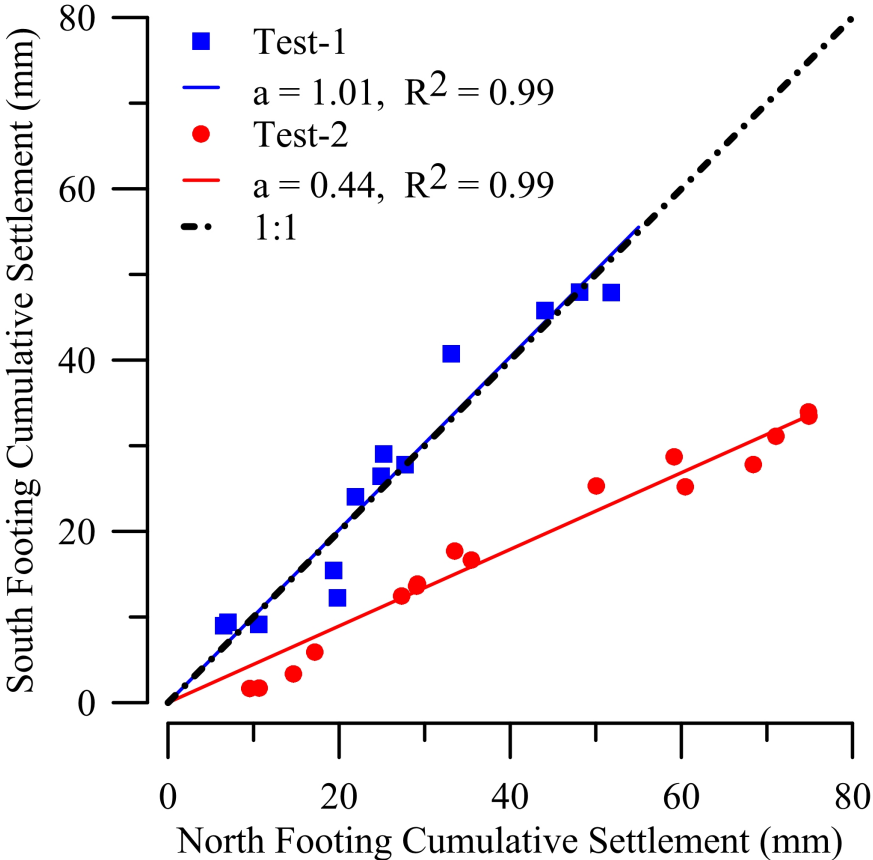


Figure 4.15: Cumulative settlement summary plot comparing the North Footing and the South Footing for Test-1 and Test-2.

For Test-2, a linear trend reveals that the free North Footing cumulative settlements are approximately 2.3 times larger than those of the restrained South Footing for each earthquake motion. This result is a manifestation of SSSI. The restrained South Footing displaces less than the free North Footing during Test-2 because of the influence of the adjacent basement structure. This difference is especially important for very intense shaking, where the difference can be significant enough for racking and distortion of the structure to be an issue. Figure 4.16 shows the initial and final locations of the free North Footing and the restrained South Footing. From this figure, it can be seen that the footings have settled differentially after all the earthquake motions. Additionally, Figure 4.16 shows that the free North Footing all slides and rotates more than the restrained South Footing.

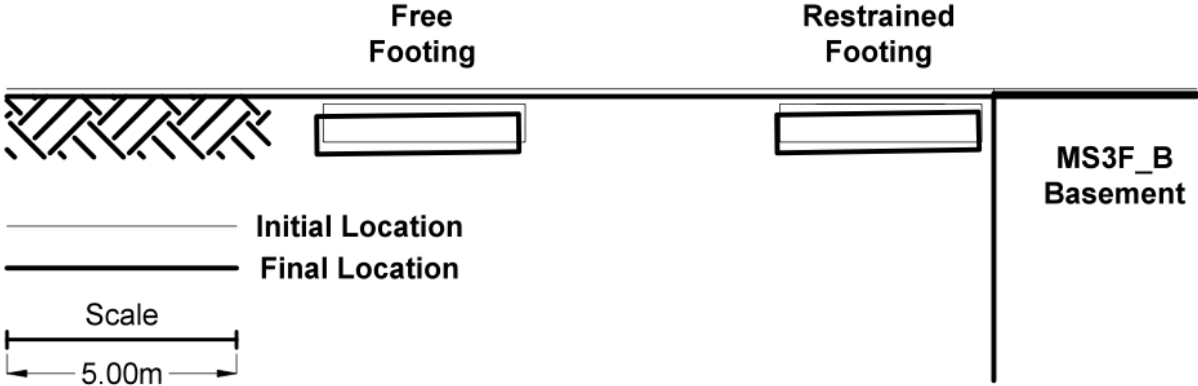


Figure 4.16: Initial and final footing locations measured during Test-2.

Figures 4.15 and 4.16 can further be explained by examining the moment-rotation relationships of the columns. The moment-rotation relationships were calculated using data from the strain gauges located on the column fuses above the North and South Footings. The moment-rotation relationships recorded during the SCS_H motion during Test-1 is shown in Figure 4.17. For the free North Footing, the moment-rotation relationship is typical. The column softens during the earthquake motion, and because the underlying footing is allowed to rotate freely, the response is symmetrical. For the restrained South Footing, however, the moment-rotation relationship shows an anomaly. In this case, the underlying footing is not allowed to freely rotate towards the adjacent basement. As a result, the moment-rotation relationship is asymmetrical. More specifically, higher moments result in the column supported by the restrained South Footing when the footing is rotating towards the basement. This is a potentially detrimental manifestation of SSSI. If these increased column moments are not accounted for in the seismic design, then unpredicted damage to the superstructure can occur.

Figure 4.18 shows the free-field surface *PGV* versus permanent settlement for the North Footing and the South Footing for Test-1 and Test-2. Examining the Test-1 data, especially

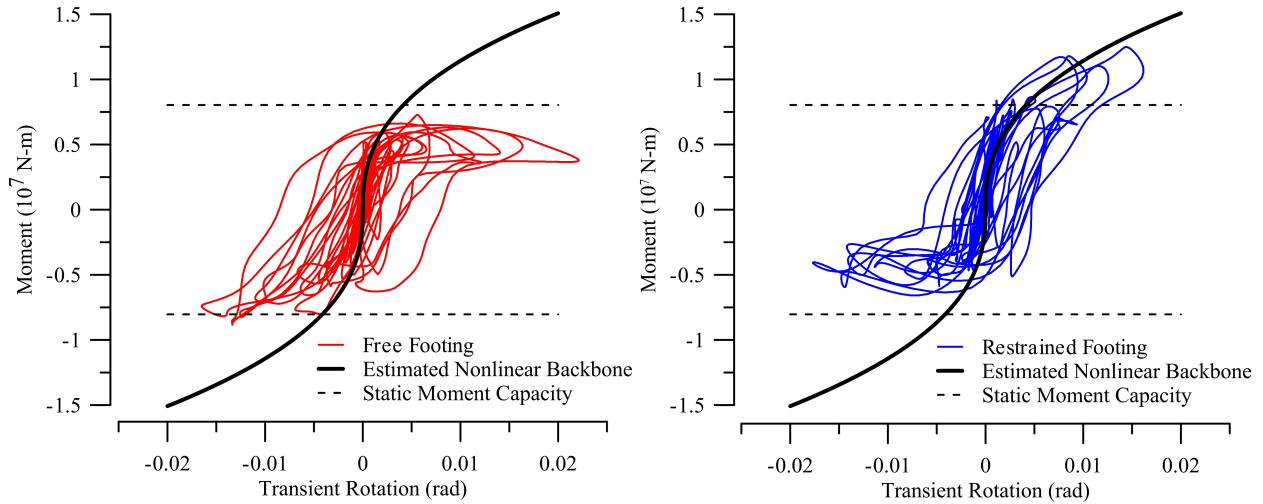


Figure 4.17: Moment-rotation relationships for (left) the free North Footing and (right) the restrained South Footing recorded during Test-2 for the SCS_H motion. After Trombetta et al. (forthcoming).

for the higher-intensity earthquake motions, it can be seen that there is not a clear trend for either the North Footing or the South Footing. That is, for some earthquake motions, the North Footing settles more than the South Footing, and vice-versa. Exponential trend lines are plotted on this figures, and these yield the regression equations $\ln(\rho) = 0.35PGV - 0.35$ and $\ln(\rho) = 0.025PGV - 0.04$ for the North Footing and the South Footing, respectively. For these regressed equations, ρ represents the permanent footing settlement. The coefficients of determination, R^2 , for these regressed equations are 0.46 and 0.28 for the North Footing and the South Footing, respectively. These low R^2 values indicate that the regressions poorly match the data.

Examining the Test-2 data, it can be seen that the free North Footing permanently settles more than the restrained South Footing. This can be seen by inspecting the points on the chart individually. This corroborates the observations from Figure 4.16. Exponential trend lines are also plotted on this figure, and these yield the regression equations $\ln(\rho) = 0.079PGV - 3.14$ and $\ln(\rho) = 0.066PGV - 2.75$ for the North Footing and the South Footing, respectively. The R^2 values for these regressed equations are 0.65 and 0.53 for the North Footing and the South Footing, respectively. These low R^2 values indicate that the regressions poorly match the data.

Figure 4.18 also shows evidence of a break-point PGV , which was also observed in Figure 4.14. Below this break-point PGV , which appears to be around 40 to 50 cm/sec (similar to Figure 4.14), the permanent settlement is nearly a linear function of PGV . Moreover, the slope of the linear fit is gentle, indicating that for less intense earthquake motions, the movement of the footing is minimal. Above the break-point PGV , the permanent settlement increases nonlinearly with PGV , with displacement becoming very large for the more intense

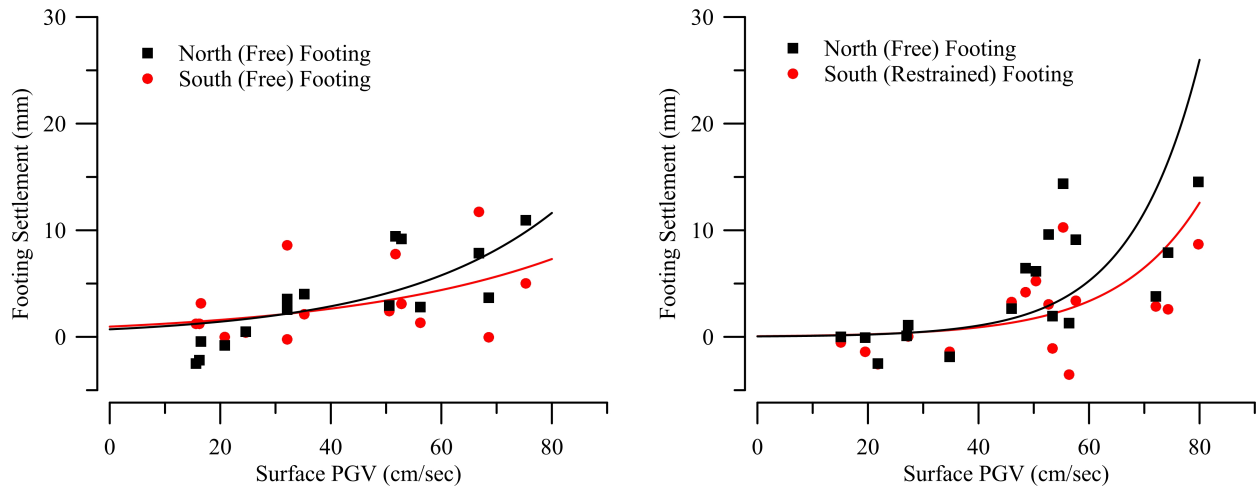


Figure 4.18: Permanent settlement versus surface free-field PGV for Test-1 (left) and Test-2 (right). The displacements of the reference frame (displacement rack) was removed from the data to make the comparisons equitable.

motions.

In addition to vertical displacement, horizontal displacement (i.e., sliding) is an important SFSI effect. This is especially true for spread footings not connected with grade beams, as the footings can slide in differing directions and accordingly place additional demands on the superstructure. This is exhibited in Figure 4.16. From this figures, it can be seen that the permanent sliding of the free North Footing is larger than the permanent sliding of the restrained South Footing during Test-2. This difference in sliding places extra demands on the superstructure, which may be unacceptable. Again, this is particularly important for progressive damage scenarios.

Figure 4.19 shows the transient horizontal displacement-time series for the SCS_L1 and LCN motions recorded during Test-1 and the corresponding SCS_L1 and LCN_1 motions recorded during Test-2. From this figure, it can be seen that there is a frequency-content difference between the horizontal displacement-time series recorded during Test-1 and Test-2, which was also observed in the transient vertical displacement-time series seen in Figure 4.13. This observation is also likely a manifestation of SSSI. The adjacent MS3F_B structure is likely modifying the frequency content of the MS1F_SF80 footings during Test-2.

Figure 4.20 shows the peak transient horizontal displacement versus the PGV recorded at the surface in the free-field for the North Footing and the South Footing for Test-1 and Test-2. This figure shows that the transient horizontal displacement is roughly the same for the North Footing and the South Footing during Test-1. This result indicates that the footings are sliding roughly equal amounts, and thus, extra demands are not being placed on the superstructure. The Test-2 data, which is shown on the right side of Figure 4.20, show that the free North Footing slides more than the restrained South Footing during strong

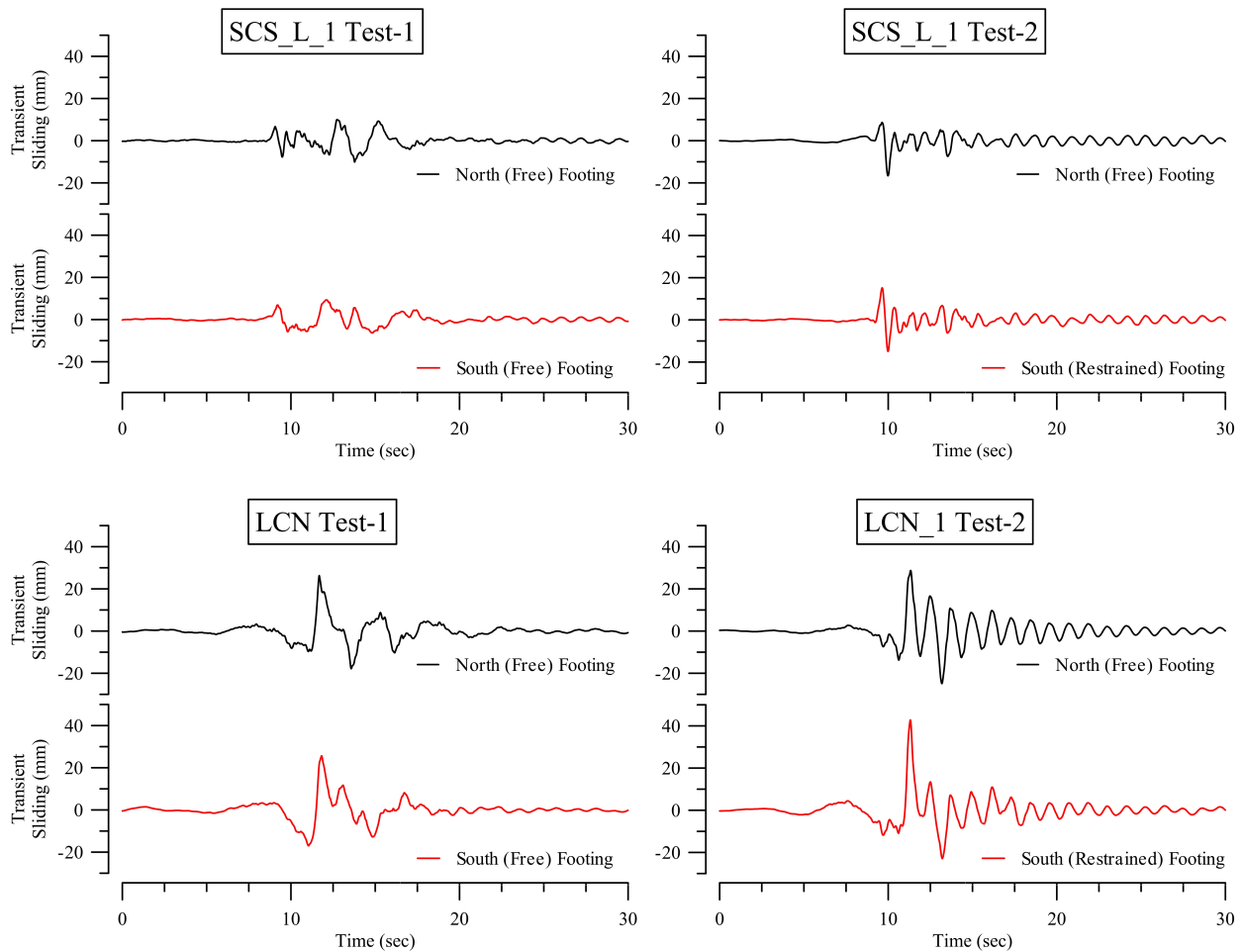


Figure 4.19: Transient horizontal displacement-time series recorded during Test-1 (left) and Test-2 (right) for the SCS_L_1, LCN and LCN_1 motions for the North and South Footings.

shaking. This is especially true for the higher-intensity ($PGV > 60$ cm/sec) motions. Thus, the two footings slide by different amounts during the earthquake motions. This can put extra demands on the superstructure, and is a potentially detrimental effect of SSSI.

Figure 4.20 contains exponential trendlines. These trendlines yield the regression equations $\ln(\rho) = 0.033PGV - 4.61$ and $\ln(\rho) = 0.036PGV - 4.31$ for motions recorded on the North Footing and the South Footing during Test-1, respectively. The values of R^2 for these regressions are 0.51 and 0.56 for the North Footing and the South Footing, respectively. The Test-1 data indicate that the North Footing and the South Footing slide by roughly similar amounts for earthquake motions of varying intensities. There are, however, some outliers, which cause the R^2 values to be low. The Test-2 regression equations are $\ln(\rho) = 0.050PGV - 2.57$ and $\ln(\rho) = 0.052PGV - 2.28$ for the North Footing and the South Footing, respectively. The R^2 values for these regressed lines are 0.92 and 0.93 for the North Footing

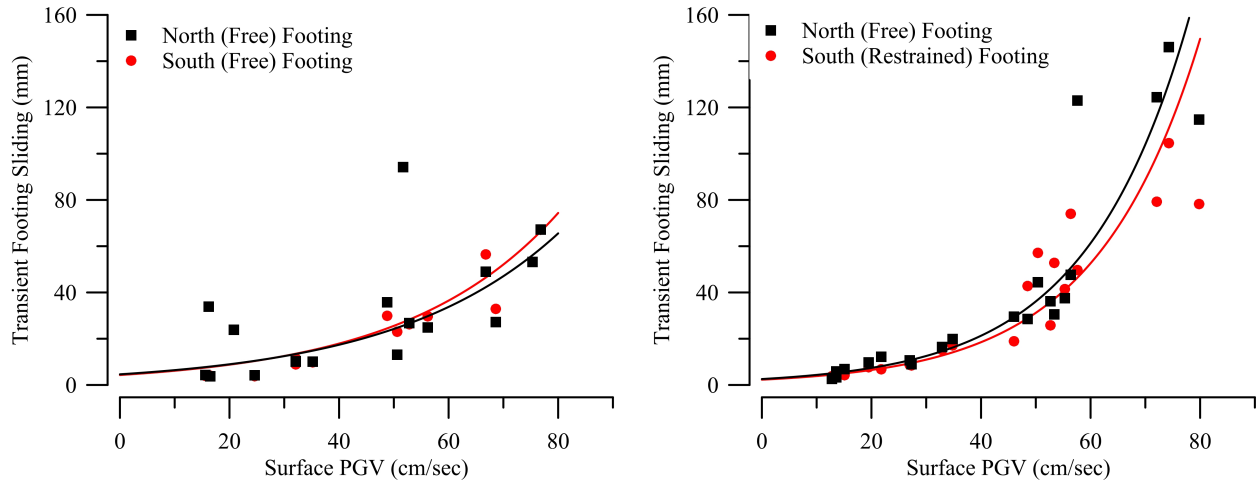


Figure 4.20: Transient horizontal footing displacement versus surface free-field PGV for Test-1 (left) and Test-2 (right).

and the South Footing, respectively. The R^2 values obtained for the Test-2 regressions indicate that they match the recorded data well. The Test-2 data indicate that the restrained South Footing slides less than the free North Footing, which has already been observed in Figure 4.16.

4.4 Summary of findings

4.4.1 Kinematic interaction

Kinematic interaction can be described analytically in the frequency domain by employing transmissibility functions, which are frequency-domain ratios of spectral density functions. Further, an analytical functional form can be fit to the transmissibility functions, and this yields an incoherency parameter, κ_a . κ_a is a proxy for kinematic interaction; as its value increases, kinematic interaction becomes more important.

The values of κ_a are sensitive to the frequency range over which the transmissibility functions are calculated as well as the window length (i.e., filtering parameters). The frequency range and window length need to be selected on a case-specific basis. This adds a layer of subjectivity to this analysis, which must be accounted for when interpreting the results. For selecting the frequency range, it is suggested that the frequency range of the problem of interest be considered. A frequency range of 0.1 to 5 Hz was considered for this research, which encapsulates the fundamental frequencies of the structural models and their higher modes as well as the fundamental frequency of the soil model. Additionally, a high-coherency threshold should be defined, and only points above this threshold should be considered when determining κ_a . A high-coherency threshold of 0.8 was used for this

research, which follows previous work (e.g., Kim and Stewart 2003). A higher or lower value can be used, depending on the case being studied. The window length should be selected after examining different lengths and interpreting the results. For this research, a length of 4096 was used, because this was determined to be a length that did not filter the results too aggressively, but filtered enough to remove the most speculative data.

There is some evidence SSSI affects kinematic interaction. Based on preliminary results presented in this dissertation, it appears that as a structure puts energy back into the surrounding soil via inertial interaction during an earthquake that this energy is subsequently picked up by adjacent basement structures. This energy introduces higher frequency shaking to the adjacent basement, and as a result, masks kinematic interaction. It is possible that in urban areas, enough inertial interaction is occurring and enough of the energy is picked up by embedded basements that kinematic interaction is offset. If this result holds, then ignoring kinematic interaction effects in densely populated, seismically active areas—which is currently the state-of-practice—may not be a bad assumption. More work is needed to verify this finding.

4.4.2 Seismic footing response

When examining the seismic footing response, the first major observation is that different footings supporting the same superstructure can respond differently during earthquakes. This is important mainly because the difference in response leads to an asymmetric superstructure response, which can lead to torsion, racking and distortion. This can be important for a structure founded on shallowly embedded spread footings located at the corner of a city block. In this case, there will be one free footing, two footings restrained on one edge, and one footing restrained on two edges. It can be expected, after examining the results in this chapter, that each of these footings will respond differently during an earthquake. Assuming that similar soil conditions exist under each of the footings, it can be expected that the footing restrained on two edges will rock, slide and settle less than the footings restrained on one edges, which will in turn rock, slide and settle less than the free footing. This can cause buildings located at the corners of city blocks to accumulate more damage during earthquakes. This observation has been made following earthquakes in urban areas; for example, in San Luis Obispo, California following the 2003 San Simeon earthquake (e.g. Hardenbeck et al. 2004).

This finding, which is backed by case history observation, has potential implications for engineering design. Specifically, corner buildings may need to be designed differently than interior buildings to withstand asymmetric seismic demands. Based on preliminary results from this research, this is particularly important when smaller buildings founded on shallowly embedded spread footings are the corner building, and are adjacent to larger buildings with deeper foundations. More numerical modeling work is needed to fully understand this result.

The asymmetric superstructure response is also important when considering progressive damage scenarios. A typical progressive damage scenario is when a large mainshock is followed

by significant aftershocks. The 11 March 2011 M9.0 Great East Japan Earthquake is an example of this type of progressive damage scenario. Another progressive damage scenario is when multiple mainshocks occur near the same site. A recent example of this is the 4 September 2010 M7.1 Canterbury, New Zealand earthquake followed by the 22 February 2011 M6.3 Christchurch, New Zealand earthquake. For buildings located in regions where multiple seismic events are possible, such as the San Francisco Bay Area, this is an important consideration. The subsequent events after the first event can exacerbate the asymmetry of the superstructure. This can lead to extra demands, which are realized in the structural members and connections. Accordingly, progressive damage needs to be considered when designing buildings in seismically active areas.

Another major finding is embodied within Figure 4.17. Specifically, the columns of the MS1F_SF80 structure adjacent to the MS3F_B structure experience higher demands than the non-adjacent columns. This extra demand arises because the footings supporting the adjacent columns are not allowed to rotate fully. The restrained rotation is caused by the presence of the adjacent basement. Depending on the structural properties, the configuration of the city block, and the characteristics of the earthquake motion, the extra demands experienced by the adjacent columns could lead to unacceptable seismic performance. This is a potentially detrimental manifestation of SSSI.

Performance-based earthquake engineering (PBEE) is gaining popularity in the earthquake engineering community. A key step for PBEE is linking ground motion intensity measures with engineering demand parameters. Using this approach, a model can be used to predict the ground motion intensity measure at the site of interest, and this intensity measure can be used to predict seismic performance of a building. For example, the NGA relationships (Power et al. 2008) can be used to predict the peak ground acceleration (PGA), and this PGA can be used to predict the interstory drift of a building. In this dissertation research, a preliminary correlation study was performed, and it was found that the peak ground velocity, PGV , correlates most closely with settlement and sliding of footings. PGV is a useful intensity measure for many earthquake engineering problems. For instance, Newmark (1965) found that the seismic displacement of a rigid block is proportional to the square of PGV . As noted in Kramer (1996), the PGV is not as sensitive to the higher-frequency portion of the earthquake motion, and thus correlates better with intermediate-frequency types of problems. The structure models used for Test-1 and Test-2 have natural periods in the range of approximately 1 to 3 sec, which is an “intermediate-frequency” range. Another reason that PGV may correlate well with the displacement data is that many of the motions performed during the centrifuge tests, and especially the higher-intensity motions, are forward-directivity earthquake motions. The correlation between PGV and settlement and sliding data is preliminary. Some correlations yield low R^2 values, which indicates that other ground motion intensity measures may correlate better than PGV . This is the subject of future work.

An overarching conclusion, reached by examining the data from both Test-1 and Test-2, is that seismic footing response is both erratic and inconsistent. The erratic and inconsistent response could be caused by (1) complex wave reflections that occur from the centrifuge

container boundaries; (2) SSSI; (3) nonuniform loading of the frame structure; or (4) other complex phenomenon. In the end, the response will most likely be explained by all of these factors. The data recorded during Test-1 and Test-2 are complicated, and more work is needed to quantify observations from the data to draw more concrete conclusions.

Chapter 5

Centrifuge Test-3

5.1 Introduction

In Test-1 and Test-2, it was desirable to use structural models that represented prototypical structures found in Los Angeles when subjected to 55 g of centrifugal acceleration. A careful design process was employed to ensure that this design objective was met, as described in Chapter 4. During Test-3, this design objective was relaxed. Instead, the structural models were designed to test specific scientific objectives. In particular, it was desired to design a set of structures that would maximize SFSI effects. This was accomplished using a threefold strategy: (1) the fundamental periods of all of the structural models were matched as closely as possible with each other and with the assumed site period of the soil model (i.e., 0.6 sec); (2) dimensionless parameters that are correlated with SFSI were optimized; and (3) a transmitter-receiver pair of structural models was specified. In this case, a transmitter structure refers to a structure that “pumps” seismic energy into the surrounding soil; contrastingly, a receiver structure is a structure that receives seismic energy from the surrounding soil. In reality, every structure transmits and receives energy during an earthquake; however, the transmitter-receiver nomenclature is advantageous for explaining concepts within this chapter, which is why it is adopted. By maximizing inertial SFSI effects, inertial SSSI effects would also be maximized, allowing the research team to “see” SSSI effects more clearly in the data.

The Test-3 setup consisted of three structural models: two identical one-story frame structure models, and one two-story rocking shear wall model. One frame structure was placed in isolation within the container to act as a control structure, while a second frame structure was placed directly adjacent to the much larger, heavier rocking wall to create a transmitter-receiver relationship. The basic design of the Test-3 frame structures was similar to the design of the frame structures used for Test-1 and Test-2 (i.e., MS1F_SF80). However, the Test-3 frame structure featured shorter columns, lighter footings and modified fuse sections to meet the design goals outlined in the previous paragraph. In prototype

scale, the frame structures represented three-story special moment-resisting frame structures founded on spread footings. Likewise, in prototype scale, the rocking shear wall model represented a six-story shear wall founded on a large mat foundation.

Figure 5.1 shows a schematic of the Test-3 setup. On this schematic are labels for each of the model structures. The northernmost frame structure is referred to as a *control structure*, while the southernmost frame structure is referred to as a *receiver structure*. The rocking shear wall is referred to as a *transmitter structure*. This nomenclature is used throughout this chapter.

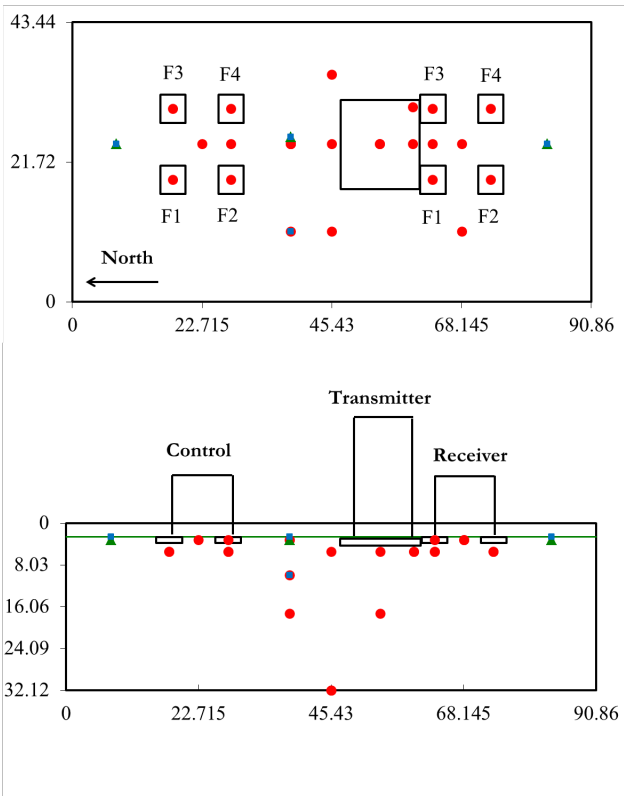


Figure 5.1: Schematic of Test-3 with important soil instrument locations; circles = horizontal accelerometers; triangles = vertical accelerometers; lines = displacement gauges. All measurements are in prototype scale units, meters.

The purpose of this chapter is to compare the seismic response of the receiver structure to the seismic response of the control structure. By comparing these responses, insights can be made into how SSSI affects the seismic response of structures. This chapter will focus on the seismic soil-foundation response, though necessary details concerning the superstructure response will also be discussed.

5.2 Experimental setup

The experimental setup of Test-3 closely follows the experimental setup of Test-1 and Test-2. For Test-3, dense, dry Nevada sand with a relative density of approximately 80% was also used. In addition, the types of instrumentation—accelerometers, displacement gauges, strain gauges and cameras—were the same. The reader should refer back to the “Experimental Setup” section of Chapter 4 for more information about the soil and instrumentation types. Moreover, the model construction process was the same for Test-3 as it was for Test-1 and Test-2; accordingly, the reader is referred to the “Model Construction” subsection of Chapter 4 for more information.

The structural models used during Test-3 and their configurations were different compared to Test-1 and Test-2. In addition, the ground motion plan was different. These differences are explained in the subsequent subsections.

5.2.1 Structural models

The design goal for the structural models used during Test-3 was made with consideration to the overarching scientific objective of the test; i.e., to exacerbate inertial SFSI and as a result, maximize the SSSI effects between the transmitter-receiver structures. As previously mentioned, this design goal was met by: (1) matching the fundamental periods of all three structural models with each other and to the site period; (2) optimizing dimensionless parameters correlated with inertial SFSI; and (3) creating a transmitter-receiver pair of structures. Each of these three design strategies are described in more detail below.

Fundamental period matching

The site period of the Nevada sand was first calculated by examining results from the previous centrifuge tests. Pseudo-acceleration response spectra were calculated at the base and the surface of the model using free-field accelerometers. The ratio of the response spectra was taken (surface to base), and the peak was identified. This peak was taken to represent the fundamental site period of the soil model. The site period changes as a function of the earthquake motion. In addition, the order that the earthquake motions were performed is also important. The soil model becomes stiffer as it is subjected to more earthquake motions, and accordingly, the site period decreases. To simplify the design process, it was desirable to have a single site period that best represented the entire testing sequence. Examining the results, it was found that the site period was approximately 0.6 sec.

The next step was to design the control and receiver structural models to have fundamental periods near 0.6 sec. At this stage, the decision was made for these control and receiver structural models to closely mimic the design of the MS1F_SF80 structural models used in Test-1 and Test-2. This decision was made because: (1) it was desirable to compare seismic

responses of structural models, and (2) the previous tests showed that this type of structural model could be successfully tested.

The finite element program OpenSees (<http://opensees.berkeley.edu>) was used during the design process. Within the OpenSees model, basic geometry and material properties were varied until a satisfactory *macro-level* design was achieved. The corresponding *micro-level* design, such as the details of the welds and moment connection, was performed separately.

The next step was to design the transmitter structure. The design goals for the transmitter structure included: (1) designing an elastic rocking wall that maximized inertial SFSI effects, (2) ensuring a prototype rocking period of 0.6 sec, and (3) ensuring a structure heavy enough to affect the seismic response of the adjacent receiver structure. An elastic rocking wall was specified because it is known that tall, slender, stiff structures maximize inertial SFSI effects (e.g., Stewart et al. 1999a). As with the control and receiver structures, OpenSees was used to complete the macro-level design, and the connection were designed separately. A challenging part of this design was selecting a shear modulus reduction ratio, G/G_{max} , for the soil underlying the rocking wall given an estimate of the earthquake-induced shear strains. Based on results from Test-1 and Test-2, a shear modulus reduction ratio of 40% was selected.

Optimizing dimensionless SFSI parameters

As discussed in the “Inertial Interaction” section of Chapter 2, there are certain dimensionless parameters that correlate well with inertial SFSI. Table 5.1 shows a list of the parameters used for this research project and definitions of the parameters. Additionally, the numerical ranges of these parameters needed for inertial SFSI to be important are noted in this table. In this table, ρ is the soil mass density, $M_{structure}$ is the total superstructure mass, M_{fdn} is the total foundation mass, D_f is the embedment depth of the foundation, \bar{r} is the effective foundation radius (translation), r_θ is the effective foundation rocking (rocking), and L is the foundation length in the direction of translation. The dimensionless parameters σ^{-1} , \bar{h}/r_θ , and δ were discussed in Chapter 2. D_f/\bar{r} is important to consider because as the embedment depth increases, and this ratio also increases, rocking of the structure is constrained, thus leading to a reduction of inertial interaction. Importantly, this ratio is also an important indicator of kinematic interaction. As this ratio increases, the kinematic interaction effects, and specifically embedment effects, become more important (Stewart et al. 1999a). As the ratios $M_{fdn}/M_{structure}$ and $L/(2\bar{h})$ decrease, the likelihood for rocking increases (Gajan and Kutter 2008). Thus, decreasing these ratios increases the likelihood that the transmitter structure will rock and transmit energy to the receiver structure.

Transmitter-receiver relationship

A transmitter is a structure that transmits energy into the surrounding soil during an earthquake. A good example of a transmitter type structure is a massive shear wall, which

Table 5.1: Target dimensionless parameters governing the design of the transmitter structure (Pitilakis et al. 2008)

Parameter	Definition	Optimizing Criteria
σ^{-1}	$\frac{\bar{h}}{V_s T}$	> 0.2
$\frac{\bar{h}}{r_\theta}$	—	> 0.1 and < 0.4
δ	$\frac{m}{\rho \pi \bar{r}^2 h}$	> 0.15
$\frac{D_f}{\bar{r}}$	—	< 0.25
$\frac{M_{fnd}}{M_{structure}}$	—	minimize
$\frac{L}{2h}$	—	minimize

can rock during intense earthquake shaking. A receiver is a structure that receives energy during an earthquake. All structures are receivers, as they inevitably receive energy from the surrounding soil and surrounding buildings during earthquakes. For the case of Test-3, the elastic rocking wall structure was designed as the transmitter and the smaller frame structure on spread footings was designed as the receiver. By tuning the fundamental periods of the transmitter and receiver structures with the site period, the transmitter-receiver relationship was enhanced.

Final structural model designs

In the end, there were competing interests for the structural model design. It was desirable for the structural models to share a common fundamental period, for dimensionless parameters indicating the importance of inertial SFSI (i.e., how much the period of the structure is expected to lengthen from the fixed-based case) to be maximized, and for a transmitter-receiver relationship to be established between two of the structural models. While these design goals are generally in line with one another, there were some tradeoffs that needed to be made. In addition, there were practical concerns. The structural models needed to be constructible, and they also needed to fit within the centrifuge container. It was decided that the first priority was matching the fundamental periods of the structural models with the site period of the soil. This design goal was given priority, because it was thought to be the design aspect that maximized interaction the most. The second priority was creating the transmitter-receiver relationship between two of the structural models. This was given priority, because it was an important component of meeting the Test-3 scientific objectives.

The third priority was optimizing the dimensionless SFSI parameters. Of the dimensionless SFSI parameters, the structure-to-soil stiffness ratio was given the highest priority, because previous researchers correlated this parameter most closely with period shift due to inertial SFSI (Stewart et al. 1999a).

The final designs of the structural models are presented in Figures 5.2 and 5.3 for the one-story frame structures (i.e., control structure and receiver structure) and the transmitter structure, respectively. Figure 5.4 shows pictures of these structural models.

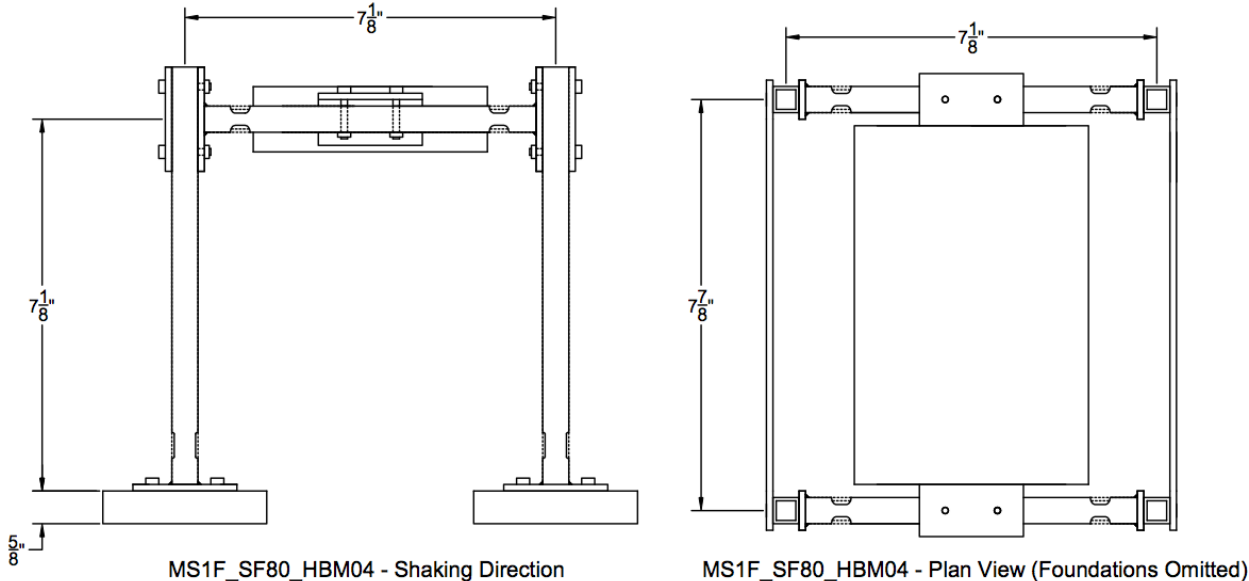


Figure 5.2: Schematic of the frame structures used in Test-3; i.e., the control and receiver structures

5.2.2 Instrumentation

During Test-3, accelerometers, displacement gauges, strain gauges and cameras were also employed to measure the important seismic response of the SFS systems. Descriptions of these instruments are given in the “Instrumentation” subsection of Chapter 4. The configuration of the instruments used during Test-3 is different, however. The configuration of the soil instrumentation is shown in Figure 5.1. More complete instrumentation tables are given in Mason et al. (2011c). In addition, these tables, along with known data limitations, are presented in Appendix A of this dissertation.

5.2.3 Earthquake motions plan

Test-3 utilized the same earthquake motions that were used during Test-1 and Test-2, but in a different order. Table 5.2 shows the earthquake motion order along with important

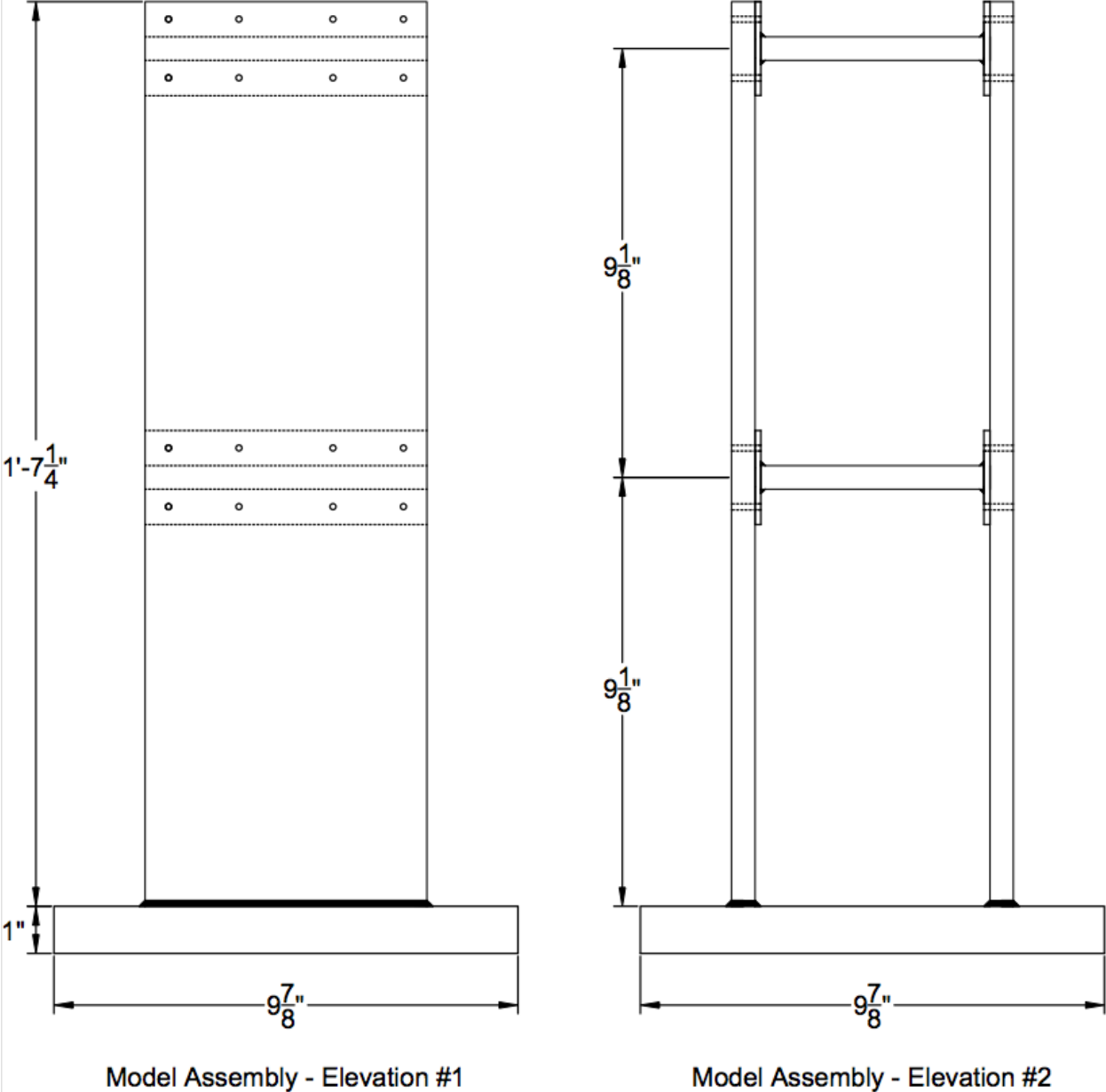


Figure 5.3: Schematic of the rigid rocking wall used in Test-3; i.e., the transmitter structure

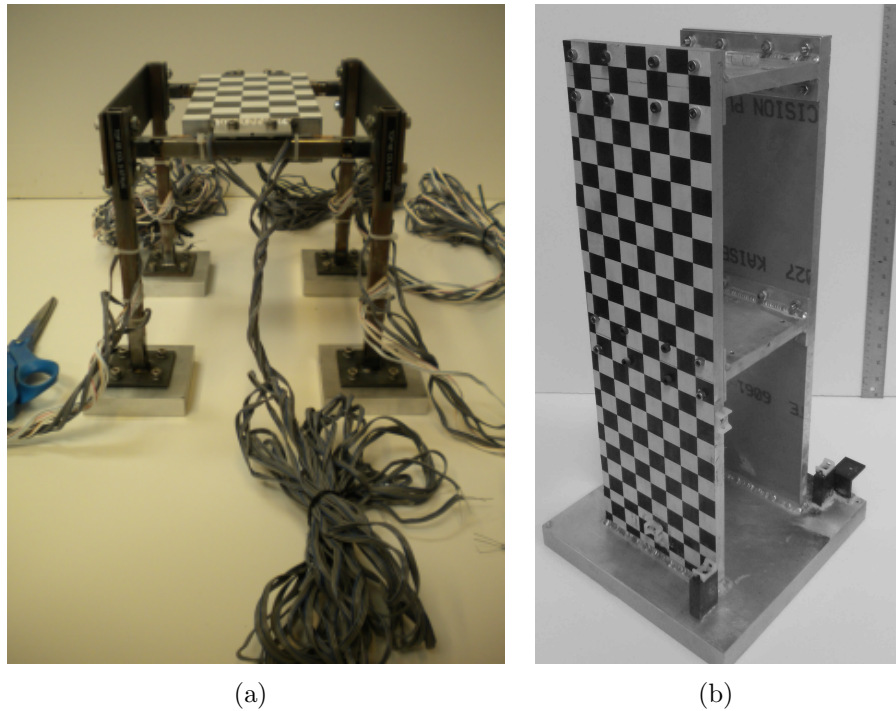


Figure 5.4: Pictures of the instrumented model buildings: (a) 3-story frame structure on spread footings (modeled as a 1-story structure), and (b) 6-story rocking shear wall on a large mat foundation (modeled as a 2-story rocking wall).

earthquake motion intensity measures recorded at the base, and Table 5.3 is the corresponding table for earthquake motions recorded in the free-field at the surface.

5.3 Experimental results

The goal of the experimental results section of the chapter is to present some of the results that have been deduced from the raw data. This chapter will focus on the seismic soil-foundation response observed during Test-3. However, important superstructure response quantities will be discussed when necessary.

For Test-3, nearly 200 channels of instruments were employed and 23 earthquake motions were performed. The collected data are available online at the NEES Hub and as an electronic appendix to this dissertation.

During Test-3, the footings of the control and receiver structures were instrumented with vertical and horizontal accelerometers as well as vertical displacement gauges. Data from the accelerometers allow for the measurement of the dynamic rocking, sliding, settlement, and uplift of the footings during the earthquake motions. Data from the vertical displacement

Table 5.2: Earthquake motions achieved during Test-3 at the base.

Motion	PGA (g)	PGV (cm/sec)	D_{5-95} (sec)	I_a (m/sec)	$Sa[T_s]^1$ (g)
JOS_L_1	0.06	9.5	19.2	0.07	0.21
JOS_L_2	0.06	9.4	19.3	0.07	0.19
TCU_L_1	0.13	11.0	20.4	0.29	0.21
JOS_L_3	0.07	9.3	20.0	0.08	0.19
JOS_L_4	0.06	9.2	19.7	0.07	0.18
TCU_L_2	0.12	11.0	20.1	0.31	0.20
RRS	0.40	34.0	5.1	0.51	0.65
PTS	0.10	15.0	10.3	0.17	0.31
SCS_L_1	0.15	15.5	7.4	0.21	0.48
LCN	0.26	44.8	6.6	0.36	0.45
WVC_L	0.24	32.1	7.5	0.65	0.55
SCS_H_1	0.58	58.0	14.8	4.82	1.86
PRI_1	0.65	42.3	6.7	3.05	1.02
JOS_L_5	0.06	8.6	20.2	0.06	0.16
JOS_L_6	0.06	8.9	20.0	0.07	0.18
JOS_H	0.36	34.7	20.7	2.82	1.29
WPI	0.42	46.2	4.5	0.56	0.49
TCU_H	0.33	20.9	20.1	1.94	0.45
WVC_H	0.35	49.7	10.3	1.75	0.65
SCS_H_2	0.60	54.1	15.4	4.74	1.70
PRI_2	0.63	42.8	6.8	3.24	1.00
SCS_H_3	0.63	57.7	15.4	5.03	1.77
JOS_L_7	0.07	9.1	20.6	0.07	0.18

¹ β = damping ratio = 5%; T_s = 0.6 sec

gauges allow for the measurement of permanent footing displacement.

Using the aforementioned measurements, insights into the seismic response of moment-resisting frame structures typically found in urban environments can be made. By comparing the seismic response of the control structure with the seismic response of the receiver structure, insights into structure-soil-structure interaction can also be made. In this chapter, settlement, uplift, and sliding are reported as the difference between the total footing displacement and the surface free-field displacements. Any displacements calculated solely from integrated acceleration measurements are referred to as transient displacements.

Table 5.3: Earthquake motions achieved during Test-3 at the surface in the free-field.

Motion	PGA (g)	PGV (cm/sec)	D_{5-95} (sec)	I_a (m/sec)	$Sa[T_s]^1$ (g)
JOS_L_1	0.13	16.9	20.5	0.43	0.51
JOS_L_2	0.13	16.7	20.5	0.45	0.52
TCU_L_1	0.22	20.6	21.1	1.49	0.49
JOS_L_3	0.15	17.5	20.5	0.57	0.59
JOS_L_4	0.14	15.9	20.6	0.45	0.51
TCU_L_2	0.22	20.3	21.8	1.54	0.50
RRS	0.34	52.8	6.2	1.28	0.70
PTS	0.21	25.8	10.5	0.92	0.82
SCS_L_1	0.25	30.5	8.3	1.07	0.91
LCN	0.30	50.4	7.3	0.93	0.69
WVC_L	0.37	47.2	7.5	2.08	0.97
SCS_H_1	0.62	67.7	19.7	10.80	2.43
PRI_1	0.84	58.5	7.2	7.07	1.66
JOS_L_5	0.15	15.8	20.3	0.42	0.53
JOS_L_6	0.15	15.9	20.4	0.44	0.53
JOS_H	0.44	49.5	21.6	10.40	2.10
WPI	0.40	60.0	5.1	1.33	0.68
TCU_H	0.42	35.3	23.1	7.08	0.91
WVC_H	0.46	67.6	11.4	4.91	1.26
SCS_H_2	0.66	70.2	19.3	13.03	2.60
PRI_2	0.87	64.8	7.2	8.08	1.76
SCS_H_3	0.73	75.4	19.0	14.28	2.82
JOS_L_7	0.18	17.0	20.9	0.51	0.59

¹ β = damping ratio = 5%; T_s = 0.6 sec

5.3.1 Transient vertical displacement response

Figures 5.5, 5.6, and 5.7 show the transient vertical displacement-time series for the JOS_L_4, LCN, and SCS_L_1 earthquake motions recorded during Test-3, respectively. These transient vertical displacement-time series are shown for each footing on both the control structure and the receiver structure. In these figures, some lines are flat, indicating that the sensor malfunctioned for that earthquake motion. For the receiver structure, Footings 1 and 3 are considered “restrained” because they are adjacent to the mat foundation of the transmitter structure. Accordingly, the restrained footings are plotted in red for clarity.

From Figure 5.5, it can be seen that the transient vertical displacement-time series of Footings 1 and 2 of the receiver structure are generally out-of-phase with one another. That is, as one footing settles, the other footing uplifts, and vice-versa. This indicates that during this earthquake motion, the receiver structure was rocking in the plane of shaking. Rocking

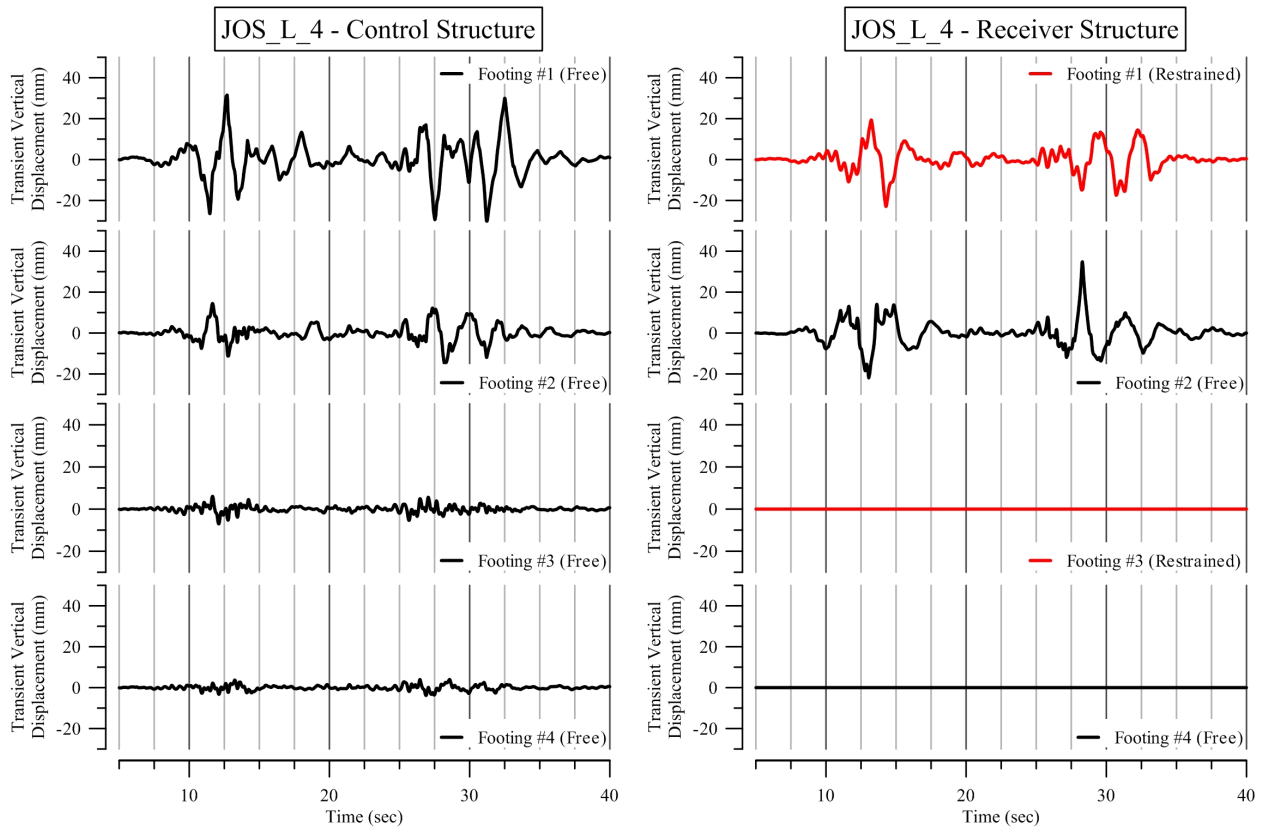


Figure 5.5: The transient vertical displacement recorded during the JOS_L_4 motion on all the footings on the control and receiver structures. Positive values indicate downward movement, and negative values indicate upward movement.

is also seen in the data recorded on the control structure for Footing 1 and 2, as the transient vertical displacement-time series of Footing 1 and 2 of the control structure are generally out-of-phase with one another. The amplitude of the Footing 1 recording is approximately twice as large as the amplitude of the Footing 2 recording. Additionally, the Footings 3 and 4 data have smaller amplitude, though the validity of these measurements is questionable. The JOS_L_4 earthquake motion was performed early in the motion sequence, so some of these recording anomalies could be caused as the spread footings were still “settling in to place.” It is expected, due to anomalies in the model construction process, that the soil surface under the footings is not uniform. Therefore, it is typical to see different footing response for the first couple of motions. These anomalies are also seen in the data from other earthquake motions, and they are discussed in more detail below.

By examining Figure 5.6, which shows the transient vertical displacement-time series for the LCN motion recorded during Test-3, it can be seen that the control structure recordings have more high-frequency content than the receiver structure recordings. This difference is

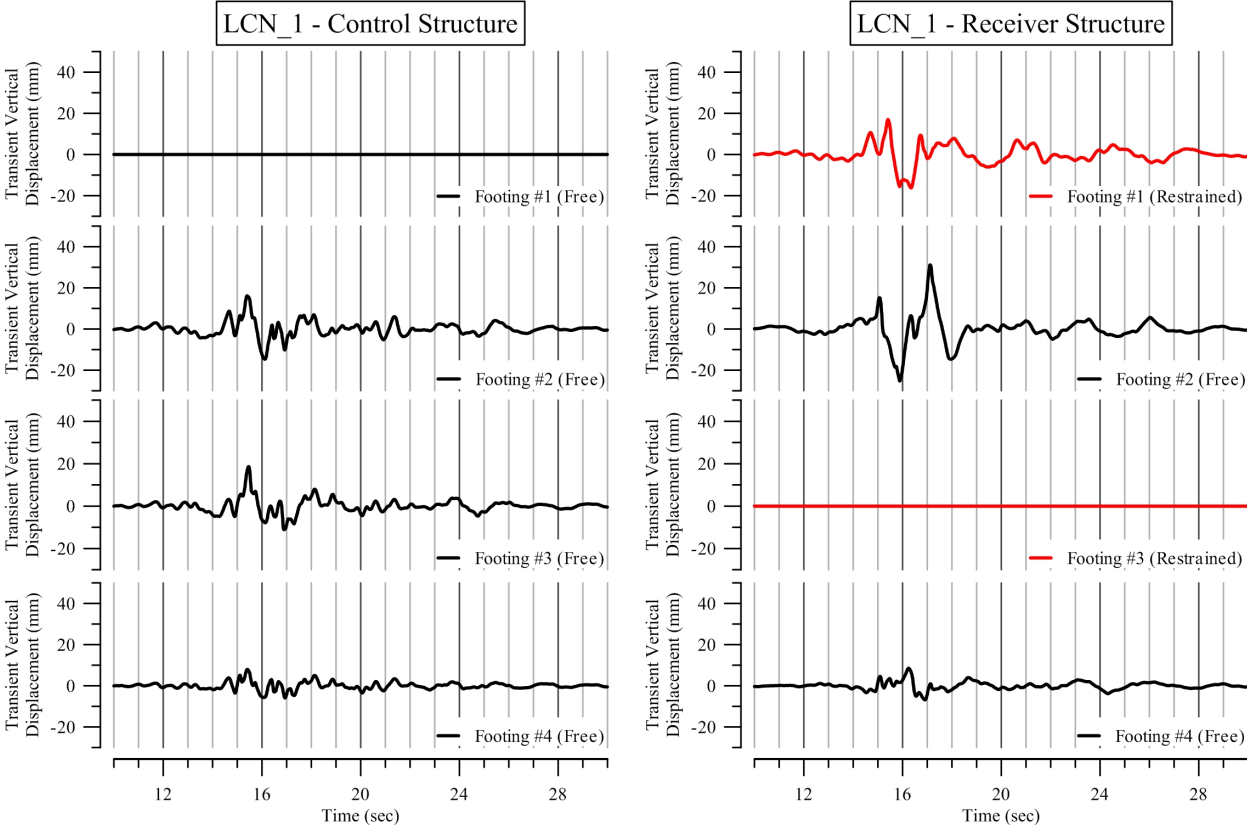


Figure 5.6: The transient vertical displacement recorded during the LCN motion on all the footings on the control and receiver structures. Positive values indicate downward movement, and negative values indicate upward movement.

likely caused by the adjacent transmitter structure, which modifies the frequency-content of the receiver structure to be more in line with its own frequency-content. The LCN earthquake motion is a higher-intensity, forward-directivity earthquake motion that places larger demands on the SFS systems—especially when compared to the previously discussed JOS_L4 motion. The amplitude of the transient vertical displacements recorded on the receiver structure are also larger than those recorded on the control structure, which would indicate that the transmitter structure is driving the receiver structure for this higher-intensity earthquake motion.

Figure 5.6 shows that the transient vertical displacements of the footings are generally in-phase for both the receiver and control structures. This indicates that the superstructure is generally either settling or uplifting at the same time during the LCN motion. The differences in amplitude of the recordings, however, indicate that there will be some superstructure distortion during strong shaking. As with the JOS_L4 motion, the recordings for Footings 3 and 4 are lower than those for Footings 1 and 2. The sensor sensitivity factors were repeatedly

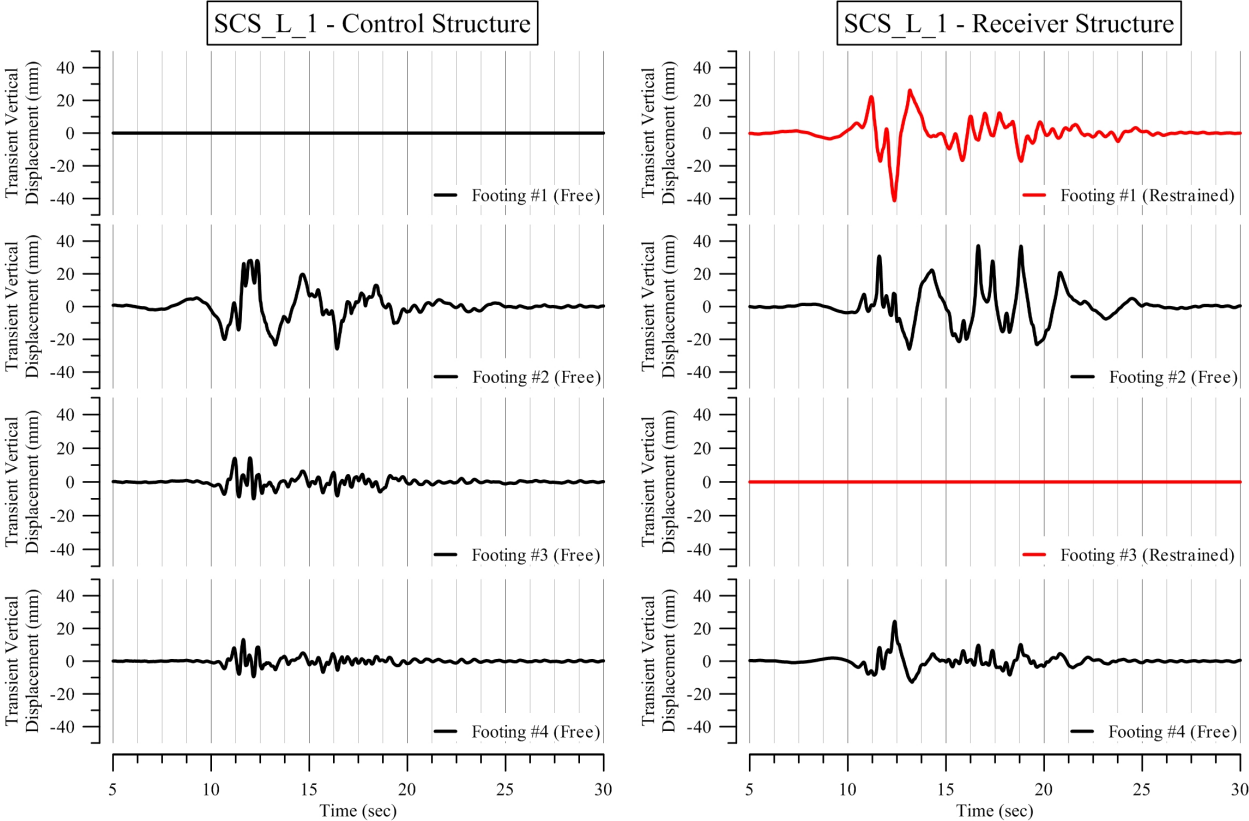


Figure 5.7: The transient vertical displacement recorded during the SCS_L_1 motion on all the footings on the control and receiver structures. Positive values indicate downward movement, and negative values indicate upward movement.

checked during the data processing phase, so it is unlikely that this effect is due to errant data processing. The sensitivity factors for the instrument could be incorrect, or the data acquisition system could have set different gains for these instruments. In this figure, three instruments—two on the control structure and three on the receiver structure—show this type of response; therefore, this decreases the likelihood that these observed responses are caused by errant data processing or data collection. When this transient vertical displacement-time series data are used to compute other response quantities, such as footing rocking, the results are reasonable. This observation strengthens the conclusion that this response difference is physical and not a relic of errant processing or incorrect acquisition.

Figure 5.7 shows evidence that the footings on the receiver structure were displacing out-of-phase during the SCS_L_1 motion. This is especially true when examining Footing 1 and 2, which are restrained and free footings, respectively. This indicates that the receiver structure was likely rocking in the plane of shaking during this motion. The control structure trends are more difficult to quantify. It appears like the footings of the control structure were

displacing in-phase during this motion. The SCS_L_1 earthquake motion is a higher-intensity, forward-directivity motion, like the LCN motion. Once again, there are differences between the Footing 3 and 4 amplitudes versus the Footing 1 and 2 amplitudes.

For many of the earthquake motions, at least one sensor was not working properly, and transient vertical displacement could not be measured. During routine spin-downs, sensors were replaced, or fixed, if possible. The WVC_H motion is one of the few motions that did not have sensor malfunction. The transient vertical displacement-time series for this motion is shown in Figure 5.8. The WVC_H motion is another higher-intensity, forward-directivity motion that places large seismic demands on the SFS systems. An observation from this figure is that the transient vertical displacement-time series are roughly the same amplitude for all footings on the control structure. For the receiver structure, the Footing 1 and 2 recordings are larger in amplitude than the Footing 3 and 4 recordings, which is consistent with observations from the other earthquake motions. However, it should be noted that the difference in amplitude is not as large as was observed in the previously discussed motions, which occurred earlier in the earthquake motion sequence.

Figure 5.8 also allows a comparison of the seismic response of the restrained footings and free footings to be made for the receiver structure. Comparing the Footing 2 response with the Footing 4 response (i.e., the free footing responses), it can be seen that the shape of the waveform is similar, even if there are differences in amplitude. Specifically, at the beginning of strong shaking, the seismic response of the free footings is characterized by high-frequency “bouncing” mainly in the positive (i.e., settlement) direction. At the end of strong shaking, the seismic response of the free footings is characterized by lower-frequency and nearly harmonic oscillations, which signify that the footings were freely vibrating. Notably, the Footing 3 waveform is similar to the Footing 2 and 4 waveforms, though there are some differences in frequency-content, duration, and amplitude. The Footing 1 waveform differs from the others. Specifically, there is a dominant frequency seen in the middle part of the motion, during strong shaking. This dominant frequency, which is approximately 1.0 Hz, is also prevalent in other parts of the motion. This frequency is not equal to the rocking period of the transmitter structure, which is approximately equal to 0.6 Hz. Therefore, it is premature to conclude that this effect is a result of SSSI. There are a number of other possible explanations for this observed response, which include the effects of the earthquake motion, possible sensor error, or a possible sensor decoupling from the footing. The fact that the Footing 3 response is not similar suggests that the Footing 1 response is incorrect, though more work is needed to strengthen this preliminary conclusion.

The transient vertical displacement effects can further be examined by investigating scatter plots of peak values. Figure 5.9 shows the values of the peak transient vertical displacement of the control structure (x-axis) plotted against the peak transient vertical displacement of the receiver structure (y-axis) for each earthquake motion and for each footing. For plotting purposes, the bad recordings (i.e., zero readings) were removed. Additionally, the SCS_H_2 motion was determined to be an outlier. The peak transient vertical displacement recorded on the control structure was high compared to the value recorded on the receiver structure,

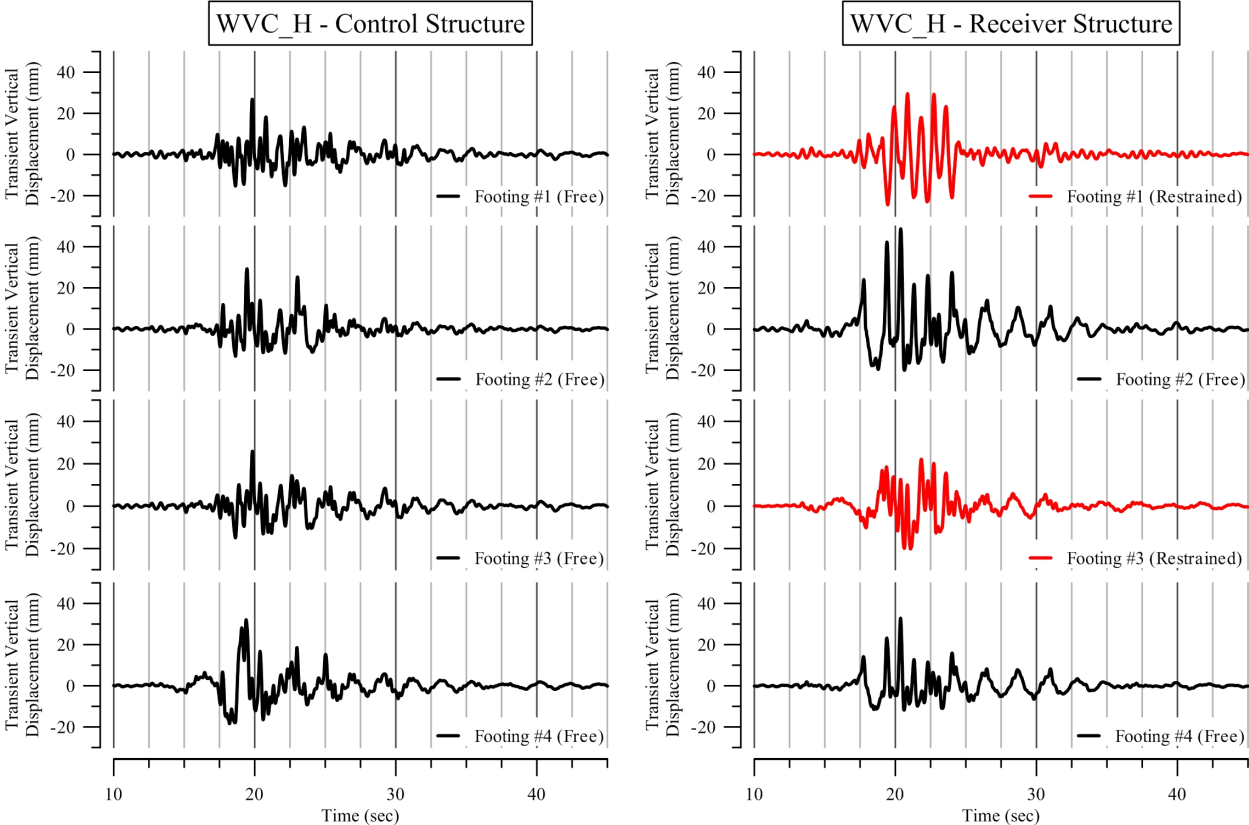


Figure 5.8: The transient vertical displacement recorded during the WVC_H motion on all the footings on the control and receiver structures. Positive values indicate downward movement, and negative values indicate upward movement.

which was likely the result of an acceleration spike. Acceleration spikes can be caused by structural pounding, by an accelerometer losing and regaining contact during an earthquake motion, or by electric surges within the data acquisition system, among other reasons.

Table 5.4 shows linear regressions from the data presented in Figure 5.9, along with the corresponding R^2 values. The linear regressions are forced through the origin. The SCS_H_2 motion was removed from the data set before the regressions were performed.

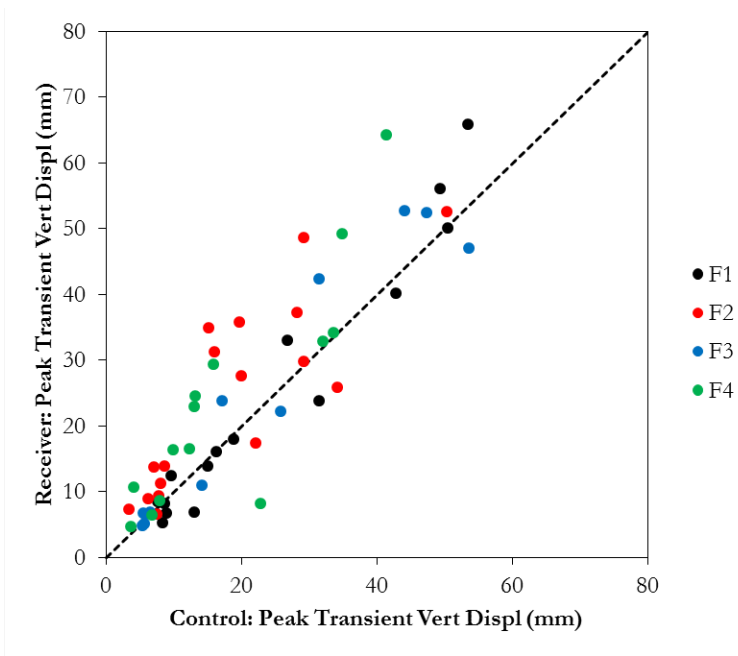


Figure 5.9: Peak transient vertical displacement recorded for each motion on the control structure footings versus peak transient vertical displacement recorded for each motion on the receiver structure footings. The one-to-one line is plotted as a dashed line. For the receiver structure, Footings 1 and 3 are restrained and Footings 2 and 4 are free. For the control structure, all Footings are free.

Table 5.4: Equations for the linear regression lines from the peak transient vertical displacement data along with their corresponding R^2 values. In this table, c is the control structure peak transient vertical displacement, and r is the receiver structure peak transient vertical displacement.

Footing	Regression Equation	R^2
1	$r = 1.05c$	0.94
2	$r = 1.20c$	0.64
3	$r = 1.06c$	0.93
4	$r = 1.27c$	0.76

The results presented in Table 5.4 show that the peak transient vertical displacements of Footings 1 and 3, which are the restrained footings on the receiver structure, nearly follow the one-to-one line with little scatter. This indicates that these footings on the control and receiver structure respond roughly equally during the earthquake motions, with the receiver structure footing response being approximately 5% higher than the control structure footing response, in general. In contrast, the peak transient vertical displacements of Footings 2 and

4, which are the free footings on the receiver structure, deviate from the one-to-one line by about 20 to 30%; that is, the response of the receiver structure footing is approximately 20 to 30% larger than the response of the control structure. In addition, the R^2 values for these footings are low, indicating that the linear regression with a forced intercept does not fit the data well.

These results suggest that the free footings of the receiver structure vertically displace more than the restrained footings of the receiver structure. In addition, the receiver structures vertically displace more than the control structure. Accordingly, these results indicate that the adjacent rocking structure does have an effect on the receiver structure at the footing level, and especially for the higher-intensity earthquake motions. The asymmetric response between the free and restrained footings could lead to superstructure damage via racking and distortion.

The correlation between earthquake intensity measures and engineering demand parameters are also explored for Test-3 data, as was the case with the Test-1 and Test-2 data. The peak transient vertical displacement of the control structure versus the free-field surface PGV is plotted in Figure 5.10. In this figure, the SCS_H_2 data point is plotted for completeness, and is demarcated on the plot. Notably, this point was removed when the regressions were performed. The scatter on this figure is significant. The R^2 values for the data, considering a linear regression with and without a forced zero intercept, are in the range of 0.45 to 0.65, except for the Footing 3 data, which has an R^2 value of approximately 0.8. Exponential regressions were also employed, and the R^2 values were within the same range as those from the linear regressions. Because of the significant scatter, it is difficult to make definitive conclusions from this data. In general, however, the peak transient vertical displacements of the footings of the control structure increase linearly as a function of surface free-field PGV.

The peak transient vertical displacement of the receiver structure versus the surface free-field PGV is plotted in Figure 5.11. The linear regressions from these data, both with and without forced zero intercepts, are in the range of 0.5 to 0.7, except for the Footing 3 data, which has a R^2 value of 0.88. Exponential regressions were also tried for these data, and found to be an even poorer fit than the linear regressions, except again for the Footing 3 data, which has a R^2 value of 0.91. Compared to the data shown for the control structure, the receiver structure does show evidence of a “break-point” PGV at around 50 to 60 cm/sec, other than for the Footing 2 data, which show significant scatter. After this break-point, the peak transient vertical displacement increases more rapidly as the free-field surface PGV increases. Notably, the break-point is not as distinct in these data as was exhibited in the Test-2 data.

5.3.2 Permanent vertical displacement response

The permanent vertical displacement of the footings was also tracked using displacement gauges. The value measured at the end of an earthquake motion was subtracted from the values measured before the earthquake motion to obtain the permanent vertical displacement

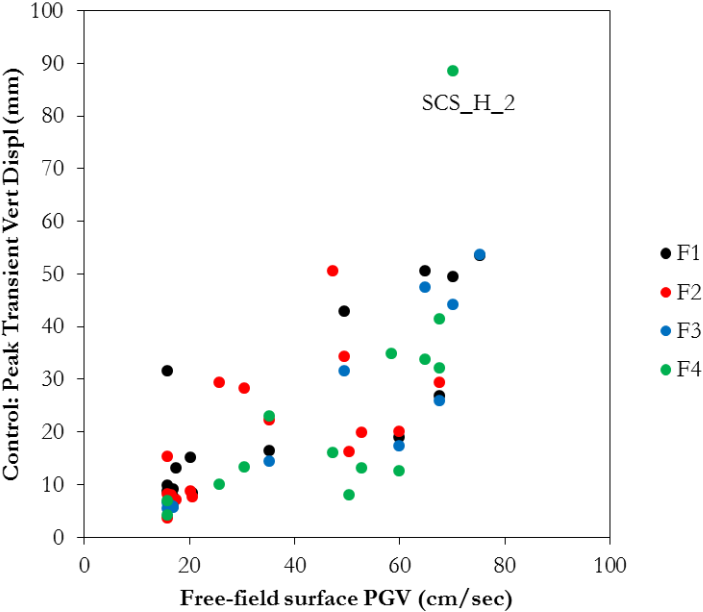


Figure 5.10: Peak transient vertical displacement of the control structure footings versus surface free-field PGV for each earthquake motion. All Footings are free.

caused by each earthquake motion for each footing of the frame structures. Figures 5.12(a) and 5.12(b) show the permanent vertical displacement caused by each earthquake motion for the control structure and receiver structure, respectively. In these figures, positive values of permanent vertical displacement indicate permanent settlement, whereas negative values of permanent vertical displacement indicate permanent uplift. The y-axes of these figures have been reversed to match intuitive understanding of permanent settlement and permanent uplift.

Figure 5.12(a) shows that in general, the permanent settlement or permanent uplift of the control structure is relatively small during most earthquake motions (i.e., less than 5 mm). An exception is the permanent settle recorded during the first four JOS earthquake motions. The footings permanently settled on the order of 12 to 15 mm, 8 to 10 mm, 7 to 10 mm, and 5 to 6 mm, for the JOS_L_1, JOS_L_2, JOS_L_3, JOS_L_4 motions, respectively. Given that the JOS motions are lower-intensity motions, this result indicates that the structural models “settle in” during the first couple earthquake motions. There are likely model construction imperfections, such as gaps below the footings, which are compensated for during the first couple of earthquake motions. This result also suggests that centrifuge researchers examining earthquake engineering problems should perform a couple of lower intensity earthquake or sinusoidal motions during the initial part of their research program, in order to “set” the model. Interestingly, the TCU_L_1 motion, which took place in the middle of the initial JOS motion sequence, shows a negligible permanent uplift. This observation is likely linked to the

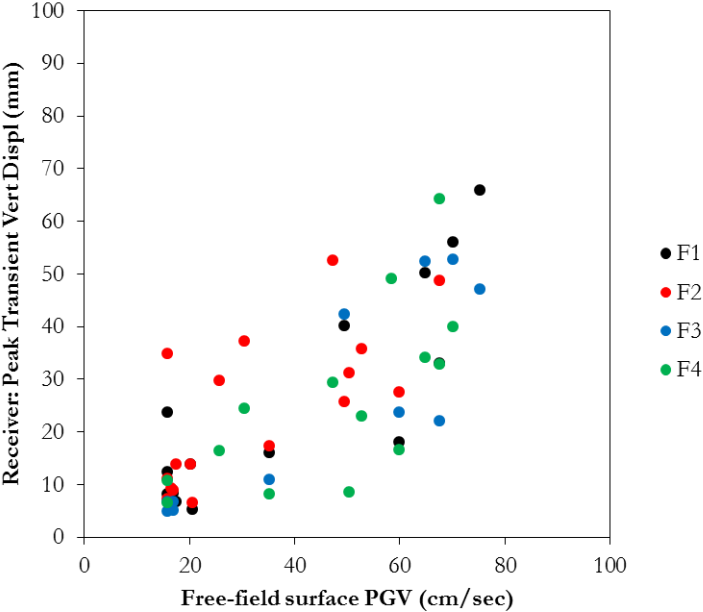
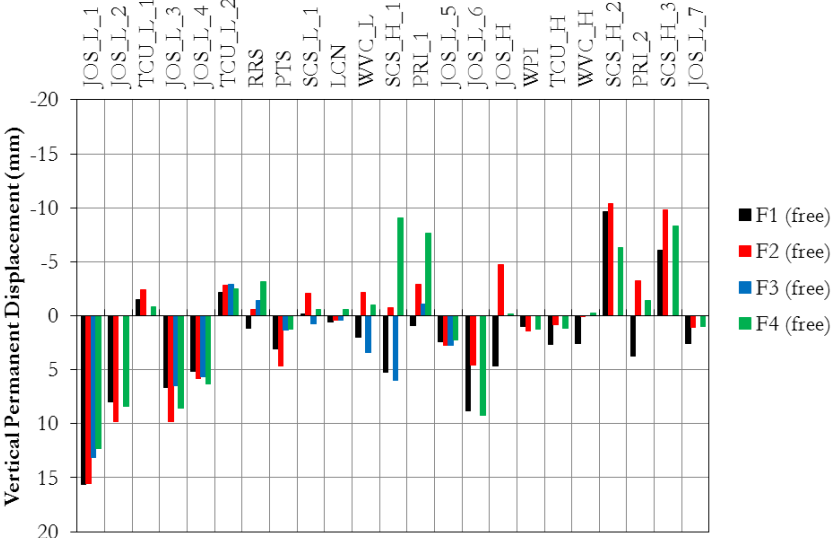


Figure 5.11: Peak transient vertical displacement of the receiver structure footings versus surface free-field PGV for each earthquake motion. Footings 1 and 3 are restrained, and Footings 2 and 4 are free.

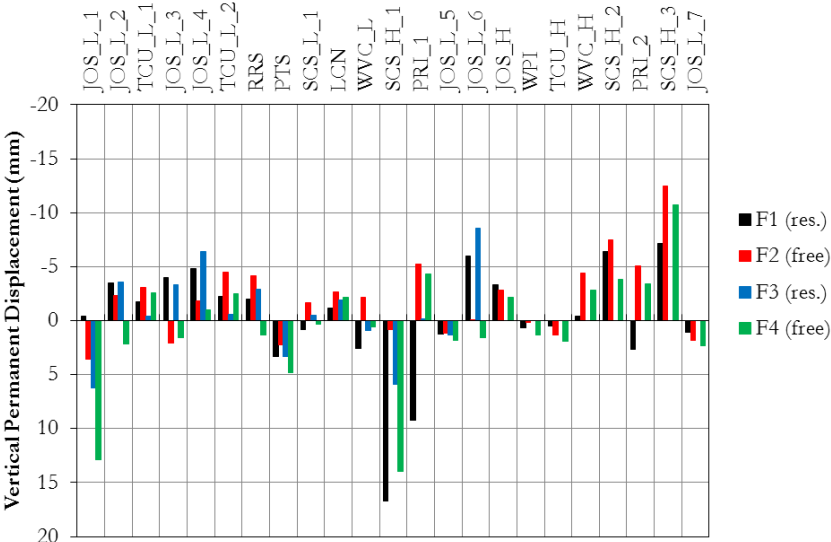
waveform of the earthquake motion. This same result, i.e., negligible permanent uplift, is observed for the TCU.L.2 motion, which occurs later in the sequence.

Another observation from Figure 5.12(a) is that in general, either all of the footings on the control structure permanently settled or permanently uplifted. There are a few exceptions to this observation. The most dramatic observation is from the SCS.H.1 motion, where Footing 3 permanently settles about 6 mm, and Footing 4 permanently uplifts around 9 mm. These types of distortions, especially within lower-story frame structures, can lead to superstructure damage.

Figure 5.12(b), which shows the permanent settlement and uplift for footings of the receiver structure for each earthquake, can be compared to Figure 5.12(a) to reveal differences in footing response due to SSSI. The first observation is that the initial large displacement readings, which were seen in the control structure recordings, are absent from these data, with the exception of the very first motion, JOSL.1. The second observation is that for most earthquake motions, the footings either permanently uplift or permanently settle a negligible amount (i.e., less than 5 mm). This permanent uplift trend is caused by the adjacent transmitter structure, which permanently settles with each motion. Because dry, dense sand is used in these models, when the large transmitter structure does settle, particle rearrangement occurs. The sand particles get pushed laterally and upwards towards the surfaces during this settlement process. As a result, the adjacent and less massive receiver structure footings uplift.



(a)



(b)

Figure 5.12: The permanent vertical displacement of each footing of the (a) control structure, and the (b) receiver structure for each earthquake motion. In the legend, “free” indicates that the footing was free, and “res.” indicates that the footing was restrained.

This observation is a manifestation of SSSI, and is an important scenario to consider when designing similar structures in urban areas. Depending on the structural configurations, the earthquake motion, the surrounding soil properties, and specific performance requirements of the structures, this settlement-uplift response could be unacceptable. More work is needed in this area, both experimentally and numerically, to understand how the structural configuration and surrounding soil properties affect the results. An exception, other than the first JOS motion, is the SCS_H_1 motion, in which Footing 1 settled nearly 17 mm.

5.3.3 Transient horizontal displacement response

Figures 5.13, 5.14, and 5.15 show the transient sliding-time series for the JOS_L_4, LCN, and SCS_L_1 earthquake motions recorded during Test-3, respectively. The term sliding is used instead of horizontal displacement to indicate that these time series are plotted relative to the free-field motion (i.e., the free-field earthquake motion is subtracted from the horizontal time-series of the footing to produce the sliding time-series). The transient sliding-time series are shown for each footing on both the control structure and the receiver structure. Additionally, for the receiver structure, Footings 1 and 3 are considered “restrained” because they are adjacent to the mat foundation of the transmitter structure. Accordingly, the restrained footings are plotted in red for clarity.

By examining Figure 5.13, several possible trends can be observed. First, for the Footing 1 and Footing 2 recordings, there is a difference in amplitude and waveform. In fact, Footing 1 of the receiver structure and Footing 2 of the control structure show nearly no sliding during this earthquake motion. This can be expected, since JOS_L_4 is a lower-intensity earthquake motion. The Footing 3 response, for both the control and receiver structures, is similar in both amplitude and waveform. The Footing 4 response, however, is different between the control and receiver structures; specifically, the transient sliding of Footing 4 on the control structure has a larger amplitude, and a different frequency-content. It must be noted that all the differences discussed in this paragraph are relatively small. There is a possibility that these observed differences are caused by measurement errors.

Figures 5.14 and 5.15 show that in general, the amplitudes and waveforms for corresponding footings on the control and receiver structures are very similar. This result indicates that the transient sliding of the receiver structure is not very sensitive to the presence of the adjacent transmitter structure. Because the transmitter structure was designed to transmit energy mainly via a rocking mode, this result is expected. The transmitter structure is expected to affect the settlement and uplift response of the footings because of this rocking mode, and this was seen in the transient vertical displacement data presented earlier in this chapter. Additionally, the shallowly-embedded mat foundation of the transmitter structure does not have the same restraining capabilities as the deeply-embedded basement used in Test-1 and Test-2.

Another observation from Figures 5.13, 5.14, and 5.15 is that the recordings from Footings 3 and 4 are slightly larger in amplitude (in general) than the recordings from Footings 1 and

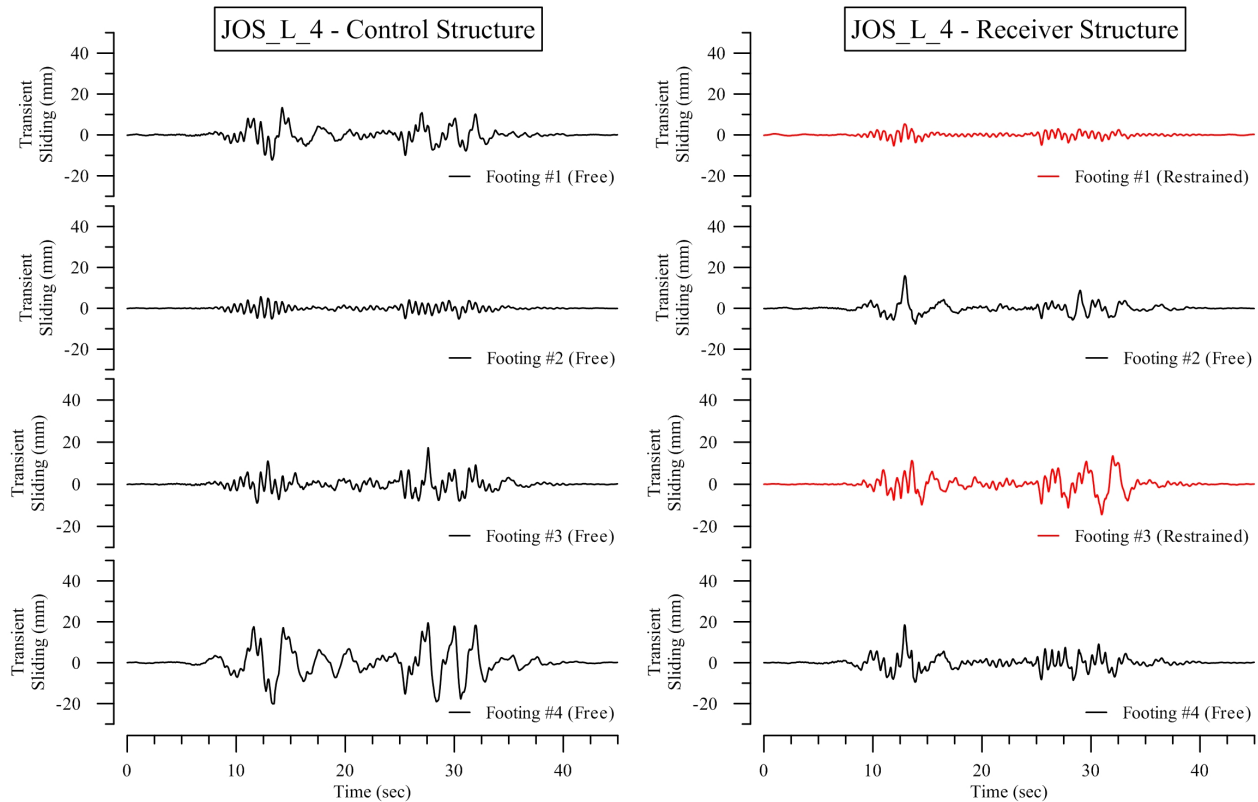


Figure 5.13: The transient sliding recorded during the JOS_L_4 motion on all the footings on the control and receiver structures.

2. This trend is more apparent for the higher-intensity, forward-directivity motions (i.e., LCN and SCS_L_1). A similar trend was observed for the transient vertical displacement data presented earlier in this chapter, except in the case of the transient vertical displacement data, the Footing 1 and Footing 2 recordings were larger than the Footing 3 and Footing 4 recordings, in general. It is difficult to explain this observation without a more careful examination of centrifuge container boundary effects. It is possible that complex wave reflections off the relatively rigid centrifuge container walls significantly affect the seismic response of the spread footings.

In conjunction with the time series plots, it is instructive to examine scatter plots peak transient sliding data. Figure 5.16 shows the peak transient footing sliding of the receiver structure versus the peak transient footing sliding of the control structure. The dashed line in this figure represents the one-to-one line. Notably, the horizontal accelerometer on Footing 1 of the receiver structure malfunctioned after the JOS_L_5 motion, and thus the peak transient sliding values for this footing are not available the remainder of the performed earthquake motions.

From Figure 5.16, it can be seen that most of the points reasonably follow the one-to-one

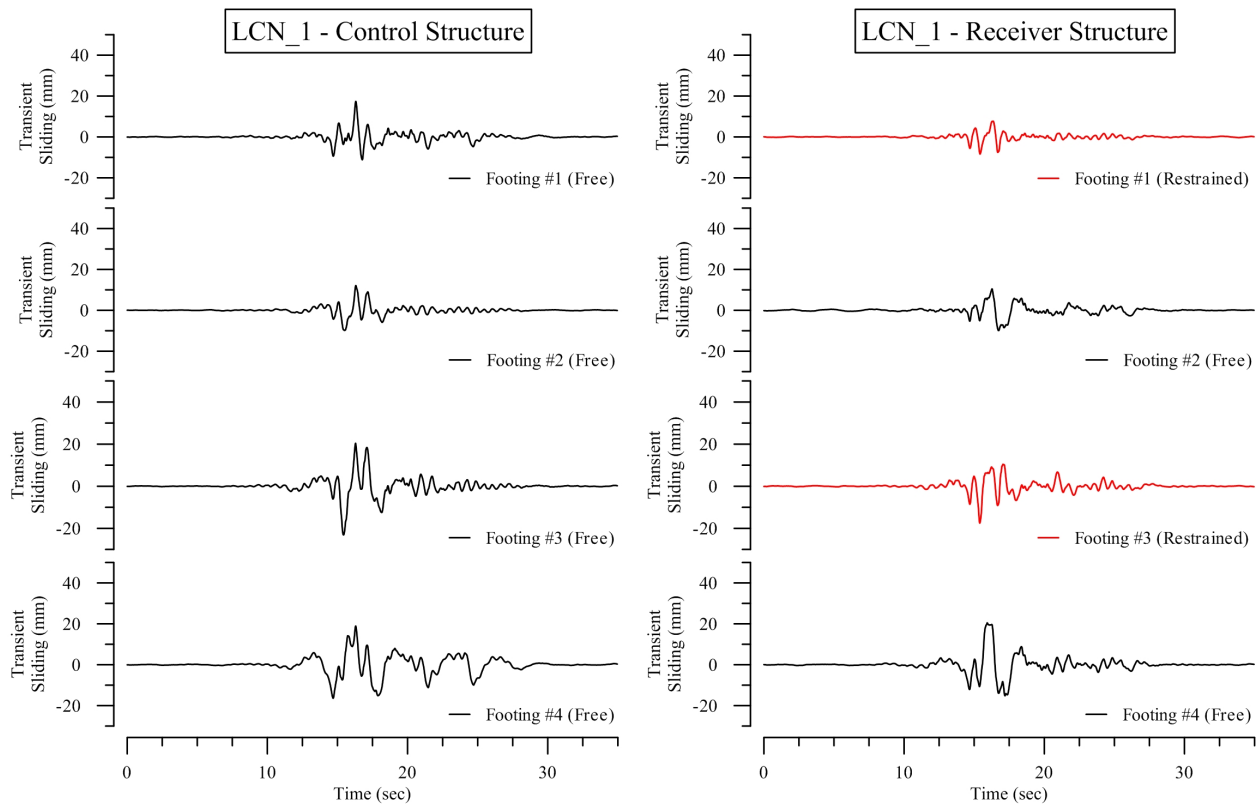


Figure 5.14: The transient sliding recorded during the LCN motion on all the footings on the control and receiver structures.

line, which indicates that peak transient sliding of the corresponding footings between the control structure and the receiver structure are reasonably equal for each earthquake motion. The one exception is Footing 4, which does deviate from the one-to-one line for higher intensity earthquake motions. More specifically, the values of the peak transient sliding recorded on Footing 4 of the receiver structure are larger than the values recorded on Footing 4 of the control structure. Footing 4 is the Southeast footing of the receiver structure, and it is not directly adjacent to the transmitter structure.

The peak transient footing sliding data obtained for Footing 4 reasonably follow expected trends that were also observed in Test-1 and Test-2. The adjacent transmitter structure might be inputting seismic energy into the soil and then, in turn, into the receiver structure. As a result, the seismic responses of the footings are changed with respect to the control structure. Footing 4 of the receiver structure likely experiences more peak transient sliding with respect to Footing 4 of the control structure because of this additional energy being transmitted by the transmitter structure. Footing 2 of the receiver structure, which is the other footing non-adjacent to the transmitter structure, also shows this trend, though it is slighter than the trend observed for Footing 4.

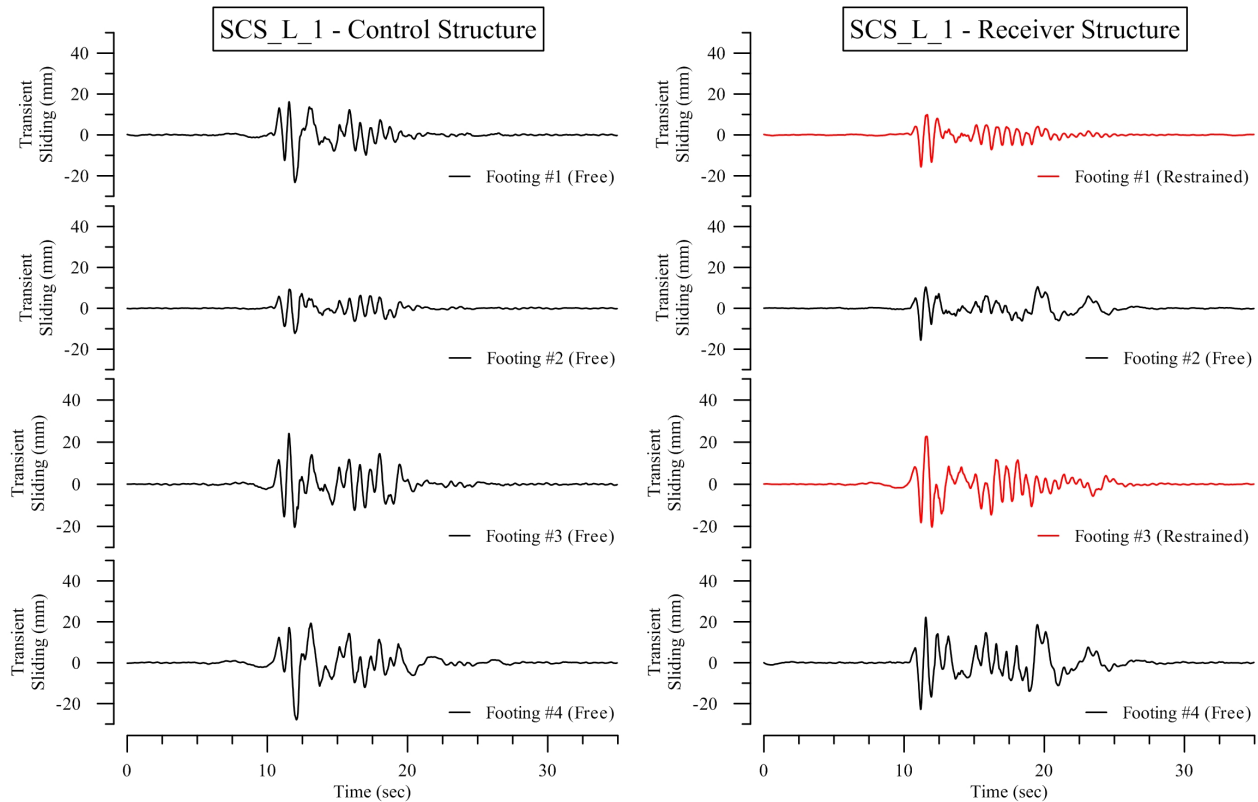


Figure 5.15: The transient sliding recorded during the SCS_L_1 motion on all the footings on the control and receiver structures.

The differences in peak transient sliding recorded on Footings 1 and 3 of the receiver structure do not differ much from the corresponding recordings on the control structure (i.e., the data follow the one-to-one line closely, even for higher-intensity motions). It would be expected that the transmitter structure would “restrain” the adjacent footings of the receiver structure, which was a phenomenon observed during Test-2. This restraining effect would in turn cause the data to plot under the one-to-one line. A possible explanation for the observation that the peak transient sliding of Footings 1 and 3 on the control structure does not differ much from the peak transient sliding on the corresponding footings of the receiver structure is that the transmitter structure does not have a large basement, like the MS3F_B structure used in Test-1 and Test-2. This can be seen by examining moment-rotation curves. Moment-rotation curves were also discussed in Chapter 4, and the same discussion applies to examination of moment-rotation curves within this chapter. Figure 5.17 shows the moment-rotation curves for Footing 4 recorded for the SCS_H.1 motion during Test-3. The moment-rotation curves presented in Chapter 4 were also for the SCS_H motion.

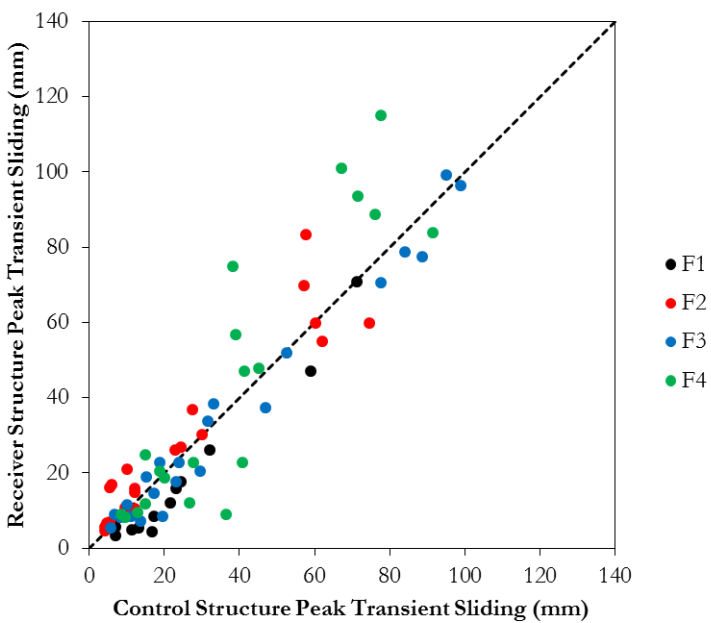


Figure 5.16: Peak transient sliding recorded for each motion on the control structure footings versus peak transient vertical displacement recorded for each motion on the receiver structure footings. The one-to-one line is plotted as a dashed line. For the receiver structure, Footings 1 and 3 are restrained and Footings 2 and 4 are free. For the control structure, all Footings are free.

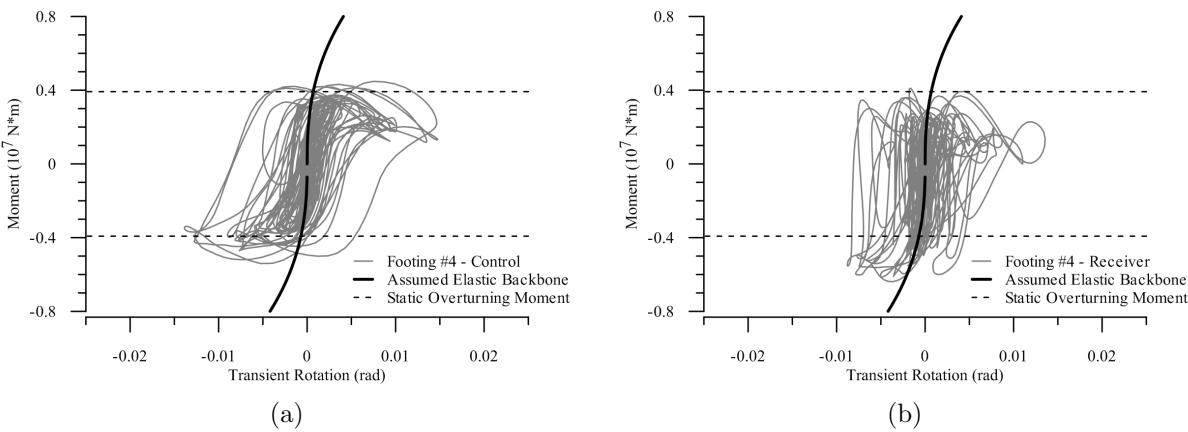


Figure 5.17: Moment-rotation relationships for (a) Footing 4 of the control structure, and (b) Footing 4 of the receiver structure recorded during Test-3 for the SCS_H.1 motion.

Both moment-rotation curves shown in Figure 5.17, as well as other moment-rotation curves examined for other footings and other earthquake motions in Test-3, show this “typical” moment-rotation response. The columns respond inelastically as their overturning moment capacities are reached during seismic loading. This column inelasticity, or ductility, is well captured in this figure. Both the footing on the control structure and the footing on the receiver structure (i.e., the restrained footing) show this type of response. This result is in contrast to the moment-rotation response for footings adjacent to the large basement structure shown in Chapter 4. In Test-2, the footings adjacent to the basement were restrained from rocking in the direction of the basement, and this increased the moment in the supporting column. The result seen in Test-3 is positive, because it indicates that an adjacent mat structure will not place the same type of seismic demand on columns supported by spread footings.

The values of peak transient sliding are also plotted versus the PGV recorded at the surface in the free-field for each earthquake motion. Figure 5.18 shows data from the control structure, and Figure 5.19 shows data from the receiver structure. The same trends that were seen in Test-2 are also visible in Test-3. Primarily, the trend between the peak transient sliding is linear with a relatively shallow slope until a break-point PGV of 50 cm/sec is reached. After this break-point, the trend becomes nonlinear.

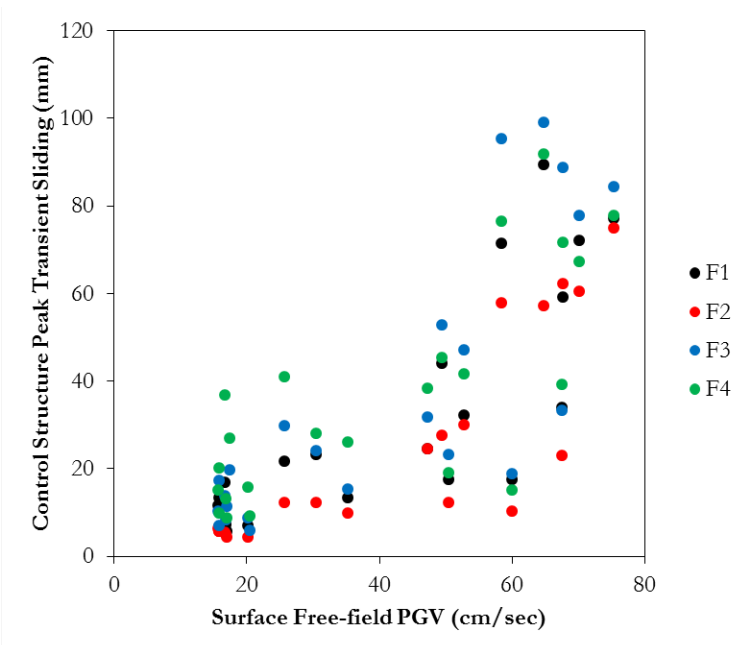


Figure 5.18: Peak transient sliding of the control structure footings versus surface free-field PGV for each earthquake motion. All footings are free.

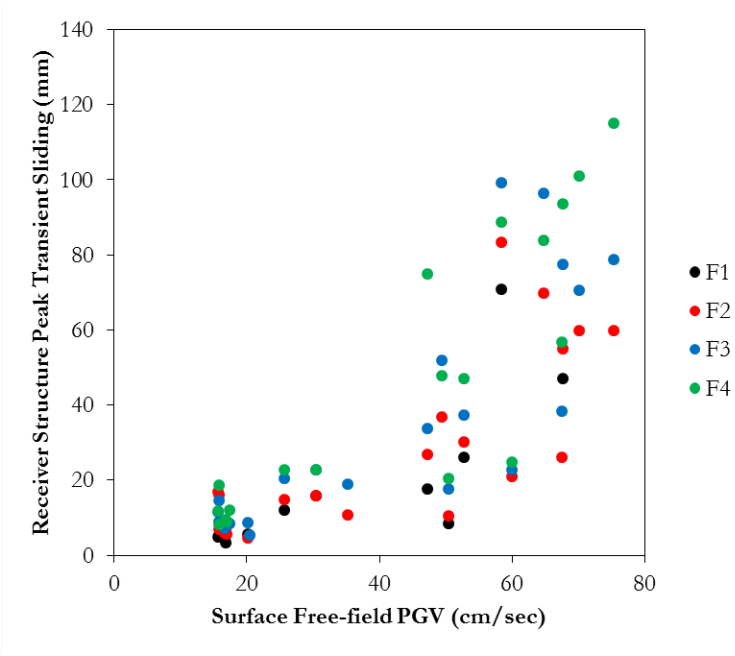


Figure 5.19: Peak transient sliding of the control structure footings versus surface free-field PGV for each earthquake motion. Footings 1 and 3 are restrained and Footings 2 and 4 are free.

Exponential trendlines are determined for peak transient sliding data obtained for all the footings for both the control and receiver structures. The equations for the regressed lines and their corresponding R^2 values are given in Table 5.5. From this table, it can be seen that exponential trendlines fit the data reasonably well. The one exception is the peak transient sliding measurement from Footing 4 of the control structure, which has a low value of R^2 .

5.4 Summary of findings

In this chapter, the seismic response of the control structure footings, receiver structure footings, and transmitter structure mat was examined. By comparing the seismic response of the control structure footings with the receiver structure footings, some insights into SSSI were made. The test design, as discussed at the beginning of this chapter, was specified to increase the interaction between the transmitter-receiver pair. Accordingly, the superstructure response, and specifically the difference in superstructure response between the receiver structure and control structure, is important to consider. The superstructure response was outside the scope of this dissertation, but will be examined in the upcoming dissertation of another project team member.

The transient vertical displacement measurements yielded several insights, which deserve

Table 5.5: Equations for the regression lines from the peak transient sliding data along with their corresponding R^2 values. In this table, F1 = Footing 1, F2 = Footing 2, F3 = Footing 3 and F4 = Footing 4. Additionally, ρ is the peak transient sliding and PGV is the surface free-field PGV .

Value	Regression Equation	R^2
Control, F1	$\ln(\rho) = 0.034PGV - 5.38$	0.74
Control, F2	$\ln(\rho) = 0.042PGV - 2.70$	0.82
Control, F3	$\ln(\rho) = 0.035PGV - 6.17$	0.72
Control, F4	$\ln(\rho) = 0.025PGV - 10.7$	0.55
Receiver, F1	$\ln(\rho) = 0.046PGV - 2.29$	0.78
Receiver, F2	$\ln(\rho) = 0.035PGV - 4.41$	0.70
Receiver, F3	$\ln(\rho) = 0.039PGV - 4.80$	0.81
Receiver, F4	$\ln(\rho) = 0.038PGV - 6.00$	0.83

further study. Most importantly, the difference in amplitudes between the Footings 1 and 2 and Footings 3 and 4 needs to be further investigated. This observation could not be easily dismissed as a data processing or data acquisition error, and thus, may be physical. Footings 1 and 2 are the northwest and southwest footings; accordingly, they are in line with the direction of shaking. Likewise, Footings 3 and 4 are the northeast and southeast footings, and are also in line with the direction of shaking. Footings 1 and 2 are closer to the center of the container, and accordingly, may not experience the same container boundary effects experienced by Footings 3 and 4. Additionally, complex reflections and refractions of seismic waves off the container boundaries occur during each earthquake motion; accordingly, Footings 1 and 2 could be located in an area where energy is focused. Another possible reason for this observation is imperfections in model construction. This reason has some merit, because many earthquake motions were employed during Test-3 and the amplitude difference became less noticeable for the later, higher-intensity motions (i.e., WVC.H). Model construction issues, such as spatial differences in the sand's relative density and gaps under model foundations, might tend to correct themselves in a dry, dense sand model as more motions are applied.

Another insight gained from examining the transient vertical displacement measurements is that the free footings of the receiver structure generally displace more than the restrained footings of the receiver structure. Also, the receiver structure displaces more in general than the control structure. Thus, the adjacent rocking structure (i.e., the transmitter) does have an effect on the vertical motion of the adjacent footings, especially during higher-intensity earthquake motions. The difference in footing response between the restrained footings and the free footings, which is caused by the adjacent rocking structure, has implications for similar building pairs found in urban areas. More specifically, the asymmetric response of the superstructure likely leads to extra demands on the structural members, which could cause significant damage.

The permanent vertical displacement data provide an interesting observation: the receiver structure uplifts permanently after most earthquake motions due to the corresponding permanent settlement of the adjacent mat foundation. For the Test-3 data, the permanent uplifts of the spread footings were minor (i.e., on the order of 5 mm or less). For different structural configurations, different soil conditions or different geometries, however, this uplift may not be as minor, and needs to be considered further.

The transient sliding data, in general, is not sensitive to SSSI. That is, the transient sliding observed in the footings of the control structure is similar in frequency-content, amplitude and duration as the transient sliding observed in the footings of the receiver structure. Additionally, the moment-rotation data show that the mat foundation of the transmitter structure does not restrain the adjacent spread footings as much as the basement structure used in Test-2 did.

An overarching observation, based on examining vertical displacements of the footings (both transient and permanent) and transient horizontal displacements for each earthquake motion, is that the adjacent transmitter structure does not affect the seismic response of the footings of an adjacent receiver structure significantly. This is in contrast to results observed in Test-2, when the deeply-embedded basement structure provided a restraining effect on the adjacent spread footings of a frame structure, and in turn increased the demands on that structure. This observation is positive, because it indicates that structure-soil-structure interaction is not detrimental for this type of building pair, which is commonly found in urban areas.

This overarching observation, however, comes with a disclaimer that only a specific case was examined during Test-3; i.e., the case of the two structures specified as the transmitter-receiver pair, founded atop dense, dry sand. These observations are expected to change as a function of the superstructure properties, the problem geometry, the soil properties, and the earthquake motion characteristics. More work is needed, including field observations, experiments, and numerical work, before more concrete observations can be made. Accordingly, this overarching observation should not be construed to mean that SSSI is unimportant in urban environments and thus can be neglected when performing seismic design of structures. In addition, only seismic footing response was examined within this chapter. It is possible that the superstructure response may show more interaction between the transmitter and receiver pair, and that some detrimental effects of SSSI could be observed.

Chapter 6

Conclusions & Recommendations

6.1 Summary

In seismically active, densely populated areas, buildings are clustered in “city blocks.” During earthquakes, adjacent buildings within these city blocks interact through the soil. This is called structure-soil-structure interaction and is currently not well understood by earthquake engineers.

The focus of this dissertation work is on the results of three centrifuge tests investigating SFSI and SSSI of inelastic structures subjected to earthquake motions of varying intensities. This work is a part of a \$1.7 Million NSF grant involving six investigators and a large team of postdoctoral researchers, graduate students, and undergraduate students. As such, the work presented in this dissertation is just one part of the overall project.

The key goal of this dissertation is to provide data from three high-quality centrifuge tests. The data will help the team calibrate the numerical models moving forward. With this goal in mind, this dissertation started with a relevant literature review, and then the earthquake motion selection process was described in detail. Finally, the experimental setup and some experimental results from the three centrifuge tests were described.

This dissertation contains several contributions to the earthquake engineering community. First, a procedure for how to select earthquake motions to be used on the centrifuge shaking table was developed. This procedure uses a frequency-domain transfer function approach to calibrate a command motion (i.e., the motion that commands the shaking table). The command motion is calibrated such that the achieved motion (i.e., the motion that is measured in the centrifuge container) matches the target motion (i.e., the motion that is specified by the researcher) within a reasonable tolerance. This procedure is not specific to the UCD-CGM machine, and can be used by other researchers that need to calibrate earthquake motions for other shaking tables.

Second, to the author’s knowledge, no other researchers have performed centrifuge tests with inelastic, three-dimensional frame structures. This dissertation as well as publications by

the research team describe the design and construction of these structural models. Hopefully, future researchers will build and test more complex SFS systems within the centrifuge.

A deep basement structure was used during two of the centrifuge tests described within this dissertation. This setup allowed for the examination of kinematic interaction effects. Kinematic interaction is currently not as well studied as the related SFSI phenomenon of inertial interaction. The results within this dissertation serve to reinforce current kinematic interaction analysis techniques. However, a primary shortcoming of kinematic interaction analysis is the non-arbitrary selection of frequency range and filtering parameters, and this dissertation has highlighted this shortcoming. Ideas for how to address this shortcoming are discussed in the next section.

As previously mentioned, a contribution of this dissertation research was the complex structural models that were employed. For all three tests, at least one of the structural models was founded on shallowly-embedded spread footings. This is also a contribution of this dissertation, as few researchers have examined the seismic response of spread footings attached to a frame structure experimentally. Initial results are showing that the individual footings affect one another during earthquakes; therefore, when considering a frame structure in an urban environment, three separate, but related phenomena should be considered: soil-foundation-structure interaction, structure-soil-structure interaction, and footing-soil-footing interaction. This last type of interaction, footing-soil-footing interaction, is being investigated by other members of the research team (e.g., Choy 2011; Puangnak et al. 2012).

6.2 Conclusions

A goal of this dissertation was to develop a better understanding of SSSI effects, and several insights into SSSI have been made. Notably, the contents of this dissertation focused on the seismic foundation response of the structural models, though the superstructure response was also examined when it was deemed important. Upcoming work by other team members will examine the superstructure response more fully. Some SSSI insights described within this dissertation are:

- As mentioned previously, different footings within a frame structure respond differently during an earthquake, which can lead to superstructure damage. The difference in response can be caused by an adjacent “restraining” structure, such as a deeply-embedded basement. It was observed that a footing directly next to the restraining structure settled and slid less during an earthquake. This finding corroborates observations from the field, where the corner buildings of a city block experience more superstructure damage than “interior” buildings. This phenomenon was seen in San Luis Obispo, California following the 2003 San Simeon earthquake (observed, for example, Hardenbeck et al. 2004).
- The asymmetric superstructure response caused by SSSI (described in the previous

bullet) tends to worsen as the number of earthquake motions a structure is subjected to increases. This has important implications for aftershocks. A structure could withstand collapse from a mainshock, but then experience distress during a significant aftershock that causes a disproportionately large amount of damage.

- Columns founded on the footings adjacent to a restraining deeply-embedded basement tend to experience more moment during an earthquake than the columns supported by the non-restrained footings. A possible explanation for this observation is that the restrained footings are not allowed to rotate freely during an earthquake, and so the energy normally expended during this rotation process is instead dissipated in the supporting column. These extra seismic demands in the columns, if not accounted for, could lead to unacceptable seismic performance.
- Performance-based engineering concepts will be necessary to advance this line of research further. Initial results from this testing suggest that the peak ground velocity correlates well with important engineering demand parameters such as footing sliding and footing settlement.
- Centrifuge boundary effects may affect the results more than expected, and work should be completed to understand these boundary effects more fully. This is particularly true of SFSI and SSSI research, where wave propagation is an important component of the problem. Work has been completed at UC Davis to more fully understand these boundary effects (e.g., Ilankatharan and Kutter 2010; Choy 2011).
- A mat foundation affects the response of adjacent spread footings. More specifically, as the mat settles, the spread footings usually uplift. This result is expected, but quantifying it will be important for advancing SSSI research.
- In the case of a shallowly-embedded mat foundation adjacent to shallowly-embedded spread footings, the sliding of the spread footings is not sensitive to the presence of the mat. This observation applies to the test setup examined in Test-3.
- For the cases examined in Test-3, SSSI effects on footing response were minimal and typically not strongly detrimental. Detrimental SSSI effects include increased superstructure demands such as larger roof accelerations and increased column moments. One possible exception is the transient vertical displacement of the receiver structure footings. For higher-intensity earthquake motions, it was observed that on the receiver structure the restrained footings displaced less than the free footings. The resulting asymmetry in the superstructure could lead to extras demands in the structural members, and this could lead to damage. This observation (i.e., detrimental SSSI effects are minimal) is based on the specific case examined, and more experimental testing and numerical modeling is needed to expand this result to other important soil, foundation, and structure configurations.

- The seismic response of the footings observed in all three centrifuge tests was erratic. This dissertation attempts to address some of the more important observations, but much more work is needed in this area to understand the underlying mechanisms of SSSI.

Finally, perhaps the most significant contribution of this dissertation research is the large, high-quality data set on SFSI and SSSI experiments, which is and will be made available on NEES Hub by the research team. Interested readers should continue to monitor the NEESHub site, as data from tests described within this dissertation as well as data from future test will continue to be placed in this repository. Future researchers are encouraged to continue using this data to gain valuable insights into SSSI, SFSI, site city effects and related phenomena.

6.3 Recommendations for future research

6.3.1 Soil-foundation-structure interaction

Geotechnical and structural earthquake engineers as well as engineering seismologists have an interest in SFSI research. As such, this is a relatively mature field, and has been studied extensively (Kausel 2010). However, there are fundamental issues that need to be addressed.

- Better case history data are needed to advance SFSI research. To date, most SFSI studies have been mainly numerical and theoretical. There is a need to support this numerical and theoretical work with field-scale observations. Gathering high-quality data from fully instrumented SFS systems is becoming possible as the quality and efficiency of seismic instrumentation and data acquisition systems improve. Accordingly, there is a need to fully instrument SFS systems in seismically active areas and gather data during earthquakes. The field-scale data can then be compared to current theoretical and numerical SFSI research. This will lead to key insights and future theoretical and numerical SFSI research.
- There is also a need to gather more high-quality experimental SFSI data. The field-scale case history data is the most realistic data; however, there is no way to know with certainty when an earthquake will occur near the site of a fully instrumented SFS system. Accordingly, the experimental data are important to fill in knowledge gaps until real earthquake data can be recorded at the instrumented sites. Additionally, many experiments with specific scientific objectives can be performed; whereas, for the full-scale case, the SFS system properties are set. High-quality SFSI experiments can be performed using technologies like centrifuge testing, which allow the researcher to simulate SFS systems. Researchers can also compare experimental results with current theoretical and numerical SFSI research, which will lead to key insights.

- The direct method for analyzing SFSI is rarely used in research or practice. There is a need to advance the direct method, and make it more accessible for both researchers and practitioners. This will first require that geotechnical and structural earthquake engineers as well as engineering seismologists become comfortable using one numerical software package. The finite element program OpenSees (<http://opensees.berkeley.edu>) shows promise for this purpose. The second requirement is that models for the soil-foundation interface become more advanced. Typically, the stiffness and damping properties of this interface are specified with nonlinear Winkler springs or other related models. An issue with this approach is that it requires spring and dashpot coefficients to be specified for the soil, which is a challenging task for geotechnical earthquake engineers. For research to progress in this area, geotechnical and structural earthquake engineers need to work together. Contact interface models (e.g., Gajan et al. 2005) show promise in this area, but more work needs to be completed. The final requirement is that more calibration work be done for the direct approach. This approach is complex, and interpreting the results is non-trivial. Experienced earthquake engineers need to provide guidance on how to perform the direct approach and interpret results correctly.

6.3.2 Kinematic interaction

Kinematic interaction is a component of SFSI that has not received as much attention as inertial interaction. A key reason for this discrepancy is that foundations are often not embedded deeply enough or are not large enough for kinematic interaction to affect the results significantly. However, there are many cases of basement structures or deep pile foundations where kinematic interaction does occur, and the earthquake motions recorded at the foundation level differ significantly from those recorded at the surface in the free-field.

As seen in this dissertation, transmissibility functions calculated to understand kinematic interaction are dependent on the frequency range over which they are calculated as well as the filtering parameters employed. The frequency range and filtering parameters are user-selected, and there is some subjectivity in their selection. Accordingly, guidelines for how to incorporate kinematic interaction into seismic design have this subjectivity built in. A key first step for removing this level of subjectivity is to agree on guidelines for selecting frequency ranges and filtering parameters. Engineering judgment will always be required at this step because each situation is different, but at least the guidelines would serve as a starting point for analyzing kinematic interaction effects.

Another important future research topic is performing more sensitivity analyses to understand the importance of different parameters on kinematic interaction. Numerical models calibrated to capture field case history data could be used for these sensitivity analyses. This research would also help with the aforementioned goal of creating guidelines for frequency range and filtering parameter selection. The results of the sensitivity analyses could be used to develop guidance on when kinematic interaction is important, and when it needs to be considered.

6.3.3 Structure-soil-structure interaction

The field of structure-soil-structure interaction, unlike SFSI, is relatively new and unexplored. The potential future research topics in this field are numerous, and will become more important as the population and population density in urban areas increases. Indeed, devastating earthquakes in Chile (2010), New Zealand (2010 and 2011) and Japan (2011) have exhibited the importance of developing a better understanding of SSSI. The bulleted list below contains some ideas for future research:

- Much theoretical work concerning SSSI was completed in the early 1970s (e.g., Luco and Contesse 1973; Lee and Wesley 1973; Wong and Trifunac 1975), as discussed in Chapter 2 of this dissertation. This theoretical work provided closed-form solutions for estimating seismically-induced displacements of two adjacent shear walls based on stiffnesses of the materials and the geometry of the problem. To the author's knowledge, these theoretical models have never been confirmed experimentally or via field case history data. There is a need to replicate the theoretical models experimentally, in order to gain insights into the relative importance of the theoretical modeling assumptions. Cases slightly outside the theoretical models could then be investigated experimentally, and the theoretical models could be updated with this empirical data. This type of building-block approach, of comparing theoretical and experimental models with each other incrementally, will also help build a fundamental understanding of SSSI.
- The focus of this dissertation was on earthquake engineering; accordingly, great emphasis was placed on the seismic response of the foundations and the superstructure. SSSI effects were discussed, and will continue to be discussed by other research team members, in terms of foundation and superstructure response. There is a need, however, to also focus on the engineering seismology component of this problem. Namely, how does the earthquake motion change in an urban area with respect to the surrounding foundations and superstructures? This complex wave propagation problem—which is usually referred to as site city effects, as discussed in Chapter 2 of this dissertation—is important for understanding the entire SSSI phenomenon.
- There is a need for more numerical studies to understand SSSI. The future work of researchers on this project team, and others who use the data spawned from this research, will be important to advance this research need. In the end, it is the numerical models that will drive the seismic design of urban areas. Performing numerical modeling also provides insights into weaknesses of the models, and highlights future experimental research needs.

6.3.4 Urban earthquake engineering

The field of urban earthquake engineering will center on how to protect an urban area from earthquake damage. The central goal, therefore, is promoting urban resiliency, which

requires that the urban area remain functional after an earthquake. Functionality is required immediately after an earthquake as well as during the after-effects, such as fire and tsunamis. Another important component of resiliency is maintaining lifelines (important highways, water lines, etc.). Finally, the urban area must remain resilient against earthquakes as the urban landscape continually evolves.

The scale of this research topic, therefore, is enormous. It will require the expertise of earthquake engineers, engineering seismologists, public policy experts, city planners, architects, and decision makers. Currently, research is being performed in many of these sub-fields; for instance, this dissertation focuses on how adjacent buildings interact with one another during an earthquake. The field of urban earthquake engineering will require researchers of these sub-fields to work together towards the larger goal of promoting urban resiliency for cities of today and tomorrow. The May 2011 issue of *Earthquake Spectra* describes the “ShakeOut Scenario,” which is a hypothetical M7.8 earthquake scenario in Southern California (Porter et al. 2011). This project brought together a wide range of experts, from earthquake engineers and seismologist to sociologist, to predict how a large earthquake would affect Southern California. These predictions then drive decisions by policy makers to improve seismic resiliency. These same types of research programs need to occur for other regions and cities in seismically-prone areas.

Bibliography

- Abrahamson, N. and W. Silva (2008). Summary of the Abrahamson & Silva NGA ground-motion relations. *Earthquake Spectra* 24(1), 67–97.
- Abrahamson, N. A. (2000). Effects of rupture directivity on probabilistic seismic hazard analysis. In *Proceedings of the Sixth International Conference on Seismic Zonation*, Palm Springs, CA. Earthquake Engineering Research Institute.
- Alavi, B. and H. Krawinkler (2001). Effects of near-fault ground motions on frame structures. Technical Report Report No. 138, John A. Blume Earthquake Engineering Center, Stanford, CA. Available online: https://blume.stanford.edu/sites/default/files/TR138_Alavi.pdf.
- Allotey, N. and M. H. E. Naggar (2007). An investigation into the Winkler modeling of the cyclic response of rigid footings. *Soil Dynamics and Earthquake Engineering* 28, 44–57.
- Anastasopoulos, I., G. Gazetas, M. Loli, M. Apostolou, and N. Gerolymos (2010). Soil failure can be used for seismic protection of structures. *Bulletin of Earthquake Engineering* 8, 309–326.
- Ansal, A., N. Abrahamson, J. P. Bardet, M. Barka, M. B. Baturay, B. M. Berilgen, R. Boulanger, J. Bray, O. Cetin, L. Cluff, T. Durgunoglu, D. Erten, M. Erdik, D. Frost, I. M. Idriss, T. Karadayilar, A. Kaya, W. Lettis, J. Martin, J. Mitchell, G. Olgun, T. O'Rourke, W. Paige, E. Rathje, C. Roblee, R. Sancio, W. Savage, R. Seed, P. Somerville, J. Stewart, B. Sunman, B. Swan, S. Toprak, D. Ural, M. Yashinski, T. Yilmaz, and L. Youd (1999). Initial geotechnical observations of the August 17, 1999 Kocaeli Earthquake: A report of the Turkey-US Geotechnical Earthquake Engineering Reconnaissance Team. Technical Report GEER-001/August 1999, Geotechnical Extreme Events Reconnaissance Association, Berkeley, CA. Available online: http://geerassociation.org/Post_EQ_Reports.html.
- ASCE 7-10 (2010). *Minimum Design Loads of Buildings and Other Structures*. Reston, VA: American Society of Civil Engineers.
- ATC-40 (1996). *Seismic Evaluation and Retrofit of Concrete Buildings*, Volume 1. Redwood City, CA: Applied Technology Council.

- Aviles, J. and L. E. Perez-Rocha (1996). Evaluation of interaction effects on the system period and the system damping due to foundation embedment and layer depth. *Soil Dynamics and Earthquake Engineering* 15, 11–27.
- Baker, J. W. (2007). Quantitative classification of near-fault ground motions using wavelet analysis. *Bulletin of the Seismological Society of America* 97(5), 1486–1501.
- Bertero, V., S. Mahin, and R. Herrera (1978). Aseismic design implications of near-fault San Fernando earthquake records. *Earthquake Engineering & Structural Dynamics* 6(1), 31–42.
- Bielak, J. (1975). Dynamic behaviour of structures with embedded foundations. *Earthquake Engineering & Structural Dynamics* 3(3), 259–274.
- Bommer, J. J. and A. B. Acevedo (2004). The use of real earthquake accelerograms as input to dynamic analysis. *Journal of Earthquake Engineering* 8(S1), 43–91.
- Boore, D. M. and G. M. Atkinson (2008). Ground-motion prediction equations for the average horizontal component of PGA, PGV, and 5%-damped PSA at spectral periods between 0.01 s and 10.0 s. *Earthquake Spectra* 24(1), 99–138.
- Boore, D. M. and J. J. Bommer (2005). Processing of strong-motion accelerograms: needs, options and consequences. *Soil Dynamics and Earthquake Engineering* 25(2), 93–115.
- Bray, J. D. and A. Rodriguez-Marek (2004). Characterization of forward-directivity ground motions in the near-fault region. *Soil Dynamics and Earthquake Engineering* 24(11), 815–828.
- Campbell, K. W. and Y. Bozorgnia (2008). NGA ground motion model for the geometric mean horizontal component of PGA, PGV, PGD and 5% damped linear elastic response spectra for periods ranging from 0.01 to 10 s. *Earthquake Spectra* 24(1), 139–171.
- Chang, B. J., P. Raychowdhury, T. C. Hutchinson, S. Gajan, B. L. Kutter, and J. Thomas (2006). Centrifuge testing of combined frame-wall-foundation structural systems. In *Proceedings of the National Conference on Earthquake Engineering*, San Francisco, CA. Earthquake Engineering Research Institute.
- Chang, S. W., J. D. Bray, and R. B. Seed (1994). Chapter three: Ground motions and local site effects. In J. P. Stewart, J. D. Bray, R. B. Seed, and N. Sitar (Eds.), *Preliminary Report on the Principal Geotechnical Aspects of the January 17, 1994 Northridge Earthquake*. Berkeley, CA: Geotechnical Engineering Extreme Events Association. Available online: http://geerassociation.org/Post_EQ_Reports.html.
- Chen, Z., T. C. Hutchinson, N. W. Trombetta, H. B. Mason, J. D. Bray, K. C. Jones, C. Bolisetti, A. S. Whittaker, B. Y. Choy, G. L. Fiegel, J. Montgomery, R. J. Patel, and

- R. D. Reitherman (2010). Seismic performance assessment in dense urban environments: evaluation of nonlinear building-foundation systems using centrifuge tests. In S. Prakash (Ed.), *Proceedings of the Fifth International Conference on Recent Advances in Geotechnical Earthquake Engineering and Soil Dynamics*, Rolla, MO. University of Missouri, Rolla.
- Chiou, B. S.-J. and R. R. Youngs (2008). An NGA model for the average horizontal component of peak ground motion and response spectra. *Earthquake Spectra* 24(1), 173–215.
- Choy, B. Y. (2011). Forced vibration test in a centrifuge test examining SSSI effects. Master's thesis, University of California at Davis, Davis, CA.
- Clouteau, D. and D. Aubry (2001). Modifications of the ground motion in dense urban areas. *Journal of Computational Acoustics* 9(4), 1659–1676.
- Dashti, S. (2009). *Toward developing an engineering procedure for evaluating building performance on softened ground*. Ph. D. thesis, University of California, Berkeley, Berkeley, CA.
- Deierlein, G. G., H. Krawinkler, and C. A. Cornell (2003). A framework for performance-based earthquake engineering. In *Proceedings of the 2003 Pacific Conference on Earthquake Engineering*, Christchurch, New Zealand.
- Ditommaso, R., M. Mucciarelli, M. R. Gallipoli, and F. C. Ponzio (2010). Effect of a single vibrating building on free-field ground motion: numerical and experimental evidences. *Bulletin of Earthquake Engineering* 8, 693–703.
- Duke, C. M., J. E. Luco, A. R. Carriveau, P. J. Hradilek, R. Lastrico, and D. Ostrom (1970). Strong earthquake motion and site conditions: Hollywood. *Bulletin of the Seismological Society of America* 60(4), 1271–1289.
- Ellsworth, W. L. (2003). Appendix D: Magnitude and area data for strike slip earthquakes in Earthquake Probabilities in the San Francisco Bay Region: 2002-2031. Technical Report U.S. Geological Survey Open-File Report 03-214, United States Geological Survey, Reston, VA. Available online: <http://pubs.usgs.gov/of/2003/of03-214/>.
- Ewins, D. J. (2000). *Modal Testing: Theory, Practice and Application* (2nd ed.). Baldock, England: Research Studies Press Ltd.
- FEMA-440 (2005). *Improvement of Nonlinear Static Seismic Analysis Procedures*. Washington, DC: Federal Emergency Management Agency.
- Fenves, G. L. and R. D. DesRoches (1994). Response of the Northwest Connector in the Landers and Big Bear Earthquakes. Technical Report UCB/EERC-94/12, Earthquake Engineering Research Center, Richmond, CA.

- Fiegel, G. L. and B. L. Kutter (1994). A mechanism of liquefaction for layered soils. *Journal of Geotechnical Engineering* 120(4), 737–755.
- Gajan, S. and B. L. Kutter (2008). Capacity, settlement, and energy dissipation of shallow footings subjected to rocking. *Journal of Geotechnical and Geoenvironmental Engineering* 134(8), 1129–1141.
- Gajan, S., B. L. Kutter, J. D. Phalen, T. C. Hutchinson, and G. R. Martin (2005). Centrifuge modeling of load-deformation behavior of rocking shallow foundations. *Soil Dynamics and Earthquake Engineering* 25(7-10), 773–783.
- Gallipoli, M. R., M. Mucciarelli, F. Ponzio, M. Dolce, E. D’Alema, and M. Maistrello (2006). Buildings as a seismic source: Analysis of a release test at Bagnoli, Italy. *Bulletin of the Seismological Society of America* 96(6), 2457–2464.
- Ganzua, E. (2006). Seismic behavior of hybrid lateral-force-resisting systems. Master’s thesis, State University of New York at Buffalo, Buffalo, NY.
- Garnier, J., C. Gaudin, S. M. Springman, P. J. Culligan, D. Goodings, D. Konig, B. Kutter, R. Phillips, M. F. Randolph, and L. Thorel (2007). Catalogue of scaling laws and similitude questions in geotechnical centrifuge modelling. *International Journal of Physical Modelling in Geotechnics* 3, 1–23.
- Gazetas, G. (1991). Foundation vibrations. In H.-Y. Fang (Ed.), *Foundation Engineering Handbook* (2nd ed.). New York, NY: Chapman and Hall.
- Ghergu, M. and I. R. Ionescu (2009). Structure-soil-structure coupling in seismic excitation and “city effect”. *International Journal of Engineering Science* 47(3), 342–354.
- Guéguen, P., P.-Y. Y. Bard, and C. S. Oliveira (2000). Experimental and numerical analysis of soil motions caused by free vibrations of a building model. *Bulletin of the Seismological Society of America* 90(6), 1464–1479.
- Hanks, T. C. and W. H. Bakun (2002). A bilinear source-scaling model for M-log A observations of continental earthquakes. *Bulletin of the Seismological Society of America* 92, 1841–1846.
- Hanks, T. C. and A. G. Brady (1991). The Loma Prieta earthquake ground motion, and damage in Oakland, Treasure Island, and San Francisco. *Bulletin of the Seismological Society of America* 81(5), 2019–2047.
- Harden, C., T. Hutchinson, G. R. Martin, and B. L. Kutter (2005). Numerical modeling of the nonlinear cyclic response of shallow foundations. Technical Report PEER 2005/04, Pacific Earthquake Engineering Research Center, Berkeley, CA.

- Hardenbeck, J. L., J. Boatwright, D. Dreger, R. Goel, V. Graizer, K. Hudnut, C. Ji, L. Jones, J. Langbein, J. Lin, E. Roeloffs, R. Simpson, K. Starks, R. Stein, and J. C. Tinsley (2004). Preliminary report on the 22 December 2003 m6.5 San Simeon, California, Earthquake. *Seismological Research Letters* 75(2), 155–172.
- Harichandran, R. S. and E. Vanmarke (1986). Stochastic variation of earthquake ground motion in space and time. *Journal of Engineering Mechanics* 112, 154–174.
- Hausler, E. A. (2002). *Influence of ground improvement on settlement and liquefaction: A study based on field case history evidence and dynamic geotechnical centrifuge tests*. Ph. D. thesis, University of California, Berkeley, Berkeley, CA.
- Housner, G. W. (1957). Interaction of building and ground during an earthquake. *Bulletin of the Seismological Society of America* 47(3), 179–186.
- Huang, Y.-H., A. S. Whittaker, and N. Luco (2008). Maximum spectral demands in the near-fault region. *Earthquake Spectra* 24(1), 319–341.
- Ilnkatharan, M. and B. Kutter (2010). Modeling input motion boundary conditions for simulations of geotechnical shaking table tests. *Earthquake Spectra* 26(2), 349–369.
- Jennings, P. C. (1970). Distant motions from a building vibration test. *Bulletin of the Seismological Society of America* 60(6), 2037–2043.
- Jennings, P. C. and J. Bielak (1973). Dynamics of building-soil interaction. *Bulletin of the Seismological Society of America* 63(1), 9–48.
- Johansson, R. (1993). *System Modeling and Identification*. New Englewood Cliffs, NJ: Prentice Hall, Inc.
- Kanamori, H., J. Mori, D. L. Anderson, and T. H. Heaton (1991). Seismic excitation by the space shuttle Columbia. *Nature* 349, 781–782.
- Kausel, E. (2010). Early history of soil-structure interaction. *Soil Dynamics and Earthquake Engineering* 30(9), 822–832.
- Kausel, E., R. V. Whitman, J. P. Morray, and F. Elsabee (1978). The spring method for embedded foundations. *Nuclear Engineering and Design* 48(2-3), 377–392.
- Kayen, R., R. T. Pack, J. Bay, S. Sugimoto, and H. Tanaka (2006). Terrestrial-LIDAR visualization of surface and structural deformations of the 2004 Niigata Ken Chuetsu, Japan, Earthquake. *Earthquake Spectra* 22(S1), S147–S162.
- Kim, S. and J. P. Stewart (2003). Kinematic soil-structure interaction from strong motion recordings. *Journal of Geotechnical and Geoenvironmental Engineering* 129(4), 323–335.

- Kottke, A. and E. M. Rathje (2008). A semi-automated procedure for selecting and scaling recorded earthquake motions for dynamic analysis. *Earthquake Spectra* 24(4), 911–932.
- Kramer, S. L. (1996). *Geotechnical Earthquake Engineering*. Upper Saddle River, NJ: Prentice Hall.
- Kramer, S. L. (2011). Performance-based design in geotechnical earthquake engineering practice. In *Proceedings of the 5th International Conference on Earthquake Geotechnical Engineering*, Santiago, Chile.
- Kramer, S. L. and J. P. Stewart (2004). Geotechnical aspects of seismic hazards. In Y. B. Bozorgnia and V. V. B. Bertero (Eds.), *Earthquake Engineering: from Engineering Seismology to Performance Based Engineering*. Boca Raton, FL: CRC Press.
- Kutter, B., L. Deng, and S. Kunnath (2010). Estimation of displacement demand for seismic design of bridges with rocking shallow foundations. In S. Prakash (Ed.), *Proceedings of the Fifth International Conference on Recent Advances in Geotechnical Earthquake Engineering and Soil Dynamics*, Rolla, MO. University of Missouri, Rolla.
- Kutter, B. L. (1995). Recent advances in centrifuge modeling of seismic shaking. In S. Prakash (Ed.), *Proceedings of the Third International Conference on Recent Advances in Geotechnical Earthquake Engineering and Soil Dynamics*, St. Louis, MO.
- Kutter, B. L., I. M. Idriss, T. Kohnke, J. Lakeland, X. S. Li, W. Sluis, X. Zeng, R. C. Tauscher, Y. Goto, and I. Kubodera (1994). Design of a large earthquake simulator at UC Davis. In C. F. Leung, F. H. Lee, and T. S. Tan (Eds.), *Centrifuge 94*, Rotterdam, pp. 169–175. A. A. Balkema.
- Lee, T. H. and D. A. Wesley (1973). Soil-structure interaction of nuclear reactor structures considering through-soil coupling between adjacent structures. *Nuclear Engineering and Design* 24(3), 374–387.
- Liu, L. and R. Dobry (1994). Seismic response of shallow foundations on liquefiable sand. *Journal of Geotechnical and Geoenvironmental Engineering* 123(6), 557–567.
- Luco, J. E. (1969). Dynamic interaction of a shear wall with the soil. *Journal of the Engineering Mechanics Division* 95(EM2), 333–346.
- Luco, J. E. and L. Contesse (1973). Dynamic structure-soil-structure interaction. *Bulletin of the Seismological Society of America* 63(4), 1289–1303.
- Luco, J. E. and A. Mita (1987). Response of circular foundation to spatially random ground motion. *Journal of Engineering Mechanics* 113(1), 1–15.

- Luco, J. E., M. D. Trifunac, and H. L. Wong (1988). Isolation of soil-structure interaction effects by full-scale forced vibration tests. *Earthquake Engineering & Structural Dynamics* 16(1), 1–21.
- Luco, J. E. and H. L. Wong (1986). Response of a rigid foundation to a spatially random ground motion. *Earthquake Engineering & Structural Dynamics* 14(6), 891–908.
- Luco, N. and C. A. Cornell (2007). Structure-specific scalar intensity measures for near-source and ordinary earthquake ground motions. *Earthquake Spectra* 23(2), 357–392.
- Mason, H., N. Trombetta, Z. Chen, B. Choy, C. Bolisetti, J. Bray, T. Hutchinson, B. Kutter, and A. Whittaker (2011a). Seismic performance assessment in dense urban environments: Centrifuge Data Report for HBM02. Technical report, Center for Geotechnical Modeling, Davis, CA.
- Mason, H., N. Trombetta, Z. Chen, B. Choy, C. Bolisetti, J. Bray, T. Hutchinson, B. Kutter, and A. Whittaker (2011b). Seismic performance assessment in dense urban environments: Centrifuge Data Report for HBM03. Technical report, Center for Geotechnical Modeling, Davis, CA.
- Mason, H., N. Trombetta, Z. Chen, B. Choy, C. Bolisetti, J. Bray, T. Hutchinson, B. Kutter, and A. Whittaker (2011c). Seismic performance assessment in dense urban environments: Centrifuge Data Report for HBM04. Technical report, Center for Geotechnical Modeling, Davis, CA.
- Mason, H. B., J. D. Bray, B. L. Kutter, D. W. Wilson, and B. Y. Choy (2010). Earthquake motion selection and calibration for use in a geotechnical centrifuge. In S. Springman, J. Laue, and L. Seward (Eds.), *Proceedings of the Seventh International Conference on Physical Modelling in Geotechnics*, London, England. Taylor & Francis.
- Merritt, R. G. and G. W. Housner (1954). Effect of foundation compliance on earthquake stresses in multistory buildings. *Bulletin of the Seismological Society of America* 44(4), 551–569.
- Mucciarelli, M., M. R. Gallipoli, F. Ponzio, and M. Dolce (2003). Seismic waves generated by oscillating buildings: analysis of a release test. *Soil Dynamics and Earthquake Engineering* 23, 255–262.
- Mulliken, J. S. and D. L. Karabalis (1998). Discrete model for dynamic through-the-soil coupling of 3-D foundations and structures. *Earthquake Engineering & Structural Dynamics* 27(7), 687–710.
- Mylonakis, G. and G. Gazetas (2000). Seismic soil-structure interaction: Beneficial or detrimental? *Journal of Earthquake Engineering* 4(3), 277–301.

- Mylonakis, G., S. Nikolaou, and G. Gazetas (2006). Footings under seismic loading: Analysis and design issues with emphasis on bridge foundations. *Soil Dynamics and Earthquake Engineering* 26, 824–853.
- Mylonakis, G., C. Syngros, G. Gazetas, and T. Tazoh (2006). The role of soil in the collapse of 18 piers of Hanshin Expressway in the Kobe Earthquake. *Earthquake Engineering & Structural Dynamics* 35(5), 547–575.
- Newmark, N. M. (1965). Effects of earthquakes on dams and embankments. *Geotechnique* 15(2), 139–160.
- Oppenheim, A. V. and R. W. Schaffer (2009). *Discrete-Time Signal Processing* (3rd ed.). New Englewood Cliffs, NJ: Prentice Hall, Inc.
- Oskin, M., K. Sieh, T. Rockwell, G. Miller, P. Gupta, M. Curtis, S. McArdle, and P. Elliot (2000). Active parasitic folds on the Elysian Park anticline: Implications for seismic hazard in central Los Angeles, California. *GSA Bulletin* 112(5), 693–707.
- Padrón, L. A., J. J. Aznárez, and O. Maeso (2009). Dynamic structure-soil-structure interaction between nearby piled buildings under seismic excitation by bem-fem model. *Soil Dynamics and Earthquake Engineering* 29(6), 1084–1096.
- Pais, A. and E. Kausel (1988). Approximate formulas for dynamic stiffnesses of rigid foundations. *Soil Dynamics and Earthquake Engineering* 7(4), 213–227.
- Parmelee, R. A., D. S. Perelman, and S.-L. Lee (1969). Seismic response of multiple-story structures on flexible foundations. *Bulletin of the Seismological Society of America* 29(3), 1061–1070.
- Peterson, M. D., A. D. Frankel, S. C. Harmsen, C. S. Mueller, K. M. Haller, R. L. Wheeler, R. L. Wesson, Y. Zeng, O. S. Boyd, D. M. Perkins, N. Luco, E. H. Field, C. J. Wills, and K. S. Rukstales (2008). Documentation for the 2008 update of the United States National Seismic Hazard Maps. Technical Report U.S. Geological Survey Open-File Report 2008-1128, United States Geological Survey, Reston, VA. Available online: <http://pubs.usgs.gov/of/2008/1128/>.
- Pitilakis, D., M. Dietz, D. M. Wood, D. Clouteau, and A. Modaressi (2008). Numerical simulation of dynamic soil-structure interaction in shaking table testing. *Soil Dynamics and Earthquake Engineering* 28, 453–467.
- Porter, K., L. Jones, D. Cox, J. Goltz, K. Hudnut, D. Miletic, S. Perry, D. Ponti, M. Reichle, A. Z. Rose, C. R. Scawthorn, H. A. Seligson, K. I. Shoaf, J. Treiman, and A. Wein (2011). The ShakeOut scenario: A hypothetical M_w 7.8 earthquake on the Southern San Andreas Fault. *Earthquake Spectra* 27(2), 239–261.

- Power, M., B. Chiou, N. Abrahamson, Y. Bozorgnia, T. Shantz, and C. Roblee (2008). An overview of the NGA project. *Earthquake Spectra* 24(1), 3–21.
- Puangnak, H., B. L. Kutter, H. B. Mason, B. Choy, and J. D. Bray (2012). Constructive and destructive footing-soil-footing interaction for vertically vibrating footings. In *Proceedings of GeoCongress 2012*, Oakland, CA.
- Qian, J. and D. E. Beskos (1995). Dynamic interaction between 3-D rigid surface foundations and comparison with the ATC-3 provisions. *Earthquake Engineering & Structural Dynamics* 24(3), 419–437.
- Rathje, E. M. and B. J. Adams (2008). The role of remote sensing in earthquake science and engineering: Opportunities and challenges. *Earthquake Spectra* 24(2), 471–492.
- Raychowdhury, P. (2009). *Nonlinear Winkler-based Shallow Foundation Model for Performance Assessment of Seismically Loaded Structures*. Ph. D. thesis, University of California, San Diego, La Jolla, CA.
- Scott, M. H. and G. L. Fenves (2006). Plastic hinge integration methods for force-based beam-column elements. *Journal of Structural Engineering* 132(2), 244–252.
- Shahi, S. K. and J. W. Baker (2011). An empirically calibrated framework for including the effects of near-fault directivity in probabilistic seismic hazard analysis. *Bulletin of the Seismological Society of America* 101(2), 742–755.
- Somerville, P. G., N. F. Smith, R. W. Graves, and N. A. Abrahamson (1997). Modifications of empirical strong ground motion attenuation relations to include the amplitude and duration effects of rupture directivity. *Seismological Research Letters* 68(1), 199–222.
- Spudich, P. and B. S. J. Chiou (2008). Directivity in NGA earthquake ground motions: Analysis using isochrone theory. *Earthquake Spectra* 24(1), 279–298.
- Stewart, J. P. (1996). *An Empirical Assessment of Soil-Structure Interaction Effects on the Seismic Response of Structure*. Ph. D. thesis, University of California, Berkeley, Berkeley, CA.
- Stewart, J. P., G. L. Fenves, and R. B. Seed (1999a). Seismic soil-structure interaction in buildings. I: Analytical methods. *Journal of Geotechnical and Geoenvironmental Engineering* 125(1), 26–37.
- Stewart, J. P., G. Mylonakis, M. Givens, T. Hutchinson, and F. Ostadan (Forthcoming). *Baseline Knowledge Report on Soil-Foundation-Structure Interaction of Building Structures*. Redwood City, CA: Applied Technology Council.

- Stewart, J. P., R. B. Seed, and G. L. Fenves (1998). Empirical evaluation of inertial soil-structure interaction effects. Technical Report PEER-98/07, Pacific Earthquake Engineering Research Center, Berkeley, CA.
- Stewart, J. P., R. B. Seed, and G. L. Fenves (1999b). Seismic soil-structure interaction in buildings. II: Empirical findings. *Journal of Geotechnical and Geoenvironmental Engineering* 125(1), 38–48.
- Stewart, J. P. and S. Tileylioglu (2007). Input ground motions for tall buildings with subterranean levels. *The Structural Design of Tall and Special Buildings* 16(5), 543–557.
- Taborda, R. (2010). *Three Dimensional Nonlinear Soil and Site-City Effects in Urban Regions*. Ph. D. thesis, Carnegie Mellon University, Pittsburgh, PA.
- Trifunac, M. D. (1972). Interaction of a shear wall with the soil for incident plane SH waves. *Bulletin of the Seismological Society of America* 62(1), 63–83.
- Veletsos, A. S. and J. W. Meek (1974). Dynamic behaviour of building-foundation systems. *Earthquake Engineering & Structural Dynamics* 3(2), 121–138.
- Veletsos, A. S. and V. V. D. Nair (1975). Seismic interaction of structures on hysteretic foundations. *Journal of the Structural Division* 101(1), 109–129.
- Veletsos, A. S. and A. M. Prasad (1989). Seismic interaction of structures and soils: stochastic approach. *Journal of Structural Engineering* 115(4), 935–956.
- Veletsos, A. S., A. M. Prasad, and W. H. Wu (1997). Transfer functions for rigid rectangular foundations. *Earthquake Engineering & Structural Dynamics* 26(1), 5–17.
- Veletsos, A. S. and B. Verbic (1973). Vibration of viscoelastic foundations. *Earthquake Engineering & Structural Dynamics* 2(1), 87–102.
- Veletsos, A. S. and Y. T. Wei (1971). Lateral and rocking vibration of footings. *Journal of the Soil Mechanics and Foundations Division* 97(SM9), 1227–1248.
- Wirgin, A. and P.-Y. Y. Bard (1996). Effects of buildings on the duration and amplitude of ground motion in Mexico City. *Bulletin of the Seismological Society of America* 86(3), 914–920.
- Wolf, J. P. (1985). *Dynamic Soil-Structure Interaction*. Upper Saddle River, NJ: Prentice Hall, Inc.
- Wong, H. L. and M. D. Trifunac (1975). Two-dimensional, antiplane, building-soil-building interaction for two or more buildings and for incident planet SH waves. *Bulletin of the Seismological Society of America* 65(6), 1863–1885.

Appendix A

Known Limitations & Instrumentation Tables

A.1 Known Data limitations

Best construction practices were used to place the structural models in the model container. However, due to the fact that imperfections existed in the construction of the building components, the models were not perfectly in line and parallel with the container edges. During each centrifuge test, measurements were taken of the structures location in the container (prior to spinning and post-spinning). These measurements are located in the respective test data reports.

During Test-3, once during the model construction, and once when the model was on the arm, sand was vacuumed from the model and replaced using a small bucket pluviator. There was no way to ensure that the replaced sand was at the target relative density (80% during model construction, and somewhat higher when the model was on the arm due to the shaking-induced densification). Since only the top 30 mm of soil was disturbed during these processes, it was judged as more beneficial to disturb the soil than to continue with poor instrumentation or misaligned structures.

A number of sensors did not work during the different spins during all three tests. These bad sensors were tracked after every ground motion. Between spins, attempts were made to repair non-working sensors. In addition, a number of sensors did not work, or were deemed to have recorded inaccurate data during a given motion. The data reports for the respective tests more details about malfunctioning sensors.

Significant drift in the strain gages affected measurements during spin-up, while in flight, during spin-down, and while at 1 g. Due to the short duration of ground motions the dynamic measurements are not affected by the drift.

In addition to the drifting, some of the strain gages show odd “nose-diving” behavior. This is likely non-physical, though its exact cause (or causes) is unknown. The dynamic

strain data from these gages is likely correct, but the nose-diving problem should be kept in mind when examining and interpreting the data.

The MEMS accelerometers malfunctioned often during all three centrifuge tests. This issue was deemed to not be with the MEMS accelerometers themselves, but with problem associated with their connection to the DAQ.

A.2 Tables of Important Instrumentation

The following tables list important instrumentation (soil, structure and container) used for all three tests. The instrument name, instrument type and location of the instrument are given in this table. More complete information about the instrumentation is given in the data reports for each test.

Centrifuge Test-1

No.	Label	Type	Location
1	HA3	ICP	Southside of container on base plate
2	HA1	ICP	East container at base
3	HA2	ICP	West container at base
4	HA4	ICP	Soil, North container at half elevation
5	HA5	ICP	Soil, South container at half elevation
6	HA6	ICP	Soil, North container at basement elevation
7	HA7	ICP	Soil, Center container at basement elevation
8	HA8	ICP	Soil, South container at basement elevation
9	HA9	ICP	Soil, North container at sixth elevation
10	HA10	ICP	Soil, North, center container at sixth elevation
11	HA11	ICP	Soil, Center container at sixth elevation
12	HA12	ICP	Soil, Northside of MS3F_B basement at sixth elevation
13	HA13	ICP	Soil, North, center at surface
14	HA14	ICP	Soil, Center at surface
15	HA15	ICP	Soil, Northside of MS3F_B basement at surface
16	HA16	ICP	Soil, North container at surface
17	HA17	ICP	Soil, West, Center container at surface
18	HA18	ICP	Soil, Southside of MS1F_SF80 at surface
19	HA19	ICP	North on Container
20	HA20	ICP	Upper Rack
21	HA21	ICP	East Shaker (House)
22	HA22	ICP	West Shaker (House)
23	VA1	ICP	Vertical Soil, Southside of MS1F_SF80 at basement elevation
24	VA2	ICP	Vertical Soil, Northside of MS3F_B at basement elevation
25	VA3	ICP	Vertical Soil, Southside of MS3F_B at surface
26	VA4	ICP	Vertical Soil, Northside of MS3F_B at surface
27	VA5	ICP	Vertical Soil, Center at surface
28	VA6	ICP	Vertical Soil, Southside of MS1F_SF80 at surface
29	VA7	ICP	Vertical Soil, Northeast corner at surface
30	VA8	ICP	Vertical Soil, Westside of MS3F_B at surface
31	VA9	ICP	Vertical Soil, Westside of MS1F_SF80 at surface
32	VA10	ICP	North on Container
33	VA11	ICP	South on Container
34	VA12	ICP	North Rack
35	VA13	ICP	Center Rack
36	FA101	ICP	Center Massless Foundation 1 - horizontal
37	FA102	ICP	Center Massless Foundation 1 - vertical
38	FA201	ICP	Northeast Massless Foundation 2 - horizontal
39	FA202	ICP	Southeast Massless Foundation 2 - horizontal
40	FA203	ICP	Center Massless Foundation 2 - vertical
41	FA301	ICP	Center Massless Foundation 3 - horizontal
42	FA302	ICP	Center Massless Foundation 3 - vertical
43	A_MS3FB_1_x_COM	ICP	In-plane @ COM (center-of-mass); 1st floor
44	A_MS3FB_1_y_COM	ICP	Out-of-plane @ COM; 1st floor
45	A_MS3FB_1_z_COM	ICP	Vertical @ COM; 1st floor
46	A_MS3FB_1_x_B3-4	ICP	In-plane @ East Edge of mass; 1st floor
47	A_MS3FB_2_x_COM	ICP	In-plane @ COM; 2 nd floor

48	A_MS3FB_2_y_COM	ICP	Out-of-plane @ COM; 2 nd floor
49	A_MS3FB_2_z_COM	ICP	Vertical @ COM; 2 nd floor
50	A_MS3FB_2_x_B3-4	ICP	In-plane @ East Edge of mass; 2 nd floor
51	A_MS3FB_3_x_COM	ICP	In-plane @ COM; 3 rd floor
52	A_MS3FB_3_y_COM	ICP	Out-of-plane @ COM; 3 rd floor
53	A_MS3FB_3_z_COM	ICP	Vertical @ COM; 3 rd floor
54	A_MS3FB_3_x_B3-4	ICP	In-plane @ East Edge of mass; 3 rd floor
55	A_MS3FB_Ft_x_C2	MEM	In-plane, Top of Foundation near C2 (Column 2)
56	A_MS3FB_Ft_z_C2	MEM	Vertical, Top of Foundation near C2
57	A_MS3FB_Ft_x_C4	MEM	In-plane, Top of Foundation near C4
58	A_MS3FB_Ft_z_C4	MEM	Vertical, Top of Foundation near C4
59	A_MS3FB_Ft_z_C1-C3	MEM	Vertical, Top of Foundation between C1/C3
60	A_MS3FB_Ft_y_C1-C3	MEM	Out-of-plane, Top of Foundation between C1/C3
61	A_MS3FB_Fb_y_C1-C3	ICP	Out-of-plane, Bottom of Foundation between C1/C3
62	A_MS3FB_Fb_x_C2-C4	ICP	In-plane, Bottom of Foundation between C2/C4
63	A_MS3FB_Fm_x_C2-C4	ICP	In-plane, Mid-Height of Foundation between C2/C4
64	A_MS1FS_1_x_COM	ICP	In-plane @ COM
65	A_MS1FS_1_y_COM	ICP	Out-of-plane @ COM
66	A_MS1FS_1_z_COM	ICP	Vertical @ COM
67	A_MS1FS_1_x_B3-4	ICP	In-plane @ East Edge of mass
68	A_MS1FS_f_x_F1	MEM	In-plane, F1 (Footing 1)
69	A_MS1FS_f_x_F2	MEM	In-plane, F2
70	A_MS1FS_f_x_F3	MEM	In-plane, F3
71	A_MS1FS_f_z_F1(N)	MEM	Vertical, F1 (N)
72	A_MS1FS_f_z_F1(S)	MEM	Vertical, F1 (S)
73	A_MS1FS_f_z_F2(N)	MEM	Vertical, F2 (N)
74	A_MS1FS_f_z_F2(S)	MEM	Vertical, F2 (S)
75	A_MS1FS_f_z_F3(N)	MEM	Vertical, F3 (N)
76	A_MS1FS_f_z_F3(S)	MEM	Vertical, F3 (S)
77	D1	Displ. Gage	Soil, North container at half elevation
78	D2	Displ. Gage	Soil, North container at quarter elevation
79	D3	Displ. Gage	Soil, Center container at quarter elevation
80	D4	Displ. Gage	Soil, South of container at quarter elevation
81	D5	Displ. Gage	Soil, Southside MS1F_SF80 at surface
82	D6	Displ. Gage	Soil, Northside MS3F_B at surface
83	D7	Displ. Gage	Soil, Center east container at surface
84	D8	Displ. Gage	Soil, Center west container at surface
85	D9	Displ. Gage	Soil, Eastside of MS1F_SF80 at surface
86	D10	Displ. Gage	Soil, Eastside of MS3F_B at surface
87	D_MS3FB_1_x_C1	Displ. Gage	Horizontal, C1 at 1st Story Height
88	D_MS3FB_1_x_C3	Displ. Gage	Horizontal, C3 at 1st Story Height
89	D_MS3FB_2_x_C1	Displ. Gage	Horizontal, C1 at 2nd Story Height
90	D_MS3FB_2_x_C3	Displ. Gage	Horizontal, C3 at 2nd Story Height
91	D_MS3FB_3_x_C1	Displ. Gage	Horizontal, C1 at 3rd Story Height
92	D_MS3FB_3_x_C3	Displ. Gage	Horizontal, C3 at 3rd Story Height
93	D_MS3FB_Ft_x_C1	Displ. Gage	Horizontal, Top of Foundation near C1
94	D_MS3FB_Ft_x_C3	Displ. Gage	Horizontal, Top of Foundation near C3
95	D_MS3FB_Ft_z_C1-C3	Displ. Gage	Vertical, Top of Foundation between C1/C3
96	D_MS3FB_Ft_z_C2-C4	Displ. Gage	Vertical, Top of Foundation between C2/C4

97	D_MS1FS_1_x_C2	Displ. Gage	Horizontal, C2 at 1st Floor Height
98	D_MS1FS_1_x_C4	Displ. Gage	Horizontal, C4 at 1st Floor Height
99	D_MS1FS_f_x_F2	Displ. Gage	Horizontal, F2
100	D_MS1FS_f_x_F1	Displ. Gage	Horizontal, F1
101	D_MS1FS_f_z_F2(COR)	Displ. Gage	Vertical, F2 corner
102	D_MS1FS_f_x_F3	Displ. Gage	Horizontal, F3
103	D_MS1FS_f_x_F4	Displ. Gage	Horizontal, F4
104	D_MS1FS_f_z_F1(COR)	Displ. Gage	Vertical, F1corner
105	D_MS1FS_f_z_F4(N)	Displ. Gage	Vertical, F4 northside
106	D_MS1FS_f_z_F4(S)	Displ. Gage	Vertical, F4 southside
107	D_MS1FS_f_z_F3(N)	Displ. Gage	Vertical, F3 northside
108	D_MS1FS_f_z_F3(S)	Displ. Gage	Vertical, F3 southside
109	SA_MS3FB_1_NT_B1-2	Strain Gage	Top of F1 B1-2 Fuse nearest to C1
110	SA_MS3FB_1_NB_B1-2	Strain Gage	Bottom of F1 B1-2 Fuse nearest to C1
111	SA_MS3FB_1_NT_B3-4	Strain Gage	Top of F1 B3-4 Fuse nearest to C3
112	SA_MS3FB_1_NB_B3-4	Strain Gage	Bottom of F1 B3-4 Fuse nearest to C3
113	SA_MS3FB_1_N_C1	Strain Gage	C1 (N) below 1st Floor B/C connection
114	SA_MS3FB_1_S_C1	Strain Gage	C1 (S) below 1st Floor B/C connection
115	SA_MS3FB_1_N_C2	Strain Gage	C2 (N) below 1st Floor B/C connection
116	SA_MS3FB_1_S_C2	Strain Gage	C2 (S) below 1st Floor B/C connection
117	SA_MS3FB_1_S_C3	Strain Gage	C3 (S) below 1st Floor B/C connection
118	SA_MS3FB_1_N_C3	Strain Gage	C3 (N) below 1st Floor B/C connection
119	SR_MS3FB_1_E_C1	Strain Gage	C1 (W) at mid-height of 1st Story
120	SR_MS3FB_1_E_C2	Strain Gage	C2 (W) at mid-height of 1st Story
121	SR_MS3FB_1_E_C3	Strain Gage	C3 (E) at mid-height of 1st Story
122	SR_MS3FB_1_E_C4	Strain Gage	C4 (E) at mid-height of 1st Story
123	SA_MS3FB_1_ST_B1-2	Strain Gage	Top of F1 B1-2 Fuse nearest to C2
124	SA_MS3FB_1_SB_B1-2	Strain Gage	Bottom of F1 B1-2 Fuse nearest to C2
125	SA_MS3FB_1_ST_B3-4	Strain Gage	Top of F1 B3-4 Fuse nearest to C4
126	SA_MS3FB_1_SB_B3-4	Strain Gage	Bottom of F1 B3-4 Fuse nearest to C4
127	SA_MS3FB_0_N_C1	Strain Gage	C1 (N) at column fuse
128	SA_MS3FB_0_S_C1	Strain Gage	C1 (S) at column fuse
129	SA_MS3FB_0_N_C2	Strain Gage	C2 (N) at column fuse
130	SA_MS3FB_0_S_C2	Strain Gage	C2 (S) at column fuse
131	SA_MS3FB_0_S_C3	Strain Gage	C3 (S) at column fuse
132	SA_MS3FB_0_N_C3	Strain Gage	C3 (N) at column fuse
133	SA_MS3FB_0_S_C4	Strain Gage	C4 (S) at column fuse
134	SA_MS3FB_0_N_C4	Strain Gage	C4 (N) at column fuse
135	SA_MS3FB_2_NT_B1-2	Strain Gage	Top of F2 B1-2 Fuse nearest to C1
136	SA_MS3FB_2_NB_B1-2	Strain Gage	Bottom of F2 B1-2 Fuse nearest to C1
137	SA_MS3FB_2_NT_B3-4	Strain Gage	Top of F2 B3-4 Fuse nearest to C3
138	SA_MS3FB_2_NB_B3-4	Strain Gage	Bottom of F2 B3-4 Fuse nearest to C3
139	SA_MS3FB_2_N_C1	Strain Gage	C1 (N) below 2nd Floor B/C connection
140	SA_MS3FB_2_S_C1	Strain Gage	C1 (S) below 2nd Floor B/C connection
141	SA_MS3FB_2_N_C2	Strain Gage	C2 (N) below 2nd Floor B/C connection
142	SA_MS3FB_2_S_C2	Strain Gage	C2 (S) below 2nd Floor B/C connection
143	SA_MS3FB_2_S_C3	Strain Gage	C3 (S) below 2nd Floor B/C connection
144	SA_MS3FB_2_N_C3	Strain Gage	C3 (N) below 2nd Floor B/C connection
145	SR_MS3FB_2_E_C1	Strain Gage	C1 (W) at mid-height of 2nd Story

146	SR_MS3FB_2_E_C2	Strain Gage	C2 (W) at mid-height of 2nd Story
147	SR_MS3FB_2_E_C3	Strain Gage	C3 (E) at mid-height of 2nd Story
148	SR_MS3FB_2_E_C4	Strain Gage	C4 (E) at mid-height of 2nd Story
149	SA_MS3FB_2_ST_B1-2	Strain Gage	Top of F2 B1-2 Fuse nearest to C2
150	SA_MS3FB_2_SB_B1-2	Strain Gage	Bottom of F2 B1-2 Fuse nearest to C2
151	SA_MS3FB_2_ST_B3-4	Strain Gage	Top of F2 B3-4 Fuse nearest to C4
152	SA_MS3FB_2_SB_B3-4	Strain Gage	Bottom of F2 B3-4 Fuse nearest to C4
153	SA_MS3FB_3_NT_B1-2	Strain Gage	Top of F3 B1-2 Fuse nearest to C1
154	SA_MS3FB_3_NB_B1-2	Strain Gage	Bottom of F3 B1-2 Fuse nearest to C1
155	SA_MS3FB_3_NT_B3-4	Strain Gage	Top of F3 B3-4 Fuse nearest to C3
156	SA_MS3FB_3_NB_B3-4	Strain Gage	Bottom of F3 B3-4 Fuse nearest to C3
157	SA_MS3FB_3_N_C1	Strain Gage	C1 (N) below 3rd Floor B/C connection
158	SA_MS3FB_3_S_C1	Strain Gage	C1 (S) below 3rd Floor B/C connection
159	SA_MS3FB_3_N_C2	Strain Gage	C2 (N) below 3rd Floor B/C connection
160	SA_MS3FB_3_S_C2	Strain Gage	C2 (S) below 3rd Floor B/C connection
161	SA_MS3FB_3_S_C3	Strain Gage	C3 (S) below 3rd Floor B/C connection
162	SA_MS3FB_3_N_C3	Strain Gage	C3 (N) below 3rd Floor B/C connection
163	SR_MS3FB_3_E_C1	Strain Gage	C1 (W) at mid-height of 3rd Story
164	SR_MS3FB_3_E_C2	Strain Gage	C2 (W) at mid-height of 3rd Story
165	SR_MS3FB_3_E_C3	Strain Gage	C3 (E) at mid-height of 3rd Story
166	SR_MS3FB_3_E_C4	Strain Gage	C4 (E) at mid-height of 3rd Story
167	SA_MS3FB_3_ST_B1-2	Strain Gage	Top of F3 B1-2 Fuse nearest to C2
168	SA_MS3FB_3_SB_B1-2	Strain Gage	Bottom of F3 B1-2 Fuse nearest to C2
169	SA_MS3FB_3_ST_B3-4	Strain Gage	Top of F3 B3-4 Fuse nearest to C4
170	SA_MS3FB_3_SB_B3-4	Strain Gage	Bottom of F3 B3-4 Fuse nearest to C4
171	SA_MS3FB_1_S_C4	Strain Gage	C4 (S) below 1st Floor B/C connection
172	SA_MS3FB_1_N_C4	Strain Gage	C4 (N) below 1st Floor B/C connection
173	SA_MS3FB_2_S_C4	Strain Gage	C4 (S) below 2nd Floor B/C connection
174	SA_MS3FB_2_N_C4	Strain Gage	C4 (N) below 2nd Floor B/C connection
175	SA_MS3FB_3_S_C4	Strain Gage	C4 (S) below 3rd Floor B/C connection
176	SA_MS3FB_3_N_C4	Strain Gage	C4 (N) below 3rd Floor B/C connection
177	SA_MS1FS_1_NT_B1-2	Strain Gage	Top of B1-2 Fuse nearest to C1
178	SA_MS1FS_1_NB_B1-2	Strain Gage	Bottom of B1-2 Fuse nearest to C1
179	SA_MS1FS_1_NT_B3-4	Strain Gage	Top of B3-4 Fuse nearest to C3
180	SA_MS1FS_1_NB_B3-4	Strain Gage	Bottom of B3-4 Fuse nearest to C3
181	SA_MS1FS_1_N_C1	Strain Gage	C1 (N) below B/C connection
182	SA_MS1FS_1_S_C1	Strain Gage	C1 (S) below B/C connection
183	SA_MS1FS_1_N_C2	Strain Gage	C2 (N) below B/C connection
184	SA_MS1FS_1_S_C2	Strain Gage	C2 (S) below B/C connection
185	SA_MS1FS_1_S_C3	Strain Gage	C3 (S) below B/C connection
186	SA_MS1FS_1_N_C3	Strain Gage	C3 (N) below B/C connection
187	SR_MS1FS_1_E_C1	Strain Gage	C1 (E) at mid-height
188	SR_MS1FS_1_E_C2	Strain Gage	C2 (E) at mid-height
189	SR_MS1FS_1_E_C3	Strain Gage	C3 (E) at mid-height
190	SR_MS1FS_1_E_C4	Strain Gage	C4 (E) at mid-height
191	SA_MS1FS_0_N_C1	Strain Gage	C1 (N) at column fuse
192	SA_MS1FS_0_S_C1	Strain Gage	C1 (S) at column fuse
193	SA_MS1FS_0_N_C2	Strain Gage	C2 (N) at column fuse
194	SA_MS1FS_0_S_C2	Strain Gage	C2 (S) at column fuse

195	SA_MS1FS_1_ST_B1-2	Strain Gage	Top of B1-2 Fuse nearest to C2
196	SA_MS1FS_1_SB_B1-2	Strain Gage	Bottom of B1-2 Fuse nearest to C2
197	SA_MS1FS_1_ST_B3-4	Strain Gage	Top of B3-4 Fuse nearest to C4
198	SA_MS1FS_1_SB_B3-4	Strain Gage	Bottom of B3-4 Fuse nearest to C4
199	SA_MS1FS_1_S_C4	Strain Gage	C4 (S) below B/C connection
200	SA_MS1FS_1_N_C4	Strain Gage	C4 (N) below B/C connection
201	SA_MS1FS_0_S_C3	Strain Gage	C3 (S) at column fuse
202	SA_MS1FS_0_N_C3	Strain Gage	C3 (N) at column fuse
203	SA_MS1FS_0_S_C4	Strain Gage	C4 (S) at column fuse
204	SA_MS1FS_0_N_C4	Strain Gage	C4 (N) at column fuse

Centrifuge Test-2

No.	Label	Type	Location
1	HA1	ICP	Soil, East container at base
2	HA2	ICP	Soil, West container at base
3	HA3	ICP	Soil, West container at base
4	HA4	ICP	Soil, Center container at half elevation
5	HA5	ICP	Soil, North container at basement elevation
6	HA6	ICP	Soil, Center container at basement elevation
7	HA7	ICP	Soil, South container at basement elevation
8	HA8	ICP	Soil, North container at quarter basement elevation
9	HA9	ICP	Soil, North container at quarter basement elevation under north footings
10	HA10	ICP	Soil, Center container at quarter basement elevation
11	HA11	ICP	Soil, South container at quarter basement elevation
12	HA12	ICP	Soil, North container at surface
13	HA13	ICP	Soil, Center container at surface
14	HA14	ICP	Soil, South container at surface
15	HA15	ICP	Soil, Middle of MS1F_SF80 at surface
16	HA16	ICP	Soil, West container at surface
17	HA17	ICP	Soil, North Free Field at half elevation
18	HA18	ICP	Soil, North Free Field at basement elevation
19	HA19	ICP	Soil, North Free Field at quarter elevation
20	HA20	ICP	Soil, North Free Field at surface elevation
21	HA21	ICP	Soil, South Free Field at quarter elevation
22	HA22	ICP	Soil, South Free Field at surface elevation
23	HA23	ICP	North on container
24	HA24	ICP	East shaker (house)
25	HA25	ICP	West shaker (house)
26	VA1	ICP	Vertical Soil, Southside of MS3F_B at surface
27	VA2	ICP	Vertical Soil, Center at surface
28	VA3	ICP	Vertical Soil, Between the south footings of MS1F_SF80 at surface
29	VA4	ICP	Vertical Soil, North of MS1F_SF80 at surface
30	VA5	ICP	Vertical Soil, West of MS3F_B at surface
31	VA6	ICP	Vertical, Northside on Container
32	VA7	ICP	Vertical, Southside on Container
33	FA101	ICP	Edge Massless Foundation, horizontal
34	FA102	ICP	Edge Massless Foundation, vertical
35	FA201	ICP	Middle Massless Foundation, horizontal
36	FA202	MEM	Middle Massless Foundation, vertical
37	FA301	ICP	Closest Massless Foundation, horizontal
38	FA302	MEM	Closest Massless Foundation, north vertical
39	FA303	MEM	Closest Massless Foundation, south vertical
40	A_MS1FS_f_x_F1	ICP	In-plane MS1F_SF80 Column 1
41	A_MS1FS_f_x_F2	ICP	In-plane, MS1F_SF80 Column 2
42	A_MS1FS_f_x_F4	ICP	In-plane, MS1F_SF80 Column 4
43	A_MS1FS_f_z_F1(N)	ICP	Vertical, MS1F_SF80 Column 1 north
44	A_MS1FS_f_z_F1(S)	ICP	Vertical, MS1F_SF80 Column 1 south
45	A_MS1FS_f_z_F2(N)	ICP	Vertical, MS1F_SF80 Column 2 north

46	A_MS1FS_f_z_F2(S)	ICP	Vertical, MS1F_SF80 Column 2 south
47	A_MS1FS_f_z_F4(N)	ICP	Vertical, MS1F_SF80 Column 4 north
48	A_MS1FS_f_z_F4(S)	ICP	Vertical, MS1F_SF80 Column 4 south
49	A_MS1FS_1_x_COM	ICP	In-plane, MS1F_SF80 Floor 1 COM
50	A_MS1FS_1_y_COM	ICP	Out-of-plane, MS1F_SF80 Floor 1 COM
51	A_MS1FS_1_z_COM	MEM	Vertical, MS1F_SF80 Floor 1 COM
52	A_MS1FS_1_x_B3-4	ICP	In-plane, MS1F_SF80 Floor 1, between C3 and C4 (Shaker 1 Center)
53	A_MS3FB_Fb_x_Center	ICP	In-plane, Bottom of basement foundation, center
54	A_MS3FB_Fb_y_Center	ICP	Out-of-plane, Bottom of basement foundation, center
55	A_MS3FB_F1/4_x_C1-C3	ICP	In-plane, Quarter of basement foundation, between C1 and C3
56	A_MS3FB_Ft_x_C2	MEM	In-plane, Top of basement, Column 2
57	A_MS3FB_Ft_x_C4	MEM	In-plane, Top of basement, Column 4
58	A_MS3FB_Ft_y_C1-C2	MEM	Out-of-plane, Top of basement, between C1 and C2
59	A_MS3FB_Ft_z_C1-C3	MEM	Vertical, Top of basement, between C1 and C3
60	A_MS3FB_Ft_z_C2	MEM	Vertical, Top of basement, Column 2
61	A_MS3FB_Ft_z_C4	MEM	Vertical, Top of basement, Column 4
62	A_MS3FB_1_x_COM	ICP	In-plane, MS3F_B Floor 1 COM
63	A_MS3FB_1_y_COM	ICP	Out-of-plane, MS3F_B Floor 1 COM
64	A_MS3FB_1_x_B3-4	ICP	In-plane, MS3F_B Floor 1, between C3 and C4
65	A_MS3FB_2_x_COM	ICP	In-plane, MS3F_B Floor 2 COM
66	A_MS3FB_2_y_COM	ICP	Out-of-plane, MS3F_B Floor 2 COM
67	A_MS3FB_2_x_B3-4	ICP	In-plane, MS3F_B Floor 2, between C3 and C4
68	A_MS3FB_3_x_COM	ICP	In-plane, MS3F_B Floor 3 COM
69	A_MS3FB_3_y_COM	ICP	Out-of-plane, MS3F_B Floor 3 COM
70	A_MS3FB_3_z_COM	MEM	Vertical, MS3F_B Floor 3 COM
71	A_MS3FB_3_x_B3-4	ICP	In-plane, MS3F_B Floor 3, between C3 and C4 (Shaker 2 Center)
72	RA1	ICP	Displacement Rack Performance
73	RA2	ICP	Displacement Rack Performance
74	RA3	ICP	Displacement Rack Performance
75	D1	Displ. Gage	Soil, Northside of MS1F_SF80, basement elevation
76	D2	Displ. Gage	Soil, Northside of MS1F_SF80, half basement elevation
77	D3	Displ. Gage	Soil, Center of container, half basement elevation
78	D4	Displ. Gage	Soil, Southside of MS3F_B, half basement elevation
79	D5	Displ. Gage	Soil, Center of container, surface
80	D6	Displ. Gage	Soil, East of container, surface
81	D7	Displ. Gage	Soil, West of container, surface
82	D8	Displ. Gage	Soil, Eastside of MS1F_SF80, surface
83	D9	Displ. Gage	Soil, Eastside of MS3F_B, surface
84	D_MS1FS_1_x_C1	Displ. Gage	Horizontal, C1 at 1st Floor Height
85	D_MS1FS_f_x_F1	Displ. Gage	Horizontal, F1
86	D_MS1FS_f_x_F2	Displ. Gage	Horizontal, F2 (RELATIVE TO BASEMENT)
87	D_MS1FS_f_x_F3	Displ. Gage	Horizontal, F3
88	D_MS1FS_f_x_F4	Displ. Gage	Horizontal, F4 (RELATIVE TO BASEMENT)
89	D_MS1FS_f_z_F3(COR)	Displ. Gage	Vertical, F3 corner
90	D_MS1FS_f_z_F4(COR)	Displ. Gage	Vertical, F4 corner
91	D_MS1FS_f_z_F2(S)	Displ. Gage	Vertical, F2 (S)

92	D_MS1FS_f_z_F2(N)	Displ. Gage	Vertical, F2 (N)
93	D_MS1FS_f_z_F1(S)	Displ. Gage	Vertical, F1 (S)
94	D_MS1FS_f_z_F1(N)	Displ. Gage	Vertical, F2 (N)
95	D_MS3FB_1_x_C2	Displ. Gage	Horizontal, C2 at 1st Story Height
96	D_MS3FB_Ft_x_C2-C4	Displ. Gage	Horizontal, Top of Foundation between C2/C4 (Avg. Sliding)
97	D_MS3FB_Ft_z_C2-C4	Displ. Gage	Vertical, Top of Foundation between C2/C4 (Avg. Settlement)
98	SA_MS1FS_1_NT_B1-2	Strain Gage	Top of B1-2 Fuse nearest to C1
99	SA_MS1FS_1_N_C1	Strain Gage	C1 (N) below B/C connection
100	SA_MS1FS_1_S_C1	Strain Gage	C1 (S) below B/C connection
101	SA_MS1FS_1_N_C2	Strain Gage	C2 (N) below B/C connection
102	SA_MS1FS_1_S_C2	Strain Gage	C2 (S) below B/C connection
103	SR_MS1FS_1_E_C1	Strain Gage	C1 (E) at mid-height
104	SR_MS1FS_1_E_C2	Strain Gage	C2 (E) at mid-height
105	SR_MS1FS_1_E_C3	Strain Gage	C3 (E) at mid-height
106	SR_MS1FS_1_E_C4	Strain Gage	C4 (E) at mid-height
107	SA_MS1FS_0_N_C1	Strain Gage	C1 (N) at column fuse
108	SA_MS1FS_0_S_C1	Strain Gage	C1 (S) at column fuse
109	SA_MS1FS_0_N_C2	Strain Gage	C2 (N) at column fuse
110	SA_MS1FS_0_S_C2	Strain Gage	C2 (S) at column fuse
111	SA_MS1FS_1_ST_B1-2	Strain Gage	Top of B1-2 Fuse nearest to C2
112	SA_MS1FS_1_SB_B1-2	Strain Gage	Bottom of B1-2 Fuse nearest to C2
113	SA_MS1FS_0_S_C3	Strain Gage	C3 (S) at column fuse
114	SA_MS1FS_0_N_C3	Strain Gage	C3 (N) at column fuse
115	SA_MS1FS_0_S_C4	Strain Gage	C4 (S) at column fuse
116	SA_MS1FS_0_N_C4	Strain Gage	C4 (N) at column fuse
117	SA_MS1FS_1_NT_B3-4	Strain Gage	Top of B3-4 Fuse nearest to C3
118	SA_MS1FS_1_NB_B3-4	Strain Gage	Bottom of B3-4 Fuse nearest to C3
119	SA_MS1FS_1_S_C3	Strain Gage	C3 (S) below B/C connection
120	SA_MS1FS_1_N_C3	Strain Gage	C3 (N) below B/C connection
121	SA_MS1FS_1_ST_B3-4	Strain Gage	Top of B3-4 Fuse nearest to C4
122	SA_MS1FS_1_SB_B3-4	Strain Gage	Bottom of B3-4 Fuse nearest to C4
123	SA_MS1FS_1_S_C4	Strain Gage	C4 (S) below B/C connection
124	SA_MS1FS_1_N_C4	Strain Gage	C4 (N) below B/C connection
125	SA_MS3FB_1_NB_B1-2	Strain Gage	Bottom of F1 B1-2 Fuse nearest to C1
126	SA_MS3FB_1_N_C1	Strain Gage	C1 (N) below 1st Floor B/C connection
127	SA_MS3FB_1_S_C1	Strain Gage	C1 (S) below 1st Floor B/C connection
128	SA_MS3FB_1_S_C2	Strain Gage	C2 (S) below 1st Floor B/C connection
129	SR_MS3FB_1_E_C1	Strain Gage	C1 (E) at mid-height of 1st Story
130	SR_MS3FB_1_E_C2	Strain Gage	C2 (E) at mid-height of 1st Story
131	SR_MS3FB_1_E_C3	Strain Gage	C3 (E) at mid-height of 1st Story
132	SR_MS3FB_1_E_C4	Strain Gage	C4 (E) at mid-height of 1st Story
133	SA_MS3FB_1_ST_B1-2	Strain Gage	Top of F1 B1-2 Fuse nearest to C2
134	SA_MS3FB_1_SB_B1-2	Strain Gage	Bottom of F1 B1-2 Fuse nearest to C2
135	SA_MS3FB_0_N_C1	Strain Gage	C1 (N) at column fuse
136	SA_MS3FB_0_S_C1	Strain Gage	C1 (S) at column fuse
137	SA_MS3FB_0_N_C2	Strain Gage	C2 (N) at column fuse
138	SA_MS3FB_0_S_C2	Strain Gage	C2 (S) at column fuse
139	SA_MS3FB_0_S_C3	Strain Gage	C3 (S) at column fuse

140	SA_MS3FB_0_N_C3	Strain Gage	C3 (N) at column fuse
141	SA_MS3FB_0_S_C4	Strain Gage	C4 (S) at column fuse
142	SA_MS3FB_0_N_C4	Strain Gage	C4 (N) at column fuse
143	SA_MS3FB_2_NT_B1-2	Strain Gage	Top of F2 B1-2 Fuse nearest to C1
144	SA_MS3FB_2_NB_B1-2	Strain Gage	Bottom of F2 B1-2 Fuse nearest to C1
145	SA_MS3FB_2_N_C1	Strain Gage	C1 (N) below 2nd Floor B/C connection
146	SA_MS3FB_2_S_C1	Strain Gage	C1 (S) below 2nd Floor B/C connection
147	SA_MS3FB_2_N_C2	Strain Gage	C2 (N) below 2nd Floor B/C connection
148	SA_MS3FB_2_S_C2	Strain Gage	C2 (S) below 2nd Floor B/C connection
149	SR_MS3FB_2_E_C1	Strain Gage	C1 (E) at mid-height of 2nd Story
150	SA_MS3FB_2_ST_B1-2	Strain Gage	Top of F2 B1-2 Fuse nearest to C2
151	SA_MS3FB_2_SB_B1-2	Strain Gage	Bottom of F2 B1-2 Fuse nearest to C2
152	SA_MS3FB_3_NT_B1-2	Strain Gage	Top of F3 B1-2 Fuse nearest to C1
153	SA_MS3FB_3_NB_B1-2	Strain Gage	Bottom of F3 B1-2 Fuse nearest to C1
154	SA_MS3FB_3_N_C1	Strain Gage	C1 (N) below 3rd Floor B/C connection
155	SA_MS3FB_3_S_C1	Strain Gage	C1 (S) below 3rd Floor B/C connection
156	SA_MS3FB_3_N_C2	Strain Gage	C2 (N) below 3rd Floor B/C connection
157	SA_MS3FB_3_S_C2	Strain Gage	C2 (S) below 3rd Floor B/C connection
158	SR_MS3FB_3_E_C1	Strain Gage	C1 (E) at mid-height of 3rd Story
159	SR_MS3FB_3_E_C2	Strain Gage	C2 (E) at mid-height of 3rd Story
160	SA_MS3FB_3_ST_B1-2	Strain Gage	Top of F3 B1-2 Fuse nearest to C2
161	SA_MS3FB_3_SB_B1-2	Strain Gage	Bottom of F3 B1-2 Fuse nearest to C2
162	MOM_MS3FB_1_N_B3-4	Strain Gage	F1 B3-4 Northern Fuse
163	MOM_MS3FB_1_C3	Strain Gage	C3 below 1st Floor B/C connection
164	MOM_MS3FB_1_S_B3-4	Strain Gage	F1 B3-4 Southern Fuse
165	MOM_MS3FB_1_C4	Strain Gage	C4 below 1st Floor B/C connection

Centrifuge Test-3

No.	Label	Type	Location
1	SA_200_FF	ICP	Soil, free-field, 200 mm elevation
2	SA_63_FF	ICP	Soil, free-field, surface
3	SA_63_FF_SW	ICP	Soil, free-field, southwest of container, surface
4	SA_63_FF_W	ICP	Soil, free-field, west of container, surface
5	SA_63_MS1N_3-4	ICP	Soil, under MS1N between C3 and C4, surface
6	SA_63_MS1N_C	ICP	Soil, under center of MS1N, surface
7	SA_63_MS1S_3-4	ICP	Soil, under MS1S between C3 and C4, surface
8	SA_63_MS1S_C	ICP	Soil, under center of MS1S, surface
9	SA_Base_E	ICP	Soil, east of container, base
10	SA_Base_W	ICP	Soil, west of container, base
11	SA_Ftg_FF	ICP	Soil, free-field, footing elevation
12	SA_Ftg_MS1N_3	ICP	Soil, under MS1N F3
13	SA_Ftg_MS1N_4	ICP	Soil, under MS1N F4
14	SA_Ftg_MS1S_3	ICP	Soil, under MS1S F3
15	SA_Ftg_MS1S_4	ICP	Soil, under MS1S F4
16	SA_Ftg_MS2_CW	ICP	Soil, under central west edge of MS2
17	SA_Ftg_MS2_NEI	ICP	Soil, under Northeast corner of MS2
18	SA_Ftg_MS2_NEO	ICP	Soil, outside of northeast corner of MS2
19	SA_Ftg_MS2_SE	ICP	Soil, under southeast corner of MS2
20	SAV_120_MS2_NW	ICP	Vertical soil, under northwest corner of MS2, 120 elevation
21	SAV_120_MS2_SW	ICP	Vertical soil, under southwest corner of MS2, 120 elevation
22	SAV_63_FF	ICP	Vertical soil, free-field, surface
23	SAV_63_N	ICP	Vertical soil, north of container, surface
24	SAV_63_S	ICP	Vertical soil, south of container, surface
25	SAV_Ftg_MS1N_2N	ICP	Vertical soil, outside of North edge of MS1N
26	SAV_Ftg_MS1N_2S	ICP	Vertical soil, outside of South edge of MS1N
27	SAV_Ftg_MS1S_1N	ICP	Vertical soil, outside of North edge of MS1S
28	SAV_Ftg_MS1S_1S	ICP	Vertical soil, outside of South edge of MS1S
29	SAV_Ftg_MS1S_2	ICP	Vertical soil, under center of MS1S
30	SD_200_FF_W	Displ. Gage	Soil, free-field west of container, 200 elevation
31	SD_99_FF_W	Displ. Gage	Soil, free-field west of container, 99 elevation
32	SD_Surf_FF_SW	Displ. Gage	Soil, free-field, southwest of container, surface
33	SD_Surf_FF_W	Displ. Gage	Soil, free-field, west of container, surface
34	A_MS1N_1_x_B3-4	ICP	In-plane, 1 st floor @ East Edge, MS1N
35	A_MS1N_1_x_COM	ICP	In-plane, 1 st floor @ COM, MS1N
36	A_MS1N_1_z_N	MEM	Vertical, 1 st floor @ North end of Mass, MS1N
37	A_MS1N_1_z_S	MEM	Vertical, 1 st floor @ South end of Mass, MS1N
38	A_MS1N_f_x_F1	MEM	In-plane, F1, MS1N
39	A_MS1N_f_x_F1(ICP)	ICP	In-plane, F1, MS1N
40	A_MS1N_f_x_F2	MEM	In-plane, F2, MS1N
41	A_MS1N_f_x_F2(ICP)	ICP	In-plane, F2, MS1N
42	A_MS1N_f_x_F3	ICP	In-plane, F3, MS1N

43	A_MS1N_f_x_F4	ICP	In-plane, F4, MS1N
44	A_MS1N_f_z_F1(N)	ICP	Vertical, F1 (N), MS1N
45	A_MS1N_f_z_F1(S)	ICP	Vertical, F1 (S), MS1N
46	A_MS1N_f_z_F2(N)	ICP	Vertical, F2 (N), MS1N
47	A_MS1N_f_z_F2(S)	ICP	Vertical, F2 (S), MS1N
48	A_MS1N_f_z_F3(N)	MEM	Vertical, F3 (N), MS1N
49	A_MS1N_f_z_F3(S)	MEM	Vertical, F3 (S), MS1N
50	A_MS1N_f_z_F4(N)	MEM	Vertical, F4 (N), MS1N
51	A_MS1N_f_z_F4(S)	MEM	Vertical, F4 (S), MS1N
52	D_MS1N_1_x_C1	Displ. Gage	Horizontal, 1st Floor Height, MS1N
53	D_MS1N_f_x_F1	Displ. Gage	Horizontal, F1, MS1N
54	D_MS1N_f_x_F2	Displ. Gage	Horizontal, F2, MS1N
55	D_MS1N_f_x_F3	Displ. Gage	Horizontal, F3, MS1N
56	D_MS1N_f_x_F4	Displ. Gage	Horizontal, F4, MS1N
57	D_MS1N_f_z_F1	Displ. Gage	Vertical, F1 (COM), MS1N
58	D_MS1N_f_z_F2	Displ. Gage	Vertical, F2 (COM), MS1N
59	D_MS1N_f_z_F3(N)	Displ. Gage	Vertical, F3 (N), MS1N
60	D_MS1N_f_z_F3(S)	Displ. Gage	Vertical, F3 (S), MS1N
61	D_MS1N_f_z_F4(N)	Displ. Gage	Vertical, F4 (N), MS1N
62	D_MS1N_f_z_F4(S)	Displ. Gage	Vertical, F4 (S), MS1N
63	SR_MS1N_1_W_C1(D)	Strain Gage	C1 (W) at mid-height, MS1N
64	SR_MS1N_1_W_C1(H)	Strain Gage	C1 (W) at mid-height, MS1N
65	SR_MS1N_1_W_C1(V)	Strain Gage	C1 (W) at mid-height, MS1N
66	SR_MS1N_1_W_C2(D)	Strain Gage	C2 (W) at mid-height, MS1N
67	SR_MS1N_1_W_C2(H)	Strain Gage	C1 (W) at mid-height, MS1N
68	SR_MS1N_1_W_C2(V)	Strain Gage	C2 (W) at mid-height, MS1N
69	SR_MS1N_1_W_C3(D)	Strain Gage	C3 (W) at mid-height, MS1N
70	SR_MS1N_1_W_C4(D)	Strain Gage	C4 (W) at mid-height, MS1N
71	SA_MS1N_0_N_C1	Strain Gage	C1 (N) at column fuse, MS1N
72	SA_MS1N_0_N_C2	Strain Gage	C2 (N) at column fuse, MS1N
73	SA_MS1N_0_N_C3	Strain Gage	C3 (N) at column fuse, MS1N
74	SA_MS1N_0_N_C4	Strain Gage	C4 (N) at column fuse, MS1N
75	SA_MS1N_0_S_C1	Strain Gage	C1 (S) at column fuse, MS1N
76	SA_MS1N_0_S_C2	Strain Gage	C2 (S) at column fuse, MS1N
77	SA_MS1N_0_S_C3	Strain Gage	C3 (S) at column fuse, MS1N
78	SA_MS1N_0_S_C4	Strain Gage	C4 (S) at column fuse, MS1N
79	SA_MS1N_1_N_C1	Strain Gage	C1 (N) below B/C connection, MS1N
80	SA_MS1N_1_N_C2	Strain Gage	C2 (N) below B/C connection, MS1N
81	SA_MS1N_1_N_C3	Strain Gage	C3 (N) below B/C connection, MS1N
82	SA_MS1N_1_N_C4	Strain Gage	C4 (N) below B/C connection, MS1N
83	SA_MS1N_1_NB_B1-2	Strain Gage	Bottom of B1-2 Fuse nearest to C1, MS1N
84	SA_MS1N_1_NB_B3-4	Strain Gage	Bottom of B3-4 Fuse nearest to C3, MS1N
85	SA_MS1N_1_NT_B1-2	Strain Gage	Top of B1-2 Fuse nearest to C1, MS1N
86	SA_MS1N_1_NT_B3-4	Strain Gage	Top of B3-4 Fuse nearest to C3, MS1N
87	SA_MS1N_1_S_C1	Strain Gage	C1 (S) below B/C connection, MS1N
88	SA_MS1N_1_S_C2	Strain Gage	C2 (S) below B/C connection, MS1N
89	SA_MS1N_1_S_C3	Strain Gage	C3 (S) below B/C connection, MS1N

90	SA_MS1N_1_S_C4	Strain Gage	C4 (S) below B/C connection, MS1N
91	SA_MS1N_1_SB_B1-2	Strain Gage	Bottom of B1-2 Fuse nearest to C2, MS1N
92	SA_MS1N_1_SB_B3-4	Strain Gage	Bottom of B3-4 Fuse nearest to C4, MS1N
93	SA_MS1N_1_ST_B1-2	Strain Gage	Top of B1-2 Fuse nearest to C2, MS1N
94	SA_MS1N_1_ST_B3-4	Strain Gage	Top of B3-4 Fuse nearest to C4, MS1N
95	A_MS1S_1_x_B3-4	ICP	In-plane, 1 st floor @ East Edge, MS1S
96	A_MS1S_1_x_COM	ICP	In-plane, 1 st floor @ COM, MS1S
97	A_MS1S_1_z_N	MEM	Vertical, 1 st floor @ North end of Mass, MS1S
98	A_MS1S_1_z_S	MEM	Vertical, 1 st floor @ South end of Mass, MS1S
99	A_MS1S_f_x_F1	MEM	In-plane, F1, MS1S
100	A_MS1S_f_x_F1(ICP)	ICP	In-plane, F1, MS1S
101	A_MS1S_f_x_F2	MEM	In-plane, F2, MS1S
102	A_MS1S_f_x_F2(ICP)	ICP	In-plane, F2, MS1S
103	A_MS1S_f_x_F3	ICP	In-plane, F3, MS1S
104	A_MS1S_f_x_F4	ICP	In-plane, F4, MS1S
105	A_MS1S_f_z_F1(N)	ICP	Vertical, F1 (N), MS1S
106	A_MS1S_f_z_F1(S)	ICP	Vertical, F1 (S), MS1S
107	A_MS1S_f_z_F2(N)	ICP	Vertical, F2 (N), MS1S
108	A_MS1S_f_z_F2(S)	ICP	Vertical, F2 (S), MS1S
109	A_MS1S_f_z_F3(N)	MEM	Vertical, F3 (N), MS1S
110	A_MS1S_f_z_F3(S)	MEM	Vertical, F3 (S), MS1S
111	A_MS1S_f_z_F4(N)	MEM	Vertical, F4 (N), MS1S
112	A_MS1S_f_z_F4(S)	MEM	Vertical, F4 (S), MS1S
113	D_MS1S_1_x_C2	Displ. Gage	Horizontal, 1st Floor Height, MS1S
114	D_MS1S_f_x_F1	Displ. Gage	Horizontal, F1 (RELATIVE TO MAT), MS1S
115	D_MS1S_f_x_F2	Displ. Gage	Horizontal, F2, MS1S
116	D_MS1S_f_x_F3	Displ. Gage	Horizontal, F3 (RELATIVE TO MAT), MS1S
117	D_MS1S_f_x_F4	Displ. Gage	Horizontal, F4, MS1S
118	D_MS1S_f_z_F1	Displ. Gage	Vertical, F1 (COM), MS1S
119	D_MS1S_f_z_F2	Displ. Gage	Vertical, F2 (COM), MS1S
120	D_MS1S_f_z_F3(N)	Displ. Gage	Vertical, F3 (N), MS1S
121	D_MS1S_f_z_F3(S)	Displ. Gage	Vertical, F3 (S), MS1S
122	D_MS1S_f_z_F4(N)	Displ. Gage	Vertical, F4 (N), MS1S
123	D_MS1S_f_z_F4(S)	Displ. Gage	Vertical, F4 (S), MS1S
124	SR_MS1S_1_W_C1(D)	Strain Gage	C1 (W) at mid-height, MS1S
125	SR_MS1S_1_W_C1(H)	Strain Gage	C1 (W) at mid-height, MS1S
126	SR_MS1S_1_W_C1(V)	Strain Gage	C1 (W) at mid-height, MS1S
127	SR_MS1S_1_W_C2(D)	Strain Gage	C2 (W) at mid-height, MS1S
128	SR_MS1S_1_W_C2(H)	Strain Gage	C2 (W) at mid-height, MS1S
129	SR_MS1S_1_W_C2(V)	Strain Gage	C2 (W) at mid-height, MS1S
130	SR_MS1S_1_W_C3(D)	Strain Gage	C3 (W) at mid-height, MS1S
131	SR_MS1S_1_W_C4(D)	Strain Gage	C4 (W) at mid-height, MS1S
132	SA_MS1S_0_N_C1	Strain Gage	C1 (N) at column fuse, MS1S
133	SA_MS1S_0_N_C2	Strain Gage	C2 (N) at column fuse, MS1S
134	SA_MS1S_0_N_C3	Strain Gage	C3 (N) at column fuse, MS1S
135	SA_MS1S_0_N_C4	Strain Gage	C4 (N) at column fuse, MS1S
136	SA_MS1S_0_S_C1	Strain Gage	C1 (S) at column fuse, MS1S

137	SA_MS1S_0_S_C2	Strain Gage	C2 (S) at column fuse, MS1S
138	SA_MS1S_0_S_C3	Strain Gage	C3 (S) at column fuse, MS1S
139	SA_MS1S_0_S_C4	Strain Gage	C4 (S) at column fuse, MS1S
140	SA_MS1S_1_N_C1	Strain Gage	C1 (N) below B/C connection, MS1S
141	SA_MS1S_1_N_C2	Strain Gage	C2 (N) below B/C connection, MS1S
142	SA_MS1S_1_N_C3	Strain Gage	C3 (N) below B/C connection, MS1S
143	SA_MS1S_1_N_C4	Strain Gage	C4 (N) below B/C connection, MS1S
144	SA_MS1S_1_NB_B1-2	Strain Gage	Bottom of B1-2 Fuse nearest to C1, MS1S
145	SA_MS1S_1_NB_B3-4	Strain Gage	Bottom of B3-4 Fuse nearest to C3, MS1S
146	SA_MS1S_1_NT_B1-2	Strain Gage	Top of B1-2 Fuse nearest to C1, MS1S
147	SA_MS1S_1_NT_B3-4	Strain Gage	Top of B3-4 Fuse nearest to C3, MS1S
148	SA_MS1S_1_S_C1	Strain Gage	C1 (S) below B/C connection, MS1S
149	SA_MS1S_1_S_C2	Strain Gage	C2 (S) below B/C connection, MS1S
150	SA_MS1S_1_S_C3	Strain Gage	C3 (S) below B/C connection, MS1S
151	SA_MS1S_1_S_C4	Strain Gage	C4 (S) below B/C connection, MS1S
152	SA_MS1S_1_SB_B1-2	Strain Gage	Bottom of B1-2 Fuse nearest to C2, MS1S
153	SA_MS1S_1_SB_B3-4	Strain Gage	Bottom of B3-4 Fuse nearest to C4, MS1S
154	SA_MS1S_1_ST_B1-2	Strain Gage	Top of B1-2 Fuse nearest to C2, MS1S
155	SA_MS1S_1_ST_B3-4	Strain Gage	Top of B3-4 Fuse nearest to C4, MS1S
156	A_MS2_1_x_COM	MEM	In-plane, 1 st floor @ COM, MS2
157	A_MS2_1_x_E	ICP	In-plane, 1 st floor @ East Edge, MS2
158	A_MS2_1_z_COM	MEM	Vertical, 1 st floor @ COM, MS2
159	A_MS2_2_x_COM	MEM	In-plane, 2 nd floor @ COM, MS2
160	A_MS2_2_x_E	ICP	In-plane, 2 nd floor @ East Edge, MS2
161	A_MS2_2_y_COM	MEM	Out-of-plane, 2 nd floor @ COM, MS2
162	A_MS2_2_z_N	MEM	Vertical, 2 nd floor @ North end of Mass, MS2
163	A_MS2_2_z_S	MEM	Vertical, 2 nd floor @ South end of Mass, MS2
164	A_MS2_f_x_COM	ICP	In-plane, Center of Foundation, MS2
165	A_MS2_f_x_NE	ICP	In-plane, Northeast corner of mat, MS2
166	A_MS2_f_z_NE	ICP	Vertical, Northeast corner of mat, MS2
167	A_MS2_f_z_NW	ICP	Vertical, Northeast corner of mat, MS2
168	A_MS2_f_z_SE	ICP	Vertical, Southeast corner of mat, MS2
169	A_MS2_f_z_SW	ICP	Vertical, Southwest corner of mat, MS2
170	D_MS2_1_x_COM	Displ. Gage	Horizontal, at 1st Floor Height, MS2
171	D_MS2_f_x_COM	Displ. Gage	Horizontal, Center of Mass of mat, MS2
172	D_MS2_f_z_NE	Displ. Gage	Vertical, Northeast corner of mat, MS2
173	D_MS2_f_z_SE	Displ. Gage	Vertical, Southeast corner of mat, MS2
174	Base_East_House_x	ICP	East Shaker (House Accel)
175	Base_West_House_x	ICP	West Shaker (House Accel)
176	Center_Beam_x	ICP	Center Rack Beam
177	Center_Beam_z	ICP	Center Rack Beam
178	Top_Ring_Offthr_z	ICP	Center of Top Soil Box Ring (North Side)
179	Top_Ring_South_x	ICP	Center of Top Soil Box Ring (South Side)
180	Top_Ring_South_z	ICP	Center of Top Soil Box Ring (South Side)